

Universität
Rostock



Traditio et Innovatio

Methods development
for site-specific investigation of
biomolecular structure and dynamics
with DNP-enhanced solid-state NMR

Dissertation

to obtain the academic degree

doctor rerum naturalium (Dr. rer. nat.)

of the Faculty of Mathematics and Natural Science

at the University of Rostock

Submitted by

M.Sc. Thomas Biedenbänder

born on 8. May 1996

in Darmstadt, Germany.

Rostock, December 2024

First Expert Assessor	Prof. Dr.-Ing. Björn Corzilius University of Rostock Faculty of Mathematics and Natural Science Institute of Chemistry and Department Life, Light and Matter
Second Expert Assessor	Prof. Dr. Thomas Vosegaard Aarhus University Faculty of Natural Sciences Department of Chemistry and Interdisciplinary Nanoscience Center
Year of Submission	December 2024
Year of Defense	May 2025



Dieses Werk ist lizenziert unter einer Creative Commons Namensnennung-Nicht kommerziell-Share alike 4.0 International Lizenz.

For my family and girlfriend.

Table of Contents

Table of Contents	I
Declaration of Authorship	V
Summary	VII
Zusammenfassung	IX
List of abbreviations.....	XI
1. General Introduction.....	1
1.1 Concepts of Dynamic Nuclear Polarization	2
1.1.1 DNP enhancement	2
1.1.2 Spin interactions	4
1.1.3 Sample constitution	7
1.1.4 Spread of polarization.....	8
1.2 Relaxation and Dynamics.....	9
1.2.1 Stochastic relaxation theory	10
1.2.2 Transition probabilities and the Solomon equations	11
1.2.3 Methyl group dynamics.....	13
1.2.4 Paramagnetic Relaxation.....	21
2. Motivation and Aim.....	23
3. Material and Methods.....	25
3.1 Combination of Cross Relaxation with Rotational Resonance	25
3.1.1 Systematic investigation of the MAS frequency-dependency of SCREAM-DNP experiments with selectively labeled ethyl acetate.....	25
3.1.2 Applications of SCREAM-DNP experiments with dipolar recoupling in a ribonucleoprotein complex.....	27
3.2 Matrix-free DNP for the investigation of powder samples	29
3.2.1 Systematic investigation of the matrix-free DNP approach in model proteins	29

3.2.2	Characterization of A β ₁₋₄₂ -adsorbing materials using matrix-free DNP .	31
3.2.3	Site-specific investigation of API-carrying polymeric micelles.....	35
3.3	Quantification of Methyl Group Dynamics under DNP conditions.....	37
3.3.1	Investigation of Methyl Group Dynamics in A β ₁₋₄₀ fibrils by DNP-enhanced 1H–2H CPMAS NMR	37
3.3.2	Systematic investigation of methyl group dynamics under DNP conditions	41
4.	Results and Discussion.....	45
4.1	Combination of Cross Relaxation with Rotational Resonance	45
4.1.1	Systematic investigation of the MAS frequency-dependency of SCREAM-DNP experiments with selectively labeled ethyl acetate.....	45
4.1.2	Applications of SCREAM-DNP experiments with dipolar recoupling in a ribonucleoprotein complex.....	53
4.1.3	Summary and Outlook.....	61
4.2	Matrix-free DNP for the investigation of powder samples	62
4.2.1	Systematic investigation of the matrix-free DNP approach in model proteins	62
4.2.2	Characterization of A β ₁₋₄₂ -adsorbing materials using matrix-free DNP .	65
4.2.3	Site-specific investigation of API-carrying polymeric micelles.....	73
4.2.4	Summary and Outlook.....	79
4.3	Quantification of Methyl Group Dynamics under DNP conditions.....	81
4.3.1	Investigation of Methyl Group Dynamics in A β ₁₋₄₀ fibrils by DNP-enhanced 1H–2H CPMAS NMR	82
4.3.2	Systematic investigation of methyl group dynamics under DNP conditions	92
4.3.3	Summary and Conclusion	107
5.	Conclusion.....	108
6.	Appendix	111
6.1	Combination of Cross Relaxation with Rotational Resonance	111

6.1.1	Systematic investigation of the MAS frequency-dependency of SCREAM-DNP experiments with selectively labeled ethyl acetate.....	111
6.2	Matrix-free DNP for the investigation of powder samples	113
6.2.1	Systematic investigation of the matrix-free DNP approach in model proteins	113
6.2.2	Characterization of A β ₁₋₄₂ -adsorbing materials using matrix-free DNP	118
6.2.3	Site-specific investigation of API-carrying polymeric micelles.....	123
6.3	Quantification of Methyl Group Dynamics under DNP conditions.....	125
6.3.1	Investigation of Methyl Group Dynamics in A β ₁₋₄₀ fibrils by DNP-enhanced 1H–2H CPMAS NMR.....	125
6.3.1	Systematic investigation of methyl group dynamics under DNP conditions	134
7.	References	142
8.	Acknowledgements	155
9.	Publications	159
10.	Conference contributions.....	161

Declaration of Authorship

I hereby declare that I have composed the presented work independently and on my own and without other resources than the ones indicated.

Thomas Biedenbänder

Rostock, December 2024

Summary

This work presents advancements in Dynamic Nuclear Polarization (DNP) techniques, focusing on SCREAM-DNP, matrix-free DNP and techniques for relaxation measurements. All three techniques are aimed to increase the applicability of DNP towards the detailed study of structure and dynamics of biomolecules or (bio)materials in structural biology and medicinal applications.

SCREAM-DNP utilizes active motions (*e.g.* methyl group dynamics) for a cross-relaxation-induced, site-specific transfer of hyperpolarization to these active sites from which polarization is spread unselective to nearby like nuclei. Site-specific NMR experiments are especially valuable for biomolecules which are composed of four chemically similar nucleotides in the case of nucleic acids or 20 chemically similar amino acids in the case of proteins.

Accordingly, the first part of this work investigates the combination of the SCREAM-DNP experiment with rotational resonance dipolar recoupling to achieve selective and accelerated polarization transfer to specific molecular sites, such as carbonyl groups in ethyl acetate and nucleobases in ribonucleoprotein complexes. This acceleration may enable the possibility to use SCREAM-DNP as a spectral filter for multidimensional NMR experiments.

The second part is about the optimization of a DNP sample preparation technique, which mixes the molecule of interest with the polarizing agent in a matrix-free manner. This matrix-free DNP approach is advantageous for challenging systems like insoluble proteins and biomaterials, such as amyloid-beta ($A\beta$)-adsorbing cellulose and drug-carrying micelles. The medicinal interest in these kinds of systems is large due to the necessity of an effective medicinal product or drug candidate for treating Alzheimer's disease or studying the increasingly large number of hydrophobic drug candidates. Large DNP enhancements, for example, allow the quantification of adsorbed $A\beta$ peptides and reveal structural details, providing insights into the material's efficacy as a potential therapeutic filter.

The third part investigates the applicability of DNP for relaxation measurements. Two types of systems were used: $A\beta$ fibrils in a matrix-free sample and ethanol in a glycerol:water matrix. Both samples experience large sensitivity enhancements by DNP and are affected by an expected effect which is based on paramagnetic relaxation enhancement (PRE). In both

cases, further unexpected effects occur concerning the coupling of dynamics with the paramagnetic interaction as well as matrix morphology effects and detection of relaxation hot spots.

In total, this work demonstrates the potential of DNP for site-specific investigations of biomolecular structures and applications towards challenging and insoluble systems. In addition, this work displays the advantages and disadvantages of using DNP for measurements of nuclear relaxation time constants. The results, but also the remaining challenges presented in this work indicate future directions. On the one hand, the matrix-free DNP approach as well as SCREAM-DNP greatly expands the applicability of DNP, for example, enabling two-dimensional NMR experiments with controlled polarization pathways in medically relevant, but insoluble systems such as A β plaques or hydrophobic drugs like the HIV-1 drug efavirenz. On the other hand, this work displays the necessity for a deeper understanding of PRE-like effects in DNP. Future directions include systematic investigations of PRE-like effects on nuclear and electron relaxation times and strategies to mitigate these effects, such as photochemically switching paramagnetic centers or the decoupling of electron-nuclear interactions during NMR detection. These advancements may pave the way for more efficient and targeted DNP experiments to study biomolecular structures and dynamics.

Zusammenfassung

Diese Arbeit präsentiert Entwicklungen in der Methode der dynamischen Kernpolarisation (DNP), wobei der Schwerpunkt auf SCREAM-DNP, Matrix-freier DNP und der Anwendung von DNP für Messungen von Relaxationszeiten liegt. Alle drei Techniken zielen darauf ab, die allgemeine Anwendbarkeit der DNP für die Untersuchung der Struktur und Dynamik von Biomolekülen oder (Bio-)Materialien in der Strukturbiologie und bei medizinischen Anwendungen zu verbessern.

Die Methode der SCREAM-DNP nutzt aktive Bewegungen (z. B. Methylgruppendynamik) für eine Kreuzrelaxations-induzierte, ortsspezifische Übertragung der Hyperpolarisation auf diese aktiven Stellen, von denen aus die Polarisation nicht-selektiv auf nahe gelegene Kerne übertragen wird. Ortsspezifische NMR-Experimente sind besonders wertvoll für Biomoleküle, die entweder aus vier chemisch ähnlichen Nukleotiden im Falle von Nukleinsäuren oder aus 20 ähnlichen Aminosäuren im Falle von Proteinen zusammengesetzt sind.

Dementsprechend wird im ersten Teil dieser Arbeit die Kombination von SCREAM-DNP mit *rotational resonance*, einer dipolaren Rückkopplungsmethode, untersucht, um einen selektiven und beschleunigten Polarisationstransfer zu bestimmten Molekülstellen, beispielsweise Carbonylgruppen in Ethylacetat oder Nukleobasen in Ribonukleoprotein-Komplexen, zu erreichen. Diese Beschleunigung könnte es möglich machen, SCREAM-DNP als Spektralfilter für multidimensionale NMR-Experimente zu verwenden.

Der zweite Teil der Arbeit befasst sich mit der Optimierung einer Technik zur DNP-Probenvorbereitung. Hier wird das Molekül von Interesse mit dem Polarisationsmittel auf eine Matrix-freie Weise gemischt. Daher ist der Ansatz vorteilhaft für Proben, darunter unlösliche Proteine und Biomaterialien, wie zum Beispiel Amyloid- β ($A\beta$)-adsorbierende Cellulose oder arzneimitteltragende Mizellen. Das medizinische Interesse dieser Proben ist groß, da ein wirksames Arzneimittel oder Medizinprodukt zur Behandlung der Alzheimer-Krankheit oder zur Untersuchung der immer zahlreicher werdenden hydrophoben Arzneimittelkandidaten benötigt wird. Die starken Signalverstärkungen durch die DNP-Methode ermöglichen zum Beispiel die Quantifizierung der adsorbierten $A\beta$ -Peptide und geben Aufschluss über Details in ihrer Struktur oder Wirksamkeit des Materials als potenzieller therapeutischer Filter.

Der dritte Teil dieser Arbeit untersucht die Anwendbarkeit der DNP für die Messungen von Relaxationszeitkonstanten. Dafür wurden zwei unterschiedliche Proben verwendet: A β ₁₋₄₀-Fibrillen mit der Matrix-freien Präparationstechnik und Ethanol in einer Glycerol:Wasser-Matrix. Beide Proben zeigen einerseits eine große Empfindlichkeitsverstärkung durch DNP, aber auch den erwarteten Effekt, der auf der paramagnetischen Relaxationsverstärkung (PRE) basiert. In beiden Fällen treten weitere unerwartete Effekte auf, wie zum Beispiel die Kopplung der untersuchten molekularen Dynamik mit der paramagnetischen Wechselwirkung, sowie die Auswirkungen der Matrixmorphologie und die Detektion von Relaxations-Hotspots.

Insgesamt zeigt diese Arbeit das Potenzial von DNP für die ortsspezifische Untersuchung von biomolekularen Strukturen oder für die Anwendung in schwierigen oder unlöslichen biologischen Systemen. Darüber hinaus behandelt die Arbeit die Vor- und Nachteile der Verwendung von DNP für Messungen von Kernrelaxationszeitkonstanten. Die Ergebnisse sowie die verbleibenden Herausforderungen, die in dieser Arbeit vorgestellt werden, stellen die Weichen für zukünftige Studien. Einerseits erweitert der Matrix-freie DNP-Ansatz sowie SCREAM-DNP die Anwendbarkeit von DNP erheblich und ermöglicht beispielsweise zweidimensionale NMR-Experimente mit kontrolliertem Polarisationstransfer in medizinisch relevanten, aber unlöslichen Systemen wie A β -Plaques oder hydrophoben Medikamenten wie dem HIV-1 Medikament Efavirenz. Andererseits zeigt diese Arbeit die Notwendigkeit eines tieferen Verständnisses der PRE-ähnlichen Effekte, welche in der DNP auftreten. Zukünftige Richtungen umfassen die systematische Untersuchung des PRE-ähnlichen Effekts durch Messung von Kern- und Elektronrelaxationszeitkonstanten oder Strategien zur Abschwächung des Effekts, wie zum Beispiel das photochemische Umschalten der paramagnetischen Zentren oder die Entkopplung von Elektron-Kern-Wechselwirkungen während der NMR-Detektion. Diese Fortschritte könnten den Weg für effizientere und gezieltere DNP-Experimente zur Untersuchung biomolekularer Strukturen und Dynamiken ebnen.

List of abbreviations

API	Active Pharmaceutical Ingredient
A β	Amyloid- β
CPMAS	Cross Polarization under MAS
cryo-EM	Cryogenic Electron Microscopy
CSA	Chemical Shift Anisotropy
DARR	Dipolar-assisted Rotational Resonance
DMSO	Dimethyl Sulfoxide
DNA	Desoxyribonucleic Acid
DNP	Dynamic Nuclear Polarization
DQ	Double-quantum Coherence
EPR	Electron Paramagnetic Resonance
FID	Free Induction Decay
hetNOE	Heteronuclear Nuclear Overhauser Enhancement
HIV-1	Human Immunodeficiency Virus Type 1
ITC	Isothermal Titration Calorimetry
LAC	Level Anti Crossing
MAS	Magic Angle Sample Spinning
MBM	MeO _x -BuO _z i-MeO _x
mRNA	Messenger RNA
NMR	Nuclear Magnetic Resonance
NNRTI	Non-nucleoside Reverse Transcriptase Inhibitor
NOE	Nuclear Overhauser enhancement
PDA	Polydopamine
PDSO	Proton-driven Spin Diffusion
PRE	Paramagnetic Relaxation Enhancement
R ²	Rotational Resonance
REDOR	Rotational Echo Double Resonance
rf	Radiofrequency
RMS	Root-mean-square
RNA	Ribonucleic Acid
RNP	Ribonucleoprotein
rRNA	Ribosomal RNA
SCREAM-DNP	Specific Cross Relaxation by Active Motions under DNP
SD	Spin Diffusion
SNR	Signal-to-noise Ratio
SQ	Single-quantum Coherence
TCE	1,1,2,2-tetrachloroethane
TEDOR	Transfer Echo Double Resonance
TFSI	Bis(trifluoromethanesulfonyl)imide
tRNA	Transfer RNA
ZQ	Zero-quantum Coherence

1. General Introduction

The complexity of organisms stems from a variety of biomolecules which regulate and interact with each other in a very specific way. Most interestingly, the fundamental basis of these biomolecules is composed of only a few compounds such as nucleotides or amino acids, assembling in different sequences and subsequently taking on different shapes, which determine their functional origin. As a good example, transfer ribonucleic acid (tRNA) consists of 4 basic nucleotides, which assemble into the famous cloverleaf secondary structure and the L-shaped tertiary structure, nevertheless, display minor differences in their shapes to be distinguishable for the manifold of aminoacyl tRNA synthetase and the ribosome during protein expression.^[1] As a conclusion, understanding the structure and dynamics of one biomolecule can give key insights into its biological function. This started more than a century ago, when the first three-dimensional molecular structure was solved by X-ray diffraction.^[2] Despite being the structure of salt, it was the starting point for a new aspect in life sciences,^[3] producing biological important results such as the first 3D structure of a DNA (desoxyribonucleic acid) helix.^[4] However, a crystal of the molecule of interest is mandatory, which cannot always be achieved, for example for membrane proteins, where the for the proteins' native state required lipid bilayer/mimic often interferes with the crystallization process.^[5] Besides XRD, cryogenic electron microscopy (cryo-EM) evolved as a valuable tool due to its simple sample preparation and applicability to a variety of large biomolecules. As both methods involve a rigid matrix, local dynamics cannot be resolved with those, rendering nuclear magnetic resonance (NMR) spectroscopy a valuable tool for structural dynamics.^[6]

NMR spectroscopy can be performed in solution or solid state. In general, solution-state NMR yields high-resolution due to fast molecular tumbling of small molecules, favorable for determination of structure and dynamics of those.^[7] As the size of biomolecules increases, the molecular tumbling time constant prolongs and broadened resonance lines are observed resulting in a loss of resolution. Here, solid-state NMR has evolved as an important method for characterization of high-molecular mass complexes^[8], membrane proteins and interactions,^[9] and insoluble or disordered systems.^[10] These large numbers of studies are indicative of the potential of solid state NMR. Nonetheless, NMR is an intrinsically insensitive method rendering these studies time intensive. One solution to this problem is dynamic nuclear

polarization (DNP), where the underlying concept and the potential for structural biology will be discussed in the following.

1.1 Concepts of Dynamic Nuclear Polarization

This section will introduce and discuss the sensitivity enhancement by DNP as well as the required spin interactions for polarization transfer. In addition, practical aspects of DNP such as sample constitution and exemplary experiments are discussed.

1.1.1 DNP enhancement

Many nuclei possess an intrinsic property known as spin which is described by a spin quantum number I .^[11] In addition, the nuclei possess $2I + 1$ spin states, which are degenerate under standard conditions.^[12] In the presence of a strong magnetic field B_0 , the degeneracy of the spin states is broken and quantized into the $2I + 1$ states with distinct energy levels:

$$E = -\hbar m_I \gamma B_0, \quad (1)$$

where m_I is the quantum number of the spin state and γ the gyromagnetic ratio of the nucleus. This Zeeman spin interaction with the external magnetic field is described with the Hamiltonian $\hat{\mathcal{H}}_Z$ and results in the nuclear Zeeman splitting:

$$\Delta E = \hbar \gamma B_0 = \hbar \omega_0, \quad (2)$$

where ΔE is the energy difference, \hbar the reduced Planck constant, and ω_0 the nuclear Larmor frequency. The magnetic field-dependent energy difference results in a polarization P between the spin states which can be calculated following the Boltzmann distribution, for example, for a spin- $1/2$:

$$P = \frac{N_\alpha - N_\beta}{N_\alpha + N_\beta} = \tanh\left(\frac{\hbar \gamma B_0}{2k_B T}\right), \quad (3)$$

where N_α and N_β denotes the two spin states of the spin- $1/2$ nucleus, k_B is the Boltzmann constant, and T the temperature. In the case of ^1H , this polarization is $\sim 0.01\%$ at room temperature indicating that only 1 out of 10^4 active spins are resulting in a detectable signal (Figure 1A). In contrast, the spin of an unpaired electron has a tremendously larger gyromagnetic ratio than any nucleus, resulting in higher polarization differences and thus, higher signal sensitivities.

The transfer of the high electron polarization to a nucleus is the idea of DNP. This was first proposed by Overhauser in 1953^[13] and experimentally confirmed by Carver and Slichter at the same time in 1953.^[14] However, the applicability for structural biology required a high-frequency, high-power microwave source in order to obtain sufficient nuclear sensitivity enhancements at high magnetic fields. The development of a continuous wave cyclotron resonance maser (gyrotron) in the groups of Griffin and Temkin in 1993 enabled DNP for higher magnetic fields and thus, for NMR on biomolecules (see Ref. ^[15] for a full description on the historical development of DNP).^[16] With the development of the gyrotron, 10-fold higher DNP enhancement factors, being one measure of sensitivity enhancement, can be observed.^[17] Here, the enhancement factor is defined as the following:

$$\epsilon_{\max} = \frac{P_e}{P_n} \approx \left| \frac{\gamma_e}{\gamma_n} \right| \text{ for } \gamma_e \hbar B_0 \ll k_B T, \quad (3)$$

where ϵ_{\max} is the maximal signal enhancement, P_e and P_n the spin polarizations, and γ_e and γ_n the gyromagnetic ratio of the electron spin and the nuclear spin, respectively. From Equation 3 follows that the $\epsilon_{\max, \text{H}}$ will be ~ 658 and other nuclei will display greater DNP enhancement factors in theory (Figure 1B). In practice, this reduces to lower values, where ^1H DNP enhancement factors of ~ 250 are routinely observed in standard DNP experiments.^[18] The reasons for the *in praxi* reduced enhancement factors are manifold and can be summed up in a temperature-dependent efficiency factor $\xi(T)$. In addition, the actual DNP enhancement factor cannot always be determined directly from microwave on/off comparison of the doped sample due to depolarization of the nuclei, happening during the most-commonly used DNP mechanism, the cross effect, if microwaves are absent (*vide infra*).^[19] Hence, to obtain the actual signal enhancement, the signal amplitude per time unit of the doped sample must be compared to an undoped sample. Additionally, with increased knowledge of DNP mechanisms, it becomes evident that both the final signal amplitude and the rate constant are crucial parameters for achieving maximum sensitivity. The DNP build-up rate constant being the inverse of the time constant ($R_B = T_B^{-1}$) is given by:

$$R_B = R_{\text{DNP}} + R_{1,n}, \quad (4)$$

where R_{DNP} is rate the constant building up polarization on the nucleus, whereas $R_{1,n}$ is the nuclear spin-lattice relaxation rate driving P_n towards thermal polarization. This resulted in the following measure:

$$S = \frac{\epsilon}{\sqrt{T_{\text{DNP}}}} \quad (5)$$

where S is the relative sensitivity gain measuring the obtained enhancement factor per unit time.^[20]

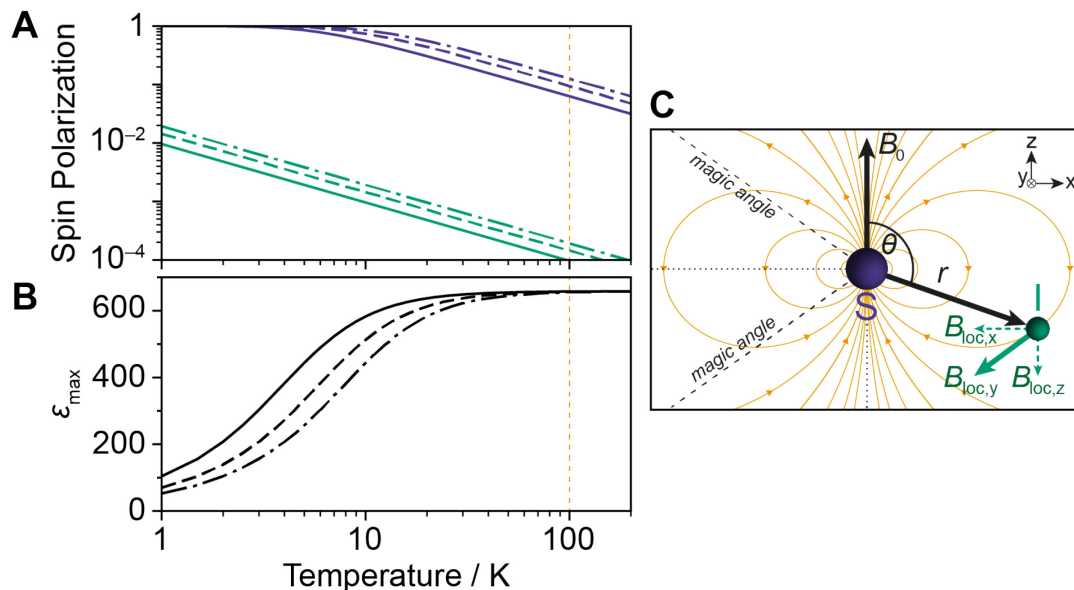


Figure 1: (A) Absolute spin polarization for a ¹H spin (green) and an electron spin (violet) and (B) the resulting maximum theoretical DNP enhancement factor as a function of temperature. A g -factor of 2 is assumed for the electron and all values are calculated with Equation 3 using magnetic fields (B_0) of 9.4 T (solid lines), 14.1 T (dashed lines), and 18.8 T (dash-dotted lines). The commonly used temperature for DNP experiments ($T = 100$ K) is marked by a vertical green line. (C) Dipole-dipole interaction between an electron spin S and a nuclear spin I relative to the external magnetic field B_0 . The presence of the electron spin induces a local magnetic field B_{loc} which consist of the transverse component $B_{\text{loc},x}$ and the longitudinal component $B_{\text{loc},z}$. The strength of B_{loc} is defined by the distance r , separating the nuclear and the electron spin and the angle θ between the distance vector and the external magnetic field B_0 . Reprinted and adapted with permission from Biedenbänder *et al.*^[15] (Copyright 2022 by the American Chemical Society)

1.1.2 Spin interactions

Several spin interactions are present during NMR experiments and they can be categorized into an external and an internal part.^[21] One of the two major external interactions is the above-described Zeeman interaction. The second one describes the spin interaction with radiofrequency (rf) pulses ($\hat{\mathcal{H}}_{\text{rf}}$), tilting the magnetization into the transversal plane. The internal nuclear spin interactions mainly involve 4 parts: (1) the chemical shift anisotropy (CSA) $\hat{\mathcal{H}}_{\text{CSA}}$ describing the unique local magnetic fields induced by the surrounding electron environment; (2) the dipolar coupling $\hat{\mathcal{H}}_{\text{d}}$, characterizing the coupling of two adjacent nuclear magnetic moments; (3) the scalar or J -coupling $\hat{\mathcal{H}}_{\text{j}}$, which is an indirect nuclear dipole-dipole coupling as it involves assistance of the electrons in the chemical bonds; (4) the quadrupolar interaction $\hat{\mathcal{H}}_{\text{Q}}$, being present in nuclei with spins $I > 1/2$, where the quadrupole moment of the spin couples to the electric field gradient induced by the surrounding electrons. Besides,

nuclear-electron spin-spin interactions exist, which are called hyperfine interactions (HFI). In the following, the dipolar coupling and the HFI will be described in more detail as both are mandatory for DNP experiments.

1.1.2.1 Dipolar coupling

The dipolar coupling describes the interaction of two spins. As both spins possess a magnetic moment, both are independently generating a magnetic field (Figure 1C), which the other spin is affected by. The general form of the coupling Hamiltonian is given by:^[22]

$$\hat{\mathcal{H}}_d = \hat{I}_j^\dagger D_{jk} \hat{I}_k, \quad (6)$$

where $\hat{I}_{j/k}$ is the spin operator, \dagger denotes the adjoint of the spin operator, and D_{jk} is the dipolar coupling tensor. The tensor involves the dipolar coupling constant d_{jk} , which is a measure of the interaction strength and is given by:

$$d_{jk} = -\frac{\mu_0 \gamma_j \gamma_k \hbar}{4\pi r_{jk}^3}, \quad (7)$$

where μ_0 is the vacuum magnetic permeability, and r_{jk} the distance between the two interacting spins. In most cases, the Hamiltonian from Equation 6 is simplified by omitting all non-secular parts of the interaction tensor D_{jk} . Note, secular parts are commuting with the Zeeman Hamiltonian \hat{H}_Z . Using this simplification, Equation 6 yields two cases: dipolar coupling between like (homonuclear case) and between unlike spins (heteronuclear case). The Hamiltonian for the homonuclear case is as following:

$$\hat{\mathcal{H}}_d^{\text{homo}} = \frac{1}{2} d_{jk} (1 - 3 \cos^2 \theta_{jk}) \left[3 \hat{I}_{j,z} \hat{I}_{k,z} - \hat{I}_j \cdot \hat{I}_k \right], \quad (8)$$

where θ_{jk} is the angle between the vector connecting the two spins and the external magnetic field, $\hat{I}_{j/k,z}$ is the z component of the respective spin operator, and $\hat{I}_j \cdot \hat{I}_k$ is referred to as the *flip-flop* term indicating that this term is responsible for polarization exchange between the spins. This *flip-flop* term is missing in the dipolar Hamiltonian of the heteronuclear case, which is given by:

$$\hat{\mathcal{H}}_d^{\text{hetero}} = d_{jk} (1 - 3 \cos^2 \theta_{jk}) \hat{I}_{j,z} \hat{S}_{k,z}, \quad (9)$$

where $\hat{S}_{k,z}$ is the z component of the heteronuclear spin operator. Due to the *flip-flop* term, an energy-conserving propagation of polarization is possible in the homonuclear case allowing for

the phenomena of spin diffusion,^[23] which will be discussed later. In addition, Equations 8 and Equation 9 display an orientation-dependent factor, which can be important for structural investigations in the static case. On the other hand, this factor becomes zero at an angle of $\sim 54.74^\circ$ (*viz.* the magic angle), resulting in no contribution of the orientation-dependent internal spin interactions, which would otherwise cause tremendous line broadening. In practice, this is utilized during magic angle sample spinning (MAS), where the sample is spun around the magic angle. Note, that the spin interactions are refocused during one MAS rotor period and thus effectively average to zero. Nonetheless, depending on the magnitude of the spin interaction, refocusing of the interaction is not complete, resulting in a time-dependent part of the spin Hamiltonian, which arises as rotational side bands at multiples of the MAS frequency in the NMR spectrum.

1.1.2.2 Hyperfine interaction

The interaction between an electron spin (\hat{S}) and a nucleus (\hat{I}) is described by the HFI.^[24] The corresponding Hamiltonian is as following:

$$\hat{\mathcal{H}}_{\text{HFI}} = \hat{S}A\hat{I}, \quad (10)$$

where A is the interaction tensor of the HFI and consists of two contributions: the isotropic *Fermi*-contact interaction and the dipolar coupling of the electron and nuclear magnetic moments. The first contribution is isotropic and arises due to the probability density of the electron at the site of the nucleus.^[25] The dipolar contribution of the HFI (Figure 1C) is the driving contribution for the cross effect, which is the main mechanism used in DNP studies, including this work, mainly due to its higher transition moment and transition probability as compared to other DNP mechanisms.^[26] In short, the cross effect occurs in a three-spin system, where two electron spins and one nucleus are coupled by dipolar interaction or in the case of the nucleus, HFI to at least one electron spin. The therefrom resulting matching condition is as following:

$$\omega_{\Delta} = \omega_{0S_1} - \omega_{0S_2} \approx \pm\omega_{0I}, \quad (11)$$

where ω_{Δ} is the difference in electron Larmor frequencies, ω_{0S_1} and ω_{0S_2} the Larmor frequencies of the two electron spins, and ω_{0I} the nuclear Larmor frequency. The electron dipolar coupling and/or the exchange interaction and the HFI between one electron and the nuclear spin demands a rigid spin network, otherwise the transition moment of the cross effect will be drastically reduced. This requirement renders this DNP mechanism a pure solid-state

mechanism. Aspects to achieve the solid state for all kinds of biomolecules as well as the mechanisms to spread the transferred hyperpolarization will be discussed in the next sections.

1.1.3 Sample constitution

The electron spin polarization, which is central for hyperpolarization by DNP, is transferred by DNP mechanisms such as the cross effect to the nuclear spins. This necessitates the doping of the sample with unpaired electrons, which are incorporated into the sample by adding polarizing agents (PAs). In the most cases, the PAs are bis-nitroxide radicals such as TOTAPOL (1-(TEMPO-4-oxy)-3-(TEMPO-4-amino)propan-2-ol),^[27] AMUPol (Aix-Marseille Université polarizing agent),^[28] and ASYMPol-POK;^[29] however, PAs with mixed radical moieties such as trityl-nitroxide^[30] and BDPA-nitroxide^[31] are developed, indicating that the field of PAs is in constant development and optimization.

In addition to the doping of the sample, DNP experiments are typically performed at cryogenic temperature of about 100 K to ensure slow relaxation of the electron and nuclear spins and to provide a rigid matrix for efficient DNP transfer (*vide supra*) and spread of polarization (*vide infra*).^[15] In the case of biomolecules, glycerol as cryoprotecting agent is added to the dissolved biomolecules to achieve a glass suitable for microwave penetration and preventing sample crystallization,^[32] though, not always completely.^[33] However, the addition of glycerol is reducing the sample concentration which decreases the obtainable NMR sensitivity. In addition, it was shown that glycerol can decrease the biomolecule's functionality^[34] or cell viability.^[35] One solution is to decrease the amount of glycerol in the sample in order to reduce biological stress on the sample, but maintain the cryoprotecting function.^[36] Other cryoprotecting agents were studied as well, including dimethyl sulfoxide (DMSO),^[37] frozen polyacrylamide gels,^[38] and sugar-based cryoprotecting agents like sucrose,^[39] trehalose,^[40] and sorbitol.^[41] However, they either are under development (trehalose and sorbitol), have not been studied with biomolecules (polyacrylamide gels), or have a higher toxicity and/or larger potential for degradation of biomolecules than glycerol (DMSO).^[42] In contrast, research on the feasibility of experiments performed without solvent—thus dubbed matrix-free DNP—was investigated by several groups.^[43] These studies introduced the PA either by attaching it to the molecule of interest, by impregnating the sample with PA in water or glycerol:water solutions (or any solvent), or by preparing a suspension and subsequent freeze-drying to obtain a powder. In general, these matrix-free approaches are especially useful for molecules which are either insoluble in aqueous solutions or sensitive towards glycerol-

induced effects such as the disruption of their hydration shell. As a side note, the sample filling factor for the sample is increased as glycerol is not added.

1.1.4 Spread of polarization

After the generation of hyperpolarization on the nuclei at a spatially limited spot (around the PA), the polarization propagates throughout the sample in order to polarize distant molecules which are less affected by strong HFI with the electron (*vide infra*). This propagation is based on spin diffusion (SD), which utilizes flip-flop processes between dipolar-coupled spins.^[44] These flip-flop processes happen spontaneously between like spins which are in opposite spin states (*viz.* spin up and down or vice versa). Additionally, if a strong network of like spins uniformly distributed across the matrix is given, the flip-flops are energy-conserving and the propagation can be described as a mechanical diffusion of polarization over time following Fick's second law. Note, that the strength of dipolar coupling directly influences the rate of spin diffusion resulting in the highest celerity of SD for ^1H . Other nuclei with low gyromagnetic ratios can be used as well, however, display slower DNP build-up rate constants R_B as SD is retarded due to the lower gyromagnetic ratios and/or the dilution of the spin in the sample.^[45] It has to be noted that for a system with strongly diluted spins, the term spin diffusion is misleading as this propagation process cannot be described by Fick's second law anymore. A heteronuclear dipolar coupling of a dilute species to a highly abundant species increases significantly the celerity of SD (*e.g.*, ^{13}C to ^1H); hence, this type of SD is called proton-driven spin diffusion (PDSD).

1.1.4.1 Indirect and Direct DNP

As discussed above, ^1H nuclei in a DNP sample display a fast SD process, whereas low- γ nuclei such as ^{13}C possess a low celerity due to the low gyromagnetic ratio and the lower abundance in a biomolecule. Furthermore, direct DNP requires a direct interaction of electron with an adjacent nucleus (*e.g.*, ^{13}C), both contributions rendering direct DNP time-intensive. The required proximity severely limits the applicability of the direct DNP approach as the proximity of the ^{13}C nucleus to the PA introduces paramagnetic relaxation enhancement (PRE)-like effects.^[46] Consequently, these nuclei are usually indirectly detected using a relayed pathway involving a heteronuclear polarization transfer such as cross polarization (Figure 2)^[47] or cross relaxation (see Subsection 1.2.3.1). Here, due to the fast celerity of the ^1H spin diffusion process, a selective excitation of nuclei of interest is often impossible. Due to the significantly lower polarization spreading in the direct DNP case, direct DNP can be a valuable

tool as it provides selectivity via the slow polarization build-up kinetics and/or the labeling of the PA.

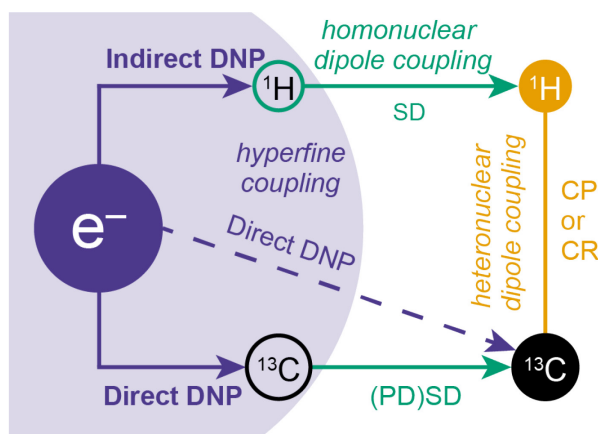


Figure 2: Scheme of the possible transfer pathways in DNP experiments. The electron spin (violet) is transferring its polarization via the cross effect to nearby nuclei which are affected by strong PRE-like effects (highlighted by the light violet sphere). From these nuclei, the polarization is spread among like nuclei. In the case of ^1H , this polarization spreading with spin diffusion is significantly more efficient than in the case of ^{13}C due to the strong homonuclear dipolar coupling of ^1H . After the fast polarization spreading across all ^1H nuclei in the sample, the polarization can be transferred to ^{13}C by either cross polarization (CP) or heteronuclear cross relaxation (CR). In the case of ^{13}C , the polarization spreading has a lower celerity of spin diffusion. The spin diffusion can be either purely homonuclear (SD) or it can be assisted by ^1H - ^{13}C dipolar couplings, resulting in proton driven spin diffusion (PDS). Note that the latter has a higher celerity as this again is relying on the large dipolar couplings of ^1H . An additional direct DNP transfer (dashed violet line) is possible to a more distant nucleus if strong electron-nucleus interactions are present. Reprinted and adapted from ref. [48].

1.2 Relaxation and Dynamics

Relaxation in magnetic resonance describes the return of perturbed polarization to its thermal equilibrium given by the Boltzmann distribution (Equation 3). Several theories describing spin relaxation were developed throughout the years, among them the phenomenological Bloch equations^[49] and the semi-classical Redfield theory.^[50] Other relaxation theories which are based on either transition probabilities or completely on a quantum-mechanical basis are described in the literature as well.^[45] The number of different approaches to describe relaxation in magnetic resonance is indicative of its importance. This subsection will firstly introduce the key experimental observables associated with relaxation processes, before subsequently elucidating their relationship with the underlying molecular dynamics that give rise to spin relaxation within the sample. In addition, methyl group dynamics as an example of molecular dynamics will be discussed in detail and other techniques to measure dynamics will be presented. Finally, paramagnetic relaxation in the presence of electron spins will be elucidated.

1.2.1 Stochastic relaxation theory

The stochastic relaxation theory describes spin relaxation as a consequence of stochastic/Markovian molecular processes.^[45] These processes yield time-dependent fluctuations in local magnetic fields by changing the orientation of a given anisotropic interaction (*e.g.*, CSA, dipolar coupling, quadrupolar interaction).^[21] The autocorrelation function $\mathcal{G}(\tau)$ describes these fluctuations by correlating a state (*e.g.*, molecular, quantum-mechanical, etc.) at one moment t with a later time $t + \tau$. The spectral density function, which is twice the Fourier transformation of the autocorrelation function, displays the distribution of the local magnetic field fluctuations as a function of angular frequency. It is given by:^[51]

$$\mathcal{J}(\omega) = 2\mathcal{G}(0) \frac{\tau_c}{1 + \omega^2 \tau_c^2}, \quad (12)$$

where τ_c is the correlation time of the fluctuations, ω is the angular frequency, and $\mathcal{G}(0)$ is the autocorrelation function of the stochastic molecular process at $\tau = 0$. The latter can be further described as the ensemble average of the squared fluctuating fields B_{fluc} of the given spin interaction:

$$\mathcal{G}(0) = \langle B_{\text{fluc}}(t)^2 \rangle. \quad (13)$$

Thus, $\mathcal{G}(0)$ is dependent on the type and strength of the relevant spin interaction.

As the relaxation time constants (*viz.* T_1 and T_2) can be described in terms of spectral density functions, the relaxation time constants can be correlated to the correlation time τ_c of the molecular process. The relation between the relaxation time constants and the correlation time can be described with a log-log plot (Figure 3A). Here, a minimum for the T_1 spin-lattice relaxation time constants can be observed for correlation times τ_c matching the inverse Larmor frequency. Because the correlation time τ_c is representative for the molecular process, this T_1 minimum demonstrates that the energy transfer between the fluctuating fields is most efficient when the molecular process is at the same frequency as the spin precession. In contrast, the spin-spin relaxation time constant T_2 displays no minimum, but steadily decreases with increasing correlation times due to very short coherence times found for large molecules or in the solid state.

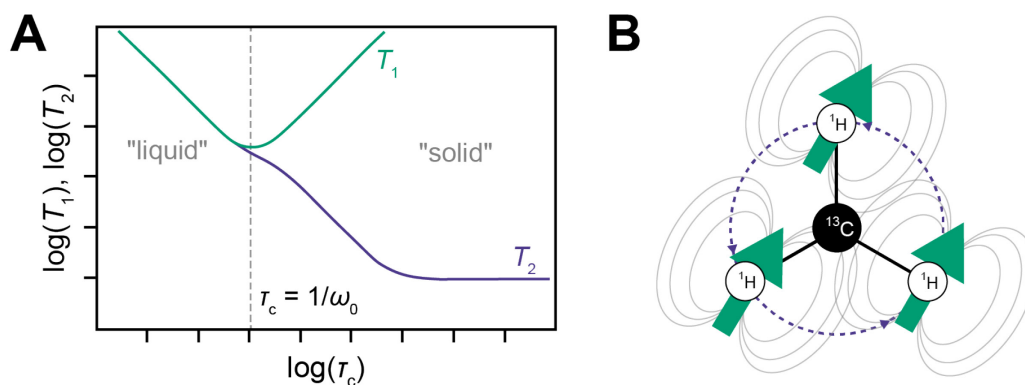


Figure 3: (A) Logarithmic plot of the spin-lattice relaxation time constant T_1 (green) and the spin-spin relaxation time constant T_2 (violet) against the correlation time τ_c of the motion. Small τ_c values are usually observed in liquids or very mobile sites. Large τ_c values are solid-like, displaying slow motions. The gray vertical line highlights the T_1 minimum, where the τ_c is equal to the inverse of the Larmor frequency ω_L . In contrast, no T_2 minimum, but a steady decrease with increasing τ_c is observed. (B) Schematic of the fluctuating fields which are induced by dynamics such as a reorientation of methyl protons. The green arrows indicate the magnetic moment and the gray lines the magnetic field of 1H . The magnetic field of ^{13}C is not displayed as it is perpendicular to the 1H magnetic fields. The violet dashed line which forms a circle represents the reorientation dynamics of the methyl group. Reprinted and adapted from ref. [48].

In practice, the correlation between relaxation time constants, spectral density function and the correlation time τ_c enables the description of molecular dynamics by measuring the relaxation time constants. This description can be done in two ways: changing the magnetic field B_0 and thus the Larmor frequency and/or changing the temperature. By changing B_0 the spectral density function is read out at different Larmor frequencies, giving rise to a different section of the distribution of local magnetic fields. Thus, determining relaxation time constants at two or more magnetic fields enables to pinpoint the exact correlation time τ_c of the motion. On the other hand, a change of temperature has a direct impact on the motion: a decrease in temperature decreases the amplitude and an increase in temperature increases the amplitude of the motion and thus, the correlation time τ_c . Consequently, the motion-induced fluctuations of local magnetic fields (Figure 3B) are altered and subsequently, the spectral density function, which connects the correlation time to the relaxation time constants.

1.2.2 Transition probabilities and the Solomon equations

In addition to autocorrelation functions, relaxation can be described in terms of transition probabilities.^[12] Here, the fluctuating fields caused by molecular dynamics introduce a probability that an involved spin undergoes a spin state transition. These spin state transitions drive the system towards thermal equilibrium.^[21] The Solomon equations use transition probabilities between different spin states to describe the motion of the respective state

populations after a perturbation of two coupled spins with $I = S = 1/2$ undergoing dipole-dipole relaxation between.^[52] The Solomon equations are given in the following:

$$\frac{d}{dt} \begin{pmatrix} P_I \\ P_S \end{pmatrix} = - \begin{pmatrix} R_{I,\text{auto}} & R_{\text{cross}} \\ R_{\text{cross}} & R_{S,\text{auto}} \end{pmatrix} \begin{pmatrix} P_I - P_I^{\text{eq}} \\ P_S - P_S^{\text{eq}} \end{pmatrix}, \quad (14)$$

where $P_{I/S}$ are the spin polarizations of spin I and spin S , respectively, at time t , $R_{I/S,\text{auto}}$ is the auto-relaxation rate constant, R_{cross} is the cross-relaxation rate constant, and $P_{I/S}^{\text{eq}}$ is the equilibrium thermal polarization. Four different spin state transitions are possible in this system: the zero-quantum transition (ZQ) that flips both spins in an opposite manner, the two single-quantum transitions (SQ), changing one of the two spins, and the double-quantum transition (DQ) that changes both spins to the same state. The probabilities of these transitions are denoted as W_0 , $W_{1,I/S}$, and W_2 for the ZQ, SQ, and DQ transitions, respectively. Both relaxation rate constants, which are the inverse of the relaxation time constants (*e.g.*, $R_1 = T_1^{-1}$), can be described as a sum of, at least, two of these three transition probabilities: R_{auto} involves all three transition probabilities:

$$R_{\text{auto}} = W_0 + 2W_{1,I/S} + W_2, \quad (15)$$

whereas R_{cross} is the difference between W_0 and W_2 :

$$R_{\text{cross}} = W_0 - W_2. \quad (16)$$

Note that the transition probabilities are connected to the stochastic relaxation theory. Each transition probability can be represented as a product of the squared interaction coupling constant—being in the discussed case the dipolar coupling constant d_{IS} —and the spectral density function:

$$W_0 = \frac{1}{10} d_{IS}^2 \mathcal{J}(\omega_I - \omega_S), \quad (17)$$

$$W_{1,I/S} = \frac{3}{20} d_{IS}^2 \mathcal{J}(\omega_{I/S}), \quad (18)$$

and

$$W_2 = \frac{3}{5} d_{IS}^2 \mathcal{J}(\omega_I + \omega_S). \quad (19)$$

As the Solomon equation describes the motion of polarization with time, the nuclear Overhauser enhancement (NOE) can be predicted in theory; in practice, a two-spin system is

often not sufficiently representative. The NOE signal enhancement of the S spin ($\varepsilon_S^{\text{NOE}}$) after a perturbation of the I spin is defined as the following:

$$\varepsilon_S^{\text{NOE}} = \frac{P_S}{P_S^{\text{eq}}}, \quad (20)$$

and the signal enhancement of the I spin (ε_I) after its perturbation is given by:

$$\varepsilon = \frac{P_I}{P_I^{\text{eq}}}. \quad (21)$$

Assuming that P_S is in a steady-state equilibrium, Equation 14 can be rearranged to an explicit term of the NOE enhancement factor for a dipolar-coupled two-spin system:

$$\varepsilon_S^{\text{NOE}} = 1 - (\varepsilon_I - 1) \frac{\gamma_I R_{\text{cross}}}{\gamma_S R_{\text{auto}}}. \quad (22)$$

As mentioned above, a perturbation of the spin system is required in order to achieve a non-equilibrium state of spin I . This non-equilibrium state can be, for example, a saturation of the I spin ($\varepsilon_I = 0$), which is achieved by saturation pulses during an experiment. The saturation results in a simplified Equation 23, which is the general form of the NOE enhancement factors for the heteronuclear case:^[53]

$$\varepsilon_S^{\text{NOE}} \approx 1 + \frac{\gamma_I R_{\text{cross}}}{\gamma_S R_{\text{auto}}} \quad (23)$$

Equation 23 demonstrates that the polarization of spin S increases—or decreases if the two gyromagnetic ratios possess different signs—relatively to its thermal polarization upon saturation of spin I . The hyperpolarization of spin I is also a possibility to perturb the thermal polarization, which will be discussed in detail in Subsection 1.2.3.1.

1.2.3 Methyl group dynamics

Methyl groups dynamics possess remarkable properties, which are both advantageous and disadvantageous in NMR spectroscopy. As an example, the methyl TROSY (transverse optimized spectroscopy) experiment in liquid-state NMR yields reliable results in structural biology, even for biomolecules which are exceeding the size limitation.^[54] This is possible due to the fast reorientation dynamics around the C3 symmetry axis of a methyl group at timescales exceeding the correlation time of molecular tumbling (at least in the case of large biomolecules). This difference in timescales leads to a unique relaxation of methyl groups. In the solid state, these unique relaxation properties often interferes with rf pulses during spinlocks and decoupling sequences.^[55] Additionally, the fast relaxation of methyl groups can cause

significant line broadening of all resonances, decreasing the already low signal resolution. Nonetheless, methyl group dynamics can also cause line-narrowing of ^{13}C resonances by self-decoupling^[56] and offer a selectivity filter. The first case is the basis of TROSY, whereas the second case is induced by using a heteronuclear NOE (hetNOE)-based transfer from ^1H to ^{13}C and can achieve a quantitative excitation of ^{13}C .^[57]

In the case of hyperpolarization techniques, especially for MAS DNP, which is routinely performed at cryogenic temperatures, the dynamics of $-\text{CH}_3$ groups are still active due to the low activation barrier of the reorientation.^[55] This causes again fast ^1H relaxation in the sample, resulting in a decrease of obtainable sensitivity enhancement (*cf.* Equation 4). In 2016, a hetNOE-based technique for directing hyperpolarization to mobile groups was quantitatively described by the group of Corzilius^[58] and also observed by the group of Buntkowsky^[59] in the same year. This method, dubbed SCREAM-DNP (Specific Cross Relaxation Enhancement by Active Motions under DNP) is explained in the following subsection.

1.2.3.1 SCREAM-DNP

SCREAM-DNP is a hyperpolarization-exclusive, hetNOE-based experiment. It requires active motions of functional groups at typical DNP temperatures (100 to 160 K) as these active motions induce cross relaxation.^[46] In subsection 1.2.2, the NOE enhancement factor ϵ_S^{NOE} was discussed for the case that the I spin is saturated ($\epsilon_I = 0$). It was additionally mentioned that hyperpolarization ($\epsilon_I > 1$) can be considered as a perturbation of the I spin as hyperpolarization is a non-equilibrium state. With the condition that $\epsilon_I > 1$, Equation 22 can be rearranged to the following:^[58]

$$\epsilon_S^{\text{SCREAM}} \approx -\epsilon_I \frac{\gamma_I R_{\text{cross}}}{\gamma_S R_{\text{auto}}} \quad (24)$$

In the SCREAM-DNP experiment (Figure 4), two polarization pathways are contributing to the detected signal: the coherent, direct DNP pathway (direct $e^{-13}\text{C}$ transfer, violet arrow in Figure 4A) with an enhancement factor ϵ_C , and the incoherent, cross relaxation-induced pathway (Figure 4A, green arrow) with the above derived enhancement factor $\epsilon_C^{\text{SCREAM}}$ (note that the subscript S is exchanged to C for the current example of ^{13}C). In direct DNP, the involved nuclei are often localized around the PA—as ^{13}C spin diffusion is inefficient (see subsection 1.1.4.1 and Figure 2)—and the proximity of the ^{13}C nuclei to the PA leads to line broadening of the resulting ^{13}C signal. The signal contribution arising due to ^1H – ^{13}C cross relaxation is the sought-after signal. Because it involves an indirect transfer from ^1H to ^{13}C ,

fast ^1H spin diffusion can be utilized, allowing the efficient spreading of polarization to ^{13}C nuclei which are distant to the PA and thus avoiding line broadening caused by fast paramagnetic relaxation.

In terms of experiments, a one-pulse (Bloch decay) experiment produces a signal with a line shape that includes both positive and negative contributions (Figure 4B, light blue spectrum). This occurs because both polarization pathways are active simultaneously ($\varepsilon_{\text{DP}} = \varepsilon_{\text{C}} + \varepsilon_{\text{C}}^{\text{SCREAM}}$), resulting in a superposition of the cross-relaxation-induced pathway and the direct pathway. The two pathways have opposite phases, causing the resulting signals to appear with non-absorptive phases or partially cancel out. To obtain a signal exclusively from cross relaxation, additional experiments are required. The most effective method involves performing a second, interleaved experiment with identical parameters, where ^1H polarization build-up is suppressed by additional pulses after the initial saturation block (*cf.* Figure 4A). This additional experiment, dubbed DP_{sat} , consists of the direct ^{13}C contribution (ε_{C}) and the traditional hetNOE ($\varepsilon_{\text{C}}^{\text{hetNOE}}$) (Figure 4B, violet spectrum):

$$\varepsilon_{\text{DP}_{\text{sat}}} = \varepsilon_{\text{C}} + \varepsilon_{\text{C}}^{\text{hetNOE}}. \quad (25)$$

Subtracting Equation 24 with Equation 25 yields the sought-after, cross relaxation-based ^1H - ^{13}C transfer of hyperpolarization (Figure 4B, green spectrum):

$$\varepsilon_{\Delta\text{DP}_{\text{sat}}} = \varepsilon_{\text{DP}} - \varepsilon_{\text{DP}_{\text{sat}}} = \varepsilon_{\text{C}}^{\text{SCREAM}} - \varepsilon_{\text{C}}^{\text{hetNOE}} \approx -\varepsilon_{\text{H}} \frac{\gamma_{\text{H}} R_{\text{cross}}}{\gamma_{\text{C}} R_{\text{auto}}}. \quad (26)$$

Equation 26 demonstrates the significance of SCREAM-DNP: a polarization filter induced by active motions of molecules causing nuclei in the proximity to these mobile sites to be enhanced. Consequently, SCREAM-DNP is a site-specific method without relying on site-specific labeling strategies, but using the advantages of the non-specific ^1H bath. Nevertheless, not all the advantages can be applied to SCREAM-DNP. In comparison to, for example, cross polarization, a loss of sensitivity due to the required mathematical subtraction is obtained, which is negligible for the most cases due to the significantly larger specificity. The methyl group is the most often studied mobile group.^[60] Further functional groups were demonstrated to induce SCREAM-DNP as well.^[60c, 61] In the next sections, the dynamics of methyl groups are elucidated and NMR methods to quantify dynamics are discussed.

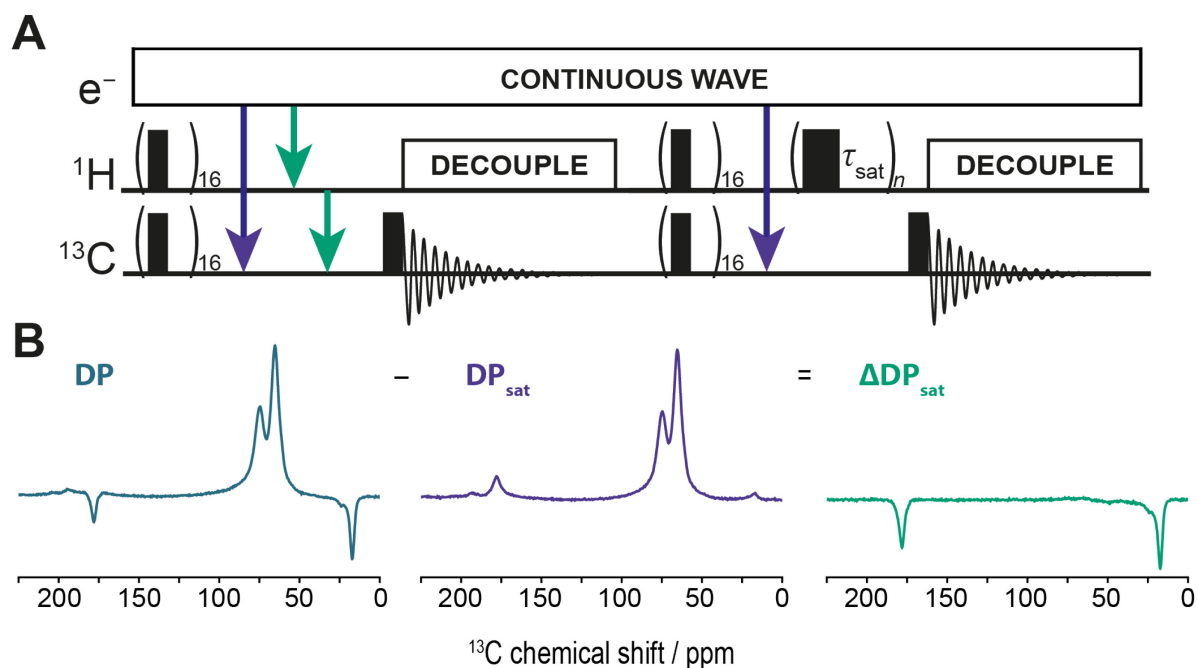


Figure 4: Pulse sequence for the interleaved acquisition of the SCREAM-DNP experiment (A) and exemplary spectra resulting from the two blocks in the pulse sequence (DP and DP_{sat}) and the difference spectra ($\Delta\text{DP}_{\text{sat}}$) (B). (A) The arrows in the pulse sequence indicates the transfer process: the blue arrows are the direct DNP transfer from electron spin to ^{13}C , whereas the red arrows are the indirect DNP transfer, which involves a relay of the polarization through ^1H before transferring it by cross relaxation (CR) to ^{13}C . (B) The DP spectrum (violet) consists of contributions of both transfer pathways, whereas the DP_{sat} spectrum (blue) is based only in the direct DNP transfer. The difference spectrum $\Delta\text{DP}_{\text{sat}}$ is exclusively based on the indirect DNP transfer induced by CR. The studied sample consisted of 2 vol-% $1\text{-}^{13}\text{C}$ -ethyl $2\text{-}^{13}\text{C}$ -acetate mixed with 7.5 mM AMUPol, 50 vol-% glycerol- d_8 , 39 vol-% D_2O , and 9 vol-% H_2O . The experiment was performed with 8 s SCREAM-DNP polarization time and at 8 kHz MAS frequency and 102 K.

1.2.3.2 Theory of methyl group dynamics

Due to the above-described potential of methyl groups for site-specific DNP, understanding the precise type and timescale of the motion is beneficial for designing future experiments. In general, methyl groups can undergo three types of motions: quantum tunneling, libration, and rotation (Figure 5A). All three types display a motion of the C–H bond around the C_3 symmetry axis composed of the C–CH₃ bond and their contribution to the total dynamics are dependent on the sample temperature. So far, quantum tunneling was observed only for ultra-low temperatures ($T < 30$ K),^[62] indicating that the other two types will be dominant for higher temperatures ($T > 30$ K). An example of this dominance of the other two motional modes is the study of Overhauser DNP in a methyl-bearing radical. Here, the cross relaxation was mainly induced by libration at temperatures between 18 to 80 K.^[63] Typical librational frequencies are on the THz-range at elevated temperatures and motion rate decreases with decreasing temperatures, becoming attractive at low temperatures of ~ 80 K to induce cross relaxation between the electron spin of the radical and the protons/deuterons of the –CH₃/–CD₃

group of the radical. The rotational mode is mostly frozen at temperatures below 60 to 80 K,^[64] but is activated with increasing temperatures due to the increase of thermal energy exceeding the required rotational activation barrier E_A . Here, the activation barrier describes the required potential energy for achieving the unfavorable transition state of the proton displacement by an angle of $2\pi/3$. This leads to a potential energy surface (Figure 5B) as given, for example, by a $2\pi/3$ -periodic function:^[65]

$$V(\phi) = \frac{E_A}{2} (1 - \cos 3\phi), \quad (27)$$

where $V(\phi)$ is the potential energy of the rotation, and ϕ the angle of displacement of the proton. This type of motion can be treated completely classically with normal kinetics with an Arrhenius-like temperature dependency. Numerous models exist to explain the dynamics,^[66] for example, a simple 3-site exchange of the three proton sites as assumed in Equation 27. More complex models can be derived by adding more sites (*e.g.*, 6 sites), or by describing the motion continuously and assuming a diffusion around the symmetry axis. More complex motions can be considered if a second exchange motion is added, for example, a two-site exchange of 3 sites. This motion could be accomplished by considering, for example, a librational mode between 2 sites of a 3-site rotational mode. A framework for describing these models in a molecular context is the cone model (Figure 5C).^[66-67] Here, a cone is constructed between the dihedral angle θ between the C–C–H atoms and an azimuthal angle ϕ between the proton sites and a reference axis, which is usually the C–C bond located along the z-axis. In the cone model, it is assumed that the motions are isotropic and periodic, and are restricted to a cone, which simplifies the dynamics as no motions along the z-axis are allowed. This is valid for simple chemical environments but can misrepresent more complex environments typically found in the hydrophobic cores of proteins or more complex motions involving libration and rotation (*cf.* 2-times 3-site exchange).^[68] In these cases, a model-free distribution of different activation barriers is assumed. Nonetheless, a structural model is beneficial for connecting measured dynamics to molecular structure. Molecular dynamics (MD) simulation can fill the gap, but it is technically challenging to describe methyl dynamics over the whole temperature range (down to ~ 100 K).^[69] To the best knowledge, only one MD study describes methyl groups in proteins at cryogenic temperatures.^[70] As the theoretical framework is now set, NMR techniques and observables to derive (methyl group) dynamics are discussed in the next section.

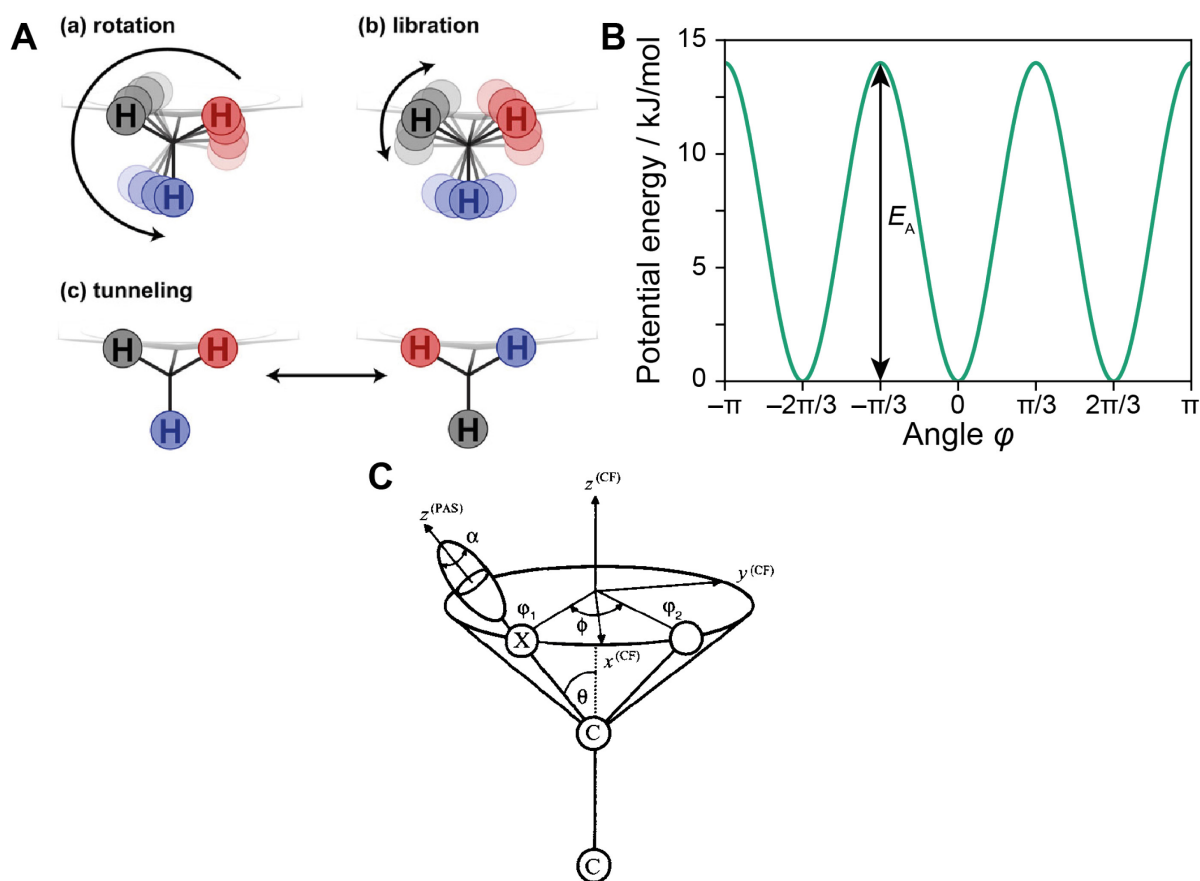


Figure 5: (A) The three motional modes of a methyl group: (a) rotation, (b) libration, and (c) quantum tunneling. (B) Potential energy surface of the methyl group rotation. The energy surface is calculated with Equation 27 using an activation barrier E_A of 14 kJ/mol. (C) Cone model representing the reorientation dynamics of a methyl group. The cone has an angle θ relative to the reference axis which is the z -axis (in the crystal frame CF) and the C–CH₃ bond. The angle θ is usually 70.5° assuming a tetrahedral angle and also represents the second Euler angle for the transformation from the crystal frame to the principal axis frame (PAS). Reprinted from Perras *et al.* (A)^[63] (Copyright 2023 by AIP Publishing) and Macho *et al.* (C)^[67] (Copyright 2001 by Springer).

1.2.3.3 Measuring structures and dynamics with NMR

The sections before have described the theory of certain spin interactions as well as how molecular dynamics interact with those interactions, resulting in relaxation. This subsection discusses techniques to measure quantities of these spin interactions, the most important—at least for solid-state NMR—are CSA,^[71] dipolar coupling,^[22, 72] and, if a spin-1 or higher is present, quadrupolar interaction.^[73]

As dipolar coupling is omnipresent in all NMR samples, manifold experiments to measure dipolar coupling constants are developed. Here, prominent examples for biomolecular solid-state NMR are the REDOR (Rotational Echo Double Resonance) or the related TEDOR (Transfer Echo Double Resonance) experiment. The former is widely applied for heteronuclear distance measurements, whereas the latter experiment transfers polarization from one nucleus to an unlike nucleus (*e.g.*, ¹³C to ¹⁵N) and the resulting cross peaks may be additionally used

for the measurement of heteronuclear distances. Manifold experiments are used for homonuclear distance measurement or dipolar recoupling such as rotational resonance (R^2), RFDR (radiofrequency driven recoupling) or DIPSHIFT (dipolar chemical shift).^[72]

In general, dipolar recoupling can be divided into a homonuclear case and a heteronuclear case. The comparison of Equation 8 and Equation 9 shows that the flip-flop term is only present in the homonuclear case. This term is required for efficient polarization exchange between like spins; however, also results in dipolar truncation,^[74] which hinders the analysis of all present dipolar coupling for many experiments. A few experiments are not affected by dipolar truncation because they are selective towards one specific dipolar coupling. One of those experiments is R^2 , which is a passive recoupling sequence as no rf pulses have to be applied for recoupling.^[75] The recoupling is based on the modulation of the dipolar Hamiltonian $\hat{\mathcal{H}}_d$ by MAS, which leads to the introduction of static components of the dipolar term at matching conditions given by:

$$\Delta\omega_{\text{iso}} = n\omega_r \text{ with } n = \pm 1, \pm 2, \pm 3, \dots, \quad (28)$$

where $\Delta\omega_{\text{iso}}$ is the difference between the isotropic chemical shift of two resonances, n is an arbitrary integer, and ω_r the MAS frequency. Because this recoupling technique is enabled by setting the MAS frequency to the same value as the difference of isotropic chemical shifts, it does not only require no rf pulses, but is also inherently frequency selective, recoupling only the dipolar coupling between spins which resonate at the given isotropic chemical shift difference.

Molecular dynamics can be measured with dipolar recoupling techniques as well. Restraints can, for example be derived by comparing the motionally averaged dipolar coupling constants—if the frequency of the studied motion is significantly larger than the coupling constant (fast exchange regime: $d_{jk} \ll k_{\text{ex}}$)—to non-averaged/static constants.^[76] The resulting ratio $d_{jk,\text{avg}}/d_{jk,\text{static}}$ yields the order parameter. As a model-independent measure of the spatial restriction of an internal motion, Lipari and Szabo introduced the so-called generalized order parameter S in 1982.^[77] Its squared value, the squared order parameter S^2 can range from 0 to 1.^[78] If $S^2 = 0$, the internal motion is isotropic, meaning all possible orientations of the mobile group/bond are equally probable. Consequently, the amplitude of the motion is maximum. At the other extreme ($S^2 = 1$), the motion is completely restricted and experiences static conditions. Here, the amplitude of motion is minimal. The order parameter includes a manifold of special cases and existing models (e.g. free diffusion or 3-site jump in

the cone model). In these two examples, the motion is azimuthally symmetric about an axis, meaning that the motion is independent of the azimuthal angle ϕ .^[77] In such a case, the order parameter S^2 can be directly derived from the angle θ between the bond vector and the reference axis:

$$S^2 = \frac{1}{2}(3 \cos^2(\theta) - 1). \quad (29)$$

Noteworthy, the S^2 order parameter vanishes in this case if θ is equal to the magic angle (54.74°).

In practice, knowledge—or at least an estimation—of the static dipolar coupling constant is required to obtain the order parameter S^2 . Here, REDOR experiments can, for example, be employed to measure dipolar order parameters of ^{13}C - ^1H spin pairs.^[10g]

Molecular dynamics can also be measured with quadrupolar interactions instead of dipolar interactions. The quadrupolar interaction is given by the following first-order Hamiltonian $\hat{H}_Q^{(1)}$:

$$\hat{H}_Q^{(1)} = \omega_Q^{(1)} \frac{1}{6} (3\hat{I}_z^2 - I(I+1)\hat{1}), \quad (30)$$

where $\omega_Q^{(1)}$ is the first-order quadrupolar coupling, I the spin quantum number, and $\hat{1}$ the unity matrix. The first-order quadrupolar coupling is given by:

$$\omega_Q^{(1)} = \frac{3eQ\bar{V}_{zz}}{2I(2I-1)\hbar}, \quad (31)$$

Where e is the elementary charge, Q the quadrupole moment of the given nucleus, \bar{V}_{zz} is the average of the largest secular component of the electric field gradient tensor. A quadrupolar coupling constant C_Q is usually used as a measure of the interaction strength in units of Hertz. C_Q is defined as:

$$C_Q = \frac{e^2qQ}{h}, \quad (32)$$

where eq is the largest principal axis component of the electric field gradient tensor. Similar to the averaging of the dipolar coupling constant, the quadrupolar coupling constant is motionally averaged as given by:

$$C_{q,\text{eff}} = S^2 C_q, \quad (33)$$

The advantage of using quadrupolar interaction over dipolar coupling is the magnitude of both interactions: the dipolar interaction has a magnitude of Hz to kHz, whereas the quadrupolar coupling constant starts at ~ 150 kHz for ^2H and increases to MHz for nuclei such as ^{14}N . This large magnitude of the interaction guarantees that all other interactions are negligible, whereas cross-correlation of dipolar coupling with, for example, CSA can happen. In the case of ^2H , an exchange of ^1H with ^2H is often possible and thus, it can be selectively incorporated into a manifold of molecules and the quadrupolar line shape and relaxation are sensitive to motions over a large timescale, ranging from ps to ms.^[79] Therefore, the measurement of methyl group dynamics at typical DNP temperatures (100 to 160 K) with ^2H is useful due to expected transitions of the motion at ~ 100 K from the fast exchange regime ($C_Q \ll k_{\text{ex}}$) to the slow exchange regime ($C_Q \geq k_{\text{ex}}$). This transition is directly visible in the ^2H line shapes as the ^2H Pake pattern allows to read out the effective quadrupolar coupling constant $C_{\text{Q,eff}}$. Consequently, the measurement of dynamics with ^2H using DNP techniques is, in theory, ideal. Nonetheless, DNP requires PAs in the form of stable radicals, introducing paramagnetic species. This leads to paramagnetic relaxation which will be discussed in the next subsection.

1.2.4 Paramagnetic relaxation

The large gyromagnetic ratio of electron spins is, on the one hand, advantageous for hyperpolarization of nuclei which is the basis of DNP (*cf.* Equation 3). On the other hand, the celerity of relaxation processes is more efficient due to larger fluctuating fields. Consequently, electron relaxation is a source for enhanced nuclear relaxation, which is known as PRE and is affecting both nuclear spin-lattice and spin-spin relaxation.^[25] Electron relaxation can impact nuclear relaxation through several mechanisms: Fermi-contact relaxation, dipole-dipole relaxation, and Curie relaxation.

Fermi-contact relaxation is based on the Fermi-contact interaction. As this interaction is isotropic (*viz.* the isotropic HFI, *cf.* Subsection 1.1.2.2), only chemical exchange and electron relaxation properties influence the celerity of this relaxation, whereas molecular tumbling can be neglected.^[80] Fermi-contact relaxation impacts only the nucleus at the site of the unpaired electron and thus, it is negligible for PRE-like effects in samples for DNP.

The dipole-dipole relaxation is based on the anisotropic contribution of the HFI and thus has a distance and orientation dependence. In contrast to the Fermi-contact relaxation mechanism, dipole-dipole relaxation can affect nuclear relaxation farther away from the

paramagnetic center as it is based on fluctuating fields of the dipolar contribution of the HFI. The dipolar interaction in general is proportional to an inter-spin distance dependency of r^{-3} (*cf.* Equation 7); consequently, this distance dependency is squared due to the squared contribution of local magnetic fields generated by the dipolar part of the HFI (*cf.* Equation 13). Hence, the contribution of electron relaxation to the effective nuclear relaxation is proportional to r^{-6} if the point-dipole approximation is assumed.^[25]

The Curie relaxation is a special case of dipole-dipole relaxation as the underlying dipolar interaction is between the nuclear magnetic moment and the averaged electron magnetic moment. This results in a slightly different interaction mechanism, however, the distance dependence (r^{-6}) remains the same. It becomes dominant at high magnetic fields and for molecules with slow molecular tumbling in solution.^[25]

Due to these conditions, only the dipole-dipole relaxation has to be considered in MAS DNP, facilitating the analysis. Nonetheless, to measure and/or predict the strength of PRE-like effects during MAS DNP, knowledge about electron relaxation rate constants and nuclear relaxation time constants have to be known for the used sample conditions. This significantly increases the complexity which may be the reason for the low number of studies about paramagnetic relaxation during MAS DNP.

2. Motivation and Aim

DNP is an established hyperpolarization technique and an established tool for signal-enhanced NMR spectroscopy of samples with low sensitivity and/or time consuming experiments.^[26] So far, in most of the DNP experiments the molecule of interest is non-selectively hyperpolarized together with all other sample constituents, leading to background signals and overlapping resonances and decreasing the obtainable signal resolution.^[15] In addition, these experiments are most often performed with a frozen solution which decreases either the amount of molecule of interest in the final DNP sample or hinders the use of DNP due to insolubility of the molecule in a suitable solvent. New site-specific as well as matrix-free DNP techniques are constantly improved, however, still lack a wide-range applicability. As a first example, matrix-free DNP is a promising tool, but was applied so far only for (bio)materials.^[43c]

As a second example, in the case of site-specific DNP, SCREAM-DNP has been established as a useful tool for molecules containing functional groups with active motions at cryogenic temperatures.^[46] Its applicability was, so far, only shown at MAS frequencies below 10 kHz to ensure sufficiently acceptable polarization times by spin diffusion, but which are still usually larger than 4 s.^[81] Higher MAS frequencies are retarding this transfer process even further, nevertheless, heteronuclear cross relaxation remains the dominant pathway at long polarization times (>4 s). In order to understand and predict heteronuclear cross relaxation and its transfer efficiency, the molecular dynamics have to be known. However, studies of dynamics under DNP conditions (*viz.* in the presence of a PA and microwave irradiation) are underrepresented.

The motivation of this work was therefore to improve the applicability of the two techniques—SCREAM-DNP and matrix-free DNP— as well as to establish a reliable technique for studying molecular dynamics under DNP conditions.

Accordingly, the first aim was to investigate the behavior of cross relaxation-induced polarization build-up at increasing MAS frequencies in a selectively labeled model system which can be easily synthesized. Here, the hypothesis is that rotational resonance dipolar recoupling is beneficial for the polarization build-up behavior of nuclei that are dipolar coupled to the methyl group. To investigate this hypothesis, 2-¹³C-ethyl 1-¹³C acetate is synthesized as a model system and SCREAM-DNP is measured in a glycerol:water matrix at cryogenic

temperatures and at varying MAS frequencies. The findings of this model system are additionally compared to a ribonucleoprotein complex prepared with stable isotope labeling techniques which are routinely used in NMR with biomolecules.

The aim of the second part of this work is the systematic investigation of matrix-free DNP conditions which yield the highest possible sensitivity enhancement by DNP. Here, for the systematic optimization of this approach, model proteins such as lysozyme and ubiquitin are studied with different mixtures of AMUPol and different rehydration levels. The insights of this study are then used to investigate medically relevant samples at low analyte concentration to demonstrate the applicability of the matrix-free DNP approach in challenging systems.

In the final part of this work, the aim is to establish an approach based on DNP-enhanced ^1H - ^2H cross-polarization experiments to investigate methyl group dynamics. Two different sample morphologies are used in order to test the general applicability and robustness of this approach and elaborate future directions for relaxation time measurements with DNP. The first sample consists of selectively deuterated $\text{A}\beta_{1-40}$ fibrils in the hydrated powder state which are investigated with the matrix-free DNP approach. The second system consists of ethanol- d_3 dissolved in a glycerol:water matrix, mimicking the standard DNP sample.

Overall, this work focusses on the improvement of DNP methods to widen the range of applicability, including site-specific experiments, experiments on insoluble proteins, and acceleration of relaxation measurements.

3. Material and Methods

In general, if not stated otherwise, all NMR experiments were performed on a Bruker AVANCE III HD spectrometer, operating at a field of 400.5 MHz ^1H frequency which is connected to a Bruker ASCEND DNP 9.4 T widebore (89 mm) magnet. In the case of DNP experiments, a second-harmonic gyrotron from Bruker/CPI operating at a field of 4.8 T was connected to the magnet via a waveguide, using a user-set beam current to produce microwaves with a frequency of 263.4 GHz.

3.1 Combination of Cross Relaxation with Rotational Resonance

3.1.1 Systematic investigation of the MAS frequency-dependency of SCREAM-DNP experiments with selectively labeled ethyl acetate

3.1.1.1 Synthesis of selectively labeled ethyl acetate

The synthesis of selectively labeled ethyl acetate was conducted by Edvards R. Bensons as part of his Bachelor thesis.^[82] In short, the Fischer esterification between acetic acid and ethanol was performed in a microscale apparatus using $1\text{-}^{13}\text{C}$ acetic acid (3.50 eq, 1.5 mL, 26.2 mmol), $2\text{-}^{13}\text{C}$ -ethanol (1.00 eq, 430 μL , 7.4 mmol), sulfuric acid (5 drops, 96%), and silica gel dry beads (400 mg). All substances were added to a reaction flask and the resulting solution was heated for 2 h under stirring and reflux in an oil bath which was heated to 130 to 140 $^{\circ}\text{C}$. Afterwards, the reaction mixture was cooled at room temperature and diethyl ether (2 mL) was added to the cold solution. The mixture was washed three times with 5% sodium hydrogen sulfate in distilled water and distilled. $2\text{-}^{13}\text{C}$ -ethyl $1\text{-}^{13}\text{C}$ acetate was obtained as a colorless fluid and its purity was confirmed by high-resolution liquid state NMR.

3.1.1.2 DNP sample preparation

For DNP-enhanced solid-state NMR experiments, 7.5 mM AMUPol was dissolved in a solution of 50:38:10:2 vol-% d_8 -glycerol: D_2O : H_2O : $2\text{-}^{13}\text{C}$ -ethyl $1\text{-}^{13}\text{C}$ acetate. The resulting solution was aliquoted and transferred to a 1.3 mm zirconia rotor and a 3.2 mm sapphire rotor (Bruker) and each rotor was sealed with a matching Vespel drive cap and, in the case of the 1.3 mm rotor, a Vespel bottom cap.

3.1.1.3 DNP-enhanced MAS NMR spectroscopy

All NMR experiments used rf pulse powers for the hard pulses of 60 kHz (^1H & ^{13}C) for the 3.2 mm probe and 110 kHz (^1H) and 60 kHz (^{13}C) for the 1.3 mm probe. The NMR experiments were performed with a pre-saturation sequence which consisted of 16 90° pulses separated by 5 ms on both channels to delete all magnetization. SPINAL-64 was used as a broadband ^1H decoupling sequence with a pulse power of 60 kHz (3.2 mm probe) or 100 kHz (1.3 mm probe) during acquisition of the free induction decay (FID). It has to be noted that the 3.2 mm probe was suffering from a tuning instability of the ^1H rf circuit. This instability required a relatively long time for thermostatzation, rendering the measurement of microwave on/off comparisons unfeasible in several cases. Additionally, it prevented the use of large ^1H rf field strengths over a long duration. For the CPMAS experiments, the ^1H pulse power was decreased to fulfill the Hartmann-Hahn matching condition during the 2 ms CP contact pulse. The ^1H contact pulse was ramped from 50% to 100% ^1H pulse power.

The used pulse sequence of SCREAM-DNP is shown in Figure 4A and described in detail elsewhere.^[60b] In short, the SCREAM-DNP experiment consists of two blocks, which only differ in the manipulation of the proton polarization before the read-out of magnetization on ^{13}C . The first block leaves the proton spins undisturbed after initial saturation; therefore, the proton polarization can build up again during the polarization time resulting in the buildup of ^{13}C magnetization via the direct and the indirect DNP pathway. The second block of the experiment continuously saturates the proton polarization inhibiting the indirect, cross relaxation-based transfer pathway. By subtracting both blocks, the direct DNP pathway can be filtered out resulting in purely the cross relaxation-based spectrum, which is called $\Delta\text{DP}_{\text{sat}}$.

For the acquisition of the DP_{sat} spectrum of the SCREAM-DNP-experiment, additional 180° pulses were applied every 250 ms on the ^1H channel to suppress ^1H polarization build-up during the ^{13}C polarization time. This polarization time and the accompanying ^1H 180° pulses were varied between 0.25 s up to 512 s to determine SCREAM-DNP build-up rates at MAS frequencies between 6 and 35 kHz. The MAS frequencies between 6 and 14 kHz were acquired in the 3.2 mm probe, whereas MAS frequencies between 11 and 35 kHz were measured in the 1.3 mm probe. An overlap of the MAS frequency range was chosen to check for probe- and rotor-induced variations. The temperature of all experiments was read out to be 102 K using the PT100 thermocouple inside the MAS stator.

3.1.1.4 Data analysis

All NMR experiments were processed by adding the same number of acquired points for zero-filling and applying an exponential function with 50 Hz line broadening as apodization. The ΔDP_{sat} spectra were obtained by mathematical subtraction of the DP and DP_{sat} spectra using the *accumulate* command in Bruker Topspin 4.4.0. The integration of spectral regions, normalization to the number of accumulated transients as well as baseline correction were performed in Origin. The applied baseline correction is described in detail here.^[82] To determine the polarization build-up rate constants, the integrated and normalized spectral regions of the selectively labeled methyl- ^{13}C and carbonyl- ^{13}C at polarization times between 0.25 and 512 s were fitted using the following equation:

$$I(t) = I_0 + A_f[1 - \exp(-R_f t)] + A_s[1 - \exp(-R_s t)], \quad (34)$$

where $I(t)$ is the integrated signal intensity after polarization time t , I_0 is the zero-time offset of the signal, A_f and A_s are the signal amplitudes after an infinite polarization time of the fast and the slow building-up component, and R_f and R_s are the polarization build-up rate constants of the fast and the slow building-up component.

To determine the MAS frequency-dependency of the polarization build-up rate constants in 2- ^{13}C -ethyl 1- ^{13}C -acetate, SCREAM-DNP experiments with varying polarization times were acquired at MAS frequencies between 6 and 35 kHz at a constant temperature of 102 K. The following polarization times were recorded: 0.25 s, 0.5 s, 1 s, 2 s, 4 s, 8 s, 16 s, 32 s, 64 s, 128 s for all measured MAS frequencies, and additionally 256 s and 512 s at higher MAS frequencies.

3.1.2 Applications of SCREAM-DNP experiments with dipolar recoupling in a ribonucleoprotein complex

3.1.2.1 DNP sample preparation

The sample preparation for DNP experiments was conducted by Victoria Aladin. In short, the L7Ae-RNA complexes, kindly provided by Arun K. Sreemantula and Dr. Alexander Marchanka (Institute of Organic Chemistry and Centre of Biomolecular Drug Research (BMWZ), Leibniz University Hannover, Hannover, Germany), were freeze-dried, followed by reconstitution in a solution of d_8 - $^{12}\text{C}_3$ -glycerol (98% ^2H , 99.95% ^{12}C , Eurisotop): D_2O : H_2O (50:40:10 vol-%) containing 15 mM dissolved AMUPol. This procedure yielded a final concentration of $\sim 200 \mu\text{M}$ in the case of the I93C mutant of the L7Ae protein and $\sim 400 \mu\text{M}$ in

the case of the wild type protein. In both cases, each sample was transferred into 1.3 mm zirconia or a 3.2 mm sapphire MAS sample rotor (Bruker), which were each sealed by a matching Vespel drive cap and, in the case of the 1.3 mm rotor, with a Vespel bottom cap.

3.1.2.2 DNP-enhanced MAS NMR spectroscopy

The CP and DARR experiments shown in Figure 14 were acquired on a Bruker AVANCE II DNP spectrometer, operating at a field of 400.2 MHz ^1H frequency, which is connected to a Bruker Ultrashield 9.4 T wide bore (89 mm) magnet. Microwaves were produced with a frequency of 263.4 GHz using a fundamental-mode gyrotron from Bruker/CPI with 60 mA beam current. For these experiments, rf pulse powers were set to 100 kHz (^1H) and 50 kHz (^{13}C) and for the Hartmann-Hahn matching of the CP transfer, ^1H pulse power was matched to ^{13}C for a contact time of 1.5 ms. SPINAL-64 was used with a pulse power of 100 kHz as a broadband decoupling sequence during acquisition of the FID and the MAS frequency was set to 8 kHz. In the case of the 2D DARR experiment, 256 t_1 slices in the indirect dimension with increments of 41.7 μs (TPPI) were acquired yielding a spectral width of 238 ppm and a sampling resolution of 187.5 Hz. ^1H decoupling during the acquisition of the indirect dimension was performed using the SPINAL-64 sequence with a rf pulse power of 100 kHz. The carrier frequency was set to 110 ppm for both dimensions and 32 transients were accumulated per t_1 slice with a repetition delay of 4 s. The DARR recoupling was 200 ms and the power was set to fulfill the condition $\omega_{1,\text{H}} = \omega_{\text{rot}}$, where $\omega_{1,\text{H}}$ is the Rabi frequency of the ^1H DARR recoupling and ω_{rot} is the MAS frequency (8 kHz). The rf strengths for CP excitation and broadband decoupling during acquisition of the FID are the same as for a CP experiment (see above).

The SCREAM-DNP experiments used in Figure 15 and Figure 16 were conducted on the spectrometer system introduced at the beginning of Chapter 3. Here, the beam currents were set to a range of 132 to 138 mA. For SCREAM-DNP experiments conducted at 8 kHz MAS frequency (Figure 15A), the rf pulse powers were set to 83.33 kHz (^1H) and 60 kHz (^{13}C) involving the pulses for the pre-saturation train and the SPINAL-64 broadband ^1H decoupling during acquisition of the FID. The pre-saturation train consists of 16 90° pulses for both channels which are separated by 5 ms. For all the other SCREAM-DNP experiments, the ^1H pulse powers were set to 110 kHz. The $\Delta\text{DP}_{\text{sat}}$ spectrum is acquired with additional ^1H 180° pulses every 250 ms to prevent ^1H polarization build-up during ^{13}C polarization time. The polarization time is varied between 4 and 64 s.

The temperature of all experiments was determined to 142 K using the PT100 temperature sensor inside the MAS stator.

3.1.2.3 Spectral processing and data analysis

The CP and SCREAM-DNP experiments were processed by applying the same number of points as acquired for zero-filling and an exponential apodization function with 50 Hz line broadening. In the case of the SCREAM-DNP experiments, the DP and DP_{sat} were mathematically subtracted using equal parameters with the *accumulate* function in either Bruker Topspin 4.0.7 or Bruker Topspin 4.4.0. The processed spectra were exported using the *NMRGlue* python package^[83] and spectral regions were integrated using the SIMPSON numerical integration algorithm of the SciPy python package^[84]. The integrated intensities were then normalized to the accumulated transients and furthermore divided by the normalized integrated intensity of the methyl group.

The 2D DARR experiment was processed with zero filling to yield 2048 points in the direct ¹³C dimension and 1024 points in the indirect ¹³C dimension. Apodization of the time-domain data was performed by applying a Gaussian window function with -20 Hz exponential line broadening and 0.1 Hz Gaussian line broadening.

3.2 Matrix-free DNP for the investigation of powder samples

3.2.1 Systematic investigation of the matrix-free DNP approach in model proteins

3.2.1.1 DNP sample preparation

The two model proteins ubiquitin from bovine erythrocytes and hen egg white lysozyme were purchased from Sigma-Aldrich and dissolved in deionized water without further treatment to yield stock solutions with a concentration of 250 mg/mL. Two aliquots with 16 μ L (4 mg, 470 nmol) of the ubiquitin stock were mixed with either 2.5 μ L (2.5 nmol) or 12.5 μ L (12.5 nmol) of an AMUPol stock solution in deionized water (1 mM) yielding molar ratios of 1:188 and 1:38 (PA:protein), respectively. From the lysozyme stock, four aliquots with a volume of 160 μ L (40 mg, 2.8 μ mol) were each mixed with either 0.47 μ L (35 nmol), 2.33 μ L (175 nmol), 4.67 μ L (350 nmol) or 9.33 μ L (700 nmol) of a AMUPol solution with a concentration of 75 mM in deionized water resulting in molar ratios of 1:80, 1:16, 1:8, and

1:4 (PA:protein), respectively. The AMUPol-protein solutions were freeze-dried overnight to yield a powder, from which either 2 mg ubiquitin powder or 20 mg lysozyme was packed in a 1.3 mm zirconia rotor or in a 3.2 mm sapphire rotor, respectively. The rotors were sealed with a Vespel drive cap with matching diameters and, in the case of the 1.3 mm rotor, with a Vespel bottom cap.

The lysozyme-AMUPol powder was rehydrated in the rotor by placing the open 3.2 mm rotor inside a closed 1 L desiccator filled with 250 mL of deionized water until the desired water content, being measured gravimetrically, was obtained.

3.2.1.2 DNP-enhanced solid-state NMR spectroscopy

All NMR experiments were acquired with rf pulse powers for all hard pulses of 60 kHz (^1H & ^{13}C). The CP transfer was accomplished by matching the ^1H pulse power to the ^{13}C pulse power of 60 kHz during the 2 ms Hartmann-Hahn match. ^1H DNP build-up time constants were measured with a saturation recovery block before read-out of the building-up ^1H magnetization on the ^{13}C channel by a ^1H - ^{13}C CPMAS block (Figure 6). The saturation was achieved with 16 90° pulses on both channels with an inter-pulse delay of 10 ms. The intensity of the building-up magnetization was read out after 8 delays between 0.25 and 32 s. The beam currents used to produce microwaves were set to a range spanning from 126 to 132 mA.

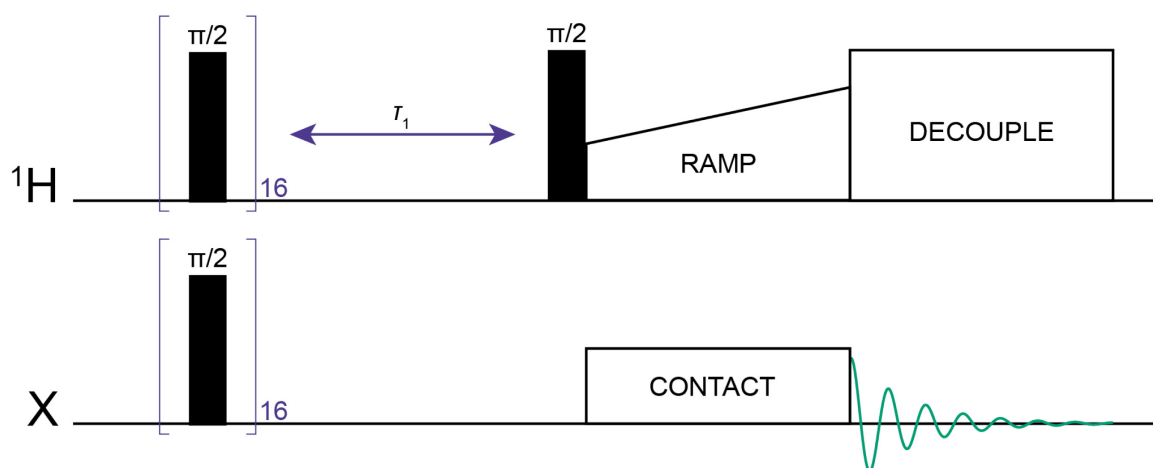


Figure 6: Pulse sequence to determine ^1H DNP build-up time constants T_B . The pulse sequence starts with an saturation train, which uses 16 90° pulses on both channels. The polarization is then allowed to build up dependent of the time τ_1 and subsequently read out after polarization transfer to the X channel, which is for example ^{13}C .

3.2.1.3 Spectral processing and data analysis

All NMR experiments were processed with zero-filling and apodization functions. For zero-filling, the acquired time domain points were either doubled or quadrupled resulting in either 4096 or 8192 points. An exponential window function with 50 Hz line broadening was

used for apodization. The ^1H DNP enhancement factors were determined by comparison of the ^1H - ^{13}C CPMAS spectra with and without microwave irradiation. The integration of the spectral regions was performed with a SIMPSON numerical integration algorithm using the SciPy python package^[84] and normalized to the accumulated number of transients. The normalized intensity was fitted with the *LMFit* python package and a monoexponential function of the following form:

$$I(t) = I_0 + A \left[1 - \exp\left(-\frac{t}{T_B}\right) \right], \quad (35)$$

where $I(t)$ is the signal intensity after the polarization time t , I_0 is the zero-time offset of the signal intensity, A is the signal amplitude after infinite time, and T_B is the ^1H DNP build-up time constant.

3.2.2 Characterization of $\text{A}\beta_{1-42}$ -adsorbing materials using matrix-free DNP

3.2.2.1 Sample preparation

The $\text{A}\beta_{1-42}$ -adsorbing materials were synthesized and kindly provided by Christoph Kamper and Dr. Jacqueline Heskamp (University Medicine Rostock and Fraunhofer Institute for Cell Therapy and Immunology IZI). In short, the material being either silica particles or cellulose in natural isotope abundance was functionalized with a layer of polydopamine (PDA) in natural isotope abundance and a layer of uniformly labeled ^{13}C , ^{15}N -lysine. After this functionalization, the materials were incubated with u - ^{13}C , ^{15}N -Arg, u - ^{13}C , ^{15}N -Lys $\text{A}\beta_{1-42}$ peptides. For the full characterization of these materials, samples of the materials at different preparation steps were prepared: a sample for the PDA-functionalized material (in the case of cellulose), a sample of the PDA- and lysine-functionalized material, and a sample of the fully functionalized sample with adsorbed $\text{A}\beta_{1-42}$ peptides. In the case of polydopamine (PDA)-functionalized cellulose, solid-state NMR experiments were conducted at 295 K. The sample was packed without further treatment in a 3.2 mm sapphire rotor (Bruker) and sealed with a Vespel drive cap. For DNP-enhanced solid-state NMR experiments, 13 mg of the silica particle-based materials and 19 to 29 mg of the cellulose-based material (Table 1) were each packed into a 3.2 mm sapphire rotor (Bruker). The powder was then impregnated with 100% (w/w) (in the case of the silica particles) or 60% (w/w) (in the case of cellulose) 20 mM AMUPol dissolved in a mixture of 67:33 vol-% D_2O : H_2O . Each rotor was then sealed using a Vespel drive cap.

Table 1: Mass of cellulose-based, A β ₁₋₄₂-adsorbing materials packed into a 3.2 mm sapphire rotor. All cellulose materials were treated first with PDA in order to introduce the functionalization required for A β ₁₋₄₂ adsorption.

Sample	Mass / mg
Cellulose	19
Lysine-functionalized cellulose	21.7
Lysine-functionalized cellulose with adsorbed A β ₁₋₄₂	29.2

3.2.2.2 Solid-state NMR experiments

The solid-state NMR experiments of PDA-functionalized cellulose was performed with rf pulse powers for all hard pulses of 100 kHz (¹H) and 58.82 kHz (¹³C). The ¹H–¹³C CPMAS experiment with a repetition delay of 5 s started with a pre-saturation block consisting of 16 90° pulses on both channels with an inter-pulse delay of 20 ms. For the Hartmann-Hahn match, a 2 ms contact pulse was applied, where the rf pulse power of the ¹H channel was matched to fulfill the matching condition and further ramped from 50% to 100% pulse power. For broadband ¹H decoupling, SPINAL-64 was used with a pulse power of 100 kHz.

3.2.2.3 DNP-enhanced solid-state NMR spectroscopy

All DNP-enhanced solid-state NMR experiments were acquired with microwave beam currents of 150 mA and rf pulse powers for all hard pulses of 100 kHz (¹H), 58.82 kHz (¹³C), and 38.46 kHz (¹⁵N). For all experiments, SPINAL-64 was used as broadband ¹H decoupling with a ¹H pulse power of 100 kHz.

The CPMAS experiments were performed with repetition delays between 5.5 s and 6.5 s and involved a pre-saturation train which consisted of 16 90° pulses on both channels separated by 25 ms and the CP transfer was accomplished with a pulse linearly increasing its pulse power from 50% to 100% and the ¹H rf pulse power was matched to the ¹³C or ¹⁵N pulse power to fulfill the Hartmann-Hahn matching condition. The length of the CP contact pulse was set to 2 ms for ¹H–¹³C CPMAS experiment and 2.5 ms for ¹H–¹⁵N CPMAS experiments.

The multiple contact CPMAS experiments^[85] (Figure 7) were recorded with eleven contacts, where each contact involved a CP transfer time of 500 μ s for ¹H–¹³C multiple contact CPMAS or 3 ms for ¹H–¹⁵N multiple contact CPMAS experiments. In both cases, the CP contact pulse of the ¹H channel was linearly increased from 70% to 100% pulse power and matched to the hard pulse power of ¹³C or ¹⁵N to fulfill the Hartmann-Hahn matching condition. The repetition time between each of the CP blocks was set to 10 s in the case of ¹³C detection

and 8 s for ^{15}N detection, which is approximately two times the average ^1H DNP build-up time constant of all spectral regions in the CPMAS experiment.

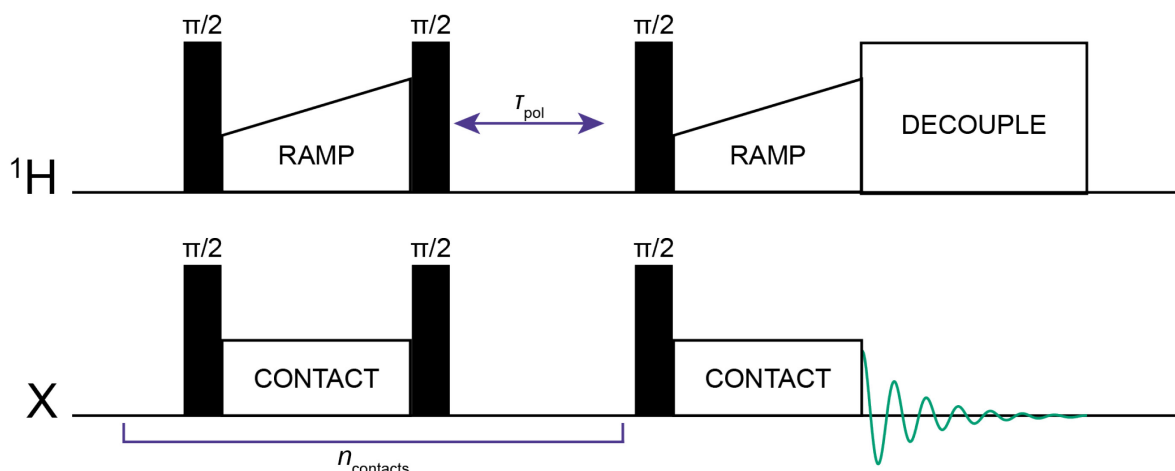


Figure 7: Pulse sequence for the multiple contact CPMAS experiment. The pulse sequence consists of a 90° pulse on both channels, followed by a contact pulse and a 90° pulse. After this block, the polarization is allowed to build up as τ_{pol} is set to $2 \cdot T_B$. The whole block is repeated n_{contacts} -times to allow for uniform distribution of polarization across all X nuclei. The last block consists of the same polarization transfer, where the final 90° pulse is not applied in order to detect the polarization in the transversal plane.

The ^1H DNP build-up time constant T_B was determined with a saturation recovery sequence (Figure 6) and the time-dependent polarization build-up was detected with 16 polarization times between 1 ms and 32768 ms with either a ^1H - ^{13}C CPMAS or a ^1H - ^{15}N CPMAS block.

The ^{13}C , ^{15}N correlation spectra were acquired with a TEDOR sequence involving a z-filter block after evolution of the indirect ^{15}N dimension.^[86] The excitation is based on a ^1H - ^{13}C CPMAS experiment. The spectral width was set to match one rotor period. The number of transients, the amount of t_1 slices, the increment delay per t_1 slice, the resulting spectral width and the recoupling time τ_{mix} are summarized in Table 2. The decoupling during the TEDOR recoupling sequence was accomplished with a Lee-Goldburg continuous wave sequence and a ^1H pulse power of 100 kHz. The broadband ^1H decoupling being applied for the acquisition of the FID was SPINAL-64 as described above.

Table 2: Parameters for the acquisition of z-filtered TEDOR experiments of the multi crystalline cellulose samples with and without adsorbed A β ₁₋₄₂ peptides at 105 K and either 8 kHz or 12.7 kHz MAS frequency.

Parameter	Cellulose without A β ₁₋₄₂		Cellulose with A β ₁₋₄₂	
	8 kHz	12.7 kHz	8 kHz	12.7 kHz
τ_{mix} / ms	1.0	5.04	1.26	5.04
Number of transients	32	32	32	32
Number of t_1 slices	32	36	64	64
t_1 increment delay / μ s	125.00	78.74	78.74	78.74
Spectral width / kHz	8.0	12.7	12.7	12.7
Spectral width / ppm	197.12	312.92	312.92	312.92

3.2.2.4 Spectral processing and data analysis

All NMR experiments were processed with zero-filling and apodization functions. For zero-filling, the number of the acquired time domain points were multiplied either by 4 or 8 resulting in either 8192 or 16384 points for the direct dimension. In the case of one-dimensional CPMAS and multiple contact CPMAS and the pseudo-two-dimensional build-up time experiments, the FID was multiplied with an exponential window function with a line broadening of 50 Hz.

The quantification of the masses of lysine and/or A β ₁₋₄₂ peptides in the cellulose samples are performed using ¹H-¹³C multiple contact CPMAS experiments. Here, the integrals of the C_O (170 ppm), Arg-C _{ϵ} (157.5 ppm), C _{α} (50 ppm), and C _{β} and Lys-C _{ϵ} (both 35 ppm) signal region of the amino acid and the C₁ signal region (100 ppm) of the cellulose are determined and normalized to the applied number of transients. The normalized intensities are then quantified using Equation 36:^[87]

$$m_x = \frac{I_x N_S M_x P_S}{I_S N_x M_S P_x} m_S, \quad (36)$$

where the subscripts refer to the reference sample (S) and analyte (x). m is the mass of the respective molecule, I the normalized NMR signal integral, N the number of nuclei associated to the NMR signal integral, M the molecular weight of the respective molecule, and P a factor considering the natural isotope abundance. The latter is set to either 0.011 or 1 if completely in natural isotope abundance or completely ¹³C-labeled, respectively. In the case of A β ₁₋₄₂ peptides, the P factor can also be greater than 1 as several nuclei can be associated with the signal, which can differ in their labeling pattern. For example, all nuclei associated with the C_O resonance are considered, yielding 37 nuclei in natural isotope abundance and three nuclei in 100% abundance. This results in a total P factor of 3.407 (see Table 3 for all constant values

used in the calculations). For the quantification, it is assumed that the mass of the reference sample (*viz.* cellulose) m_S corresponds to the total mass of the sample in the rotor (*cf.* Table 1).

Table 3: Used parameters for the quantification of analyte in the A β_{1-42} -adsorbing cellulose materials. The quantification was performed by determining the integral of the signal region of the nucleus and correlating it to the mass with Equation 36. The mass of the reference is assumed to be the total mass of the sample in the rotor. For the quantification of the lysine functionalization, the mass of the reference sample m_S is 21.7 mg; in the case of the A β_{1-42} peptides, m_S is equal to 29.2 mg (see Table 1).

Nucleus	<i>N</i>	<i>M</i> /g/mol	<i>P</i>
Cellulose C1	1	180.16	0.011
Lys-C _O	1	146.19	1
Lys-C _{α}	1	146.19	1
Lys-C _{β} & -C _{ϵ}	2	146.19	2
A β_{1-42} C _O	40	4346.8	3.407
A β_{1-42} -Arg-C _{ϵ}	1	174.2	1
A β_{1-42} -C _{α}	40	4346.8	3.407
A β_{1-42} -C _{β} & Lys-C _{ϵ}	33	4346.8	5.308

In the case of the 2D TEDOR experiments, zero-filling for the indirect dimension was applied by increasing the final points to 128 points. The direct dimension was multiplied with a squared sine function as apodization function and a sine bell shift value of 2, the indirect dimension was multiplied with either a squared sine or a sine function as apodization and a sine bell shift of 2.

For analysis of the ¹H DNP build-up time constants, the experiment is processed as described above and exported using the *NMRGlue* python package and spectral regions were integrated using the SIMPSON numerical integration algorithm of the SciPy python package^[84]. The integrated intensities were then normalized to the accumulated transients and fitted to Equation 35 to obtain the ¹H DNP build-up time constant T_B .

3.2.3 Site-specific investigation of API-carrying polymeric micelles

3.2.3.1 Sample preparation

The MeOx-BuOzi-MeOx (MBM) micelles were formulated with the thin film method by Kersten Ulrich at the University of Würzburg. In short, depending on the final constitution, MBM was dissolved together with either TOTAPOL or TEKPol and optionally efavirenz in dichloromethane and, subsequently, the solvent is evaporated at atmospheric pressure. The generated thin films were then dried in vacuo, which is followed by rehydration with water to

form micelles using a modified protocol developed by Kersten Ulrich during his Master's thesis.^[88] The freeze-dried micellar samples were then transferred into either a 1.3 mm zirconia or a 3.2 mm sapphire rotor and sealed using Vespel drive caps and in the case of the 1.3 mm rotor, a Vespel bottom cap.

3.2.3.2 Solid-state NMR experiments

The ^1H - ^{13}C CPMAS experiments of MBM micelles and pure efavirenz were conducted by Kersten Ulrich and Sebastian Scheidel, respectively, at the University of Würzburg using a 600 MHz spectrometer which is equipped with a 3.2 mm $^1\text{H}/^{19}\text{F}/^{13}\text{C}$ MAS probe from Bruker. The ^1H rf pulse power for hard pulses was set to 100 kHz and matched to the Hartmann-Hahn matching condition with ^{13}C during a 2 ms contact pulse. SPINAL-64 was used as a decoupling scheme during the acquisition of the FID. 5120 transients at 297 K and 10240 transients at 245 K were accumulated for the micelles and efavirenz, respectively, at 20 kHz MAS frequency. The repetition delay was set to 5 s and 2 s for the MBM micelles and efavirenz sample, respectively.

3.2.3.3 DNP-enhanced solid-state NMR spectroscopy

All DNP-enhanced solid-state NMR experiments were acquired with microwave beam currents of either 126 mA or 132 mA and rf pulse powers for all hard pulses of 125 kHz (^1H) and 60 kHz (^{13}C), in the case of the 1.3 mm LTMAS DNP probe operating in the $^1\text{H}/^{13}\text{C}/^2\text{H}$ triple channel mode, and 110 kHz (^1H) and 60 kHz (^{13}C), in the case of the 3.2 mm LTMAS DNP probe operating in the $^1\text{H}/^{13}\text{C}$ double channel mode. For all experiments, SPINAL-64 was used as broadband ^1H decoupling in all experiments with the pulse power used for the ^1H hard pulses.

The ^1H DNP build-up time constant T_B was determined with a saturation recovery sequence (Figure 6) and the time-dependent polarization build-up was detected with a ^1H - ^{13}C CPMAS block and 8 polarization times between 0.1 s and 16 s.

The ^1H - ^{13}C CPMAS experiments were performed with repetition delays corresponding to $1.3 \cdot T_B$ and involved a pre-saturation train which consisted of 16 90° pulses on both channels separated by 25 ms and the CP transfer was accomplished with a pulse linearly increasing its pulse power from 50% to 100% and the ^1H rf pulse power was matched to the ^{13}C pulse power to fulfill the Hartmann-Hahn matching condition. The length of the CP contact pulse was set to 2 ms.

3.2.3.4 Spectral processing and data analysis

All NMR experiments were processed with zero-filling and apodization functions. For zero-filling, the acquired time domain points were multiplied either by 4-fold or 8-fold. The resulting FID was multiplied with an exponential window function with a line broadening of 50 Hz.

For analysis of the ^1H DNP build-up time constants, the experiment is processed as described above and exported using the *NMRGlue* python package and spectral regions were integrated using the SIMPSON numerical integration algorithm of the SciPy python package^[84]. The integrated intensities were then normalized to the accumulated transients and fitted to Equation 35 to obtain the ^1H DNP build-up time constant T_B .

The ^1H DNP enhancement factor were determined by comparison of the signal intensities of the ^1H - ^{13}C CPMAS spectra with and without microwave irradiation at 102 K. The relative sensitivity gains were determined by comparing the signal amplitudes of the DNP-enhanced spectra acquired at a 400 MHz spectrometer with microwave irradiation and a temperature of 102 K to the solid-state NMR spectra recorded with a 600 MHz spectrometer at 297 K. The signal amplitudes were normalized to the number of accumulated transients before calculation of the relative sensitivity gains, which are the ratio of the signal amplitudes between the DNP-enhanced and the solid-state NMR spectra.

3.3 Quantification of Methyl Group Dynamics under DNP conditions

3.3.1 Investigation of Methyl Group Dynamics in $\text{A}\beta_{1-40}$ fibrils by DNP-enhanced ^1H - ^2H CPMAS NMR

3.3.1.1 DNP sample preparation

The chicken villin headpiece HP36 protein and the short disordered RC9 (GGKG[M-CD₃]GFGL) peptide were each dissolved in deionized water to a concentration of 1 mg/mL. The pH of the solutions was checked with pH indicator paper and adjusted with 1 M HCL to 5 and 2, respectively. AMUPol (75 mM in deionized water) was added to the two protein solutions to yield a molar ratio of 1:15 (PA:protein). Each mixture was then freeze-dried overnight and the resulting powder was transferred into a 1.3 mm zirconia rotor (Bruker). The

hydration of the two samples were performed inside the rotor by adding deuterium-depleted water (2 to 3 ppb ^2H , Cortecnet) to yield a water content of 60% (w/w) and 75% (w/w) for the HP36 protein and the RC9 peptide, respectively.

The $\text{A}\beta_{1-40}$ fibrils were prepared in the three-fold symmetric polymorph as described here^[10e, 89] and provided by Prof. Dr. Liliya Vugmeyster as freeze-dried powder. Three separate fibril samples, each with a selectively deuterated methyl group at the indicated position, were prepared: H6- τ - CD_3 , L34- CD_3 , and M35- CD_3 . Only one of the two methyl groups in leucine was deuterated yielding a 50% deuteration level per (potentially) non-equivalent methyl group. The provided fibril samples were the same as used in the previous work cited above to guarantee optimum comparability, nonetheless, the addition of PA was required for DNP. 14 mg of each fibril sample was resuspended in 50 mL deionized water at pH 7.4 containing 0.01% (w/w) sodium azide and the resulting suspension was sonicated in a bath sonicator in 1 min intervals for 5 min total. The suspension was then incubated on an orbital shaker with 60 rpm for 12 hours. 2.67 μL (200 nmol) of a 75 mM AMUPol solution in deuterium-depleted water was added to each fibril sample, which resulted in a molar ratio of 1:15 (PA:protein). The mixture was then incubated on the orbital shaker with 60 rpm for 15 minutes to ensure optimum distribution of the AMUPol through the fibril sample. Afterwards, the suspension was freeze-dried overnight and the resulting powder was transferred inside a 3.2 mm sapphire rotor (Bruker). For rehydration of the $\text{A}\beta_{1-40}$ fibrils, each protein-AMUPol powder was mixed with deuterium-depleted water to a water content of 100% (w/w). All three rotors were sealed with a silicone plug and a Vespel drive cap.

3.3.1.2 Low temperature solid-state NMR experiments

The pulse powers for all hard pulses were set to 60 kHz (^1H) and 50 kHz (^2H) for the 3.2 mm probe and 100 kHz (^1H) and 50 kHz (^2H) for the 1.3 mm probe. The ^2H MAS NMR experiments were performed as one pulse experiments.

The $T_1(^2\text{H})$ relaxation time constants of doped fibril samples in the absence of microwaves were measured with a direct excitation scheme combined with an inversion recovery sequence with delays for polarization recovery between 0.1 and 55 ms.

3.3.1.3 DNP-enhanced solid-state NMR experiments

The beam currents of the gyrotron were varied with strengths between 120 mA and 150 mA in order to obtain the highest DNP enhancement factors. All ^1H - ^2H CPMAS experiments were performed with hard pulse powers of 60 kHz (^1H and ^{13}C) and 50 kHz (^2H)

in the case of the 3.2 mm probe and 100 kHz or 131.5 kHz (^1H), 60 kHz (^{13}C), and 50 kHz (^2H) in the case of the 1.3 mm probe. The CP transfer was accomplished by matching the ^1H pulse power of the CP contact pulse to the ^2H pulse power for 2 ms in order to fulfill the Hartmann-Hahn matching condition. In addition, the ^2H CP contact pulse was linearly increased from 50% to 100% pulse power. No ^1H decoupling was applied during the detection of the FID.

The $T_1(^2\text{H})$ relaxation time constants of the doped fibrils were determined with the Torchia method.^[91] The pulse sequence starts with a constant polarization time of 3 s, followed by a ^1H - ^2H CPMAS transfer block, and a z-filter block (Figure 8). The CPMAS block is the same as described above and the z-filter is employed for a time-dependent polarization decay to determine the relaxation times. Delays between 0.1 ms and 55 ms were chosen as variable delays for the z-filter block. No ^1H decoupling is applied during the detection of the FID.

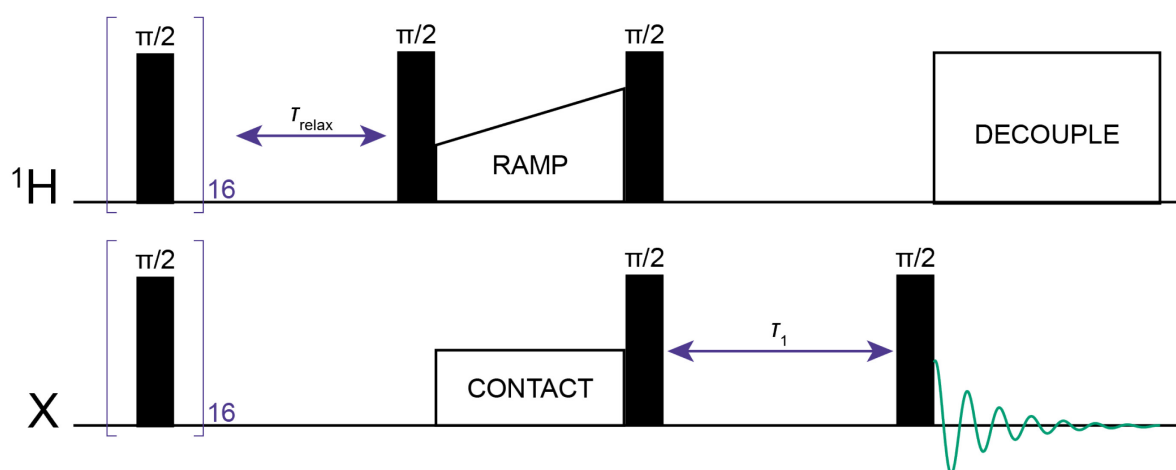


Figure 8: Pulse sequence to determine heteronuclear spin-lattice relaxation time constants $T_1(X)$ using CPMAS as excitation method. The pulse sequence starts with a saturation train consisting of 16 90° pulses which are separated by a short delay. The polarization is then allowed to build up with the time τ_{relax} , which is set to $1.3 \cdot T_B$. After polarization transfer to the heteronuclei, the polarization is flipped into the longitudinal to allow for spin-lattice relaxation during time τ_1 . The left over polarization is flipped into the transversal plane for detection, where ^1H is optionally decoupled.

The sample temperature calibration was achieved by measuring $T_1(^{79}\text{Br})$ relaxation time constants of finely ground KBr powder at various temperatures using a saturation recovery sequence. The determined $T_1(^{79}\text{Br})$ relaxation time constants are used to obtain a calibration curve between the actual sample temperature (of the KBr powder) and the detected temperature of the PT100 thermocouple inside the MAS stator following established protocols.^[92] The resulting calibration curve was used for correcting the sample temperatures after the experiments:

$$T_{\text{KBr}} = 18.86676 \text{ K} + 0.85123 \cdot T_{\text{PT100}}, \quad (37)$$

where T_{KBr} is the actual sample temperature and T_{PT100} is the detected temperature of the PT100 temperature sensor inside the MAS stator.

3.3.1.4 Spectral processing and data analysis

All ^{13}C NMR spectra were processed with an exponential apodization function with 50 Hz line broadening in Topspin 4.4.0. All ^2H NMR spectra were exported before processing and the FID was processed using the *NMRGlue* python package.^[83] The FID was left shifted by 40 time points to minimize first-order phase correction and baseline distortions. The shifted FID was Fourier transformed and processed with an exponential apodization function with line broadening between 50 and 250 Hz. The baseline was corrected with either a constant value or a linear function.

The ^1H DNP enhancement factors were determined by comparison of the signal intensities of the ^1H - ^{13}C CPMAS spectra with and without microwave irradiation. As a measure for the signal gain achieved by DNP in comparison to ^2H MAS NMR, the signal amplitudes of both experiments at temperatures between 100 K and 152 K were determined from the most intense band in the resulting ^2H spectra. The root-mean-square (RMS) value of a spectral region without any signal representing 1.6% of the full width spectrum was calculated and used for the analysis of the experimental noise. The signal amplitudes as well as the experimental noise were normalized to either the number of accumulated transients or the square root of the number of accumulated transients, respectively, to account for variations in those numbers. The signal amplitudes were further normalized to account for differences in the repetition delays in the ^1H - ^2H CPMAS and ^2H MAS experiments. A fixed repetition delay of either 3 s or 0.3 s was used for the ^1H - ^{13}C CPMAS experiments or the ^2H MAS experiments, respectively. The normalized signal amplitudes were then used to determine the relative sensitivity gains which are the ratio between the ^1H - ^{13}C CPMAS spectra and the ^2H MAS spectra.

The ^1H DNP build-up time constant was obtained by exporting the processed spectra, followed by integration of the spectral regions using the Simpson algorithm of the *SciPy* python package and normalization to the number of accumulated transients. The normalized signal intensity was then fitted to a monoexponential function (Equation 35) to yield the ^1H DNP build-up time constant T_{B} .

The $T_1(^2\text{H})$ relaxation time constant was determined by Prof. Dr. Liliya Vugmeyster. In short, a self-written MatLab program processes the ^2H FID as described above and calculates

the sum of the signal intensities of each band in the ^2H spectrum. The data was further normalized to the number of accumulated transients and fitted to either a monoexponential function:

$$I(t) = I_0 + A \left[1 - \exp\left(-\frac{t}{T_1}\right) \right], \quad (38)$$

or to a stretched exponential function:

$$I(t) = I_0 + A \left[1 - \exp\left(-\left(\frac{t}{T_1}\right)^\beta\right) \right], \quad (39)$$

where $I(t)$ is the signal intensity after time t , I_0 is the zero-time offset of the signal intensity, A is the signal amplitude after an infinite time, T_1 is the build-up time constant and β is the stretching factor.^[93]

3.3.2 Systematic investigation of methyl group dynamics under DNP conditions

3.3.2.1 Sample preparation

The ethanol- d_6 (Sigma-Aldrich) was mixed with glycerol (Sigma-Aldrich), AMUPol and deionized water to yield a solution of 30:50:20 vol-% (ethanol- d_6 :glycerol: H_2O) containing 2.5 mM AMUPol. The solution was transferred into a 3.2 mm sapphire rotor (Bruker) and the rotor was sealed with a Vespel drive cap.

The ethanol- d_3 (Sigma-Aldrich) was mixed with glycerol (Sigma-Aldrich) and deuterium-depleted water (2 to 3 ppb, Cortecnet) for stock solutions of various concentrations (Table 4). The stock solutions were degassed using the freeze-thaw-pump technique. In short, the solution was transferred into a 5 mL reaction flask, which was connected to a Schlenk line apparatus. The solution was frozen by placing the reaction flask in a liquid nitrogen bath, and the flask was evacuated for 5 min immediately after freezing. The vacuum was then broken by venting the reaction flask with the solution inside with argon and the sample was thawed for 10 min at room temperature. This freeze-pump-thaw procedure was repeated at least 3 times to ensure that the solution is oxygen-free. The solution was then stored under argon atmosphere and $-80\text{ }^\circ\text{C}$ until further treatment.

The degassed stock solutions (43.33 μL) were each mixed with either 6.67 μL of 75 mM PA dissolved in deuterium-depleted water or with 3.33 μL of 75 mM PA dissolved in deuterium-depleted water and 3.33 μL deuterium-depleted water to yield either a concentration

of 10 mM PA or 5 mM PA, respectively, in the final sample, which was transferred into a 1.3 mm zirconia rotor or a 3.2 mm sapphire rotor (Bruker). Both rotors were before packed with 1 mg (1.3 MM rotor) or 5 mg (3.2 mm rotor) of finely grounded KBr powder, which was separated from the liquid sample using a FKM spacer. Both rotors were sealed with a matching Vespel drive cap and, in the case of the 1.3 mm rotor, a Vespel bottom cap.

Table 4: Ratios of glycerol, deuterium-depleted water, and ethanol-d₃ for the stock solutions and sample solutions. The stock solutions were degassed using the freeze-pump-thaw approach. 43.33 μ L of each stock solution was mixed with 6.67 μ L deuterium-depleted water containing either 75 mM PA or 37.5 mM PA.

Ratio of glycerol:H₂O:ethanol-d₃ in stock solution / vol-%	Ratio of glycerol:H₂O:ethanol-d₃ in sample solution / vol-%
57.7:7.7:34.6	50:20:30
57.7:25:17.3	50:35:15
57.7:30.8:11.5	50:40:10
57.7:36.5:5.8	50:45:5

3.3.2.2 Low-temperature solid-state NMR experiments

The pulse powers for all hard pulses were set to 60 kHz (¹H) and 50 kHz (²H) for the 3.2 mm probe and 139 kHz (¹H) and 60 kHz (²H) for the 1.3 mm probe. The ²H MAS NMR experiments were performed as one-pulse experiments with solid-echo detection.

The T_1 (²H) relaxation time constants were measured with a direct excitation scheme combined with a saturation recovery sequence with delays for polarization recovery between 0.1 ms and 4 s and a solid echo detection. In addition, the experiments were performed without microwave irradiation if not stated otherwise.

3.3.2.3 DNP-enhanced solid-state NMR experiments

The beam currents of the gyrotron were varied with strengths between 120 mA and 150 mA in order to obtain the highest DNP enhancement factors. All ¹H-²H CPMAS experiments were performed with hard pulse powers of 60 kHz (¹H and ¹³C) and 50 kHz (²H) in the case of the 3.2 mm probe and 139 kHz (¹H), 60 kHz (¹³C), and 62.5 kHz (²H) in the case of the 1.3 mm probe. The CP transfer was accomplished by matching the ¹H pulse power of the CP contact pulse to the ²H pulse power for 2 ms in order to fulfill the Hartmann-Hahn matching condition. In addition, the ¹H CP contact pulse was linearly increased from 50% to 100% pulse power. SPINAL-64 was applied as broadband ¹H decoupling during the detection of the FID.

The ^1H DNP build-up time constant was obtained by exporting the processed spectra, followed by integration of the spectral regions using the SIMPSON algorithm of the SciPy python package and normalization to the number of accumulated transients. The normalized signal intensities were then fitted to a monoexponential function (Equation 35) to yield the ^1H DNP build-up time constant T_B .

The $T_1(^2\text{H})$ relaxation time constants of the doped ethanol- d_3 samples were determined with the Torchia method.^[91] The pulse sequence starts with a constant polarization time of $1.3 \cdot T_B$, followed by a ^1H - ^2H CPMAS transfer block, and a z-filter block (Figure 8). The CPMAS block is the same as described above and the z-filter is employed for a time-dependent polarization decay to determine the relaxation time constants. 16 to 32 delays between 0.1 ms and 4 s were chosen as variable delays for the z-filter block. SPINAL-64 was applied as broadband ^1H decoupling during the detection of the FID.

The sample temperature calibration was achieved by measuring $T_1(^{79}\text{Br})$ relaxation time constants of finely ground KBr powder at each temperature using a saturation recovery sequence. The time-dependent spectra were fitted to Equation 38 to yield $T_1(^{79}\text{Br})$ relaxation time constant which was correlated to the actual sample temperature following established protocols.^[92]

3.3.2.4 Spectral processing and data analysis

The FIDs of all NMR experiments were exported and processed with the *NMRGlue* python package.^[83] Here, each FID was shifted by 33 time points to minimize first-order phase correction and baseline distortion. before Fourier transformation. An exponential window function was multiplied with a line broadening factor of 250 Hz. The baseline was corrected with either a constant baseline or a first-order baseline correction.

The ^1H DNP enhancement factors were determined by comparison of the signal intensities of the ^1H - ^{13}C CPMAS spectra with and without microwave irradiation. As a measure for the signal gain achieved by DNP instead of ^2H MAS NMR, the same procedure for determination of the signal amplitudes, noise amplitudes, and relative sensitivity gains as described in Section 2.3.1.5 was performed.

The $T_1(^2\text{H})$ relaxation time constants were determined by processing the experiments as described above. The time-dependent ^2H spectra were integrated using the Simpson algorithm of the SciPy package in python and fitted to Equation 39 using the *LMfit* python package. The mean $T_1(^2\text{H})$ values were calculated using the fit results of Equation 40 as input for:

$$T_{1,\text{avg}} = \frac{T_1}{\beta} \Gamma\left(\frac{1}{\beta}\right), \quad (40)$$

where $\Gamma(x)$ is Euler's Gamma function.

4. Results and Discussion

4.1 Combination of Cross Relaxation with Rotational Resonance

The use of molecular dynamics and therefrom induced heteronuclear cross-relaxation as a guide towards more selectivity of hyperpolarization has shown to be very promising in a lot of biomolecules^[46, 58, 60a-e] and biomaterials^[94] during dynamic nuclear polarization (DNP) experiments. Besides methyl reorientation, this transfer has been additionally observed for the reorientation of $-NH_3$ groups^[61b] and ring conversions in cyclohexane^[61a] and proline^[60c, 95]. Nevertheless, a controlled transfer of the polarization after the cross-relaxation-based transfer step has not been shown so far and spreading of the polarization within the molecule of interest has relied on spin diffusion.^[60a, 60e] In order to increase the selectivity between different ^{13}C sites, the usage of dipolar recoupling during the SCREAM-DNP (Specific Cross Relaxation Enhancement by Active Motions under Dynamic Nuclear Polarization) experiment is investigated in this chapter. Here, rotational resonance (R^2) has to be employed since it is not driven by radio frequency (rf) pulses but is a pure phenomenon of spin dynamics.^[22, 60f, 75, 96] Hence, it can be considered as a passive dipolar recoupling sequence which recouples spins by matching the MAS (magic angle sample spinning) frequency to the difference of the isotropic chemical shifts of the spins of interest. In this chapter, the combination of cross-relaxation and R^2 will be systematically investigated with SCREAM-DNP experiments of selectively labeled ethyl acetate at MAS frequencies between 6 and 35 kHz.^[60f] This effect is furthermore adapted for a ribonucleoprotein complex highlighting its potential for DNP-enhanced biomolecular solid-state NMR (nuclear magnetic resonance).^[60e]

4.1.1 Systematic investigation of the MAS frequency-dependency of SCREAM-DNP experiments with selectively labeled ethyl acetate

In order to investigate and verify the combination of R^2 dipolar recoupling and SCREAM-DNP, a selectively labeled model system was synthesized and SCREAM-DNP experiments were acquired at MAS frequencies between 6 and 35 kHz. The synthesis of 2- ^{13}C -ethyl 1- ^{13}C -acetate, the acquisition of the 1H - ^{13}C CPMAS (cross polarization under MAS) and the SCREAM-DNP experiments for the ethyl acetate and the following analysis of the SCREAM-DNP buildup rates (Figure 9, Figure 10, and Figure 12) were conducted as part of the Bachelor thesis of Edvards R. Bensons which I supervised.^[82] The following section summarizes these results briefly and discusses additionally the SCREAM-DNP buildup

behavior via the intensity of the ΔDP_{sat} spectra after a short and long polarization time revealing spurious and slow transfer processes which are suppressed by either the dipolar recoupling and/or the efficient spin diffusion at low MAS frequencies.^[60f]

The selectively labeled ethyl acetate (2 vol-%) in solution with 50:38:10 vol-% glycerol- d_8 /D $_2$ O/H $_2$ O shows an exceptionally high ^1H DNP enhancement factor of ~ 480 for the C_O and glycerol resonances by the comparison of the microwave on/off spectra (Figure 9). The uniform enhancement factor indicates that the hyperpolarization is distributed homogeneously across the sample. However, no depolarization is taken into account^[19] which decreases the observed enhancement by a factor of approximately 0.6 as shown in the literature for AMUPol at 110 K and a MAS frequency of 10 kHz.^[19b] Note that a precise enhancement factor cannot be calculated as this requires an undoped sample in order to derive the exact depolarization factor for this sample at the given MAS frequency as depolarization is highly dependent on the sample constitution and the MAS frequency.^[97] The methyl group resonance displays an even larger apparent enhancement factor than the carbonyl group. This indicates that the three-fold reorientation dynamics around the C_3 symmetry of the methyl axis is still active at 102 K. It was shown that the methyl group reorientation interferes with the CP spinlock and/or decoupling rf fields.^[55] Furthermore, the change in sample temperature caused by the microwave irradiation significantly affects the Arrhenius-like reorientation dynamics resulting in different rf field interferences of the methyl group for the microwave on and off spectrum.

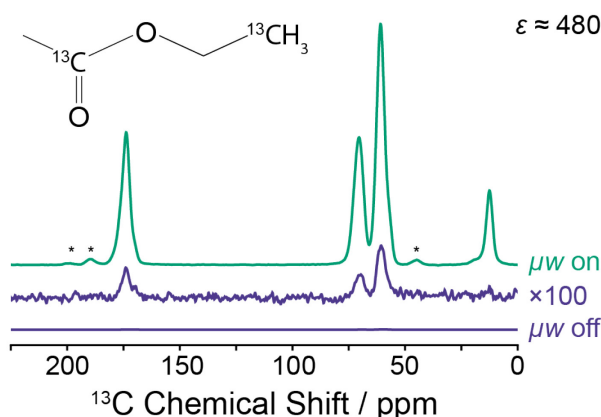


Figure 9: Comparison of ^1H - ^{13}C CPMAS spectra of 2 vol-% $2\text{-}^{13}\text{C}$ -ethyl $1\text{-}^{13}\text{C}$ -acetate mixed with glycerol- d_8 :D $_2$ O:H $_2$ O (50:38:10 vol-%) and 7.5 mM AMUPol with (μw on, green) and without (μw off, yellow) microwave irradiation at 102 K and 13 kHz MAS frequency. The ^1H DNP enhancement factor was determined by this comparison to be ~ 480 for the C_O and both glycerol resonances. The μw off spectra was scaled by a factor of 100 ($\times 100$) for better visibility. Signals denoted with an asterisk are spinning sidebands of the carbonyl or the glycerol resonances. The chemical structure with carbon-13 enrichment is depicted in the upper left corner.

The high enhancement enabled the systematic investigation of SCREAM-DNP in combination with R^2 . To identify the R^2 matching condition, ΔDP_{sat} spectra were acquired at MAS frequencies between 6 and 32.5 kHz with a polarization time of 8 s (Figure 10). For better visibility of the changes to the carbonyl signal, all spectra have been normalized to the same methyl signal intensity. At the lowest tested MAS frequency of 6 kHz, the carbonyl signal intensity is, as expected, lower than the one of the methyl group indicating a slow transfer of polarization between the two dipolar-coupled spins by spin diffusion (Figure 10, green). Noteworthy, the two resonances of glycerol at 65 ppm and 75 ppm can still be observed due to intermolecular spin diffusion. Interestingly, the two glycerol signals display a 1:1 signal intensity ratio despite the expected 2:1 concentration ratio for the two primary alcohol groups and one secondary alcohol group. This is caused by the accidental R^2 matching of the secondary alcohol group with the methyl group ($\Delta\omega_{\text{iso}} \approx 5800$ Hz). The second side band of the carbonyl signal is almost matched to the primary alcohol resonance ($\Delta\omega_{\text{iso}} \approx 11400$ Hz); however, the efficiency of this transfer, despite the rather large CSA (chemical shift anisotropy) of the carbonyl spin, is rather low as this transfer step is indirect and involves a second polarization transfer from the methyl group, being the source of ^{13}C polarization, to the carbonyl. A carbonyl signal intensity of comparable size is found at 13 kHz MAS frequency (Figure 10, yellow) suggesting a still efficient intramolecular polarization transfer by spin diffusion. Additionally, due to the missing match of the R^2 condition, no glycerol signals are visible displaying the efficiency of the SCREAM-DNP filter for suppression of solvent signal. As spin diffusion becomes more inefficient with increasing MAS frequencies, the carbonyl resonance is decoupled from the mobile methyl group and thus, a low carbonyl signal intensity is observed at very fast MAS frequencies (Figure 10, pink and orange).

Most strikingly, the carbonyl signal increases to the same intensity as the methyl group for the MAS frequencies of 8 kHz and 16.25 kHz (Figure 10, violet and blue), indicating a successful matching by R^2 and reintroduction of the strong static dipolar coupling between the two coupled spins. The comparison of the two matching conditions with each other shows that the $n = 1$ R^2 matching condition at 16.25 kHz MAS frequency is slightly stronger than the $n = 2$ matching condition at 8 kHz due to the more intense first side band. Both conditions, however, clearly demonstrate that the reintroduction of dipolar coupling by R^2 strongly enhances the signal intensity of $^{13}\text{C}_\text{O}$ at short polarization times resulting in significant time savings as longer polarization times and/or high amounts of accumulated transients are not required. Besides potential time savings, this approach also introduces increased selectivity for

transferring hyperpolarization into a biomolecule of interest. The application of this technique in a ribonucleoprotein complex will be discussed in detail in the next section (Section 4.1.2).

An opposite trend is visible for longer polarization times, for instance 128 s (Figure 10). The signal intensities at this long polarization time are considered to be in a steady-state equilibrium to the lattice; for example, the glycerol resonances are resembling the expected 1:2 signal intensity ratio due to sufficient time for the buildup of polarization with the slow and more ineffective polarization transfer relay by the ^{13}C -carbonyl. In order to compare the intensities after both polarization times, the signal intensities of the carbonyl- and methyl- ^{13}C resonances in the $\Delta\text{DP}_{\text{sat}}$ spectra at all measured MAS frequencies and two exemplary polarization times are integrated and normalized to the number of accumulated transients. Furthermore, the ratio of the carbonyl to the methyl signal intensity at each MAS frequency is calculated to display the relative signal intensity of the carbonyl (Figure 11). As expected and already visible in the $\Delta\text{DP}_{\text{sat}}$ spectra (Figure 10), the relative carbonyl intensity is lower than 1 after 8 s polarization time at all MAS frequencies indicating that the polarization buildup on the carbonyl is retarded by the slow spin diffusion transfer process. An exception are the intensities at the R^2 matching conditions, which show a stronger intensity, even increasing to a relative signal intensity of ~ 1 for the $n = 1$ condition proving again a successful acceleration of SCREAM-DNP experiments by R^2 recoupling.

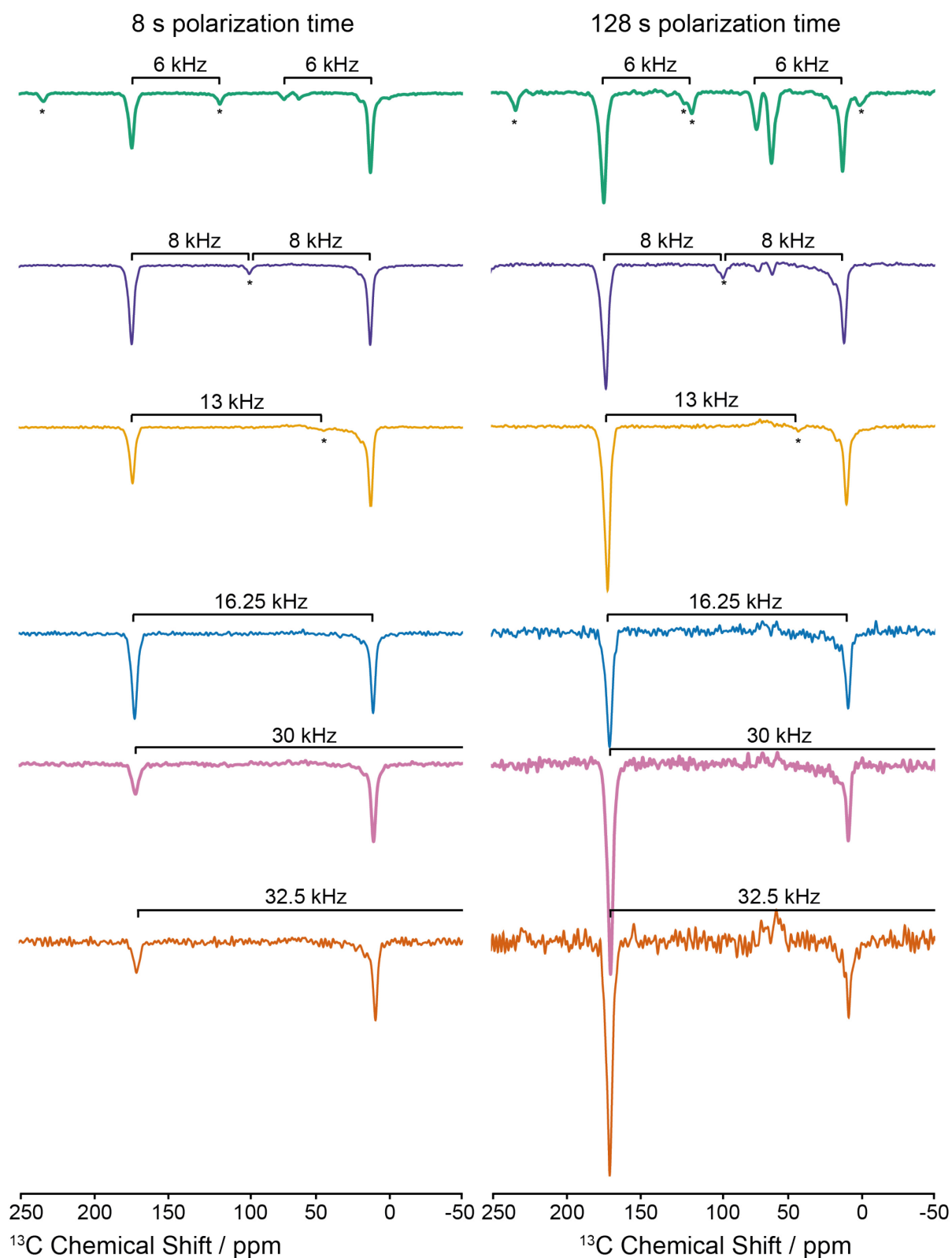


Figure 10: ^{13}C $\Delta\text{DP}_{\text{sat}}$ spectra of SCREAM-DNP experiments measured with 8 s and 128 s polarization time at different MAS frequencies for 2- ^{13}C -ethyl 1- ^{13}C -acetate at 102 K. 7.5 mM AMUPol is dissolved in 50% (v/v) glycerol- d_8 , 38% (v/v) D_2O , 10% (v/v) H_2O , and 2% (v/v) ethyl acetate. The SCREAM-DNP experiments at 6 kHz, 8 kHz, and 13 kHz are measured in a 3.2 mm, whereas the experiments at 16.25 kHz, 30 kHz, and 32.5 kHz are performed in a 1.3 mm low-temperature MAS/DNP probe. All spectra are normalized to the same methyl signal intensity. Peaks highlighted with an asterisk (*) are spinning sidebands.

In the case of a long polarization time, for example 128 s, the amplitude of the carbonyl signal is more intense than the methyl signal at all tested MAS frequencies. The relative signal intensity of the carbonyl- ^{13}C is rather low, but still greater than 1 at moderate MAS frequencies (*cf.* the intensity at 6 kHz MAS frequency in Figure 11) and becomes more pronounced at high MAS frequencies. By increasing the MAS frequencies up to 35 kHz, the relative signal intensity increases up to a value of ~ 3 . If the methyl- ^{13}C nucleus is the only source of polarization in the system, the relative intensity of the carbonyl- ^{13}C should not exceed a value of 1 at all conditions indicating that further, spurious buildup pathways are present. One such pathway could be the direct transfer of polarization from the electron to the ^{13}C nucleus (direct ^{13}C DNP), however, this is negligible due to the signal inversion of the SCREAM-DNP and the high fidelity of the interleaved acquisition.^[46] Another possible spurious pathway would be the cross-relaxation transfer of the natural abundance methyl group of the acetate group. It is expected that a polarization transfer between these two ^{13}C sites should be highly efficient given the direct bond to the carbonyl group—corresponding to a ^{13}C – ^{13}C dipolar coupling of 2 kHz—and the low energy barrier of the reorientation dynamics which was determined by Marcel Brandt as part of a scientific internship to ~ 2 kJ/mol.^[98] As the methyl group of the acetate function is only ^{13}C -labeled with natural abundance, the number of this spin pair is reduced by a factor 100, potentially rendering this contribution to the final signal negligible. In contrast, unspecific fluctuations of various ^1H – $^{13}\text{C}_\text{O}$ dipolar couplings may additionally add to the slow polarization buildup.

In general, these spurious transfer pathways display a rather slow build-up rate constant as it can be qualitatively assessed by the missing plateau signal intensity after 512 s polarization time. Interestingly, higher normalized signal intensities are observed for increasing MAS frequencies. This indicates that these spurious transfer pathways are contributing to the polarization transfer process, but play a minor role if stronger polarization pathways, such as spin diffusion or dipolar couplings, are active. Additionally, the decoupling of the $^{13}\text{C}_\text{O}$ nucleus from the other ^{13}C nuclei by elevated MAS frequencies results in a prolongation of the T_1 relaxation time constant of the $^{13}\text{C}_\text{O}$ nucleus. This further enables the accumulation of polarization by these spurious transfer pathways. Particularly, it is noticeable at the two MAS frequencies that match the R^2 condition as they exhibit smaller amplitudes for the carbonyl signal as other MAS frequencies. This behavior in the case of R^2 matching is not surprising since the R^2 recoupling not only accelerates the polarization buildup and thus leading to a higher relative intensity after short polarization times (visible maxima in Figure 11, violet), but

also matches the spin-lattice relaxation time constants towards the smaller one (negative dips at 8 and 16.25 kHz in Figure 11, green).^[75a, 75b] This explains the lower amplitudes observed for the R^2 matching conditions than for the non-matching conditions.

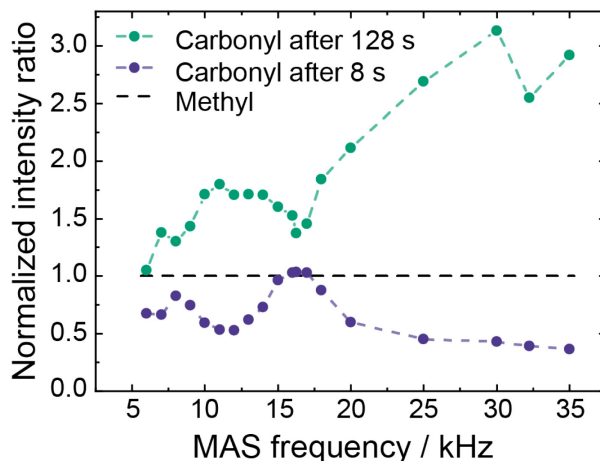


Figure 11: Normalized integrated signal intensity ratio of the carbonyl- ^{13}C resonance in the $\Delta\text{DP}_{\text{sat}}$ spectra after either 8 s (violet) or 128 s (green) polarization time of SCREAM-DNP experiments at MAS frequencies between 6 and 35 kHz. For the normalization, the integrated signal intensity was divided by the number of accumulated transients followed by the division of the measured methyl- ^{13}C integrated signal intensity at the given MAS frequency. The normalized intensity ratio of the methyl- ^{13}C group is depicted as a dashed black line. The colored dashed lines connecting the carbonyl data points serve only as a guidance to the eyes. The data points at MAS frequencies between 10 and 14 kHz which were measured in both probes reflect the averaged value of the two measured intensities, the non-averaged plot can be found in Appendix Figure A 1.

Finally, to systematically investigate the acceleration of SCREAM-DNP experiments by dipolar recoupling, the SCREAM-DNP buildup rates of the selectively ^{13}C -labeled groups in ethyl acetate are determined by variation of the polarization times from 0.5 s up to 512 s at all tested MAS frequencies.

The intensities of the ^{13}C -methyl and -carbonyl signal from the $\Delta\text{DP}_{\text{sat}}$ spectra are integrated and fitted to Equation 34 resulting in the SCREAM-DNP build-up rate constant R_f . Figure 12 shows the obtained rate constants against the corresponding MAS frequency. Here, the SCREAM-DNP build-up rate constants of the methyl group are scattered around $0.12 \pm 0.02 \text{ s}^{-1}$ without any correlation to the applied MAS frequency (Figure 12, violet circles and dashed line). This is expected because the polarization buildup on the methyl group is based on the polarization of the proton bath as well as the methyl group dynamics modulating the dipolar interaction between the ^1H - ^{13}C methyl spins, thereby inducing the cross-relaxation based transfer. In comparison to known SCREAM-DNP build-up rate constants from the literature, the observed rate for the selectively labeled methyl group in 2- ^{13}C -ethyl 1- ^{13}C -

acetate is slightly slower, however, the literature values were obtained at a partially elevated temperature of 110 K.^[60a, 60c, 60d]

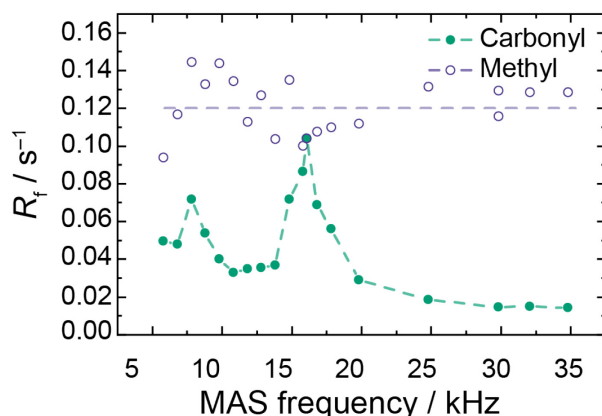


Figure 12: SCREAM-DNP polarization buildup rate constants of carbonyl- (green) and methyl- ^{13}C (violet) groups in ethyl acetate at MAS frequencies between 6 and 35 kHz at 102 K. SCREAM-DNP experiments were performed with 2 vol-% $2-^{13}\text{C}$ -ethyl $1-^{13}\text{C}$ -acetate mixed with 7.5 mM AMUPol in glycerol- $d_8/\text{D}_2\text{O}/\text{H}_2\text{O}$ (50/38/10 vol-%). The methyl buildup rate constant was observed to be independent of the MAS frequency with a mean value of 0.12 ± 0.02 which is depicted as in the graph as the dashed yellow line. The dashed green line serves as a guidance to the eyes. The experiments to obtain the buildup rate constants were measured with either a 3.2 mm DNP LTMAS probe (6 to 14 kHz) or a 1.3 mm DNP LTMAS probe (10 to 35 kHz). Four MAS frequencies were measured in both probes and observed to be similar and thus averaged. The non-averaged plot can be found in Appendix Figure A 2.

In the case of the carbonyl group, the same trend, as observed with the normalized intensities after a polarization time of 8 s, is visible where the polarization build-up rate constants reach the maximum value at the R^2 matching conditions. For the $n = 1$ matching condition, the carbonyl polarization build-up rate constant is accelerated to a rate of 0.10 s^{-1} , almost converging to the rate constant of the methyl group. This suggests a nearly instantaneous polarization transfer between the dipolar-coupled spins and points out that the rate-limiting step at the R^2 condition is the build-up of hyperpolarization on the methyl group by SCREAM-DNP. A slightly lower, but still fast polarization build-up rate constant of 0.07 s^{-1} is visible at 8 kHz MAS frequency illustrating a loss in efficiency for the $n = 2$ R^2 condition due to the lower second side band intensity. At MAS frequencies higher than 20 kHz, the buildup of carbonyl polarization is further retarded due to low efficiency of spin flip-flops required for the transfer of polarization by spin diffusion. Here, the buildup rate constant is determined to be 0.03 s^{-1} at 20 kHz and converge to 0.01 s^{-1} towards faster MAS frequencies.

In conclusion, this section proves not only the applicability of SCREAM-DNP with dipolar recoupling, but also shows a significant acceleration of detectable polarization on the site of interest, in this case the carbonyl in selectively labeled ethyl acetate. Consequently, the combination of SCREAM-DNP with R^2 can be beneficial for all experiments where a selective

transfer between a methyl site and, for example, a carbonyl site is of interest. A possible application will be discussed in the next section. Besides, this section also demonstrates that spurious transfer pathways are present, however, are only of significance if fast polarization propagation such as spin diffusion is inefficient (*e.g.*, fast MAS). The origin of these spurious pathways is discussed, and the most likely origin is various fluctuations of ^1H - ^{13}C O dipolar couplings, given by, for instance, the ^1H of the second methyl group.

4.1.2 Applications of SCREAM-DNP experiments with dipolar recoupling in a ribonucleoprotein complex

SCREAM-DNP is an ideal experiment for the investigation of biomolecular complexes involving RNA (ribonucleic acid) molecules due to the absence of methyl groups in ribonucleotides. Thus, binding studies between an RNA aptamer and a methyl-bearing ligand can easily be performed as shown for the tetracycline-binding RNA aptamer.^[60b] Apart from small molecules, proteins and protein-RNA interactions are another potential target with this approach. The investigation with a ribonucleoprotein (RNP) complex was initiated as part of the PhD thesis of Dr. Victoria Aladin.^[99] and the results were published recently.^[60e] Here, the spectra shown in Figure 14 and Figure 15A were acquired by her and my contribution to the publication—the combination of R^2 with SCREAM-DNP to investigate a biomolecular complex—is depicted in Figure 15B and Figure 16.

The studied RNP complex—illustrated in Figure 13—is part of the box C/D ribonucleoprotein complex which is involved in the posttranscriptional 2'-O-ribose methylation of ribosomal RNA (rRNA) in archaea and eukaryotes.^[100] The architecture of the box C/D RNP complex in archaea involves three core proteins which are assembled around a small guide RNA. The structure of this complex was solved with high resolution using an integrative approach based around solution-state NMR spectroscopy.^[101] The studied RNP complex consists of the 13.5 kDa large L7Ae protein which binds the small guide RNA and is therefore directly involved in the formation of the 370 kDa large box C/D RNP complex.^[102] A minimized system consisting of a short fragment of the small guide RNA (26mer) and the L7Ae protein, was extensively studied and its structure resolved by solid-state NMR.^[103] The easy synthesis of selectively labeled RNA molecules by *in vitro* transcription and sparse ^{13}C labeling^[104] of the L7Ae protein makes the RNP complex an ideal system for testing the possibility of SCREAM-DNP in biomolecules. Additionally, RNA molecules contain naturally no methyl groups, with exception of few post-transcriptional modified RNA molecules such as

rRNA or transfer RNA (tRNA), and therefore, ΔDP_{sat} spectra are representative for protein-RNA interactions.

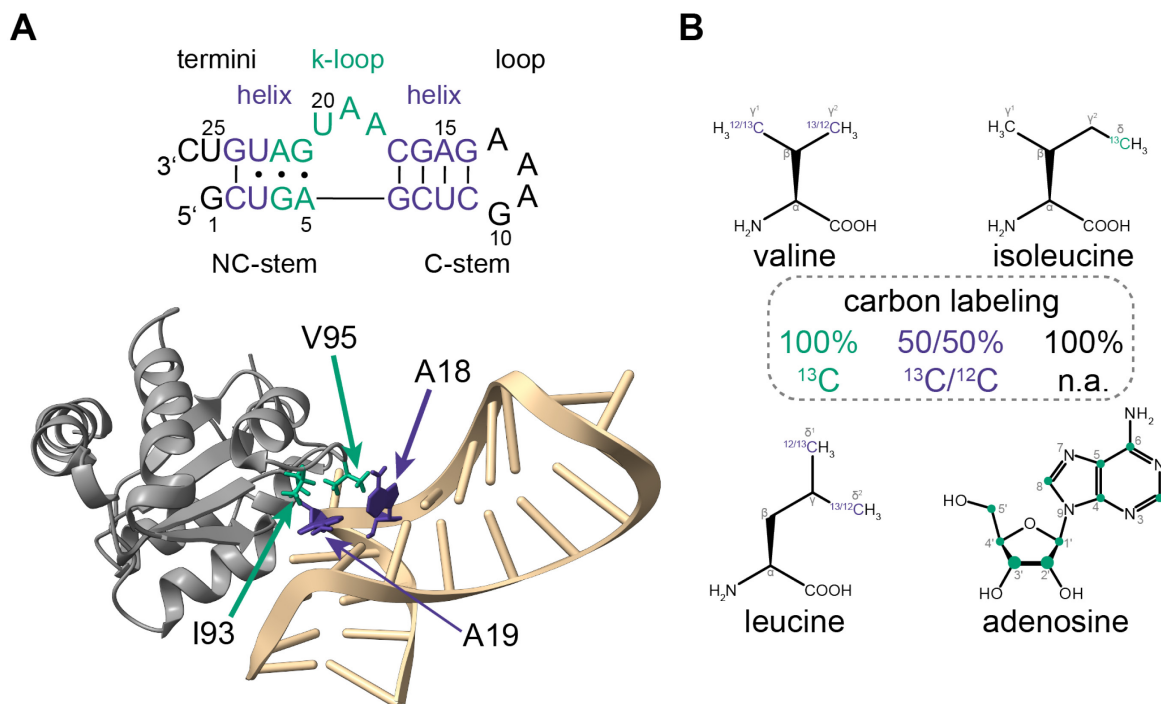


Figure 13: Sequence and secondary structure of the 26mer RNA (A), structure of the L7Ae–wt and RNA complex (B), and carbon isotope labeling scheme (C). (A) The RNA consists of helix stems (violet), the k-loop (green), and a non-structured loop and the termini (both gray). Base pairs are displayed by either a dash (Watson-Crick) or a non-canonical base pair (dot). (B) The solid-state NMR structure (PDB: 6TPH) [103b] displays the L7Ae protein in gray (residues I93 and V95 are highlighted in green) and the RNA in tan (nucleotides A18 and A19 are colored violet). (C) Carbon atoms highlighted in green are 100% ¹³C labeled and violet carbons are alternately ¹³C and ¹²C labeled on one side chain methyl each.

The ¹H–¹³C CPMAS spectrum of the RNP complex is depicted in Figure 14A (green). Due to the selective labelling of the RNA (u–[¹³C, ¹⁵N]–A, ²H–U,G,C) and the protein (–¹³CH₃ ILV), the CPMAS spectrum, being already partially selective due to the necessity of dipolar coupled ¹H–¹³C spin pairs, only shows resonances for the 8 adenosines and the methyl groups of isoleucine, leucine, and valine. In contrast, the ΔDP_{sat} spectrum acquired with 16 s polarization time (Figure 14A, violet) is better resolved and has a significant different spectral fingerprint and signal intensity heights than the ¹H–¹³C CPMAS spectrum emphasizing the increased site-specificity of SCREAM-DNP. The different spectral fingerprint is especially interesting since it reveals different chemical environments of, for example, ribose pucker. In this case, the signal peak maxima found in the ¹H–¹³C CPMAS spectrum agrees well with chemical shifts typically found for the canonical north (3'–endo) conformation of the ribose, whereas the low field shift in peak maxima of the ribose signals found in the ΔDP_{sat} spectrum represent perfectly the chemical shift of the non-canonical south (2'–endo) conformation. Structures of this RNP

complex solved by solid-state NMR reveal that only the adenosines A5 and A19 are in the south pucker, whereas A15, A18, and A22 are in the north pucker and the adenosine in the loop (A11-A13) are unstructured. This structural analysis already indicates that the signals in the $\Delta\text{DP}_{\text{sat}}$ spectrum most likely represents the ^{13}C nuclei in A5 and/or A19.

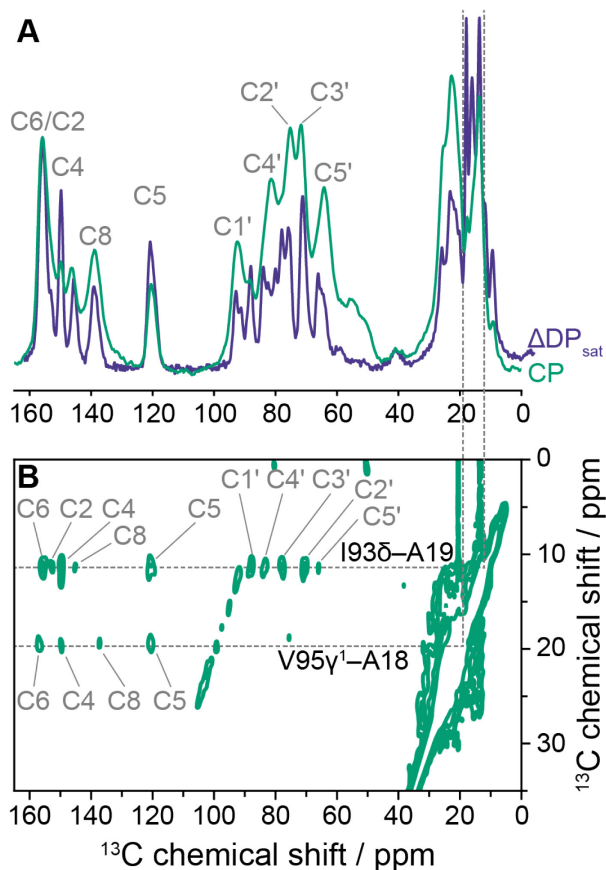


Figure 14: ^1H - ^{13}C CPMAS spectrum (green) and the $\Delta\text{DP}_{\text{sat}}$ spectrum of a SCREAM-DNP experiment after 16 s polarization time (violet) (A) and ^1H - ^{13}C CPMAS-based 2D ^{13}C , ^{13}C correlation spectra (B) of the δ - $^{13}\text{CH}_3$ ILV-L7Ae-wt protein in complex with u - $[^2\text{H}, ^{13}\text{C}, ^{15}\text{N}]$ -A, ^2H -U,G,C-RNA in glycerol- d_8 : D_2O : H_2O (50:40:10 vol-%) with 15 mM AMUPol at 8 kHz MAS frequency and 142 K. (A) The CPMAS spectrum is acquired with a polarization time of 3 s. The signals are assigned with the corresponding atoms of the adenosine nucleotide (*cf.* inset for atom numbering). The $\Delta\text{DP}_{\text{sat}}$ spectrum is inverted to positive values for an easier comparison. (B) The correlation spectrum was acquired using 200 ms of DARR recoupling. The cross peaks between the atoms of the two nucleotides A19 and A18 and the I93 δ and V95 γ^1 methyl groups are marked with grey lines

To increase spectral resolution in a ^1H - ^{13}C CPMAS-based transfer, 2D ^{13}C , ^{13}C correlation experiment can be acquired (Figure 14B). By employing a DARR (dipolar-assisted rotational resonance) recoupling sequence with a mixing time of 200 ms, a signal correlation between protein and RNA molecule can be generated. Here, two sets of cross peaks being assigned based on previous studies^[103] are most distinguishable and intense: (1) a dipolar contact which can unambiguously assigned to A18 of the RNA molecule and the methyl group V95 γ^1 of L7Ae and (2) a contact being unambiguously assigned to A19 and I93 δ . The chemical shifts of the assigned resonances of the second set agree excellent with the signals in the $\Delta\text{DP}_{\text{sat}}$ spectrum

(Figure 14A), especially the downfield shifted signal of C8 (146.1 ppm) and C4' (84.6 ppm), and the upfield shifted signal of C1' (89 ppm) representing the noncanonical south pucker instead of the typical chemical shift of the north pucker conformation (93.5 ppm). In addition, C5' which has only a weak cross peak in the 2D DARR spectrum, but an intense signal in the ΔDP_{sat} spectrum, experiences a downfield shift of ~ 2.5 ppm from the commonly reported 65 ppm to a chemical shift of 67.4 and 67.6 ppm for the 2D and 1D spectrum, respectively. Taken together, this suggests that the RNA signals in the ΔDP_{sat} spectrum are mainly arising from A19, with minor contributions from the other adenosines, most probably A18 being also located in the RNA binding pocket and assigned to the other set of intense cross peaks in the 2D DARR spectrum.

To investigate if A18 contributes to the signal in the ΔDP_{sat} spectrum, Arun Sreemantula and Dr. Alexander Marchanka provided a I93C mutant of the $\delta\text{-}^{13}\text{CH}_3$ ILV-L7Ae complex. The mutation, where the I93 residue strongly contributing to the ΔDP_{sat} spectrum is exchanged with an SCREAM-DNP inactive -SH group, is known to not alter the RNA-protein interface as reported with PRE (paramagnetic relaxation enhancement) experiments^[103b] as well as have a similar binding affinity reflected by the dissociation constant K_D determined with isothermal titration calorimetry (ITC).^[60e] However, no polarization build-up is detected in the ΔDP_{sat} spectra with polarization times between 4 and 16 s and at 8 kHz MAS frequency, whereas the wild type builds up polarization as expected suggesting that even if a dipolar contact between V95 γ^1 and A18 is present the SCREAM-DNP signal build-up is significantly retarded (Figure 15A). This is not surprising since a systematic investigation of all methyl-bearing amino acids has shown that the $\delta\text{-CH}_3$ group is more effective than both methyl groups in valine.^[60c] An analysis of the SCREAM-DNP polarization build-up of the wild type complex has furthermore shown that A5, A15, and A22 show also little contribution to the polarization build-up indicating that the dipolar contact between I93 δ and A19 is the dominating factor.^[60e] Most surprisingly, A5 is in a nucleobase stacking interaction with A19, however, only a small contribution was observed suggesting that an inter-residual polarization relay is highly inefficient.

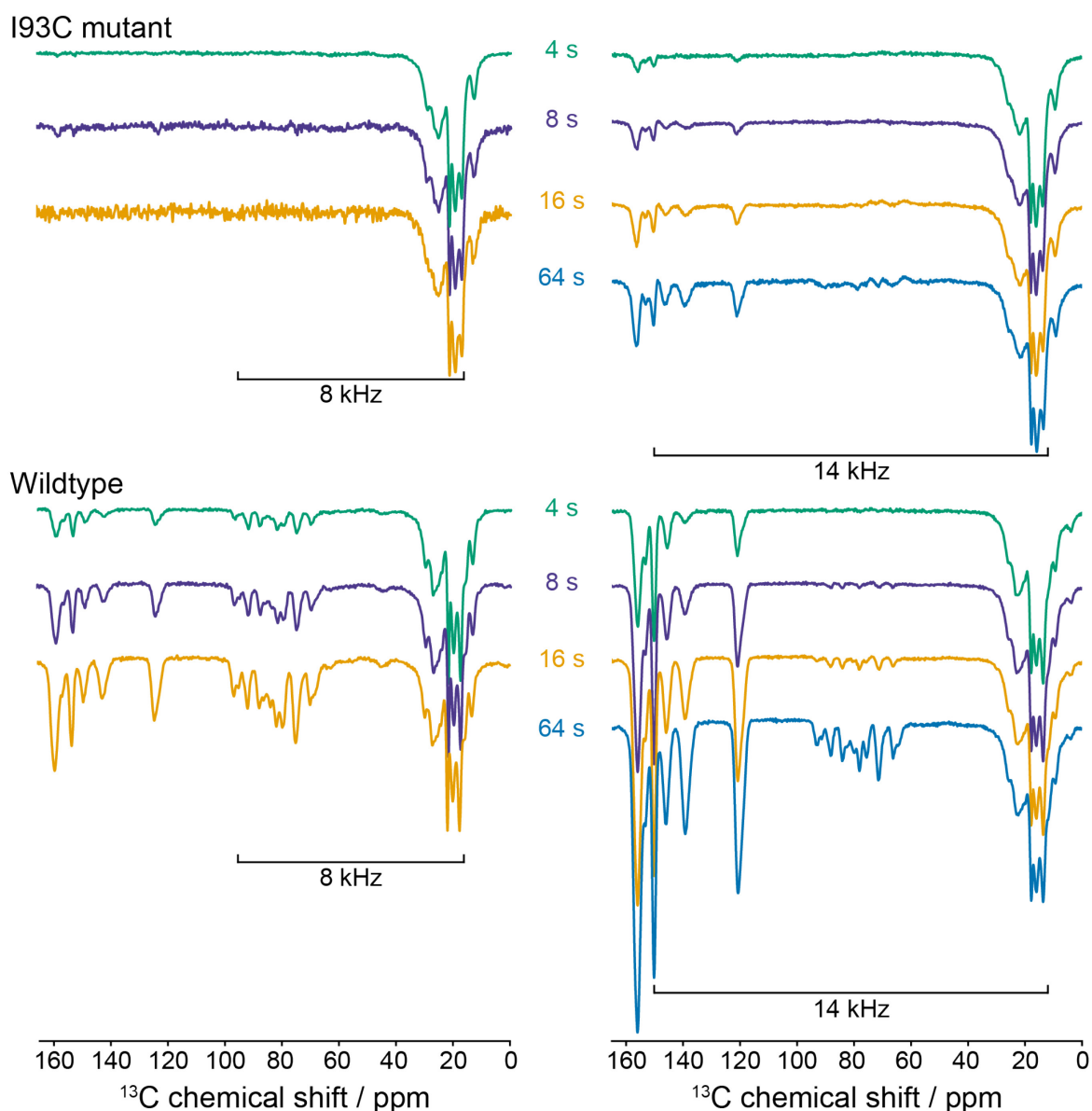


Figure 15: ΔDP_{sat} spectra of SCREAM-DNP experiments of the $\delta\text{-}^{13}\text{CH}_3\text{-ILV-L7Ae-wt}$ and $\delta\text{-}^{13}\text{CH}_3\text{-ILV-L7Ae-I93C}$ mutant, each in complex with $[\text{}^2\text{H}, \text{}^{13}\text{C}, \text{}^{15}\text{N}]\text{-A}$, $^2\text{H-U,G,C-RNA}$ recorded at polarization times between 4 and 64 s, either 8 kHz (left side) or 14 kHz (right side) MAS frequency and 142 K. The applied MAS frequency and its corresponding spectral width is highlighted.

Next, the—in Section 4.1.1 introduced and systematically investigated combination of frequency-selective dipolar recoupling (R^2) and cross relaxation (SCREAM-DNP)—is investigated towards the application in a biomolecular complex. As a first feasibility experiment, SCREAM-DNP experiments for the wild type complex were acquired at 14 kHz MAS frequency which is the spectral separation in Hertz fulfilling the $n = 1$ R^2 matching condition (Figure 15B) between the signal region of the methyl group and the nucleobase resonances. In order to qualitatively assess the build-up kinetics, polarization times between 4 s and 64 s were used for the SCREAM-DNP experiments, which was additionally done—except for the 64 s polarization time—for SCREAM-DNP experiments at 8 kHz MAS

frequency (Figure 15). Here, the spectra are all normalized to the same signal intensity of the methyl spectral region to follow the polarization build-up on nucleotide signals. The comparison of the two MAS frequencies reveals a significant signal boost by approximately a factor of two at 14 kHz MAS frequency. Additionally, at low MAS frequencies such as 8 kHz, spontaneous polarization transfer caused by spin diffusion is the most significant polarization transfer process. By increasing the MAS frequencies to 14 kHz, spin diffusion is suppressed due to a more effective decoupling of the homonuclear dipole-dipole interactions. Besides that, the ΔDP_{sat} spectrum at 14 kHz MAS frequency shows clearly that the nucleobase signals are building up faster than the ribose resonances. Especially at a short polarization time of 4 s, the nucleobase resonances, particularly the signals of C6 and C2 at 155 ppm and C4 at 150 ppm, are almost as intense as the methyl group signals, whereas no signal is observed for the ribose spectral region. With increasing polarization times, the ribose signals are also building up, however, with a much lower relative intensity to the nucleobase signals as compared to the build-up behavior at 8 kHz MAS frequency. This suggests that spontaneous polarization transfer processes are retarded and the controlled polarization transfer via the recoupled dipolar interaction is dominant as already described in the selectively labeled ethyl acetate in the Section 4.1.1.

To test this approach further, SCREAM-DNP experiments of the I93C mutant of the RNP complex were acquired at 14 kHz MAS frequency and polarization times between 4 and 64 s (Figure 15B). Although in direct contact with $V95\gamma^1$, the I93C mutant has no significant polarization build-up at 8 kHz MAS frequency due to the less mobile methyl groups in valine rendering the cross-relaxation-based polarization transfer of SCREAM-DNP more ineffective.^[60c] Most interestingly, the SCREAM-DNP experiments of the I93C mutant at 14 kHz MAS frequency show a significant polarization build-up with comparable build-up rates as seen for the wild type, nonetheless, with only ~20% of relative signal intensity as compared to the signal intensities of the wild type at a polarization time of 64 s. This displays the potential of the combination of SCREAM-DNP experiments with R^2 dipolar recoupling as the combination significantly accelerates the build-up by matching the build-up rates of the dipolar coupled nuclei with the rate of the methyl group (*cf.* Section 4.1.1, Figure 12) and thereby increasing the obtainable signal on the nuclei of interest (in this case the adenosine resonances of the I93C mutant). Since the investigation in Section 3.1.1 has proven that the combination results in a serial polarization transfer, it is most likely that the ΔDP_{sat} spectrum

of the I93C mutant at short polarization times display nucleobase signals solely stemming from A18.

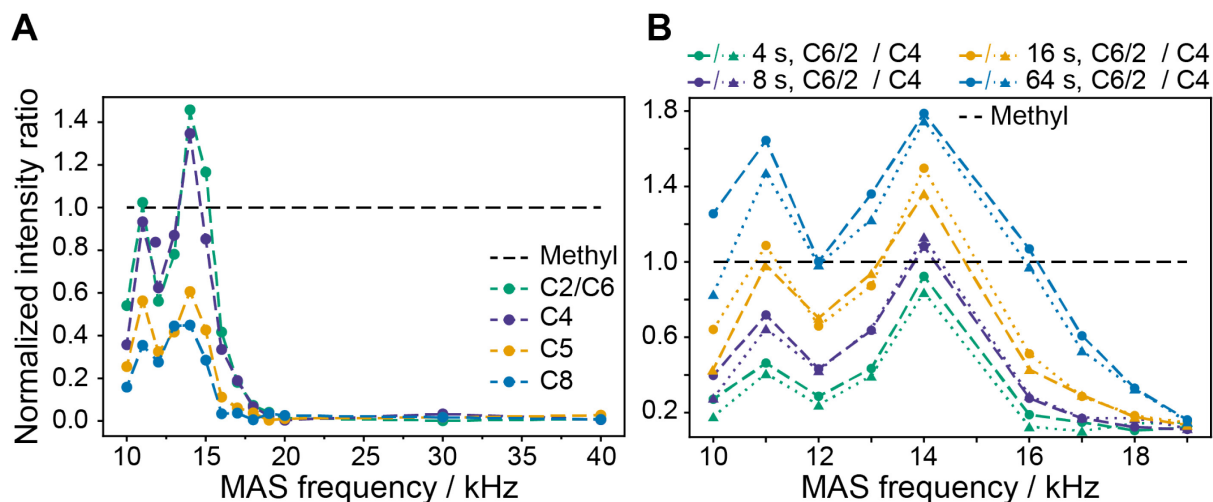


Figure 16: Normalized integrated signal intensity ratio of nucleobase resonances in the ΔDP_{sat} spectra after either 16 s polarization time of SCREAM-DNP at MAS frequencies between 10 to 40 kHz (A) or increasing polarization times at MAS frequencies between 10 to 20 kHz (B) at 142 K. (A) The normalized integrated signal intensity ratios are calculated for the overlapping C2 and C6 resonances (green), the C4 resonance (violet), the C5 resonance (yellow), and the C8 resonance (blue). (B) The normalized integrated signal intensity ratios are calculated for the overlapping C2 and C6 resonances (circles) and the C4 resonance (triangles) at polarization times of 4 s (green), 8 s (violet), 16 s (yellow), and 64 s (blue). For the calculation of the ratios in both plots, the integrated signal intensity of each resonance is divided by the number of accumulated transients followed by the division of the measured methyl-¹³C integrated signal intensity at the given MAS frequency. The normalized intensity ratio of the methyl-¹³C group is depicted as a dashed black line. The colored dashed lines connecting the carbonyl data points serve only as a guidance to the eyes.

As an ultimate proof of the MAS-dependent acceleration of the polarization build-up of the nucleobase resonances, the normalized and integrated signal intensity of these resonances after 16 s polarization time were determined for a MAS frequency range between 10 and 40 kHz (Figure 16A). This correlation shows two distinct maxima, one at 11 kHz corresponding to a matching of the C5 of adenosine and I93 δ of the protein, and the second at 14 kHz representing the dipolar-coupled A19–C4–I93 δ pair. As expected, no signal intensity is visible for MAS frequencies greater than 20 kHz due to the strong decoupling of the homonuclear transfer by spin diffusion. Interestingly, the partners involved directly in the recoupled dipolar interaction are not showing the higher signal intensity, which is especially visible for the maxima at 11 kHz. It has to be noted that the highest normalized intensity is displayed by the C6/2 carbons, which are considered as one signal due to signal overlap. Thus, the intensity has to be divided by a factor of 2 leading to the C4 carbon with the strongest overall normalized intensity. The higher signal intensity at 11 kHz for the C4 carbon than for the C5 carbon is possibly due to the slightly lower distance of the A19–C4–I93 δ spin pair

(~ 3.9 Å instead of ~ 4.1 Å) fast intra-nucleotidic spin diffusion in the uniformly ^{13}C labeled adenosine. A study about the distance dependency of the serial polarization transfer is planned, but not finished at the time of writing. The methyl group of $\text{V95}\gamma^1$ is playing a minor role in the polarization build-up—approximately 20% of the signal visible in the $\Delta\text{DP}_{\text{sat}}$ spectra are stemming from $\text{V95}\gamma^1$, and the remaining 80% are contributed by the $\text{I93}\delta$ methyl group (*cf.* Figure 15B, I93C mutant and wild type)—which is again visible for the C6/2 signal intensity, whose dipolar coupling with the $\text{V95}\gamma^1$ methyl group is recoupled by R^2 at 14 kHz. Here, the normalized signal intensity is determined to be ~ 1.5 at 16 s polarization time. As two carbons are contributing to the signal, the intensity has to be divided by 2, yielding an intensity per carbon of ~ 0.75 . This is 0.15/ $\sim 20\%$ larger than, for example, the signal intensity of C5, whose dipolar coupling is not recoupled at 14 kHz MAS frequency.

Figure 16B displays the normalized intensity ratio of the C6/2 (circles) and C4 (triangles) carbons of adenosine after polarization times between 4 and 64 s in correlation with the MAS frequency. Here, the signal intensities of these carbons were determined and normalized to the signal intensity of the methyl spectral region in the $\Delta\text{DP}_{\text{sat}}$ spectrum. This qualitative assessment of the build-up behavior indicates that the polarization build-up on these carbons is significantly accelerated as already seen for ethyl acetate in Section 4.1.1, Figure 12. In comparison with the other MAS frequencies, a factor of ~ 4 in higher signal intensity is observed at the short polarization time of 4 s, which decreases steadily with increasing polarization times to a factor of ~ 2 at 64 s polarization time. This decrease in acceleration is most likely due to an increase of polarization from other spurious sources at longer polarization times than the direct transfer of polarization between the methyl group and the dipolar coupled carbon at longer polarization times. Here, the most probable process will be a slower building up cross-relaxation based polarization transfer between a methyl group in the vicinity of the two adenosine A18 and A19. The generated ^{13}C polarization is then transferred by spin diffusion to the read-out carbons of A19, which is further supported by the large decrease in normalized intensity ratio to 0.2 after 64 s and 20 kHz MAS frequency. Interestingly, the relative signal intensity ratio reaches almost 1 after the shortest polarization time of 4 s which is faster than observed for ethyl acetate, however, expected due to the increased mobility of methyl groups with elevated temperature (*cf.* 102 K for ethyl acetate and 142 K for the RNP complex).

In summary, the results of this section have proven that SCREAM-DNP experiments in a RNP complex introduce a site-specificity which can only be obtained otherwise by 2D ^{13}C , ^{13}C

correlation experiments. This large site-specificity can be accelerated by matching the MAS frequency and thereby reintroducing the dipolar coupling between the nucleobase and the methyl group. This acceleration of the polarization build-up rate decreases the required experimental time, making multi-dimensional experiments feasible. Here, a heteronuclear ^{13}C – ^{15}N correlation experiment could be of interest to further probe nucleobases in contact with the methyl-bearing protein assisting in the assignment of those nucleobase resonances.

4.1.3 Summary and Outlook

This chapter demonstrates the combination of cross relaxation with dipolar recoupling in DNP experiments. Here, SCREAM-DNP is combined with R^2 which results in an accelerated and selective accumulation of polarization on the site of interest, for example the carbonyl group of ethyl acetate or adenosines in a RNP complex. Whereas ethyl acetate is chosen as a model system for the systematic investigation of this effect, the RNP complex displays the potential of this approach in structural biology. The next steps in this project could involve a study about the distance limit of R^2 under DNP, which is of great interest for structural biology. Additionally, this combination can enable SCREAM-DNP as a filter for multidimensional NMR experiments, where correlations between $^{13}\text{C}_\text{O}$ and ^{15}N , for instance, may be recorded with very high selectivity at short SCREAM-DNP polarization times. Finally, the study with the ethyl acetate model system can be performed at higher magnetic fields or different temperatures than the 9.4 T and 102 K used in this study. These changes yield further valuable information about the cross-relaxation based transfer by modulating either the spectral density function (via the magnetic field) or by the molecular dynamics (*viz.* temperature activation). In addition, the polarization transfer in the system can be studied by using different PAs, such as ASYMPol–POK, which is known to have a faster DNP build-up rate constant than AMUPol, subsequently changing the effective rate constant which is determined by the experiments.

4.2 Matrix-free DNP for the investigation of powder samples

With the sensitivity enhancement governed by DNP, challenging biomolecules or biologically relevant materials can be studied. Some of those systems such as amyloid fibrils or cellulose, however, cannot be prepared with the standard DNP sample preparation, including the dissolution of the molecule of interest in a glycerol:water mixture. Besides, glycerol may have a negative impact on the biomolecule's fold and function.^[34] The matrix-free DNP approach, first introduced by the groups of De Paëpe and Hediger,^[43b, 43c] removes the glycerol:water matrix in order to study insoluble systems in the powder state and furthermore increase the sample filling factor in the rotor. In this section, the matrix-free DNP approach is adapted and systematically optimized to maximize the achievable ^1H polarization in model proteins (Section 4.2.1). Additionally, the protein powder can be rehydrated for the formation of a hydration shell necessary for the correct structural fold of the biomolecule. The influence of this rehydration on the DNP properties is again studied with the model proteins. In Section 4.2.2 and 4.2.3, biomaterials relevant for the development of new drugs and medicinal products are investigated with the matrix-free DNP approach, demonstrating the applicability of this approach to a broad range of biomolecular problems.

4.2.1 Systematic investigation of the matrix-free DNP approach in model proteins

As part of the study on using DNP-enhanced ^1H - ^2H CPMAS for investigating biomolecular dynamics,^[43f] the matrix-free DNP approach was optimized to maximize the ^1H polarization transferable by cross polarization to other nuclides. Moreover, this systematic investigation was the groundwork for further project which involved insoluble materials such as $\text{A}\beta$ -adsorbing cellulose (Section 4.2.2) and polymeric micelles (Section 4.2.3). To investigate the parameters required for the highest sensitivity enhancement by DNP, ^1H - ^{13}C CPMAS spectra were measured and the ^1H DNP build-up time constants were determined of two model proteins (hen egg white lysozyme and ubiquitin from bovine erythrocytes), both in natural isotope abundance, in mixtures with various amounts of AMUPol and increasing amounts of water content (Figure 17, Appendix Figure A 3, and Appendix Figure A 4).

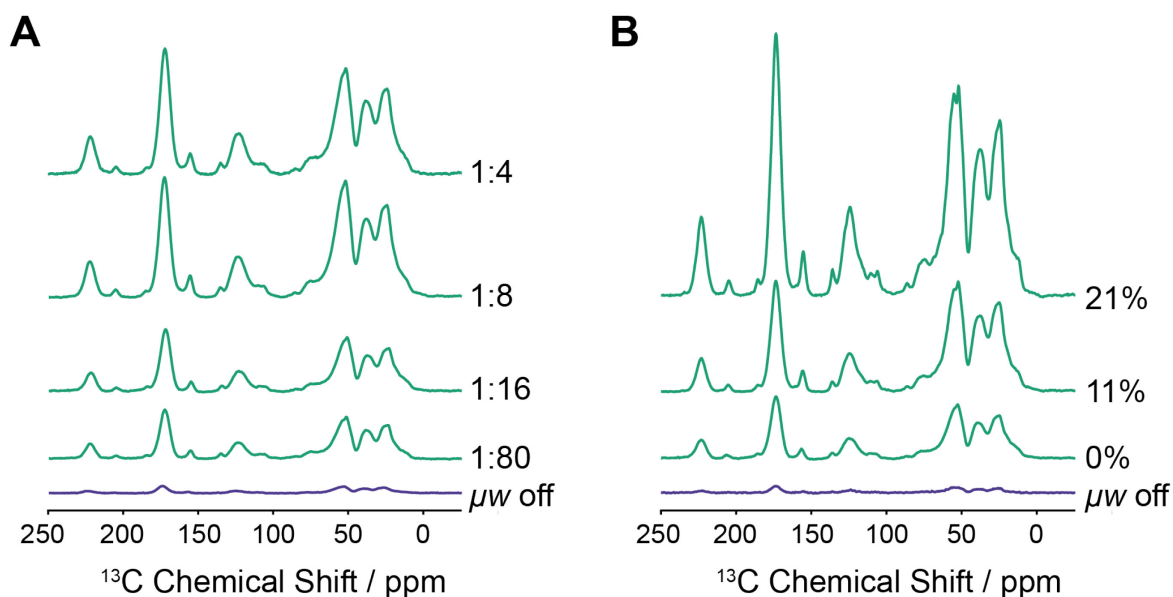


Figure 17: ^1H - ^{13}C CPMAS spectra of dry lysozyme powder in natural isotope abundance with different molar ratios of PA and protein (A) and for different levels of rehydration with a molar ratio of 1:16 (PA:protein) (B) with (μw on, green) and without (μw off, violet) microwave irradiation at 98 K and 5 kHz MAS frequency. The spectra without microwave irradiation (μw off) are shown in violet for either a molar ratio of 1:80 (PA:protein) (A) or a rehydration level of 21% for the 1:16 molar ratio. No difference in signal intensity in the μw off spectra are observed for all tested conditions. All ^1H DNP enhancement factors are summarized in Figure 18 and Appendix Table A 1 to A 4.

Figure 17 illustrates that the sensitivity governed by DNP increases with increasing amounts of AMUPol. The determined ^1H DNP enhancement factors ϵ for the lysozyme samples in the dry state are doubled from 10 to 20 with higher amounts of AMUPol, however, this requires an increase of AMUPol by a factor of 20. It must be noted that the ^1H enhancement factors were determined by a simple microwave on/off comparison and sample-rotation-induced depolarization effects of AMUPol on the sample in the absence of microwave irradiation were not considered. Nonetheless, the changes in ϵ are solely based on changes in the available hyperpolarization within the sample and not on depolarization effects as no differences in signal intensity is observed between all measured spectra without microwave irradiation (*cf.* μw off in Figure 17A and B, and in Appendix Figure A 4) A monotonic, but significant increase in enhancement factors are observed upon rehydration of the protein samples, which also induces a prolongation of the build-up time constant, mainly due to the higher amount of protons in the matrix which have to be polarized (Figure 18). At a water content of 21% (w/w), DNP properties similar to a standard DNP sample preparation are obtained for the molar ratio of 1:8 (PA:protein) with an enhancement factor of 55 and a build-up time constant of ~ 3 s.^[28] The slightly lower, but comparable DNP properties of the 1:16 (PA:protein) molar ratio as well as the non-existent increase of the 1:80 (PA:protein) molar ratio suggests the general trend that a larger amount of radical per protein results in a

better signal sensitivity. In contrast to this trend, the sample with the highest molar ratio displays a decrease in the obtained ^1H enhancement factor and the build-up time constant—the latter being reduced to ~ 1 s—indicating a potential clustering of the PA upon freezing due to the formation of the mobile phase in the sample matrix. Figure 17B displays an additional effect of protein rehydration: the signal resolution increases significantly as visible by the introduction of the splitting in the C_α (at ~ 50 ppm) and aromatic carbon (at ~ 125 ppm) resonances. This is most probably explained by the recovery of a hydration shell required for the correct formation of salt bridges in the protein structure and thus reducing the conformational variety of the protein itself. Rehydration of the protein powder sample also enables the control over the concentration of ^1H in the protein sample. This perdeuteration of the protein has shown to improve the achievable sensitivity enhancement^[105] as well as spectral resolution by decreased signal linewidths due to more efficient decoupling of the lower spin-spin interactions with deuterons.^[106]

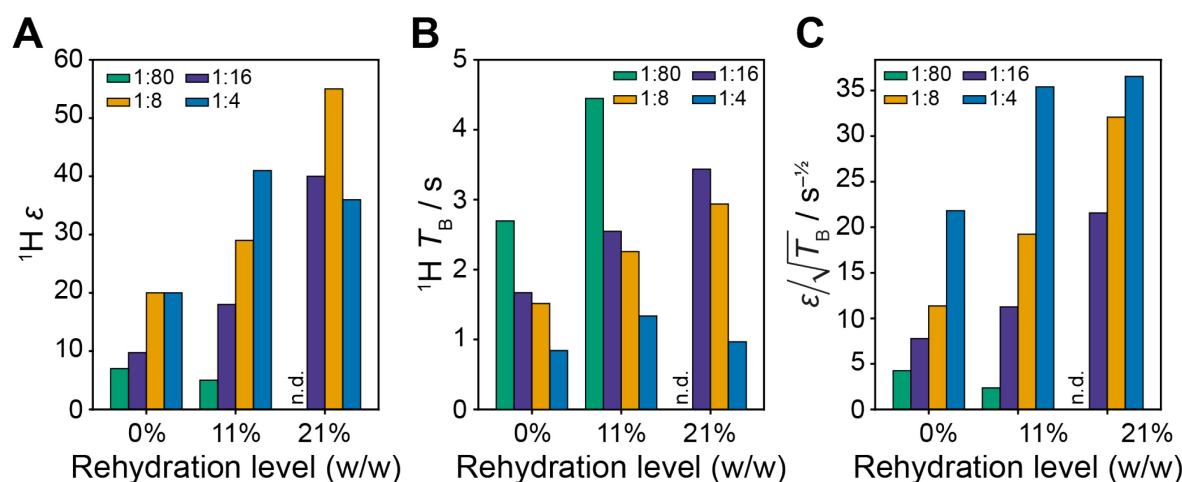


Figure 18: ^1H DNP enhancement factors ϵ (A), ^1H DNP build-up time constants T_B (B) and relative sensitivity $\epsilon/\sqrt{T_B}$ for four different molar ratios of PA to lysozyme at three different rehydration levels obtained at 98 K and 5 kHz MAS frequency. The tested molar ratios are 1:80 (green), 1:16 (violet), 1:8 (yellow), and 1:4 (blue) (PA:protein) at rehydration levels of 0%, 11%, and 21% (w/w). “n.d.” refers to “non-determinable”. The given build-up time constants are mean values of values obtained for the C_O , C_α , and sidechain resonances in the ^1H – ^{13}C CPMAS spectra (*cf.* the build-up curves in Appendix Figure A 5). The non-averaged values of T_B , the enhancement factors ϵ , and the non-averaged values of the relative sensitivities $\epsilon/\sqrt{T_B}$ are given in Appendix Table A 1 to A 4.

In summary, this investigation illustrates the potential of the matrix-free DNP approach as an alternative sample preparation for systems which cannot be dissolved or dispensed in glycerol:water mixtures. In the next sections examples for the use of the matrix-free DNP approach are shown: the characterization of medically relevant biomaterials like amyloid- β (A β)-adsorbing cellulose (Section 4.2.2) and drug-carrying micelles (Section 4.2.3) as well as

the investigation of methyl group dynamics in insoluble proteins such as A β fibrils (Section 4.3.1)

4.2.2 Characterization of A β ₁₋₄₂-adsorbing materials using matrix-free DNP

Amyloid fibrils are one of the most important medicinal research targets as they are believed to be the cause of the Alzheimer's diseases. Ways to cure the disease are under development. One potential approach could be the removal of soluble A β species from the patient's blood using an extracorporeal blood purification procedure. This involves passing the patient's blood or plasma through an adsorber, removing the target proteins and returning the purified blood or plasma to the patient. Such sorbets are being developed and pre clinically tested by Christoph Kamper and Dr. Jacqueline Heskamp.

Due to its active development involving intellectual property protection, a detailed synthesis and composition of the material cannot be given in this work. What can be revealed is that the materials are made from either cellulose or silica particles, which are incubated with dopamine hydrochloride. The resulting layer of polydopamine (PDA) around the core particles is then functionalized with lysine, which interacts with A β ₁₋₄₂ peptides. So far, it is not known if this interaction involves a covalent bond or is purely based on non-covalent interactions. In addition, the exact masses of lysine and A β ₁₋₄₂ peptides in the material as well as the polymeric state of the adsorbed A β ₁₋₄₂ peptides is unknown. It is expected that the concentration of lysine and A β ₁₋₄₂ fibrils is between 1 to 50 μ g per mg material indicating the necessity for sensitivity enhancement by DNP. Thus, the aim of this project is to study these materials by DNP-enhanced solid-state NMR using the matrix-free DNP approach. Additionally, the multiple contact CP approach—introduced first by Schmidt-Rohr and coworkers and later adopted for DNP by Emsley and coworkers^[87, 107]—unravels the amount of adsorbed lysine and A β ₁₋₄₂ peptides in the material. Besides quantification, the structure within the material can be investigated using multi-dimensional NMR techniques. ^[10d, 108]

In order to establish the matrix-free DNP approach for the A β -adsorbing materials, the materials were impregnated after the adsorption step with 60 to 100% (w/w) 20 mM AMUPol in 33:67 vol-% H₂O:D₂O and ¹H DNP enhancement factors, ¹H build-up time constants as well as values of the relative sensitivity were determined (Figure 19 and Appendix Table A 5 to A 9). Figure 19 illustrates that the cellulose-based material is displaying significantly higher enhancement factors than the silica particles. The higher enhancement factors of the cellulose materials can be explained by better swelling properties of the cellulose in comparison to the

silica particles as the porosity of both materials were equal at a grid size of 20 μm . Again, it has to be noted that the enhancement factors are obtained by simple microwave on/off comparison and sample rotation-induced depolarization of the ^1H nuclides were not taken into account. To estimate the relative sensitivity gain by DNP at 100 K over solid-state NMR experiments at 295 K,^[109] ^1H - ^{13}C CPMAS spectra are measured at these conditions for a cellulose sample only functionalized with PDA. The relative sensitivity gain is ~ 100 with slightly higher linewidths at 100 K (Appendix Table A 10) indicating the advantage of DNP in order to detect and investigate the adsorbed $\text{A}\beta_{1-42}$ peptides in this material within reasonable experimental times. Additionally, even higher relative sensitivity gains for the cellulose material with adsorbed $\text{A}\beta_{1-42}$ peptides is expected due to the higher ^1H DNP enhancement factor of 45 obtained for this sample in comparison to $\epsilon = 33$ for the cellulose sample functionalized with only PDA. This is reflected by the comparison of the DNP-enhanced ^1H - ^{13}C CPMAS spectrum of the cellulose with adsorbed $\text{A}\beta$ at 100 K and the ^1H - ^{13}C CPMAS spectrum of PDA-functionalized cellulose at 295 K. Here, the relative sensitivity gain is determined to be 128-160 (Appendix Table A 11), resulting in time-savings of up to 25000. However, the relative sensitivity gains for the cellulose with adsorbed $\text{A}\beta_{1-42}$ was not tested due to the expected high number of accumulated transients and resulting long experimental time required for sufficient signal of $\text{A}\beta_{1-42}$ resonances in absence of DNP.

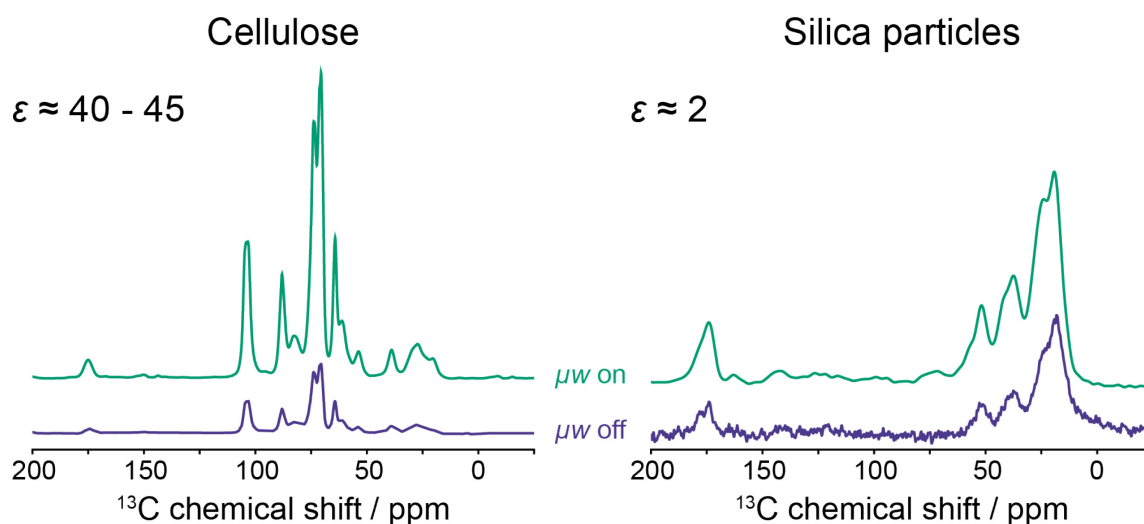


Figure 19: ^1H - ^{13}C CPMAS spectra of $\text{A}\beta_{1-42}$ -adsorbing materials mixed with 20 mM AMUPol in 33% H_2O and 67% D_2O with (μw on, green) and without (μw off, violet) microwave irradiation at 102 K and 8 kHz MAS frequency. The cellulose powder sample and the silica particles were treated with u - ^{13}C , ^{15}N -lysine and rehydrated with 20 mM AMUPol dissolved in 33:67 vol-% H_2O : D_2O to a hydration level of 60% (w/w) and 100% (w/w), respectively. All ^1H DNP build-up time constants as well as the ^1H DNP enhancement factors are listed in Appendix Table A 5 to A 9.

The comparison of the ^1H DNP build-up time constants shows a small discrepancy between the cellulose signals of the PDA-functionalized cellulose material (~ 6 s, Table 5 and Appendix Table A 5) and the PDA- and lysine-functionalized cellulose (~ 5 to 7 s, Table 5 and Appendix Table A 6). This indicates either a lower general performance of DNP in the latter sample or a larger particle size of the cellulose as the particle's core is less affected by DNP. A potential larger particle size would result in a larger portion of carbon nuclei in cellulose being less affected by the introduced PA and therefore a polarization gradient with significantly larger build-up time constants. This is further supported that similar build-up time constants are determined for the carbonyl spectral region and the sidechain spectral region for the PDA- and lysine-functionalized cellulose with and without $\text{A}\beta_{1-42}$ (both $\sim 4-5$ s, *cf.*). Surprisingly, the C_α spectral region and the shared C_β and C_ϵ spectral region of lysine in the sample without adsorbed $\text{A}\beta_{1-42}$ also display an increase in build-up time constants of ~ 2 s if compared to the sample with adsorbed $\text{A}\beta_{1-42}$. These longer build-up time constants cannot be explained, however, care has to be taken as this increase can be a consequence of overlap with cellulose resonances or MAS spinning side bands. In general, the relative sensitivity enhancement ($\epsilon T_{\text{B}}^{-1/2}$) are between 14 to 21 for all cellulose samples (Table 5 and Appendix Table A 5 to A 7). Similar build-up time constants are observed for the silica particles (Appendix Table A 8 and A 9), however, the up to 20-fold lower enhancement factors result in a significant lower relative sensitivity enhancement of 0.9 to 2.6. Consequently, further experiments only involved the cellulose-based materials due to their larger relative sensitivity enhancements. Note, as no systematic optimization of the PA concentration and hydration was conducted, the obtained relative sensitivity enhancements may still be improved. Additionally, exchange of AMUPol with, for example, ASYMPol-POK—known to yield faster build-up time constants due to a stronger electron-electron exchange interaction^[29]—should improve the relative sensitivity enhancement, making a detailed structural investigation of these materials by multi-dimensional NMR spectroscopy feasible.

Table 5: ^1H DNP build-up time constants T_B , ^1H DNP enhancement factors ϵ , and relative sensitivity enhancement $\epsilon T_B^{-1/2}$ of three different cellulose samples. All three samples are functionalized with PDA and differ only in the treatment after this functionalization: the row labeled with cellulose is the pure material, the row labeled with “+ lysine” is the cellulose material, which is further functionalized with $u\text{-}[^{13}\text{C},^{15}\text{N}]\text{-L-lysine}$, and the row labeled with “+ $\text{A}\beta_{1-42}$ peptides” refers to a cellulose material with both functionalizations (PDA and lysine) and adsorbed $u\text{-}[^{13}\text{C},^{15}\text{N}]\text{-Arg}, u\text{-}[^{13}\text{C},^{15}\text{N}]\text{-Lys-A}\beta_{1-42}$ peptides. The two build-up time constants given for the lysine-functionalized cellulose sample represent two average values: the rather fast building-up signals of the lysine and the rather slow building-up signals of cellulose. All values are average and the respective values of each resonance are summarized in Appendix Table A 5 to A 5.

	T_B / s	ϵ	$\epsilon T_B^{-1/2} / \text{s}^{-1/2}$
Cellulose	5.7	33	14
+ lysine	5.3-7.3	45	16-20
+ $\text{A}\beta_{1-42}$ peptides	4.8	45	21

To identify signals arising from the $u\text{-}[^{13}\text{C},^{15}\text{N}]\text{-Arg}, u\text{-}[^{13}\text{C},^{15}\text{N}]\text{-Lys-A}\beta_{1-42}$ the $^1\text{H}\text{-}^{13}\text{C}$ CPMAS and the $^1\text{H}\text{-}^{15}\text{N}$ CPMAS spectra of pure cellulose, cellulose functionalized with PDA- and $u\text{-}[^{13}\text{C},^{15}\text{N}]\text{-lysine}$, and PDA- and $u\text{-}[^{13}\text{C},^{15}\text{N}]\text{-lysine}$ -functionalized cellulose with adsorbed $\text{A}\beta_{1-42}$ at 8 kHz MAS frequency are compared (Figure 20A). The ^{13}C -labeled $\text{A}\beta_{1-42}$ peptides consists of the following primary sequence, where the stable isotope labeled residues are highlighted with squared brackets:



Typical resonances encountered in amino acids and proteins are found at ~ 175 ppm (C_O), at ~ 50 ppm (C_α), and below 50 ppm (sidechain) (*cf.* Figure 20A, violet and yellow). As the $\text{A}\beta_{1-42}$ peptides are uniformly ^{13}C and ^{15}N labeled at the two lysine and the one arginine residue, the $^1\text{H}\text{-}^{13}\text{C}$ CPMAS spectrum of the cellulose material with lysine and $\text{A}\beta_{1-42}$ is not differing strongly from the $^1\text{H}\text{-}^{13}\text{C}$ CPMAS spectrum of cellulose with only lysine. The best indicator is the carbon atom of the guanidinium group in arginine (C_ϵ) as it has a strongly downfield chemical shift of ~ 157 ppm. A signal with a small intensity can be found at ~ 157.5 ppm suggesting the presence of $\text{A}\beta_{1-42}$ peptides in the sample. To reduce the background signal of the naturally isotope-abundant cellulose, $^1\text{H}\text{-}^{15}\text{N}$ CPMAS experiments were conducted (Figure 20B). The spectra for the cellulose sample with (yellow) and without (violet) $\text{A}\beta_{1-42}$ show in both cases three slightly overlapping, but intense signals in the spectral region of amine groups resonating between 35 and 15 ppm. This spectral region is representative for amine groups indicating that the lysine is not attached—at least covalently—via this group to the PDA functionalization. The same signals are observed in the $^1\text{H}\text{-}^{15}\text{N}$ CPMAS spectrum of the

cellulose material with lysine and A β ₁₋₄₂, however, the signal at ~20 ppm is less intense in the case of the sample without A β ₁₋₄₂. This decrease in intensity upon adsorption of A β ₁₋₄₂ may suggest a potential involvement of the corresponding nucleus in the of A β ₁₋₄₂ peptides. Nonetheless, an unambiguous assignment of these ¹⁵N resonances is not possible with the given experiments and samples. Most surprisingly, no intense signal is detectable in the spectral region of ~125 ppm being typical for amide groups and peptide bonds. As the three labeled residues in A β ₁₋₄₂ are resonating around ~120 ppm,^[108, 110] the missing signal may arise from a stark line broadening of these signals in combination with low sensitivity due to lower abundance in the sample (*vide infra*).

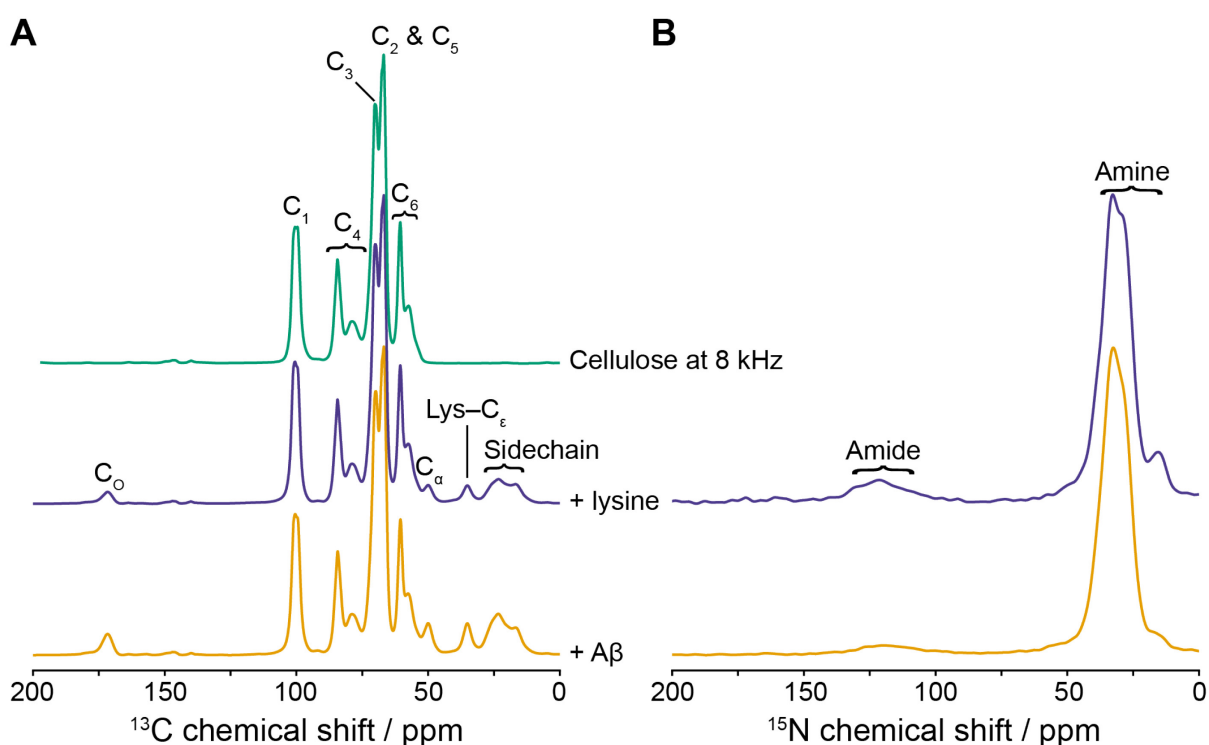


Figure 20: ¹H-¹³C CPMAS (A) and ¹H-¹⁵N CPMAS (B) spectra of PDA-functionalized cellulose (green), cellulose further functionalized with u-^[13C, 15N]-lysine (violet), and cellulose with adsorbed u-^[13C, 15N]-Arg, u-^[13C, 15N]-Lys-A β ₁₋₄₂ peptides at 8 kHz MAS frequency and 100 K. The cellulose powder sample was rehydrated with 20 mM AMUPol dissolved in 33:67 vol-% H₂O:D₂O to a hydration level of 60% (w/w).

To quantify the amount of sample, quantitative NMR has emerged as a useful tool in solution-state^[111] and solid-state NMR^[85]. Recently, the same quantification approach as used in solid-state NMR has been expanded to DNP-enhanced solid-state NMR.^[87, 107] As DNP itself is intrinsically non-quantitative due to different sensitivity enhancements by DNP of each nucleus, two conditions have to be fulfilled for quantitative DNP-enhanced NMR: (1) the enhancement factors have to be similar, and (2) the signal area of interest in the multiple contact CPMAS spectrum has to be calibrated to a signal area corresponding to a nucleus of known

mass. In the case of the cellulose samples, the C_1 resonance of cellulose was used as a reference peak and the signal areas of lysine and $A\beta_{1-42}$ were calculated relative to the signal area of the C_1 peak at 100.5 ppm (Figure 21, Appendix Table A 12 & A 13). Due to signal overlap of the lysine and the $A\beta_{1-42}$ resonances, the signal area of lysine was determined for the cellulose sample without adsorbed $A\beta_{1-42}$. To obtain signal areas purely of $A\beta_{1-42}$ peptides, the determined signal areas for the cellulose sample with adsorbed $A\beta_{1-42}$ was corrected by the signal areas accounting for lysine. The corrected signal areas of $A\beta_{1-42}$ are in good agreement with the signal areas of the difference spectrum (Figure 21, yellow) indicating that the determined signal areas are purely based on ^{13}C nuclei of $A\beta_{1-42}$. In addition, to account for signal overlap with spinning side bands, the MAS frequency was increased from 8 to 12.7 kHz, which avoids overlap of cellulose side bands with the protein resonances, however, introduces a slight overlap of the carbonyl and the C_α signal. Nonetheless, the signal areas at both MAS frequencies are very similar with values of ~ 0.12 a.u. and ~ 0.06 a.u. for signals reflecting one ^{13}C nucleus (e.g., C_O or C_α) for lysine and $A\beta_{1-42}$ resonances, respectively, indicating only a small influence of the side bands on the signal area. With Equation 36, the determined signal areas can be translated into the mass of the adsorbed molecule on the cellulose material. Here, it was assumed that the mass of cellulose—being the reference compound for the quantification—is equal to the total mass of the sample, neglecting the amounts of bound PDA, lysine, and $A\beta_{1-42}$ peptides. The determined masses from the multiple contact 1H - ^{13}C CPMAS experiments at 8 and 12.7 kHz are listed in Appendix Table A 12 and A 13. The calculated mean values of these determined masses are 25.33 μg and 3.02 μg at 8 kHz MAS frequency and 25.22 μg and 2.01 μg at 12.7 kHz MAS frequency for lysine and $A\beta_{1-42}$, respectively. Only a slight deviation in determined masses at the two MAS frequencies is observed in the case of lysine suggesting that a potential overlap with spinning side bands of the cellulose resonances is negligible. On the other hand, in the case of the $A\beta_{1-42}$, there is a higher deviation between each determined mass from the different signal areas which is reflected by the high standard deviation of 1 μg for the calculated mean values. This suggests either a potential residual contribution of lysine after the subtraction or a higher influence of signal overlap with the cellulose side bands due to the lower signal intensity of the $A\beta_{1-42}$ resonances. To reduce the influence of residual lysine contributions and thus increase the precision of this quantification approach, a cellulose sample with adsorbed $A\beta_{1-42}$ and functionality with lysine in natural isotope abundance can be prepared. In addition, signal overlap with side bands can be increasingly reduced with higher MAS frequencies, which is, however, accompanied with smaller rotor diameters and thus smaller sample amounts and therefrom derived lower

sensitivity. As the relative sensitivities for the cellulose material is relatively high, the quantification approach involving multiple contact ^1H - ^{13}C CPMAS experiments can also be performed in a 1.3 mm rotor at higher MAS frequencies.

Finally, to correct for differences in total sample masses used for the quantification of lysine and $\text{A}\beta_{1-42}$ peptides, the mass percentage of both molecules in the cellulose material correspond to 0.12 wt-% and 0.01 wt-% for lysine and $\text{A}\beta_{1-42}$, respectively. Note, no mass could be determined for PDA as no signals can be detected in the spectrum. This is, most likely, due to a low mass percentage of the PDA in natural isotope abundance. These low mass percentages agree well with the assumption that the total mass of the sample is mainly based on cellulose while the functionalization with PDA and lysine and the adsorbed $\text{A}\beta_{1-42}$ are only minor contributions to the total mass.

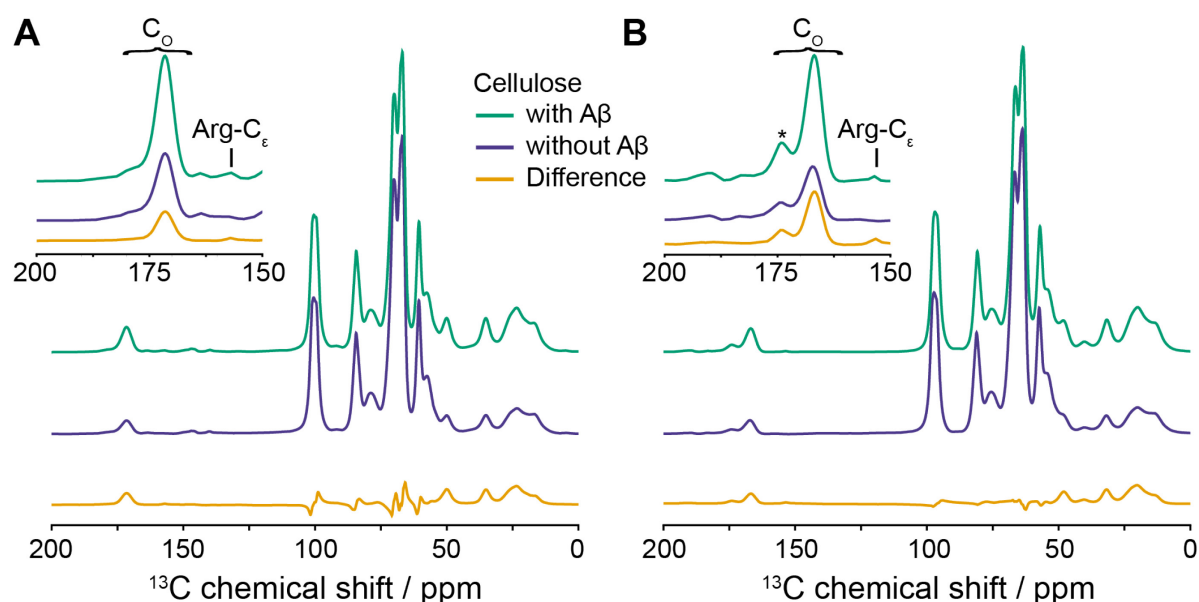


Figure 21: ^1H - ^{13}C multiple contact CPMAS spectra of PDA- and lysine-functionalized cellulose with adsorbed $\text{A}\beta_{1-42}$ peptides (green), without adsorbed $\text{A}\beta_{1-42}$ (violet), and the numerical difference between the two spectra (yellow) at either 8 kHz (A) or 12.7 kHz (B) MAS frequency and 100 K. For better visibility of the carbonyl spectral region (200 to 150 ppm), a cutout of this region is displayed in the upper left corner of the corresponding panel. The cellulose powder sample was rehydrated with 20 mM AMUPol dissolved in 33:67 vol-% $\text{H}_2\text{O}:\text{D}_2\text{O}$ to a hydration level of 60% (w/w).

The successful detection of $\text{A}\beta_{1-42}$ resonances enables further investigation of its interaction with the PDA/cellulose matrix. Therefore, ^{13}C - ^{15}N z-filtered TEDOR (Transfer Echo Double Resonance) spectra at two different TEDOR mixing times were acquired for the cellulose materials (Figure 22). Here, due to the difference in applied mixing times different ^{13}C - ^{15}N dipolar coupled spin pairs are recoupled: short mixing times result in the detection of directly bonded spin pairs, and longer mixing times are used to detect spin pairs, which are further apart.

The ^{13}C – ^{15}N TEDOR experiment with 1 ms mixing time displays two intense cross peaks with a chemical shift of ~ 35 ppm (^{15}N) and either ~ 50 ppm or ~ 35 ppm (^{13}C) corresponding to directly bonded C–N spin pairs for both samples. As the ^{15}N chemical shift of ~ 35 ppm is representative for an amine group, the peaks in the case of the cellulose sample without adsorbed A β_{1-42} peptides are unambiguously assigned to the lysine functionalization and its C_α – N_α and C_ϵ – N_ϵ bond, respectively. In the case of the A β_{1-42} -adsorbed cellulose material, the peak corresponding to the C_ϵ – N_ϵ spin pair is shifted in the ^{15}N dimension and broadened, suggesting contributions from the two lysine C_ϵ – N_ϵ spin pairs of the adsorbed peptide. Besides these two intense cross peaks, potential t_1 noise at ~ 60 ppm (^{13}C)^[112] and four peaks with low signal intensity can be observed: two out of four at a chemical shift of ~ 35 ppm (^{15}N) and ~ 175 ppm (^{13}C) and the other two at the same ^{15}N chemical shift and ~ 25 ppm (^{13}C). The first subset of cross peaks represents C_O –N spin pairs, where the ^{15}N chemical shift is the same as for the C_α – N_α cross peak (35.0 ppm) suggesting that the nitrogen is an N_α of an amino acid. However, the origin of the nitrogen cannot be determined unambiguously, as a peptide bond would resonate at ^{15}N chemical shift of ~ 125 ppm. Nonetheless, as this cross peak is not observed for the cellulose sample without A β_{1-42} , the cross peak represents a spin pair stemming either from purely within A β_{1-42} or between A β_{1-42} and lysine. The second subset can be assigned to carbons of an amino acid side chain. Again, as these two cross peaks are not observed for the sample without A β_{1-42} , at least one of the two involved nuclei must stem from A β_{1-42} .

The ^{13}C – ^{15}N TEDOR spectra with 5 ms mixing time displays the above-described cross peaks, however, with higher signal intensity emphasizing that the represented spin pairs are not directly bonded. The ^{13}C – ^{15}N TEDOR experiment for the sample without A β_{1-42} displays these cross peaks after 5 ms mixing time as well. Note that in the case of this sample, these subsets of cross peaks are not detectable at 1 ms mixing time and display a lower signal intensity in comparison to the TEDOR experiment with 5 ms mixing time of the A β_{1-42} sample. This suggests that the two subsets of cross peaks could be assigned to intramolecular pairs of C_O and side chain carbons to N_α and N_ϵ , respectively. At least for one of the two cross peak subsets (*viz.* C_O – N_α cross peak), this assumption does not involve N_α nuclei of the A β_{1-42} peptide as the ^{15}N chemical shift is not resonating at the typically encountered ^{15}N chemical shift of ~ 125 ppm for an amide or a peptide group. Another explanation is intermolecular contacts to amine groups, for example, between carbon atoms of A β_{1-42} —either R5 or K16 as K28 is lying inside the hydrophobic core—and one of the two nitrogen atoms of lysine.

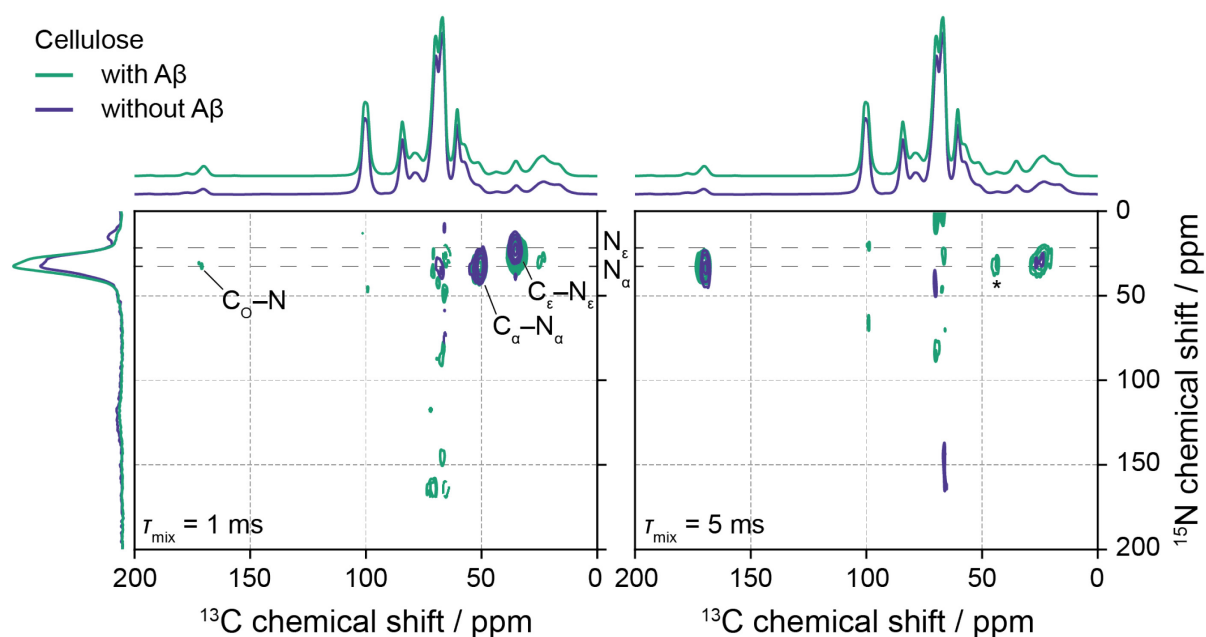


Figure 22: ^{13}C - ^{15}N z-filtered TEDOR spectra of PDA- and lysine-functionalized cellulose materials with (green) or without (violet) adsorbed $\text{A}\beta_{1-42}$ peptides at two mixing times (τ_{mix}), 102 K, and 8 to 12.7 kHz MAS frequency. The cross peaks are assigned ambiguous and are highlighted with a dashed gray line. The displayed one-dimensional ^1H - ^{13}C CPMAS (direct dimension) and ^1H - ^{15}N CPMAS (indirect dimension) spectra are separately obtained from the TEDOR experiment (*cf.* Figure 20).

In summary, this section reports relative sensitivity enhancement ($\epsilon T_{\text{B}}^{-1/2}$) of DNP by a factor of 5 to 10 and relative sensitivity gains of 100 as compared to solid-state NMR experiments at room temperature. This sensitivity enhancement is required to enable the detection of u- $[^{13}\text{C}, ^{15}\text{N}]$ -labeled $\text{A}\beta_{1-42}$ peptides of very low mass percentages in the permille range and thus proves that the cellulose material actively adsorbs these peptides. The detection and quantification of these trace amounts enables the possibility for development of better-adsorbing cellulose materials. As the project is, at time of writing, at its beginning, the reported sensitivity enhancements may be further optimized by variation of type and/or concentration of PA and method of impregnation. Additionally, structural investigations are performed, however, due to significant signal overlap with the lysine functionalization unambiguous assignments and statements cannot be made. Here, an orthogonal labeling scheme between $\text{A}\beta_{1-42}$ peptides and lysine layer can for example be employed. Advanced biochemical labeling schemes are also required for the investigation of the morphology of the adsorbed peptides.

4.2.3 Site-specific investigation of API-carrying polymeric micelles

Strict standards in manufacturing, clinical testing, and the safety and efficacy monitoring of active pharmaceutical ingredients (API) ensure high bioactivity and biocompatibility of those. As drug candidates are becoming increasingly insoluble in aqueous solutions (*e.g.*,

efavirenz)^[113] or fragile to, for example, the extracellular matrix (*e.g.*, mRNA (messenger RNA) vaccines)^[114], nanoparticles become of interest as a drug-carrying vehicle to increase bioavailability.^[115] The variety in composition of nanoparticles are vast, including inorganic materials,^[116] biomolecules,^[117] and synthetic polymers^[118]. NMR spectroscopy of these nanoparticles is complicated due to low amounts of either drugs (*e.g.*, efavirenz) or functional moieties in the nanoparticle rendering the investigation unfeasible without sensitivity enhancement. Here, DNP-enhanced solid-state NMR offers the required sensitivity enhancement, however, has to rely on spin diffusion for investigation of the nanoparticle's interior if the nanoparticles are either dissolved in or impregnated with a glycerol:water mixture containing the PA.^[117a, 119] To expand the applicability of DNP in this field, Kesten Ulrich from the working group of Ann-Christin Pöppler (University of Würzburg) investigated the applicability of DNP-enhanced solid-state NMR to detect and investigate dilute drugs and functional moieties within nanoparticles as part of his Master's thesis.^[88b] He prepared polymeric micelles using the thin film method, where the polymer MeOx–BuOzi–MeOx (MBM) is mixed with the respective PA and optionally the drug efavirenz—an antiviral drug belonging to the class of non-nucleoside reverse transcriptase inhibitor (NNRTI) for the treatment of HIV–1 (human immunodeficiency virus type 1)—in a suitable solvent, followed by solvent evaporation and subsequent rehydration in water leading to micelle formation. Due to consideration of the hydrophilicity, it is expected that the hydrophobic PA TEKPol will preferentially localize together with efavirenz in the hydrophobic micellar core, whereas the hydrophilic TOTAPOL will partition into the extra-micellar matrix. The localization of the two PAs were afterwards confirmed by continuous-wave EPR (electron paramagnetic resonance) spectroscopy. The DNP experiments were conducted in Rostock by myself, where the MBM samples with either TOTAPOL or TEKPol and without loaded efavirenz (Figure 23, Figure 24, violet, and Figure 25, violet) were part of the Master's thesis of Kersten Ulrich.

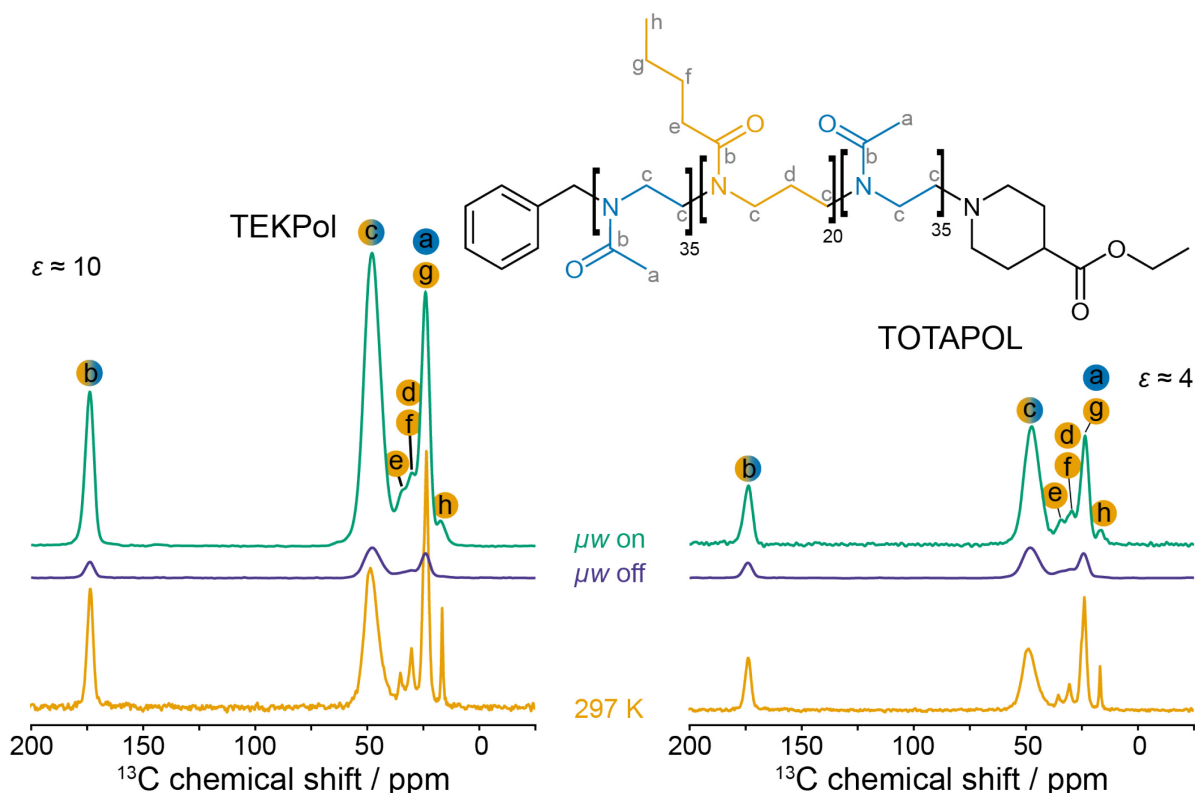


Figure 23: ^1H - ^{13}C CPMAS of freeze-dried MBM micellar formulations with either 8 nmol/mg TEKPol or 8 nmol/mg TOTAPOL with (μw on, green) or without (μw off, violet) microwave irradiation at 98 K and 12 kHz MAS frequency and without PA (yellow) at 297 K and 20 kHz MAS frequency. The ^{13}C resonances are assigned as indicated in the chemical structure of the MBM polymer, which is displayed as a subset in the figure. The assignment is adopted from here^[88b] and summarized in Appendix Table A 14. The signal intensities of the spectra obtained with microwave irradiation (green) and the spectra obtained at 297 K are normalized relative to each other (same signal intensity of the resonance assigned to *a* and *g*). In the case of the spectra at 297 K, the same spectrum with scaled signal intensity is displayed.

To assess the applicability of DNP for PA-carrying polymeric micelles, ^1H - ^{13}C CPMAS spectra of MBM micelles with either TOTAPOL or TEKPol were measured (Figure 23). As the sample consists only of the MBM polymer and the respective PA, the assignment of the resonances is straightforward, however, due to the low temperatures required for DNP experiments, signal broadening which is accompanied with loss in spectral resolution is observed relative to solid-state NMR measurements (*cf.* the spectral region from 10 to 50 ppm, Figure 23). Nonetheless, despite the signal overlap due to signal broadening at low temperatures, each resonance of the MBM resonance can be assigned (Appendix Table A 14). The comparison of the microwave on and off spectra yields the enhancement factor of ~ 10 and ~ 4 for the TEKPol and TOTAPOL samples, respectively. It must be noted that rotation-induced depolarization of the thermal polarization was not considered. Both enhancement factors are at least a factor of ~ 3 smaller as compared to those of lipid nanoparticles, which were suspended in a glycerol:water matrix containing 12 mM AMUPol.^[117a] Interestingly, TEKPol being

localized in the hydrophobic micellar core displays a two-fold higher enhancement factor being a consequence of the superior polarization characteristics of TEKPol to TOTAPOL. The ^1H DNP build-up time constants are similar for both samples, with a mean value of 1.4 s and 1.3 s for TEKPol and TOTAPOL, respectively (Appendix Table A 15). The short build-up time constants indicate a rather fast build-up with resulting low enhancement factors suggesting a high contribution of nuclear relaxation. This is reasoned with the high amount of protonated mobile sidechains in the polymer, where the hydrophilic as well as the hydrophobic part each contains one protonated methyl group per monomer (*cf.* structure in Figure 24). Finally, the relative sensitivity is reflected by the achievable enhancement factor per unit time ($\epsilon T_{\text{B}}^{-1/2}$). As the build-up time constants are rather similar, the relative sensitivity values of both samples show the same trend as the enhancement factors, but scaled, with values of 7 and 4 for TEKPol and TOTAPOL, respectively (Appendix Table A 14).

The comparison of signals obtained by DNP-enhanced ^1H - ^{13}C CPMAS experiments at 102 K and ^1H - ^{13}C CPMAS experiments at 297 K yields the relative sensitivity gain of DNP over standard solid-state NMR (Figure 23 and Appendix Table A 15). Here, relative sensitivity gains of 5 and 20 for TOTAPOL and TEKPol, respectively, are observed for all resonances except the peak assigned with *h*. This resonance is assigned to the methyl group of the hydrophobic part of MBM and its relative sensitivity gains are rather small with values of 0.9 and 1.9 for TOTAPOL and TEKPol, respectively. This low sensitivity enhancement can be caused by active reorientation dynamics, interfering with CP spinlock at this low temperature^[55] or line broadening due to accidentally matching the experimental temperature to the coalescence temperature.

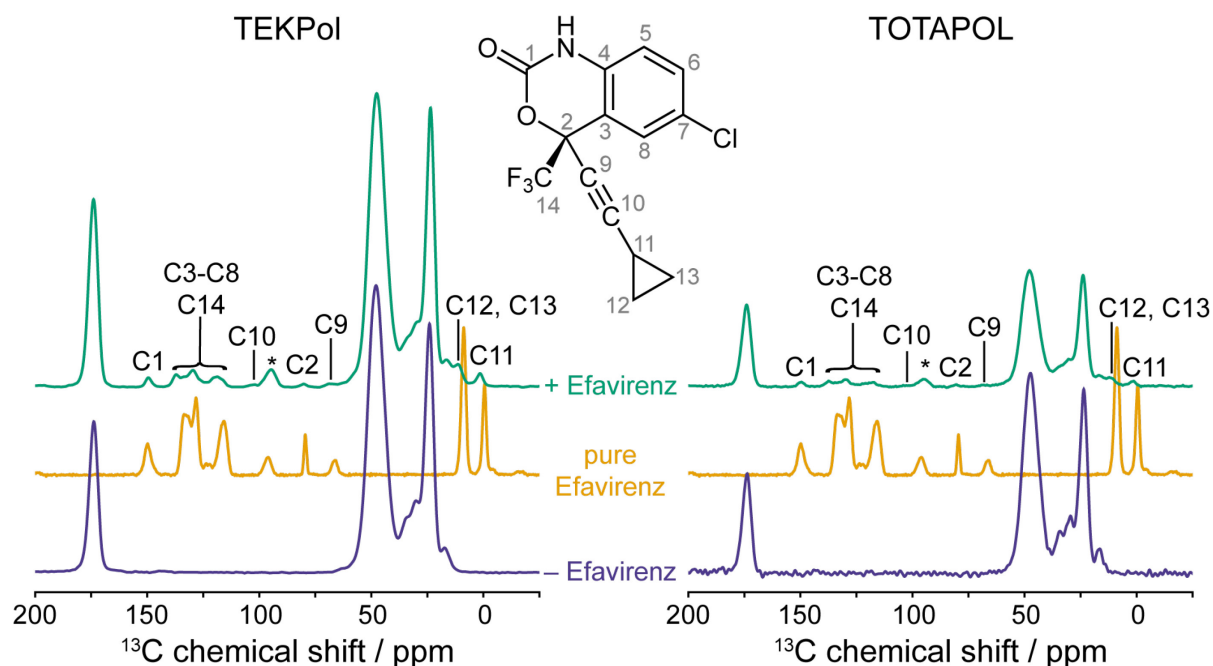


Figure 24: ^1H - ^{13}C CPMAS spectra of MBM micelles formulated with either 8 nmol/mg TEKPol or 8 nmol/mg TOTAPOL and with (green) or without (violet) efavirenz at 102 K and 8.57 kHz MAS and ^1H - ^{13}C CPMAS spectrum of pure, amorphous efavirenz (yellow) at 245 K and 20 kHz MAS frequency. The resonances of efavirenz are assigned with numbers according to the structure displayed as a subset in the figure and is based on the published assignment of pure efavirenz^[120] (Appendix Table A 16). The assignment of resonances belonging to the MBM polymer can be found in Figure 23 and Appendix Table A 14.

The high relative sensitivity gains by DNP provides a sufficient foundation for experiments on efavirenz-loaded MBM micelles. Figure 24 illustrates the DNP-enhanced ^1H - ^{13}C CPMAS spectra of MBM micelles formulated with either TEKPol or TOTAPOL and either with efavirenz loading (green) or without (violet). For both PAs, signals not visible in the pure MBM micellar sample are emerging with the presence of efavirenz. For an unambiguous assignment of these new resonances, a solid-state NMR spectrum of pure efavirenz is acquired and compared to a published assignment (Figure 24, yellow).^[120] Here, the resonances of pure efavirenz match well with the signals in the efavirenz-loaded nanoparticles—where minor discrepancies in chemical shifts are addressed to the different chemical environments of the probed efavirenz—proving the successful detection of the low amounts (*viz.* 15 wt-%) of efavirenz in natural isotope abundance. Note that the natural isotope abundance reduces further the effective concentration of ^{13}C nuclei resulting in an effective mass percentage of 0.15 wt-% ^{13}C -labeled efavirenz, which is a similar concentration as observed for ^{13}C , ^{15}N -labeled $\text{A}\beta_{1-42}$ peptides adsorbed to cellulose materials (see Section 4.2.2). It has to be noted that this mass percentage only includes one ^{13}C nucleus per efavirenz molecule and is further reduced for each additional ^{13}C spin in the same molecule. The low amount of efavirenz explains the reason why solid-state NMR experiments of these micellar formulations showed no resonances for

efavirenz (*cf.* Master's thesis of Kersten Ulrich^[88b]) and emphasizes the necessity of sensitivity enhancement by DNP.

Next, to benefit from the co-localization of TEKPol with efavirenz, directly excited ^{13}C MAS experiments of MBM micelles with and without efavirenz are acquired (Figure 25). In comparison to indirect experiments (*e.g.*, ^1H - ^{13}C CPMAS), the polarization build-up on ^{13}C is based on the direct interaction of ^{13}C nuclei with the electron spin of the PA. As ^{13}C is a dilute spin and thus the spin-diffusion process is retarded relative to ^1H spin diffusion, the polarization build-up is more sensitive towards the distance between PA and the detected ^{13}C sites. This effectively filters out signals which are more remote such as the extra-micellar matrix. The downsides of this approach are the long polarization build-up times due to the dilute ^{13}C network and therefrom resulting inefficient spin diffusion and spreading of the hyperpolarization. Nonetheless, Figure 25 illustrates the directly excited ^{13}C MAS spectra of MBM micelles formulated with (green) and without (violet) 15 wt-% efavirenz and 8 nmol/mg TEKPol. The comparison of both spectra reveals resonances with low signal intensity in the spectral region of the aromatic carbons (C3 to C8), the trifluoromethyl carbon (C14), and carbamate (C1). The cross-comparison with the directly excited ^{13}C MAS spectra of MBM micelles with 8 nmol/mg TOTAPOL verifies the applicability of this approach as either no carbon resonances or, in the case of the aromatic and trifluoro methyl carbons (C3 to C8, C14), with lower intensity are detected. A potential difference in size was probed by dynamic light scattering, where the hydrodynamic diameter is determined to be 21.53 nm and 21.46 nm for TEKPol and TOTAPOL, respectively. This similar diameter emphasizes that the co-localization of TEKPol has to be responsible for the detection of efavirenz resonances. Nonetheless, the obtained sensitivity of this approach is very low, being a direct consequence of the dilute ^{13}C spin network in the sample and therefrom derived long polarization build-up time constants. The sensitivity could be increased by using ^{13}C labeled efavirenz instead of natural isotope abundance. The formulation of MBM micelles with ^{13}C -labeled efavirenz will also be beneficial for further experiments, including two-dimensional ^{13}C - ^{13}C correlation experiments to resolve potential interactions of the drug with the hydrophobic moiety of the micelle. The trifluoromethyl group of efavirenz can be an additional target for further experiments as it is the only source of ^{19}F in the MBM micelles and thus naturally introduces site-specificity. By applying a ^1H - ^{19}F - ^{13}C double-CPMAS experiment, the fast polarization build-up kinetics of ^1H can be exploited, which is then transferred by CP first to ^{19}F before further transfer to ^{13}C . Unfortunately, as the DNP setup in Rostock cannot apply rf pulses (*e.g.*,

decoupling) on the ^{19}F and ^1H channel simultaneously, these kinds of experiments are unfeasible. The Master's thesis of Edvards Bensons,^[48] however, has shown that trifluoro methyl groups are a valuable tool as they not only introduce site-specificity due to the natural scarcity of ^{19}F , but also via ^{19}F -driven SCREAM-DNP experiments.

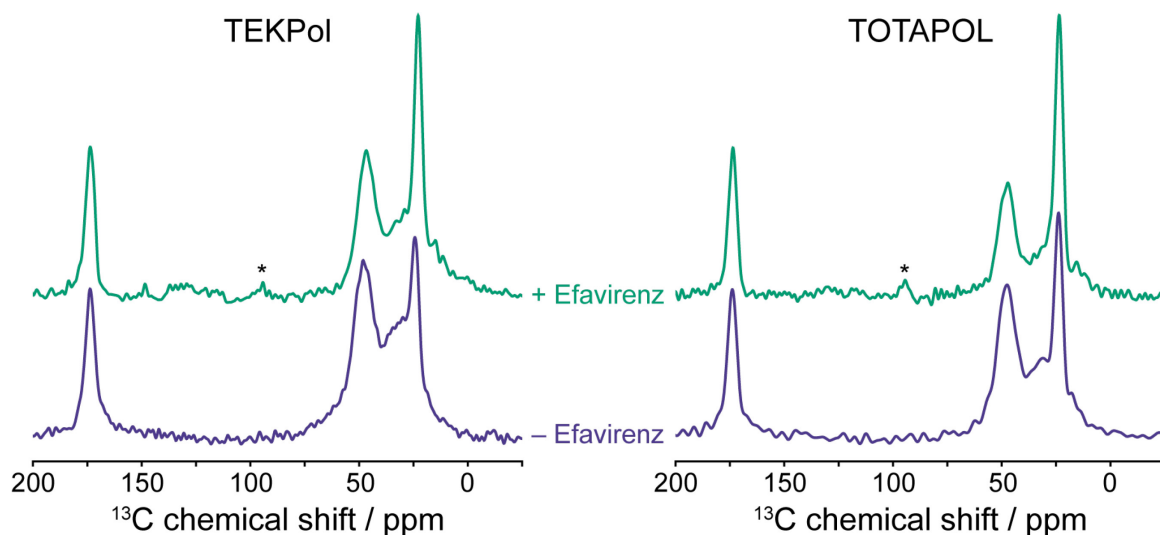


Figure 25: Direct excited ^{13}C MAS spectra of MBM micelles formulated with either 8 nmol/mg TEKPol or 8 nmol/mg TOTAPOL and with 15 wt-% efavirenz (green) at 102 K and 8 kHz MAS frequency or without (violet) efavirenz at 98 K and 12 kHz MAS frequency. Signals denoted with an asterisk are spinning sidebands.

In summary, this section emphasizes again the potential of sensitivity enhancement by DNP to detect and investigate small amounts of compounds, in this case the HIV drug efavirenz in natural isotope abundance. The comparison of signal amplitudes of the MBM resonances obtained with solid-state NMR at 297 K and with DNP at 102 K yields relative sensitivity gains of 5 to 20 transferring into an acceleration of experimental time of 25- to 400-fold. This acceleration is required as only a fraction of efavirenz can be loaded into the MBM micelles—as higher percentages result in disruption of the micellar stability^[88b]—rendering solid-state NMR experiments of efavirenz in MBM micelles unfeasible. The possible co-localization of TEKPol with efavirenz can be crucial for site-specific investigations of the micellar interior in the future. In addition to sensitivity enhancement by DNP, advanced DNP hardware involving a $^1\text{H}/^{19}\text{F}/^{13}\text{C}$ LTMAS probe or ^{13}C labeling of efavirenz furthermore increases the much-required sensitivity and introduces selectivity for structural investigations of pharmaceutically relevant nanoparticles.

4.2.4 Summary and Outlook

This chapter demonstrates alternative DNP sample preparation methods suitable for insoluble proteins and biomaterials such as cellulose and nanoparticles. Here, high relative

sensitivity gains up to ~35-fold can be obtained, enabling the detection of dilute molecules such as 0.01 wt-% of ^{13}C labeled $\text{A}\beta_{1-42}$ peptides adsorbed to cellulose materials (Section 4.2.2) or 15 wt-% of the HIV-1 drug efavirenz in natural isotope abundance in its carrier micelle (Section 4.2.3). Nevertheless, these studies are only the starting point for detailed investigations using the proposed matrix-free DNP approach. These high sensitivity enhancements by DNP enable not only the detection but also the structural investigation of these dilute molecules with their environment as already indicated with TEDOR experiments. These investigations will be helpful for future developments of artificial kidneys and drug-carrying nanoparticles, both playing an important role in medicine.

4.3 Quantification of Methyl Group Dynamics under DNP conditions

NMR spectroscopy is an ideal tool to characterize and quantify dynamics of functional groups in molecules.^[121] Here, the dynamics modulate spin interactions on their timescale and thus rendering the corresponding spin Hamiltonian time-dependent. The time evolution of this Hamiltonian can then be described by an autocorrelation function, whose Fourier transform is the spectral density function $J(\omega)$, connecting experimental observables to the correlation time τ_c via a motion model (*cf.* Section 1.2). For the liquid state, a Model-free approach^[77, 122] is assuming the best model by a statistical analysis of each one, resulting in a globular tumbling correlation time and one or more local correlation times describing the group of interest such as an imino bond in a tRNA.^[123] In contrast, the motional freedom of molecules is hindered in the solid-state, reducing the complexity of the motion model to describe the molecular dynamics, especially at cryogenic temperatures. Here, the motional freedom within the molecules is to the most extent frozen out with the methyl group dynamics being still active making methyl group dynamics an ideal system to investigate the applicability of DNP-enhanced relaxation experiments for studying molecular dynamics. Additionally, the dynamics of methyl groups are particularly interesting as they contain valuable information about their structural environment. Thus, detailed information of the dynamics and its temperature dependence provides insights into, for example, steric changes upon temperature rise or molecular binding. However, this often requires experiments conducted at a broad range of temperature, including cryogenic temperatures in the case of methyl groups.

Deuterium is ideal for measuring the dynamics of methyl groups as it is very sensitive to molecular motions over a wide range of timescales and temperatures.^[66, 124] Its quadrupolar interaction furthermore provides an acceleration of experiment as the ^2H spin-lattice relaxation time constants are typically on the millisecond timescale. Nonetheless, the intermediate exchange regime appearing at these cryogenic temperatures for deuterated methyl groups causes line broadening, resulting in drastically reduced sensitivity for ^2H NMR experiments. Here, DNP could provide sufficient sensitivity enhancement to acquire ^2H spectra at these challenging conditions. The applicability of ^2H DNP was shown so far only by a few publications^[125] as direct ^2H DNP has its own intricacies in terms of specificity. The missing chemical shift resolution of the ^2H quadrupolar nucleus requires selective labeling, whereas direct ^2H DNP relies either on a dense ^2H network throughout the sample or a close proximity between ^2H site and the PA to ensure rather fast DNP build-up time constants and rather high

sensitivity enhancement factors. As each possibility renders selective measurements of deuterated methyl groups unfeasible, due to either high solvent background or paramagnetic relaxation and resulting line broadening, an indirect ^1H DNP approach with selectively deuterated methyl groups combines the best of both worlds: efficient spin diffusion for fast transfer of the polarization within the ^1H network and site-specific detection due to selectively deuterated methyl groups. The applicability of this approach will be studied in this section, where the main focus is on the potential sensitivity gains of DNP compared to standard ^2H NMR experiments and the investigation of dynamics by measuring $T_1(^2\text{H})$ relaxation time constants in presence of PAs. These questions will be investigated by two model systems: selectively deuterated $\text{A}\beta_{1-40}$ fibrils and ethanol, where the first system is investigated using the matrix-free DNP approach introduced in chapter 3.2, and the latter is investigated as a frozen solution.

4.3.1 Investigation of Methyl Group Dynamics in $\text{A}\beta_{1-40}$ fibrils by DNP-enhanced ^1H - ^2H CPMAS NMR

The matrix-free DNP approach, which was optimized in Section 4.2.1, can be used to study biomolecular dynamics in insoluble biomolecules such as $\text{A}\beta_{1-40}$ fibrils. The work in this section and Section 4.2.1 was part of the publication which investigated the possibility of using DNP-enhanced ^1H - ^2H CPMAS as a tool for studying biomolecular dynamics at temperatures commonly applied in DNP.^[43f] In order to test this approach, I started a collaboration with Prof. Dr. Liliya Vugmeyster which is an expert in ^2H NMR and biomolecular dynamics. She provided the three selectively deuterated $\text{A}\beta_{1-40}$ fibril samples as well as the two HP36 protein samples and the RC9 peptide used as models with known methyl group dynamics in the temperature range typically employed in DNP experiments. As part of her Mare Balticum Fellowship, we had the possibility to study these samples with the matrix-free DNP approach in Rostock. The non-disruptiveness of this preparation for the fibrillar structure and the integrity of the PA were tested with transmission electron microscopy (TEM) and electron paramagnetic resonance (EPR). As these experiments were not done by me or Prof. Vugmeyster, the positive results of this two experiments are not shown in this work, instead the interested reader is referred to reference [43f]. I determined the ^1H DNP enhancement factors and the ^1H DNP build-up time constants by ^1H - ^{13}C CPMAS experiments of the $\text{A}\beta_{1-40}$ fibrils (Figure 26), the ^1H - ^2H CPMAS and the ^2H MAS NMR experiments (Figure 27) were acquired together, whereas the analysis of the T_1 relaxation data was done by her (Figure 28).

To assess the efficacy of the matrix-free DNP approach for A β fibrils, the ^1H DNP enhancement factors ϵ and the ^1H DNP build-up time constants T_B are determined (Figure 26 and Appendix Table A 17). Both protein samples show good ^1H DNP enhancement factors of 15 and 18 and rather short build-up time constants of 0.74 and 0.94 s, respectively. Note that the enhancement factors were determined as simple microwave on/off comparison and rotation-induced depolarization effects are not reflected in the given factors. The rather low enhancement factors and short build-up time constants as compared to the values obtained for the lysozyme (Section 4.2.1, Figure 17 and Figure 18) could have a manifold of reasons, one of them will be the larger ^1H concentration in the A β samples due to the higher water content used during rehydration of the proteins (*cf.* 21% for the lysozyme and 60% for the A β fibrils) which causes lower achievable ^1H enhancement factors.^[126] A huge concentration of protonated mobile sidechains like methyl groups is also known to drastically diminish the polarization build-up properties in the sample (*vide infra*). Furthermore, the low build-up time constants could indicate a potential clustering of the PA upon freezing due to the formation of a mobile phase in the sample matrix as already observed for the lysozyme sample with a molar ratio of 1:4 (PA:protein) and a water content of 21% (w/w). Nonetheless, due to the small amount of available sample, a detailed optimization of the ^1H DNP build-up properties was not feasible.

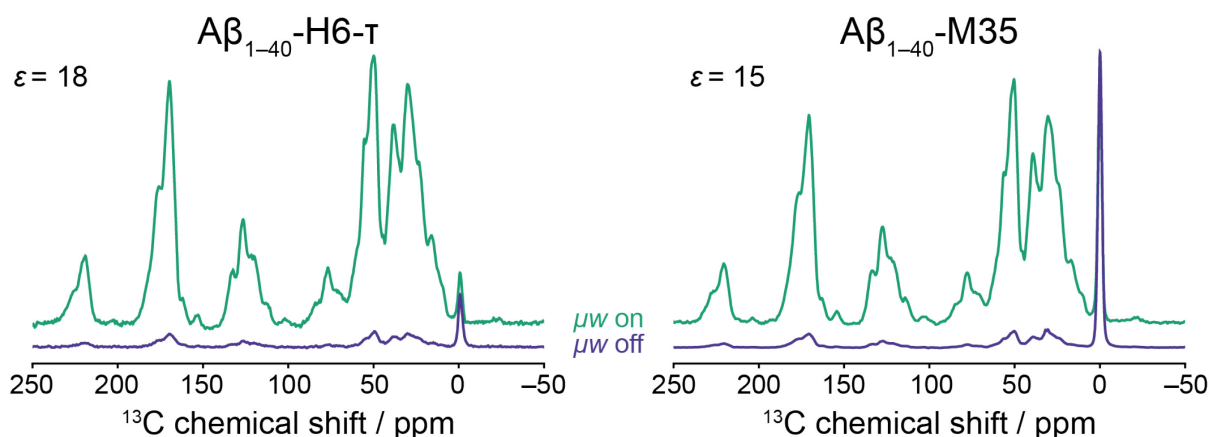


Figure 26: ^1H - ^{13}C CPMAS spectra of A β_{1-40} fibrils with a single selectively deuterated methyl group at either the H6- τ or the M35 position at a molar ratio of 1:15 (PA:protein) and 100% (w/w) rehydration with (μw on, green) and without (μw off, violet) microwave irradiation at 115 K and 5 kHz MAS frequency. The signal without an enhancement at 0 ppm corresponds to a silicone plug. The determined ^1H DNP enhancement factors ϵ , the build-up time constants T_B , and the relative sensitivities $\epsilon T_B^{-1/2}$ are listed in Appendix Table A 17.

The determined DNP properties shown in Figure 26 provide sufficient sensitivity enhancement to investigate biomolecular dynamics with deuterium labels using ^1H - ^2H CP instead of direct ^2H excitation. It must be noted that this CP transfer step would be impractical under static conditions due to the interference of the large inhomogeneous linewidths of the ^2H quadrupolar properties which interfere with normal Hartmann-Hahn CP transfer. Under MAS

rotation, however, the rotation-induced evolution of the first-order eigenfrequencies of inhomogeneously distributed ^2H spin packets result in an effective increase in bandwidth. With this increase, transfer over the whole ^2H Pake pattern can occur, albeit, the CP transfer efficiency is significantly decreased if compared to a spin- $1/2$ nuclei.^[127] Additionally, the repetition of the CP experiment is limited by the build-up of hyperpolarization on ^1H given by the ^1H DNP build-up time constant T_B in the case of DNP-enhanced CP experiments. This is favorable in the most cases due to the higher T_1 relaxation time constants for ^{13}C or ^{15}N , however, it is unfavorable for quadrupolar nuclides due to their fast quadrupolar T_1 relaxation yielding relaxation time constants in the milliseconds. To assess if the ^1H - ^2H CPMAS NMR experiment results in a sensitivity enhancement for the three selectively deuterated A β fibril samples the relative sensitivity gain of the DNP-enhanced ^1H - ^2H CPMAS experiment over directly excited ^2H MAS NMR without DNP enhancement are determined. For the calculation of this sensitivity gain, the obtained signal amplitudes of both experiments are determined and normalized to the accumulated number of transients (Figure 27A & B, Appendix Figure A 6 & A 7, and Appendix Table A 18 to A 20). No systematic difference regarding the experimental noise was observed between the two experiments, if the RMS noise is normalized to the square root of the number of accumulated transients (Appendix Table A 21 to A 23). However, the analysis of the signal amplitudes as well as the noise amplitudes revealed that random variations in the RMS noise, which are caused most probably by miniscule variations in baseline correction, result in a significant statistical error of calculated signal-to-noise ratios (SNR) and therefrom determined relative sensitivity gains (*vide infra*). Because the normalized RMS noise shows no systematic deviations, the signal amplitudes are therefore considered as a more reliable measure of sensitivity with lower proneness to the outlined statistical errors (Figure 27B and Appendix Table A 18 to A 20).

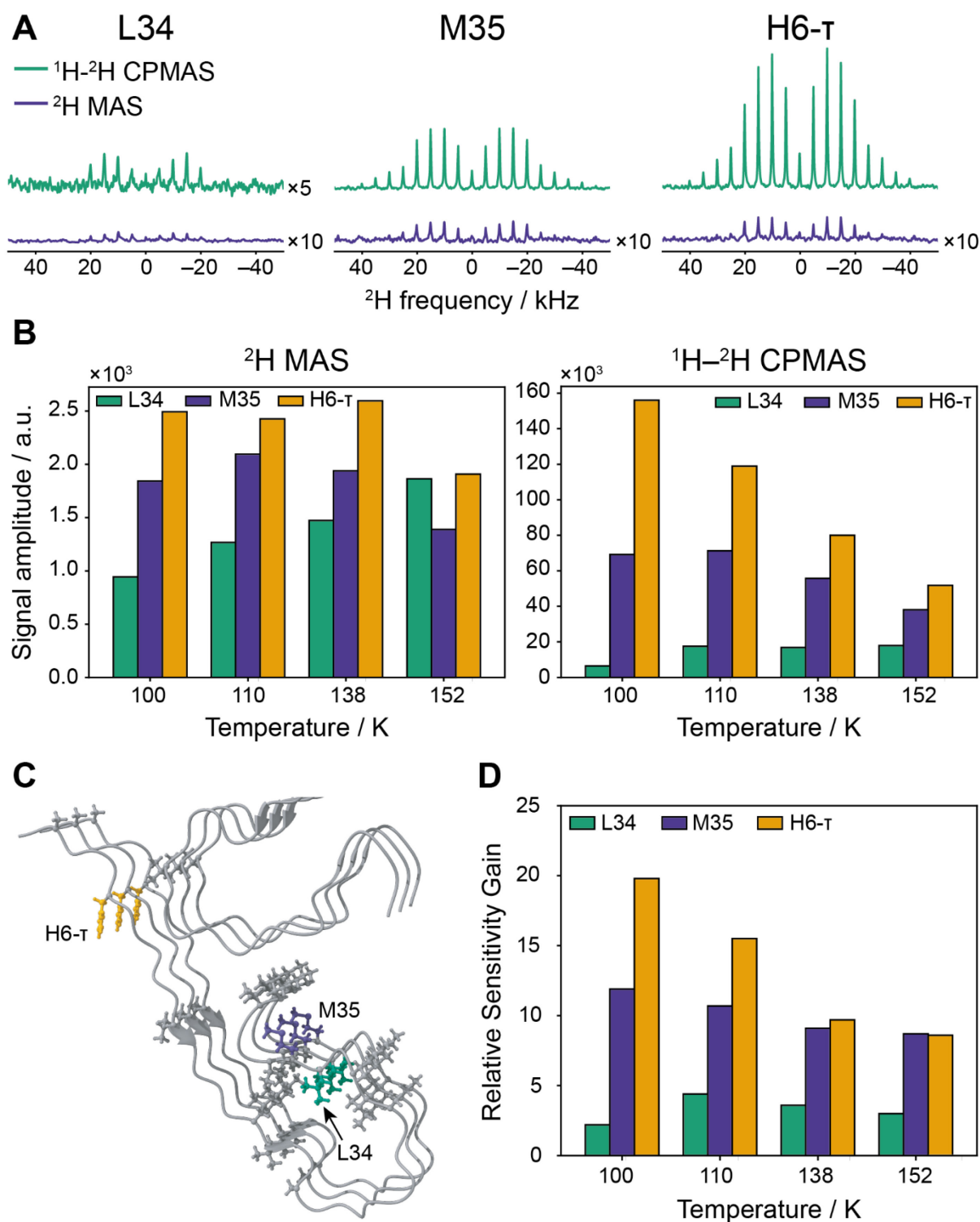


Figure 27: Comparison of signal obtained by ^1H - ^2H CPMAS and ^2H MAS NMR experiments with their representative spectra at 100 K and 5 kHz MAS frequency (A), all obtained signal amplitudes (B), the structure of one protofilament of $\text{A}\beta_{1-40}$ fibrils and the C-terminal end of one neighboring protofilament (C), and relative sensitivity gains obtained by DNP and ^1H - ^2H CPMAS over ^2H MAS NMR experiments normalized to the time (D). (A) The spectra are obtained with microwave irradiation and ^1H - ^2H CPMAS excitation (green) and without microwave irradiation and direct excitation of ^2H (violet) and are all normalized to the same intensity scale after normalization to the number of accumulated transients. If annotated at the right side, the spectra is magnified by the given number for better visibility of the signal. All spectra being only normalized to the same intensity scale, and all spectra being further normalized to the number of accumulated transients are shown in Appendix Figure

A 6 to A 7. (B) The shown signal amplitudes were normalized to the number of accumulated transients. (C) The sidechains containing the deuterated methyl groups are highlighted in green (L34), violet (M35), and yellow (H6- τ). All other methyl-bearing amino acids of the same peptide chain as well as the closest methyl group in the neighboring protofilament are displayed in gray. The structure is adapted from PDB: 2M4J.^[110a] (D) The relative sensitivity gain being the ratio of the signal amplitudes of the ^1H - ^2H CPMAS and ^2H MAS spectra are further normalized to the square root of the ratio of the repetition delays which is constant factor of square root of 10. All individual signal amplitudes and relative sensitivity gains are summarized in Appendix Table A 18 to A 20.

Figure 27 displays representative spectra of the three A β fibril samples, the therefrom calculated signal amplitudes and the derived relative sensitivity gain. In the case of the ^2H MAS NMR experiments, the calculated signal amplitudes of the H6- τ and M35 label are almost constant over the whole temperature range with a small decrease at 152 K. The L34 label, on the contrary, increases in signal amplitude linearly with temperature and shows an identical amplitude as the H6- τ label, whereas the M35 label slightly deviates. The increase in amplitude for the L34 label is reasoned by the temperature activation of its deuterated methyl group, which is in the slow exchange regime at 100 K and transitions to the fast exchange regime at elevated temperatures. The decrease in signal amplitude for the other two labels can also be explained by dynamics, however, not the dynamics of their deuterated methyl groups—both methyl groups are known to already be in the fast exchange regime at 152 K^[89, 128]—but the dynamics of nearby protonated methyl groups (Figure 27C, see below). The signal amplitudes in the case of the DNP-enhanced ^1H - ^2H CPMAS experiments are changing more drastically with temperature, especially for the H6- τ label. Here, the highest amplitude is observed at 100 K and it decreases by a factor of two at 152 K. A similar trend is visible for the M35 label, however, with much lower intensity in the signal amplitudes. A similar trend, but less steep, for the signal amplitudes as seen for the ^2H MAS NMR experiments is observed for the L34 label, for which the signal amplitude is low at 100 K and increases with elevated temperatures to a 3-fold increase at 152 K. Unlike for the ^2H MAS NMR, the signal amplitude at 152 K is 3-fold lower in intensity than for the other two labels, which is mainly caused by different dynamics of the selectively deuterated methyl groups, but also by different dynamics and different amounts of adjacent protonated methyl groups (Figure 27C):

(1) In the case of the L34 label, which lies in the hydrophobic core of the protofilament, a large number of nearby aliphatic and aromatic protonated sidechains are present which undergo dynamics at different timescales. For example, there are several protonated methyl groups of other residues within a mere few ångströms (between 3 to 7 Å) distance. For example, the sidechains of I32 and V36 have close contacts to L34 inside the hydrophobic core with distances down to 4 Å within the same peptide strand and 5 Å to the neighboring peptide of the

same protofilament. Of particular significance is the unlabeled methyl group of L34, which has a distance between the $C_{\delta 1}$ and $C_{\delta 2}$ of 3 Å and the protons and deuterons of these two methyl groups are approaching 2 Å. Noteworthy is the signature hydrophobic contact with F19 (~4 Å), nevertheless, the ring flips of F19 should be strongly attenuated at these low temperatures.^[10g, 129] Taken together, these mobile sidechains and especially the adjacent methyl groups become more and more activated with elevated temperatures and therefore cause strong fluctuations in the local dipolar fields. This introduces either ^1H dipolar relaxation, which reduces the transferable ^1H polarization, or interferes directly with the dipolar coupling-based CP transfer.

(2) The M35 residue is also situated in the C-terminal, hydrophobic core region, however, its sidechain faces outwards and inside the water-accessible cavity of the 3-fold polymorph structure. As a result, the above outlined mobile sidechains of the hydrophobic core are farther away with the closest contact to L34- $C_{\delta 1}$ (~8 Å) but are still affecting the deuterated methyl group of the C_{ϵ} carbon of methionine.

(3) In the contrary to L34 and M35, H6- τ is located in the hydrophilic N-terminal and solvent-exposed region with a lower concentration of aliphatic sidechains. Here, the nearest protonated methyl group in the same strand is more than 15 Å away and the closest interstrand contact is to V24 of the neighboring protofilament in the 3-fold polymorph structure (~10 Å). Due to the low abundance of mobile sidechains, it is the least affected and thus has the highest achievable signal amplitude by ^1H - ^2H CPMAS.

As a measure of the sensitivity enhancement by conducting DNP-enhanced ^1H - ^2H CPMAS experiments rather than ^2H MAS NMR experiments without microwave irradiation, the relative sensitivity gain being the ratio of the ^1H - ^2H CPMAS and the ^2H MAS signal amplitudes is calculated. Due to the very fast quadrupolar relaxation and the resulting fast experimental repetition delay employable in ^2H MAS NMR experiments, the different repetition delays were considered by dividing the relative sensitivity gain with the $\sqrt{10}$ with the radicand being the ratio of the typical repetition delays used in both experiments. This time-normalized relative sensitivity gain is favorable for the ^1H - ^2H CPMAS experiment at all tested temperatures (Figure 27D), even for the L34 label which displays the lowest relative sensitivity gains with values between ~2 at 100 K and ~3 at 152 K. The H6- τ and the M35 label both show a clear trend—albeit the trend for the H6- τ label is more pronounced—where the highest relative sensitivity gain is achievable at 100 K (~20 and ~11, respectively), which is decreasing with elevated temperatures to a final value of ~9 for both labels. Noteworthy, the L34 label displays a slight increase in relative sensitivity gain with decreasing temperatures (from ~3 to

~4), however, drops by a factor of two upon decreasing to 100 K, which is most likely explained with a drastic change of the dynamics of the protonated sidechains inside the hydrophobic core affecting the efficacy of the CP transfer (see above). In summary, the obtained relative sensitivity gains for all samples show the benefit of using DNP-enhanced ^1H - ^2H CPMAS instead of low-temperature ^2H MAS solid-state NMR experiments. The sensitivity enhancement obtained by DNP significantly accelerates the experiments by a factor of up to 400-fold as shown for the H6- τ label, which reflects ideal conditions due to the absence of nearby protonated sidechains and the therefrom resulting effective decoupling from proton dynamics. This acceleration drops significantly in the tested case by 100-fold to an acceleration factor of 4 if the investigated site is located within a strong proton network with a large variety of dynamics resulting in interferences with DNP polarization build-up and/or CP transfer.

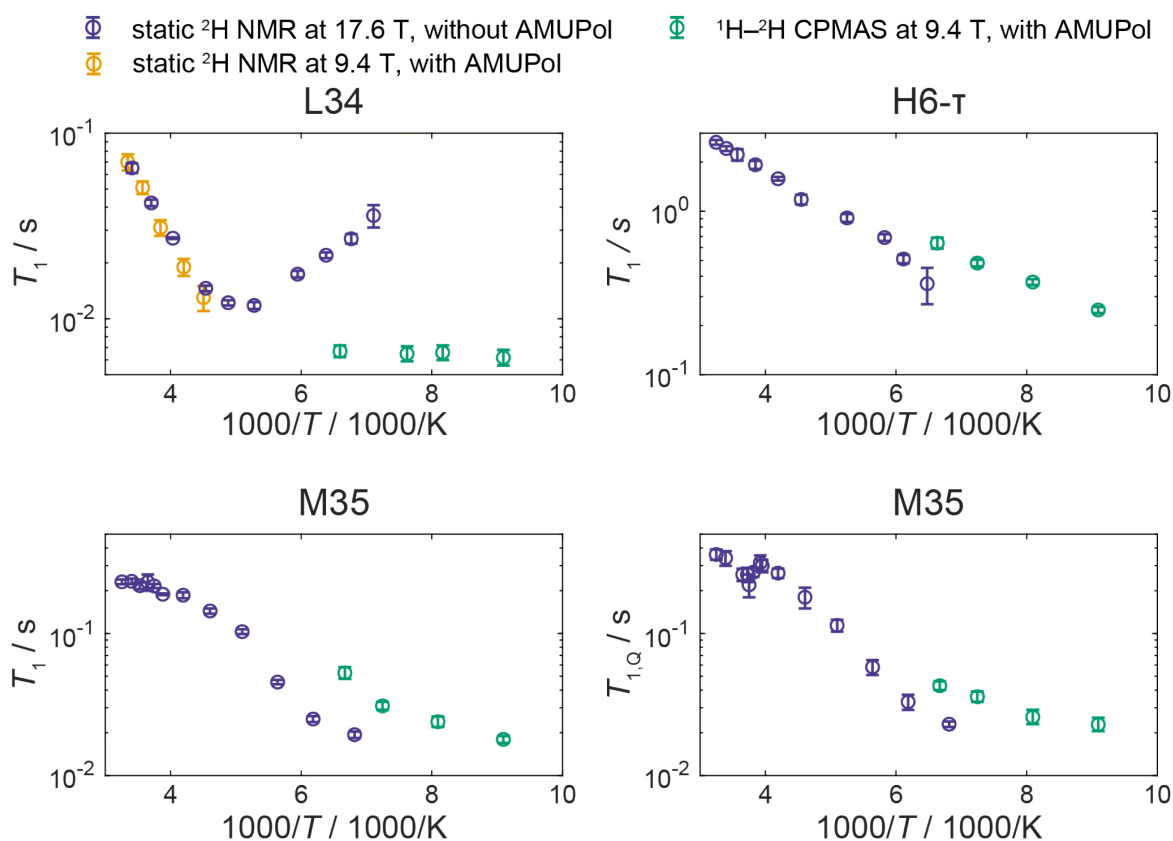


Figure 28: ^2H Zeeman (T_1) and quadrupolar order ($T_{1,Q}$) relaxation time constants of three different $\text{A}\beta_{1-40}$ fibrillar samples, each selectively deuterated with a methyl group at the given position (H6- τ , L34, and M35), obtained either with indirect DNP with AMUPol at 9.4 T and 5 kHz MAS frequency (green circles) or under static conditions without AMUPol at 17.6 T (violet circles). Additional relaxation time constants were determined for the deuterated methyl group of the $\text{A}\beta$ -L34 sample mixed with AMUPol at a molar ratio of 1:15 (PA:protein) under static conditions at elevated temperatures and magnetic field strength of 9.4 T (yellow circles). To obtain the T_1 values, the relaxation data of H6- τ and M35 fibrillar samples were fitted with a stretched exponential and the relaxation data of the L34 sample and the quadrupolar order relaxation data were fitted with a monoexponential function. The T_1 data at 17.6 T were first published and taken from references [89, 128].

In order to measure the dynamics of the selectively deuterated methyl groups in the three A β ₁₋₄₀ fibril samples, $T_1(^2\text{H})$ relaxation time constants were measured between 110 and 152 K by the Torchia method^[91] to benefit from the sensitivity gain provided by DNP. The Torchia method uses a polarization decay scheme and consists of an initial ^1H - ^2H CP polarization transfer followed by a z-filter block with variable delay times to measure the time-dependent polarization decay on ^2H . The resulting polarization decay were fitted either to a stretched exponential function in the case of the A β fibrils with either the H6- τ or the M35 label, or to a monoexponential function for the L34 label yielding the $T_1(^2\text{H})$ relaxation time constants (Figure 28, green circles) and the stretching factor β in the case of the stretched exponential function (Appendix Figure A 8).

To assess the potential of using the matrix-free DNP approach for the investigation of dynamics at low temperature, the relaxation data of the three A β ₁₋₄₀ samples obtained by DNP-enhanced ^1H - ^2H CPMAS experiments were compared to direct ^2H excitation experiments, with and without added PA. First, to validate the $T_1(^2\text{H})$ data obtained with the Torchia method, the ^2H relaxation time constants of the selectively deuterated methyl group in the L34 and M35 label were additionally measured with an inversion recovery experiment using direct ^2H detection. No significant difference is visible for the obtained $T_1(^2\text{H})$ time constants indicating that the CP transfer step is not interfering with the spin-lattice relaxation (Appendix Figure A 9).

Next, the $T_1(^2\text{H})$ relaxation time constants obtained by ^1H - ^2H CPMAS were compared to published relaxation data measured with static, low-temperature ^2H NMR and without a PA. For the A β ₁₋₄₀ fibril sample with the L34 label, T_1 relaxation time constants were additionally measured at elevated temperatures by static solid-state NMR. No difference is observed between the A β fibrils with and without PA at elevated temperatures suggesting (Figure 28, L34, violet and yellow circles). Interestingly, a systematic deviation to shorter values is visible for the relaxation time constants as well as the stretching factor β obtained by DNP-enhanced ^1H - ^2H CPMAS with the values reported in the literature at low temperatures (Figure 28, green and violet circles, Appendix Figure A 10). This deviation is most strikingly in the case of the L34 label, where the T_1 time constant differs by one order of magnitude (Figure 28, L34, green and violet circles). To rule out an effect only visible in A β fibrils, further model proteins with known $T_1(^2\text{H})$ relaxation time constants and methyl group dynamics at a temperature range between 100 and 160 K were measured with the matrix-free DNP approach. The selectively deuterated methyl group in either L63 or L69 of the chicken villin headpiece subdomain protein

(HP36)^[64, 68, 130] and the $-\text{CD}_3$ group of methionine in the short disordered peptide RC9 (GGKG[M- CD_3]GFGL)^[131] present additional examples of the systematic deviations towards shorter T_1 relaxation time constants with the matrix-free DNP approach (Appendix Figure A 11 & A 12). The same trend is also visible for the quadrupolar order relaxation time constants T_{1Q} of the M35 label which were measured with a modified Jeener-Broekart sequence^[132] and again compared to T_{1Q} values reported for the $\text{A}\beta_{1-40}$ -M35- CD_3 sample in the literature (Figure 28).^[128]

These systematic deviations caused by the matrix-free DNP approach can be categorized into two classes: (1) a slight but significant change of the negative slope resulting in a shift towards slower relaxation time constants which is visible for the H6- τ and the M35 labeling position, and (2) a strong change of more than one order of magnitude causing a stark flattening of the measured T_1 values instead of the expected positive slope for this temperatures, which is seen for the L34 methyl label. For the first category, a small deviation is expected near the coalescence temperature (*i.e.* near the minimum of the T_1 curve) due to the difference in the magnetic field of the DNP data from this study and the static NMR data reported in the literature (*cf.* 9.4 T and 17.6 T, respectively). This is further supported by the fact that no deviations are visible for the $T_1(^2\text{H})$ relaxation time constants measured under static conditions with AMUPol at 9.4 T and without AMUPol at 17.6 T at elevated temperatures, where the methyl group of the L34 label is known to be in the magnetic field-independent extreme narrowing limit of the three-site jump model (Figure 28, L34, violet and yellow). A further possible explanation of this slight deviation could be sample heating caused by microwave irradiation causing a horizontal shift of the relaxation time constants measured with the matrix-free DNP approach. This anticipated and in the literature reported effect^[133] was corrected by calibrating the PT100 temperature sensor inside the probe with a separate measurement series of the $T_1(^{79}\text{Br})$ at a temperature range between 100 and 160 K as proposed by Thurber and Tycko as well as Miéville *et al.*^[92] (Appendix Figure A 13). It is possible that the temperature calibration is not entirely correct, resulting in a discrepancy between the actual temperature and the recorded temperature of the measured protein samples, due to the slightly different dielectric properties of the samples. This is additionally supported by a recent publication reporting temperature hotspots throughout the sample in the rotor caused by microwave irradiation.^[134] In contrast to the protein samples of this study, such extreme and uneven microwave heating was shown so far only for ferroelectric materials which have tremendously higher dielectric loss tangents than proteins. Because the KBr powder and the protein powder should have a comparable thermal

coupling to the rotor wall, the temperature calibration is most likely sufficient and a large deviation between the recorded temperature and the actual temperature of the A β fibrils is unlikely.

The above discussed explanations for the deviation in T_1 relaxation time constants between the measured and reported values can only explain the small deviations visible for the H6- τ and the M35 label, but not the stark flattening of the T_1 curve as seen for the methyl group in the A β_{1-40} -L34 fibril sample (Figure 28, green circles) and the two leucine residues in the HP36 protein (Appendix Figure A 11). The only remaining effect which can explain this strong deviation is the doping of the analyte with the PA. This doping significantly accelerates the nuclear relaxation via paramagnetic interactions being a similar process as in PRE. Additionally, the variation in strength of the PRE-like effect—small contribution for the H6- τ and M35 label and a stark deviation with over one order of magnitude for the L34 label—suggests a modulation of this effect by the methyl group dynamics. These dynamics and the respective models to describe them are known due to prior measurements: a three-site jump model in the case of the H6- τ and L34 label, whereas the methyl group in M35 experiences additional rotameric interconversions to the three-site jumps.^[10e, 89] Interestingly, the transitions from the fast to the intermediate exchange regime for the H6- τ and M35 label are expected to be between 155 and 100 K or even below due to the missing transition down to 160 K of the literature data. In contrast, the methyl group dynamics of the L34 label transitions at a temperature above 155 K and thus is already in the intermediate to slow exchange regime at the temperature range tested with the matrix-free DNP approach. This furthermore explains the lower relative sensitivity of the L34 label as compared to the other two A β samples (Figure 27). Taken together, the strong visible PRE-like behavior and the slow dynamics in the L34 label and the rather minor deviation between doped and undoped $T_1(^2\text{H})$ relaxation time constants and fast dynamics in the case of the H6- τ and M35 label suggests a scaling of the paramagnetic interaction between the electron and the ^2H nuclei by the dynamics of the $-\text{CD}_3$ groups: fast methyl group dynamics result in a low and slow dynamics in a strong contribution of the PRE-like behavior. A negligible impact of the electron spin-nuclear spin distance on the strength of the paramagnetic interaction is observable because the L34 label, which has the highest distance due to its position inside the hydrophobic core, experiences the strongest PRE-like effect. Nonetheless, the impact of the protonated methyl groups in the protein and if higher MAS frequencies relay the paramagnetic interaction remains unclear.

In summary, this section proves the advantage of the matrix-free DNP approach to investigate the dynamics of insoluble biomolecules such as A β ₁₋₄₀ fibrils by employing ¹H–²H CPMAS experiments. The DNP-enhanced ¹H–²H CPMAS experiments yield favorable relative sensitivity gains as compared to ²H MAS experiments accelerating the acquisition of $T_1(^2\text{H})$ relaxation time constants by a factor of up to 400. Here, a reduction in the relative sensitivity gain can be reasoned with the number of adjacent protonated mobile side chains, most likely by interfering with DNP polarization build-up and/or CP transfer. By employing the Torchia method, which uses a CP transfer instead of direct excitation, the high relative sensitivity gain can be transferred without changing the obtained $T_1(^2\text{H})$ relaxation time constants. Finally, the section shows that the doping of the sample with a PA introduces a PRE-like effect, which is further modulated by the methyl group dynamics. In total, this proves the necessity for a better model describing the paramagnetic relaxation present in DNP samples in order to study molecular dynamics under DNP conditions. The next section systematically investigates the paramagnetic relaxation using selectively deuterated ethanol as a model system.

4.3.2 Systematic investigation of methyl group dynamics under DNP conditions

The measurement of relaxation data and therefrom obtained information about molecular dynamics is a valuable tool, however, Section 4.3.1 has demonstrated that it becomes complex under DNP conditions. Here, paramagnetic interactions between the nucleus of the mobile site and the electron spin of the required PA strongly impacts the relaxation and thus increases the complexity of the analysis. In order to establish an approach for measuring molecular dynamics, selectively deuterated methyl groups were chosen which can easily be described by simple motion models due to the high mobility of methyl groups in respect to other functional groups even at low temperatures, decreasing the molecular complexity of the system. Additionally, as shown in Section 3.3.1, the scaling of the quadrupolar interaction with values between 125 kHz to 200 kHz by a factor of $\frac{1}{3}$ due to the reorientation dynamics of the methyl group^[79b] is advantageous for employing ¹H–²H CPMAS experiments as a lower bandwidth is sufficient for full excitation of the spectral width determined by the scaled quadrupolar interaction. To test the applicability of this approach, ¹H–²H CPMAS experiments were recorded for ethanol–d₆ and ethanol–d₃ at 5 kHz MAS frequency and 102 K which were both mixed with glycerol and water to yield a solution of 50:20:30 vol-% glycerol:H₂O:ethanol (Figure 29, green).

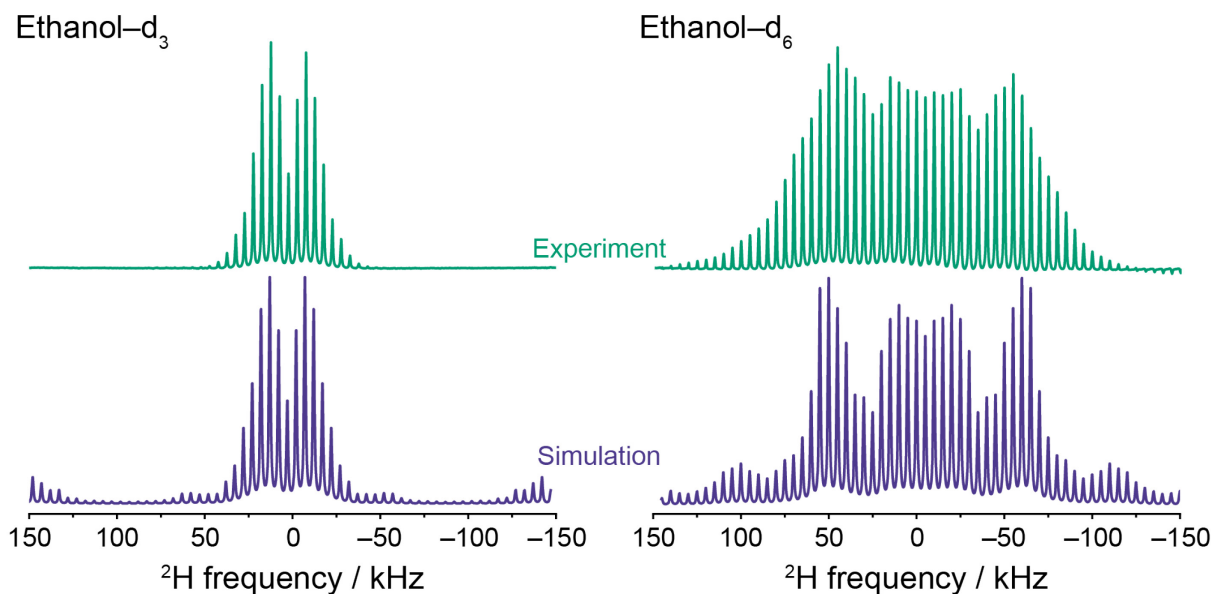


Figure 29: ^1H - ^2H CPMAS spectra (green) of 30 vol-% ethanol- d_3 or 30 vol-% ethanol- d_6 mixed with 2.5 mM AMUPol, 50 vol-% glycerol, and 20 -% deuterium-depleted water at 5 kHz MAS frequency and 102 K and fitting *NMR Weblab* simulations (violet).

Both spectra resemble a different breadth of the quadrupolar interaction, where the selectively deuterated ethanol yields a lower linewidth than the uniformly deuterated ethanol. In addition, the spectra of the uniformly deuterated ethanol is more complex due to the missing chemical shift resolution of ^2H . A possibility to introduce chemical shift resolution is by using 2D ^{13}C - ^2H or even higher dimensional correlation spectra as shown in several publications.^[124g, 135] Nonetheless, this requires isotope labeling and a 2D experiment with longer experimental times than 1D experiments and the other ^2H labels provide no useful information if only interested in the molecular dynamics of methyl groups. Additionally, it was shown that further ^2H labels within the sample influences the $T_1(^2\text{H})$ relaxation time constant of the $-\text{CD}_3$ group by ^2H - ^2H spin diffusion.^[135a] Nonetheless, these experiments can be valuable for future experiments in order to describe the molecular dynamics of amino acid side chains and/or other model systems.

Because the side bands are not representative of the actual quadrupolar interaction, ^2H NMR simulations were performed with the *NMR Weblab* interface^[67] (Figure 29, violet) using the cone model to describe the chemical/dynamical exchange of the ^2H nuclei. Using a MAS frequency of 5 kHz of, a static quadrupolar coupling $\omega_{q,0}/2\pi = 128$ kHz, and an exchange interaction which is described by a two-site exchange of 3 sites (*cf.* Verweis Introduction), both in the fast exchange regime, a rather good fit of ethanol- d_3 sample was found. The ^1H - ^2H CPMAS of the ethanol- d_3 sample in the fast exchange regime has an effective quadrupolar coupling constant of (*cf.* Equation 33):

$$C_{q,\text{eff}} = S^2 C_q \approx \frac{1}{3} \cdot 128 \text{ kHz} = 42.67 \text{ kHz}. \quad (41)$$

Here, S^2 is the order parameter of the molecular motion being equal to $\frac{1}{3}$ for a methyl group reorientation, and C_q the quadrupolar coupling constant determined to 128 kHz. Thus, the excitation bandwidth of a ^1H - ^2H CPMAS experiment will be sufficient as elucidated in the previous section.

The spectrum of ethanol- d_6 was fitted with two simulations and summed up: (1) a 2-site exchange in the slow exchange regime representing the deuterated methylene group, and (2) the same simulation used to describe the spectrum of ethanol- d_3 . The $-\text{OD}$ group was not simulated due to its chemical exchange with water and the $-\text{OH}$ groups of the glycerol which happened during the sample preparation at room temperature. Because the $-\text{OD}$ group can experience four different chemical environments (water, deuterated primary alcohol group and deuterated secondary alcohol group of glycerol, and alcohol group of ethanol), the quadrupolar coupling constant will vary, rendering a simulation of the $-\text{OD}$ group impractical for the scope of this chapter.

Next, the ^1H DNP properties were investigated in order to assess a potential sensitivity enhancement of ^2H nuclei by ^1H - ^2H CPMAS experiments. Here, the most important parameters are: (1) the sensitivity enhancement per unit time ($\epsilon T_B^{-1/2}$) by DNP, and (2) the relative sensitivity gain of DNP-enhanced ^1H - ^2H CPMAS experiments over ^2H MAS experiments with a direct excitation scheme. The first parameter was determined for different AMUPol concentrations (1 to 10 mM) at 102 K as well as for different temperatures (Appendix Table A 24, Appendix Figure A 14, and Appendix Table A 25). The obtained ^1H DNP enhancement factors are very high for all tested AMUPol concentrations, even exceeding the theoretically achievable enhancement factor of 658. The reasons for these large enhancement factors are two-fold: (1) rotation-induced depolarization which was not taken into account for the microwave off spectra and more important (2) the increase of temperature induced by microwave heating causes a transition from the slow/intermediate exchange regime to a fast exchange regime, resulting in narrower and more intense signals for the microwave on spectrum (Appendix Figure A 15). The ^1H DNP build-up time constants are decreasing from 7.84 s down to 2.93 s with increasing AMUPol concentrations which is expected due to more AMUPol molecules polarizing the constant ^1H bath concentration of ~ 92 M. Taken together, the highest relative sensitivity enhancement per unit time ($\epsilon T_B^{-1/2}$) by DNP is observed for the sample containing 5 mM AMUPol, which is followed by the sample with 10 mM AMUPol.

With increasing temperature, no significant difference is observed for the ^1H DNP build-up time constants being at a constant value of ~ 3 s, whereas the ^1H DNP enhancement factors are decreasing with increasing temperatures and thus, the sensitivity enhancement by DNP. Here, the relative sensitivity enhancement per unit time by DNP increases slightly from $355\text{ s}^{-1/2}$ at 102 K to $460\text{ s}^{-1/2}$ at 118 K and decreases to $23\text{ s}^{-1/2}$ at 155 K. The overall decrease in the ^1H DNP enhancement factor and relative sensitivity enhancement with elevated temperatures is expected due to lower DNP efficiency at high temperatures. On the contrary, the highest sensitivity enhancement value was obtained at a temperature of 118 K which is caused by the temperature activation of the methyl group dynamics resulting in narrower linewidths, especially for the microwave off spectra reflecting the linewidth of $-\text{CD}_3$ group in the intermediate or slow exchange regime at the lowest temperature of 102 K. This visible transition from the fast to the intermediate or slow exchange regime furthermore explains the very large enhancement factors observed at this temperature. Here, the sample heating caused by the microwave irradiation causes the transition in exchange regimes resulting in narrower linewidths and thus higher signal intensities in the microwave on spectrum than observed in the microwave off spectrum. This anticipated effect of sample heating (Section 4.3.1) was monitored for the analysis with finely grounded KBr powder placed at the bottom of the rotor (*vide infra*).

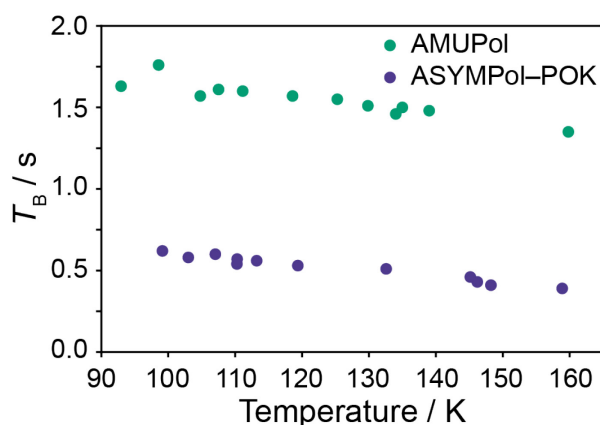


Figure 30: ^1H DNP build-up time constants of 30 vol-% ethanol- d_3 mixed with 50 vol-% glycerol, 20 vol-% deuterium-depleted water and either 10 mM AMUPol (green) or 10 mM ASYMPol-POK (violet) at varying temperatures and 15 kHz MAS frequency.

To optimize the sensitivity enhancement further, AMUPol as a PA was compared to ASYMPol-POK, where ASYMPol-POK is known to have faster polarization build-up kinetics due to a higher dipolar and J -exchange interaction between the two electron spins which drives the cross-effect polarization transfer rate.^[29, 136] In addition, it was recently reported that ASYMPol-POK significantly outperforms AMUPol in matrices with large ^1H concentrations

as is the case for the investigated samples (*cf.* ~ 92 M ^1H concentration vs. ~ 11 M in a solution of 6:3:1 vol-% glycerol- d_8 : D_2O : H_2O).^[126, 136-137] To test if ASYMPol-POK performs better than AMUPol in this case, 10 mM AMUPol is compared to 10 mM ASYMPol-POK—each mixed with 30 vol-% ethanol- d_3 , 50 vol-% glycerol, and 20 vol-% deuterium-depleted water—at temperatures between 93 K to 160 K. Due to the low signal in the microwave off spectra, it was not feasible to determine ^1H DNP enhancement factors for these two samples measured at 15 kHz MAS frequency. Nonetheless, it can be assumed that the enhancement factors will be similar to the values obtained for the sample with 10 mM AMUPol at 5 kHz MAS frequency. The ^1H DNP build-up time constant of the sample with AMUPol is determined to be ~ 1.6 s at 100 K and 15 kHz MAS frequency, decreasing slightly with increasing temperatures to a value of ~ 1.5 s at 160 K. In contrast, the sample with 10 mM ASYMPol-POK has a build-up time constant of ~ 0.6 s at 100 K, displaying the same temperature trend as the sample with AMUPol with a final value of 0.5 s at 160 K. In comparison to 5 kHz MAS frequency, the values obtained for the sample with AMUPol displays significantly faster build-up time constants, resulting in even larger relative sensitivity gain per unit time ($\epsilon T_{\text{B}}^{-1/2}$) for, most likely, both PAs if the assumption about similar enhancement factors is valid. In addition, the significantly faster build-up time constant is expected for ASYMPol-POK as PA (see above), but it is surprising for AMUPol. Here, the differences between the samples lie in: (1) the sample preparation, (2) the MAS frequency, and (3) the probe used to acquire the experiments:

(1) The ethanol- d_3 sample preparation at 5 kHz MAS frequency involved mixing of all the stock solutions (ethanol- d_3 , glycerol, deionized water, and 10 mM AMUPol) and the transfer into a 3.2 mm sapphire rotor without further treatment. In the case of 15 kHz MAS frequency, the sample was mixed and degassed using the freeze-thaw-pump protocol after preparation of the sample solution, but before transferring into a 1.3 mm zirconia rotor. Surprisingly, the observed decrease of the ^1H DNP build-up time constants with removal of paramagnetic oxygen is in contrast to the expected trend: decreased ^1H DNP build-up rate constants and thus longer time constants as the oxygen acts as a paramagnetic relaxation source for nuclear relaxation (*cf.* Equation 4).

(2) A higher MAS frequency has a multi-fold impact on the build-up time constants: Firstly, it enables, in theory, more occurrences of level anti crossings (LAC), however, with each lower adiabaticity resulting in a smaller transfer of polarization during one event. To a good approximation, this should result in a net value of the same amplitude after one rotor

period. Secondly, higher MAS frequencies can induce different sample temperatures, where high temperatures yield lower build-up time constants due to faster nuclear relaxation. The second case is negligible as it requires a large temperature difference for a minimal change (*cf.* temperature series of the sample, Appendix Figure A 14B and Appendix Table A 25), which was not observed with the KBr temperature monitoring performed as described in the literature.^[92] Additionally, systematic investigations of ^1H DNP build-up time constants obtained either for an aqueous sample with AMUPol^[138] or for a TEKPol/TCE (1,1,2,2-tetrachloroethane)^[139] solution have shown an increase in build-up time constants with increasing MAS frequency. Thirdly, spin diffusion is attenuated with increasing MAS frequency, resulting in higher ^1H DNP build-up time constants.

(3) Different probes were used to acquire the data at 5 kHz and 15 kHz MAS frequency are different (*viz.* 3.2 mm and 1.3 mm LTMAS probe, respectively). The main difference besides the rotor diameter and different quality factors of the electronics is the better focal point of the microwaves in the 1.3 mm probe resulting in a broader $B_{1,e}$ irradiation throughout the sample^[140] and thus more efficient polarization build-up kinetics. It has to be noted that for a detailed discussion of this decrease in build-up time constants more tested MAS frequencies are necessary.

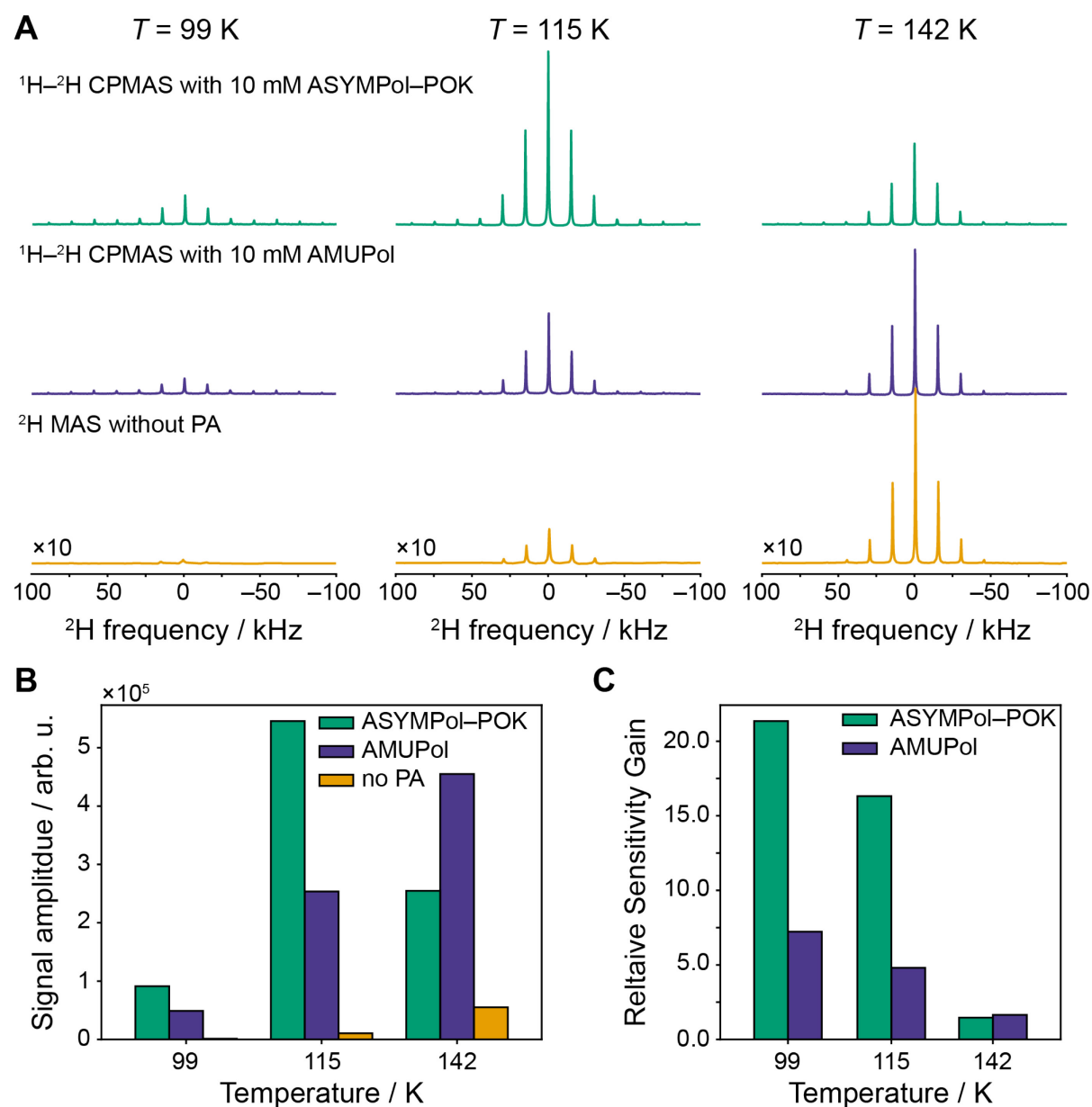


Figure 31: ^1H - ^2H CPMAS spectra (green and violet) and ^2H MAS spectra (yellow) of 30 vol-% ethanol- d_3 mixed with 50 vol-% glycerol, 20 vol-% deuterium-depleted water and either 10 mM ASYMPol-POK (green), 10 mM AMUPol (violet), or no PA (yellow) at 15 kHz MAS frequency and varying temperatures (A) the corresponding signal amplitude of the spectra (B), and the relative sensitivity gain of the ^1H - ^2H CPMAS experiments over the ^2H MAS experiments (C). (A) The spectra were all normalized to the same intensity scale and to the number of accumulated transients and are scaled by a factor of ten if given at the left side of the spectrum for better visibility of the signal. (B) The signal amplitudes of the most intense band being the center band were normalized to the number of accumulated transients. In the case of the sample without PA at 99 K, the bar height is within the line of the plot. (C) The relative sensitivity gains, being the ratio of the ^1H - ^2H CPMAS spectra and the ^2H MAS spectra, were further normalized to the square root of the applied repetition delay. All determined signal amplitudes and relative sensitivity gains are summarized in Appendix Table A 26 and A 27.

Next, the relative sensitivity gain of DNP-enhanced ^1H - ^2H CPMAS experiments over ^2H MAS solid-state NMR experiments is quantified as performed for the selectively deuterated A β_{1-40} fibrils (Section 4.3.1). Therefore, ^1H - ^2H CPMAS spectra of 30 vol-% ethanol- d_3 mixed

with 50 vol-% glycerol, 20 vol-% deuterium-depleted water and either 10 mM ASYMPol-POK or 10 mM AMUPol and the ^2H MAS spectra of the same sample constitution, but without PA were acquired at three different temperatures between 99 K and 142 K (Figure 31A). To calculate the relative sensitivity gain, the signal amplitudes and the RMS of the experiment noise were determined. No significant difference is observed for the experimental noise (Appendix Table A 28), however, as already observed in Section 4.3.1, small variations in the baseline correction result in a large statistical error of the derived SNR ratio and therefrom derived relative sensitivity gains. As a result, the transient-normalized signal amplitudes of the center band in the ^2H spectra which are shown in Figure 31A are deemed as a more reliable and less error-prone measure (Figure 31B). Here, rather small signal amplitudes are observed for the ^2H MAS spectra of ethanol- d_3 without any PA at all temperatures. On the contrary, the DNP-enhanced ^1H - ^2H CPMAS spectra yield significantly higher signal amplitudes at all temperatures for both PAs. The highest signal amplitude for the ASYMPol-POK sample is obtained at 115 K, whereas the sample with AMUPol reaches its maximum signal amplitude at the highest temperature. A maximum signal intensity is expected for ethanol at a temperature of ~ 120 K as it was also observed in ^1H - ^{19}F CPMAS experiments for $-\text{CF}_3$ groups selectively fluorinated ethanol.^[133b] The increase in signal amplitude for the sample with AMUPol, on the other hand, is surprising as the DNP signal enhancement requires a rigid, dipolar spin network; this rigidity is absent at elevated temperature for samples in glycerol:water mixtures.^[40-41] This requirement is visible for the ^1H DNP enhancement factors, which significantly drops at ~ 155 K (*cf.* Appendix Table A 25) suggesting a possible steady increase in transient-normalized signal amplitudes for the sample with AMUPol until this point. Rotation-induced depolarization effects—known to be strong for AMUPol and completely absent for ASYMPol-POK at 100 K—could additionally decrease in strength with increasing temperatures, potentially contributing to the steady increase in signal amplitudes for the sample with AMUPol.

The signal amplitudes were used for the calculation of the relative sensitivity gain of DNP-enhanced ^1H - ^2H CPMAS experiments of doped ethanol- d_3 with ^2H MAS experiments of undoped ethanol- d_3 . To account for different experimental repetition delays—1 s for the ^1H - ^2H CPMAS experiments of the sample with ASYMPol-POK, 2.5 s for the sample with AMUPol, and 0.1 s for the ^2H MAS experiments—the signal amplitudes were divided by the square root of the repetition delay before the relative sensitivity gain was calculated (Figure 31C). For both PAs, a relative sensitivity gain greater than 1 is observed for all

temperatures which is decreasing from 21 and 7 at 99 K to 1.5 and 1.7 at 142 K for the sample with 10 mM ASYMPol-POK and AMUPol, respectively. In comparison, the gain of the sample with ASYMPol-POK is a factor of ~ 3 higher than for the sample with AMUPol which is caused by the slightly higher signal amplitudes, and the 2.5-fold faster repetition delay used for the acquisition of the experiments due to the very fast ^1H DNP build-up time constant of ~ 0.6 s. Additionally, the missing depolarization effects for ASYMPol-POK in comparison to AMUPol could contribute to the 3-fold higher relative sensitivity gain as well. This is further supported by the similar values observed for the elevated temperatures (*cf.* 1.5 and 1.7 at 142 K for ASYMPol-POK and AMUPol, respectively).

Due to the temperature-induced activation of the methyl group dynamics and therefrom resulting increase of signal amplitude, the higher signal amplitudes observed for the ^1H - ^2H CPMAS experiments at 115 K for ASYMPol-POK and 142 K for AMUPol is relativized due to a similar increase in signal amplitude in the ^2H MAS spectra. The increase of signal amplitudes in the ^2H MAS spectra due to narrower ^2H line widths results in almost no relative sensitivity gain at 142 K—values of 1.5 and 1.7 were determined for the sample with ASYMPol-POK and AMUPol, respectively—highlighting the break-even point of the ^1H - ^2H CPMAS approach for the investigation of dynamics with ^2H NMR. Nonetheless, in the temperature range commonly used for MAS DNP experiments in glycerol:water mixtures, an acceleration of experiments to study molecular dynamics of up to 400-fold can be expected aiding tremendously in the acquisition of data with low signal due to the broadening of the ^2H line widths caused by the broadening at the transition from the fast exchange to the intermediate/slow exchange regime. Additionally, it was shown that trehalose-^[40] or sorbitol-based^[41] DNP sample preparation approaches result in rather good ^1H DNP enhancement factor at $T > 200$ K broadening the possible temperature range of the DNP-enhanced ^1H - ^2H CPMAS approach to investigate molecular dynamics.

The high relative sensitivity gains of DNP-enhanced ^1H - ^2H CPMAS experiments significantly accelerates the data acquisition for the analysis of the methyl group dynamics in selectively deuterated ethanol. To examine the PRE-like behavior—seen for ^2H relaxation time constants of the selectively deuterated methyl groups in $\text{A}\beta_{1-40}$ fibrils in Section 4.3.1 (Figure 28)—in more detail and in frozen solution, ^2H spin-lattice relaxation time constants were determined with the Torchia method^[91] for ethanol- d_3 with various sample constitutions in a temperature range from 100 K to 160 K. The polarization decay is fitted with a stretched exponential function (Equation 39) to yield the $T_1(^2\text{H})$ relaxation time constant and the

stretching factor β . Here, the initial inverse slope of the polarization decay is most sensitive to the fast-relaxing component being described by the $T_1(^2\text{H})$ relaxation time constant of the stretched exponential distribution, whereas the slow-relaxing component of the polarization decay is best characterized by the mean value of the stretched exponential distribution $T_{1,\text{avg}}(^2\text{H})$ which correlates the relaxation rate constant with the stretching factor β (Equation 40).

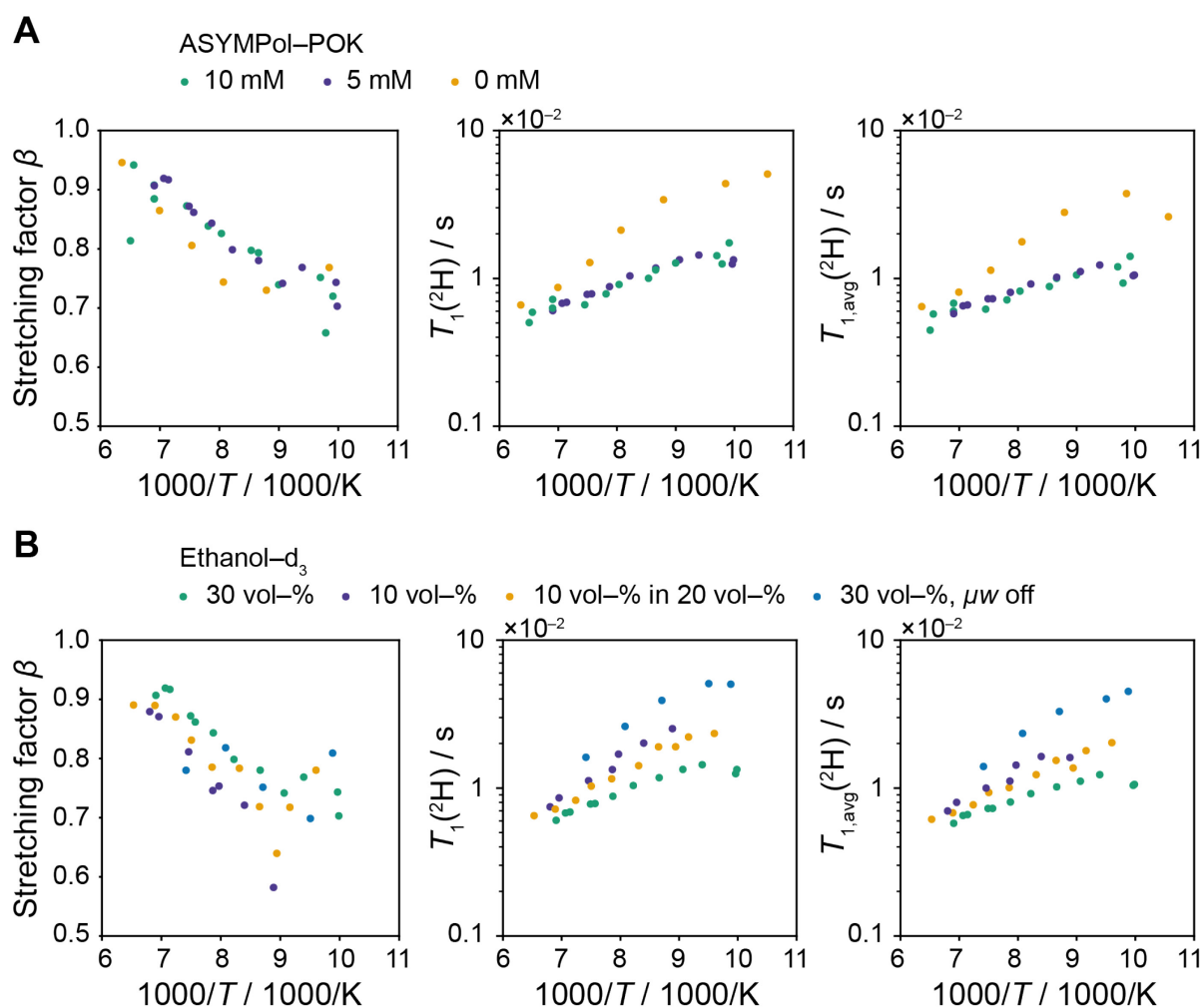


Figure 32: Stretching factor β , ^2H spin-lattice relaxation time constant $T_1(^2\text{H})$, and mean ^2H spin-lattice relaxation time constant $T_{1,\text{avg}}(^2\text{H})$ of either 30 vol-% ethanol-d₃ mixed with varying amounts of ASYMPol-POK (A) or different volume percentages of ethanol-d₃ mixed with a concentration of 5 mM ASYMPol-POK (B). (A) Ethanol-d₃ is mixed with 50 vol-% glycerol and 20 vol-% deuterium-depleted water and varying amounts of ASYMPol-POK. (B) The samples consist of varying amounts of ethanol-d₃ in 50 vol-% glycerol, varying amounts of deuterium-depleted water, and 5 mM ASYMPol-POK. The yellow data series with the annotation “10 vol-% in 20 vol-%” represents a sample which contains 10 vol-% ethanol-d₃, 20 vol-% ethanol-h₃, 50 vol-% glycerol, and 20 vol-% deuterium-depleted water with 5 mM ASYMPol-POK. All relaxation data were obtained at varying temperatures and 15 kHz MAS frequency using either ^1H - ^2H CPMAS for all series, except the data series with 0 mM ASYMPol-POK (A) and 30 vol-% ethanol-d₃ without microwave irradiation (μw off) (B).

For a systematic investigation of methyl dynamics under DNP conditions, several parameters with a possible influence on the analysis of relaxation rates have to be considered and subsequently checked: (1) the applied MAS frequency, possibly interfering with the analysis; (2) the type of PA and thus the strength of the HFI interaction which is responsible for the PRE-like effect; and (3) the distance between electron spin and ^2H nucleus, modulating the strength of the PRE-like effect with a factor of r^{-6} .

(1) To assess a potential influence of the MAS frequency on the relaxation time constants, the β factor as well as the $T_1(^2\text{H})$ time constant and the average $T_1(^2\text{H})$ value were obtained for 30 vol-% ethanol- d_3 and 10 mM AMUPol in 50 vol-% glycerol and 20 vol-% deuterium-depleted water at 5 kHz and 15 kHz MAS frequency (Appendix Figure A 16A). No significant difference between both PAs for the T_1 values and a trend towards faster relaxation within each PA series with increasing temperature is observed suggesting that the MAS frequency has no or only a marginal influence on the spin-lattice relaxation. Additionally, the minimum of the $T_1(^2\text{H})$ curve is at a temperature larger than ~ 150 K and thus displaying a similar curve as L34 in $\text{A}\beta_{1-40}$ fibrils (*vide supra*).

(2) As different PAs have different strengths of HFI interaction and different relaxation properties of the electron, the influence of the type of PA is tested. Here, the ^2H relaxation time constants were measured for ethanol- d_3 mixed with either 10 mM AMUPol or 10 mM ASYMPol-POK (Appendix Figure A 16B). Surprisingly, no discrepancy in the T_1 values is observed at all temperatures indicating a negligible influence of either the strength of the PA's HFI interaction with ^2H , the electron relaxation parameters, or both, under the tested conditions. As it was not possible to determine the relaxation time constants $T_{1,e}$ and $T_{2,e}$ of the electron due to the missing hardware in Rostock, the contribution of these parameters cannot be determined fully. Additionally, this also renders a quantitative analysis of the PRE-like effect impossible; as a consequence the PRE-like effect will be qualitatively assessed in the following part.

(3) To reduce the strength of the paramagnetic interaction on the ^2H nuclei, the amount of ASYMPol-POK is decreased from 10 mM to 5 mM, thereby increasing the average distance between the electron spin and the ^2H nuclei in theory and thus attenuating the PRE-like effect (Figure 32A). No significant difference is observed in the β factors, the $T_1(^2\text{H})$ values, and therefrom derived $T_{1,\text{avg}}(^2\text{H})$ values suggesting that either the PRE-like effect either shows an asymptotic behavior as the average distance is still low or is non-present under the tested conditions with 5 mM and 10 mM PA. To test the latter, the same ethanol- d_3 sample without

PA is prepared and measured which shows an increase in T_1 values—with and without microwave irradiation—indicating that a PRE-like effect is observed for the samples with PA (Figure 32A, yellow and Appendix Figure A 17A). Surprisingly, the ethanol- d_3 sample with 5 mM ASYMPol-POK in the presence and absence of microwave irradiation is not displaying the same PRE-like behavior (*cf.* Figure 32B, violet and 17A, yellow). Here, similar $T_1(^2\text{H})$ relaxation constants and β factors of the PA-doped sample are observed in the absence of microwave irradiation as the PA-undoped samples, yielding a stark discrepancy in the $T_1(^2\text{H})$ relaxation constants of about half an order of magnitude. This discrepancy could suggest an inactive PRE-like effect if the microwave irradiation is turned off. However, as the HFI interaction is an intrinsic electron spin-nuclear spin interaction, the reasons have to be one of the following: microwave-induced sample heating and/or the method of excitation/acquisition of the spectra (*vide infra*). The contribution of these two factors will be discussed below.

To test the observed asymptotic behavior of the PRE-like behavior, the ethanol- d_3 concentration was decreased from 30 vol-% (5.14 M) over 10 vol-% (1.72 M) to 5 vol-% (0.86 M) with a constant PA concentration of 5 mM (Figure 32B and Appendix Figure 17B). Here, the decrease in ethanol- d_3 concentration from 30 vol-% to 10 vol-% displays a linear trend, where the β values are decreasing and the $T_1(^2\text{H})$ values and the $T_{1,\text{avg}}(^2\text{H})$ values are increasing slightly with decreasing ethanol- d_3 concentration. Surprisingly, a further decrease from 10 vol-% to 5 vol-% has no effect on the observed relaxation values as both display the same slope from 20 ms to 6 ms between ~ 100 K and ~ 150 K (Appendix Figure A 17B, yellow and blue). To exclude a potential change of the matrix morphology caused by the exchange of ethanol- d_3 with H_2O , the deuteration level of ethanol was decreased without changing the ethanol concentration by creating a mixture containing 10 vol-% ethanol- d_3 and 20 vol-% ethanol- h_3 . The obtained relaxation data of this sample shows a similar trend with increasing temperatures to the 10 vol-% ethanol- d_3 in glycerol:water, but differs slightly in individual values. Both samples (*viz.* the mixture and the pure 10 vol-% ethanol- d_3 sample) show a similarly strong deviation to the 30 vol-% sample indicating a minor contribution of the different sample constitutions

In order to summarize the obtained spin-lattice relaxation data, the displayed anticipated and unanticipated effects besides the sought-after PRE-like effect are categorized: (1) microwave heating, (2) filtering of select $-\text{CD}_3$ “hotspots”, and (3) change of the matrix morphology as is explained as follows:.

(1) As the actual temperature was monitored with a KBr pellet at the bottom of the rotor (see Section 3.3.1 for a detailed discussion on this topic), a major shift in observed T_1 values is not expected and may only explain smaller discrepancies as observed for the ethanol sample without PA in presence and absence of microwave irradiation (Appendix Figure A 17A, green and violet).

(2) The filtering of select $-CD_3$ may occur due to the solid-echo detection which was employed in the direct excitation experiment to reduce baseline artifacts. Here, deuterated methyl groups which experience a strong PRE-like effect may have a shortened spin-spin relaxation time constant (T_2), inevitably being suppressed during the echo detection scheme due to the very short T_2 relaxation time constant. Possibly, this filtering effect may be a consequence of a polarization gradient within the sample; therefore, weighting the less polarized methyl groups. The latter is supported by the decrease of the stretching factor β with decreasing ethanol- d_3 concentration emphasizing a broader distribution of distinct T_1 values for the lower ethanol- d_3 concentrations or vice versa, a more uniform distribution for higher concentrations indicating a potential filtering effect in combination with a stronger PRE-like effect. This hypothesis is additionally supported by the measurement of $T_1(^2H)$ relaxation constants of selectively deuterated $A\beta_{1-40}$ fibrils (Section 4.3.1). Here, in contrast to this study, no solid-echo detection was applied, but a PRE-like behavior is detected if direct excitation is chosen to obtain the relaxation time constants.

(3) The change in matrix composition by decreasing the amount of ethanol- d_3 in the sample is affecting the obtained T_1 values only with a minor contribution as outlined above. To exclude any artifacts caused by the matrix morphology, the 2H line shapes, being sensitive to phase transitions of the sample, are compared to each other. Figure 33 illustrates the line shapes for the ethanol- d_3 concentrations of 30-vol%, 10 vol-% mixed with 20 vol-% ethanol- h_3 , and 10 vol-% at 100 K, 115 K, and 150 K. All three samples show different line shapes at the lowest temperature of 100 K. Note that the line shape of the mixed ethanol sample is more characteristic for a methyl group in the slow exchange regime as the spinning side bands at ± 60 kHz—representing the slow exchange contribution—are more intense than the center band, being representative for the fast exchange regime. At 115 K, only the 10 vol-% ethanol- d_3 in the glycerol:water matrix display a different line shape than the other two tested samples. At the highest temperature of 150 K, no difference between the samples is observed anymore and all $-CD_3$ groups are in the fast exchange regime due to the intense center band. These different temperature trends suggest possible differences in the morphology of the matrix;

however, it is surprising that the mixed sample displays a different line shape than the 30 vol-% ethanol-d₃ sample, despite the same sample constitution, differing only in the ²H concentration. For a further analysis of the line shapes, all spectra are fitted with numerical simulations performed in the *NMR Weblab* interface.^[67]

For the simulation of the ²H NMR line shapes, a 2-site exchange of a 3-site exchange with a quadrupolar coupling constant of 128 kHz yields the best results for all fitted line shapes, however, the motional exchange regime has to be modified in order to retrieve the respective line shapes of the individual samples: the 30 vol-% ethanol-d₃ sample is in the fast exchange regime, the mixed sample exhibits a superposition of a fast exchange and a slow exchange (70%:30%, respectively), and the 10 vol-% sample purely displays characteristics of a methyl group in the slow exchange. This analysis implies that the dynamics and thus the activation barrier of the methyl reorientation is increasing with decreasing amounts of deuterated ethanol. To test this, quantum-mechanical and molecular dynamics simulations have been performed by Marcel Brandt as part of his Master's thesis.^[141] The quantum-mechanical simulations displayed no concentration-dependent effect on the activation barrier as all tested samples possess an activation barrier of ~14 kJ/mol for the -CD₃ group reorientation. Additionally, no different constitutions are found; note, the simulations are performed until temperatures of ~220 K, as the molecular dynamics simulations are limited to temperature baths, where the equilibration can be obtained within a reasonable time. Nevertheless, the similarity of these three samples in the molecular dynamics simulations agrees well with the observed temperature dependency of the ²H line shapes, which all display a fast exchange regime for temperatures above 130 K. Furthermore, the simulations also reveal a large librational contribution, possibly explaining the good fit of the 2-times-3-site exchange used for the numerical simulations of the ²H line shapes.

No explanation of this concentration-dependent effect can be provided at the time of writing. As the effect is mainly visible for the highest tested ethanol concentrations, a clustering of ethanol molecules in the sample could potentially explain the line shapes. This clustering has already been shown for binary mixtures of ethanol and water and increases with decreasing temperatures;^[142] however, no literature can be found for tertiary mixtures as used in this project. The potential clustering of ethanol can also explain the differences observed for the ²H spin-lattice relaxation time constants, especially those observed for the samples with 30 vol-% ethanol-d₃. Nonetheless, it cannot explain the missing PRE-like behavior of the doped

ethanol sample without microwave irradiation, which is activated as the sample is irradiated with microwaves.

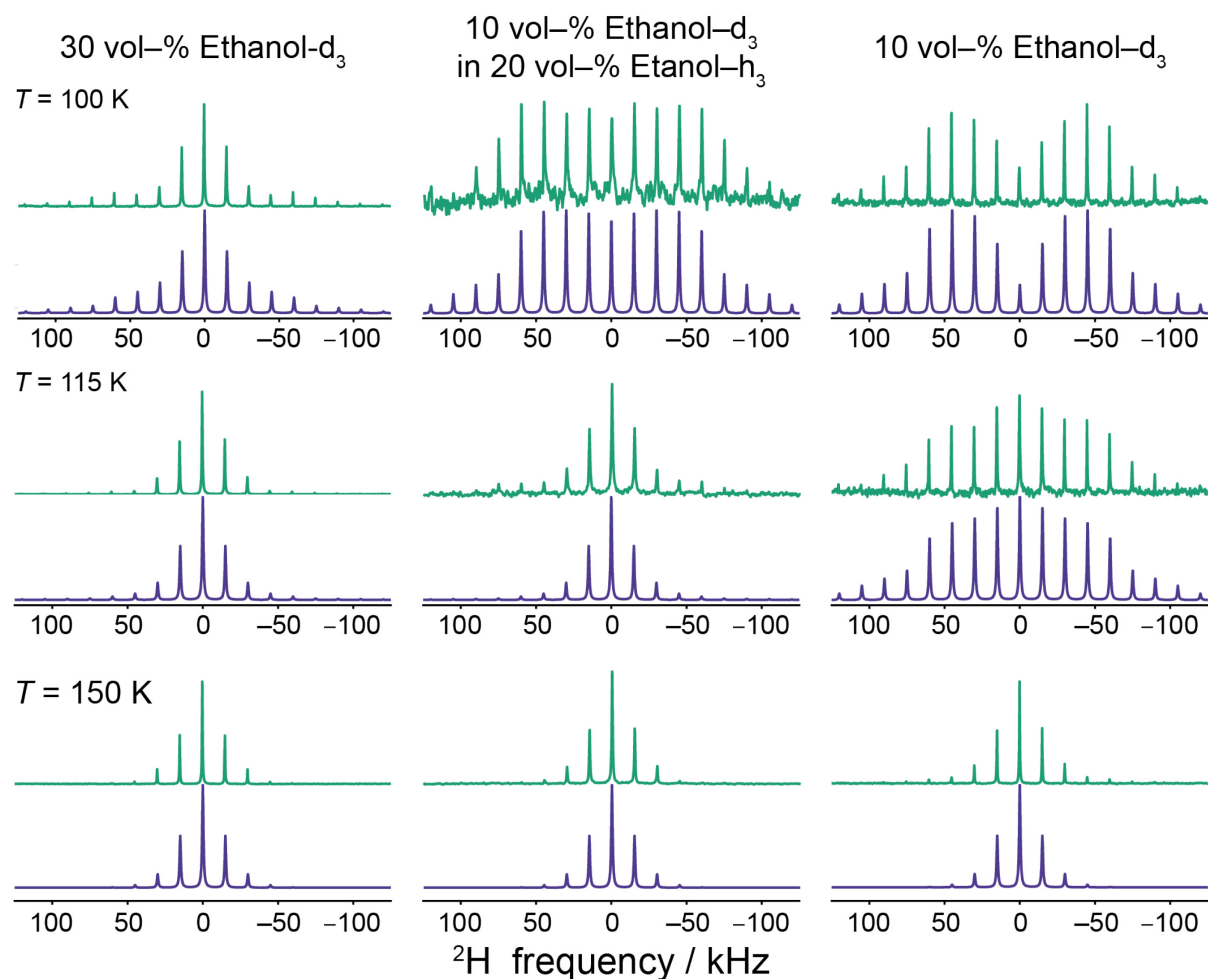


Figure 33: ^1H - ^2H CPMAS experiments (green) and *NMR Weblab* simulations (violet) of three different ethanol- d_3 samples mixed with glycerol, deuterium-depleted water, and 5 mM ASYMPol-POK at temperatures between 100 K and 150 K and 15 kHz MAS frequency. The sample consists of 30 vol-% to 10 vol-% ethanol- d_3 , 50 vol-% glycerol, and 20 vol-% to 40 vol-% deuterium-depleted water. The simulation are performed with the *NMR Weblab* interface.^[67] The spectra were all normalized to the same intensity scale.

In summary, this subsection illustrates the use of selectively deuterated methyl groups in model systems to investigate methyl group dynamics at low temperatures with DNP. Here, DNP provides sufficient sensitivity enhancement as shown by the ^1H DNP enhancement factor, the build-up time constants, therefrom derived relative sensitivities, and relative sensitivity gains, the latter being a comparison to directly excited ^2H MAS experiments. The analysis of the ^2H spin-lattice relaxation time constants at different temperatures reveals a PRE-like effect, however, also displays further unanticipated effects, for example, a filtering of the PRE-like effect by choice of detection method. Moreover, an investigation of the ^2H line shapes reveal further implications with the sample morphology, which shows a ethanol- d_3 concentration-dependent behavior, possibly being a consequence of the high concentrations of up to 5 M,

leading to a potential clustering of ethanol molecules as shown for binary ethanol:water mixtures.

4.3.3 Summary and Conclusion

In this section, molecular dynamics, particularly those of deuterated methyl groups, are investigated by DNP-enhanced ^1H - ^2H CPMAS. Here, two systems, selectively deuterated A β ₁₋₄₀ fibrils with the matrix-free DNP approach and selectively deuterated ethanol- d_3 in glycerol:water mixtures, were investigated. First, the sensitivity advantage of this approach over directly excited ^2H experiments is demonstrated. As a measure, the relative sensitivity gain is introduced, comparing the obtained signal amplitudes per unit time with each other. Here, values of up to 20 are observed transferring into time savings of up to 400-fold for both systems and displaying the strength of the proposed approach. In order to investigate methyl dynamics, $T_1(^2\text{H})$ spin lattice-relaxation time constants are determined and compared to time constants obtained without DNP enhancement. Non-surprisingly, a PRE-like behavior is observed; however, different effects are obtained for the matrix-free and the standard DNP investigation. The first case shows a correlation between strength of the paramagnetic interaction and methyl group mobility. In the second case, a stark flattening of the T_1 curve is not observed, however, different matrix-related effects are visible in the relaxation curve as well as in the line shape analysis. All these effects cannot be explained in detail as comparable studies are missing at the time of writing. This indicates the necessity for future investigations involving relaxation under DNP conditions.

5. Conclusion

This work studied new ways to prepare samples for DNP experiments (Section 4.2) as well as use the sensitivity enhancement by DNP to perform site-specific experiments (Section 4.1) as well as relaxation experiments (Section 4.3). Two of the three aims set in Section 2 were completely accomplished, whereas the third goal—the application of DNP for the investigation of methyl group dynamics—could not be completely accomplished.

The aim of Section 4.1 was the combination of SCREAM-DNP with dipolar recoupling in the form of rotational resonance. The results of this section display the potential of this combination. It not only increases the celerity of the SCREAM-DNP experiment towards polarization build-up of, for example, carbonyl groups, but also enables a controlled polarization transfer by suppressing unwanted polarization transfer pathways as shown in Subsection 4.1.1. This fast and controlled serial polarization transfer is furthermore applicable to biomolecular complexes as demonstrated with the L7Ae-RNP complex in Subsection 4.1.2. Here, the serial polarization transfer enables a fast build-up of the nucleobase signals and effectively suppresses the build-up of polarization on the sugar carbons. Moreover, by comparison to a mutant construct, spin pairs between the methyl groups of I93 and the C2, C4, and C6 carbons of the A18 are identified as the main source of polarization transfer in the complex. Overall, this section not only investigates systematically the potential of the combination of cross relaxation with dipolar recoupling in DNP experiments, but also displays potential future applications.

The aim of Section 4.2 was to adapt and optimize the matrix-free DNP approach for the investigation of biologically or medicinally relevant samples. Here, the matrix-free DNP sample preparation technique possesses a large potential as it enables the signal enhancement by DNP for sensitivity-limited samples such as drugs in polymeric micelles or A β ₁₋₄₂ peptides which are adsorbed to cellulose materials. The systematic optimization of Subsection 4.2.1 demonstrates that relative sensitivities of ~ 40 can be obtained under ideal conditions, which are comparable to relative sensitivities obtained for DNP experiments in a frozen solution of glycerol:water. Slightly reduced relative sensitivities of ~ 20 and ~ 10 are obtained for the more complex and more relevant systems in Subsection 4.2.2 and Subsection 4.2.3, respectively. Interestingly, the latter relative sensitivity coincides with the relative sensitivities obtained for lysozyme in the dry state indicating the reproducibility of this approach. Nonetheless, both relative sensitivities enabled the quantification and preliminary structural investigations of the

two systems which both possess a low concentration of the molecule of interest ($A\beta$ peptides in Subsection 4.2.2 and efavirenz in Subsection 4.2.3). To sum up, the findings of this section show the potential of matrix-free DNP for the investigation of challenging and/or insoluble biomolecular systems.

The aim of Section 4.3 was the investigation of methyl group dynamics using the sensitivity enhancement by DNP. Therefore, DNP-enhanced ^1H - ^2H CPMAS experiments were performed which revealed large relative sensitivity gains of up to 20—in comparison to ^2H solid-state NMR experiments—in both, a matrix-free DNP system consisting of $A\beta_{1-40}$ fibrils, and a frozen solution of ethanol- d_3 in a glycerol:water matrix. This demonstrates the potential of DNP for relaxation measurements. Nevertheless, the required doping of the sample with a PA introduces PRE-like effects which cannot be fully described with the results at hand. For example, the unexpected coupling of the selectively deuterated methyl group dynamics in $A\beta_{1-40}$ fibrils with the PRE-like behavior was not seen so far and already suggests the complex interaction pattern present in the studied sample and under DNP conditions. The ethanol- d_3 sample showed the PRE-like effect in the glycerol:water matrix as well; however, also displayed other, unanticipated effects, including a filtering of the PRE-like effect with the detection method or a change in the matrix morphology during titration of the analyte. In total, the results of Section 4.3 demonstrates, on the one hand, the potential of sensitivity enhancement by DNP for measurements of relaxation time constants, but, on the other hand, also shows the obstacles and the complexity, arising with the doping of the sample with the necessary PA for DNP experiments.

In conclusion, this work opens new avenues for future DNP experiments. On the one hand, fast polarization build-up in SCREAM-DNP experiments widens its applicability, for example, enabling two-dimensional NMR experiments, where the cross relaxation-induced transfer is used as a filter. On the other hand, this work shows that the large sensitivity enhancement by DNP is useful for relaxation measurements which are typically conducted at cryogenic temperatures relevant for DNP. The PRE-like effects can be an obstacle for these kinds of measurements; however, with better knowledge of these effects as well as the influence of matrix morphologies, the observed difficulties in the presented relaxation measurements can be predicted and the true nuclear relaxation time constants can be obtained. Therefore, future experiments could include a systematic investigation of this PRE-like effect by measurements of nuclear as well as electron relaxation time constants. An alternative approach could lie in the suppression of PRE-like effects in the sample by either turning the paramagnetic center of

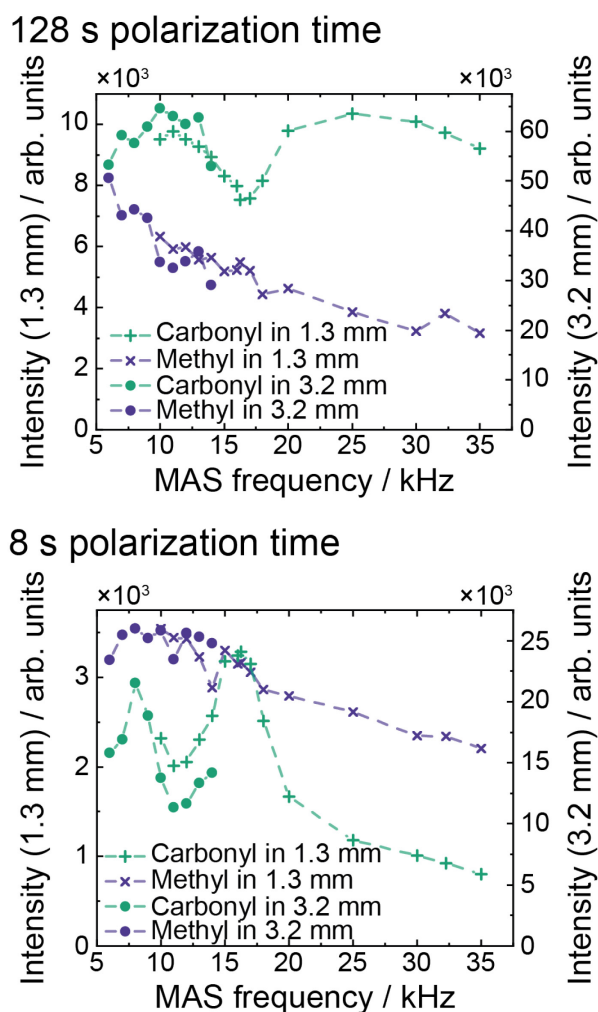
the PA on and off via a light-induced photochemical transition or by a full electron-nuclear decoupling during detection of the FID^[143].

Both DNP techniques of this work can be, in principle, combined with the matrix-free DNP approach. This was already shown in this work for A β ₁₋₄₀ fibrils with selectively deuterated methyl groups (Subsection 4.3.1). These methyl groups have been extensively studied with solid-state NMR techniques and thus, may be a perfect sample for further future studies about PRE-like effects. SCREAM-DNP and its site-specificity could be applied, for example, for the studied A β ₁₋₄₂-filtering cellulose materials (Subsection 4.2.2), which display a large quantity of amine groups. These groups were shown to induce heteronuclear cross relaxation between ¹H and ¹⁵N,^[61b] enabling the investigation of the amine groups and their surroundings. SCREAM-DNP may also be of interest in ¹³C-labeled A β samples to filter out the large cellulose background in future studies. Finally, the potential of ¹⁹F NMR can also be combined with SCREAM-DNP and/or the investigation of methyl group dynamics.^[48] Here, SCREAM-DNP would require a DNP probe which possess channels for ¹H and ¹⁹F each, whereas the use of ¹⁹F in studies of molecular dynamics could be of interest not only for biomolecular applications, but also, for example, for ionic liquids due to the commonly used TFSI (bis(trifluoromethanesulfonyl)imide) anion.

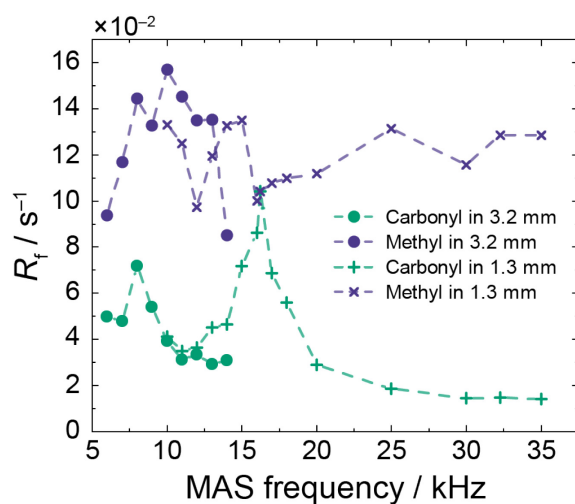
6. Appendix

6.1 Combination of Cross Relaxation with Rotational Resonance

6.1.1 Systematic investigation of the MAS frequency-dependency of SCREAM-DNP experiments with selectively labeled ethyl acetate



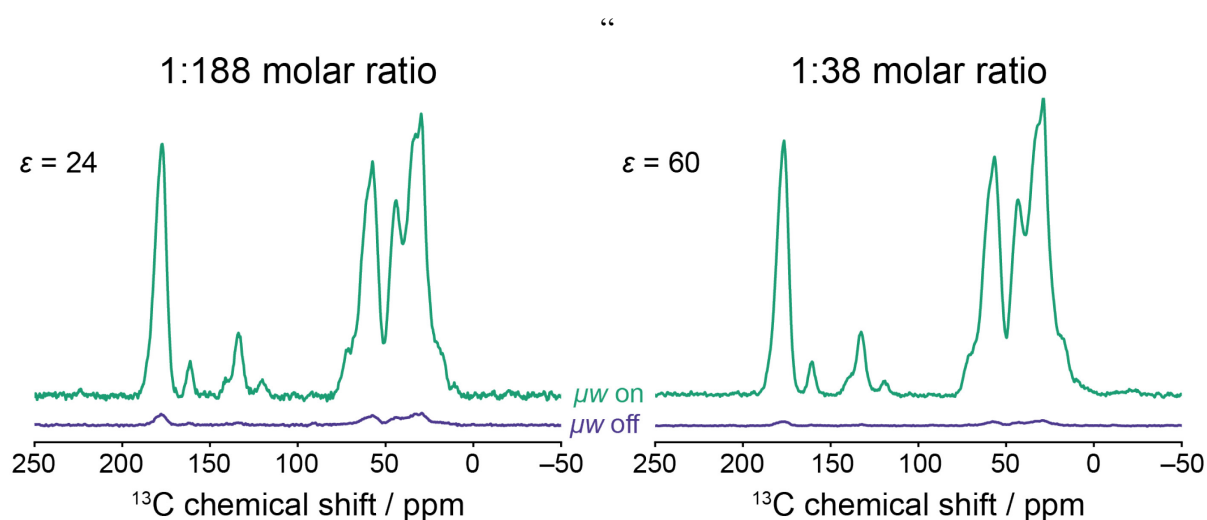
Appendix Figure A 1: Normalized integrated intensity of carbonyl- ^{13}C (green) and methyl- ^{13}C (violet) after 128 s (A) and 8 s (B) SCREAM-DNP polarization time at MAS frequencies between 6 to 35 kHz and 102 K. The normalization of the signal intensities are performed by dividing the integrated signal intensity by the number of applied transients, followed by the division of each signal intensity at each MAS frequency by the maximal signal intensity. In order to cover the full range of MAS frequencies, experiments were performed in two low-temperature MAS/DNP probes: a 1.3 mm (pluses and crosses) and a 3.2 mm (circles). The dashed lines act only as a guide to the eyes.



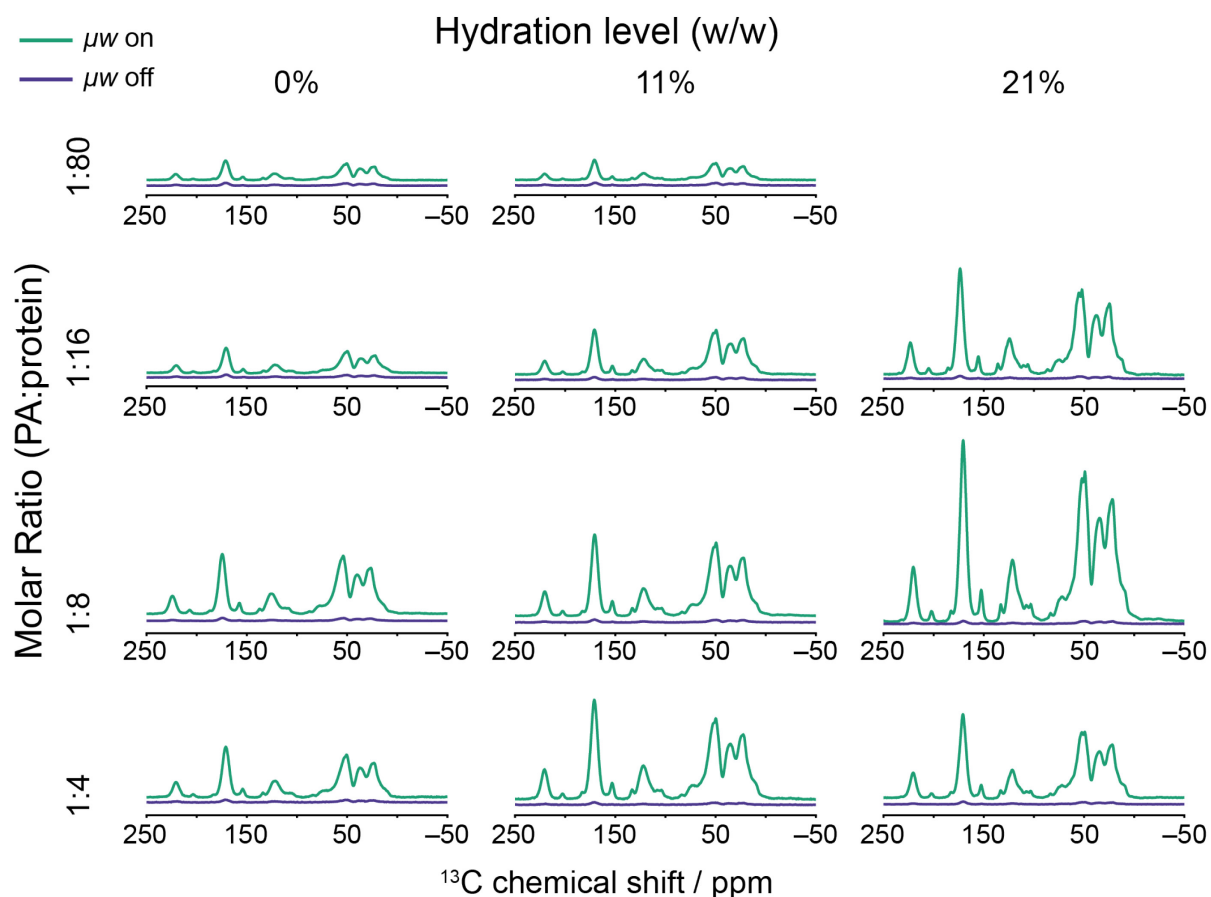
Appendix Figure A 2: SCREAM-DNP polarization build-up rate constants R_f of carbonyl- ^{13}C (green) and methyl- ^{13}C (violet) at MAS frequency between 6 to 35 kHz and 102 K. To cover the full range of MAS frequencies, the polarization build-up rate constants at MAS frequencies between 6 to 14 kHz are measured with a 3.2 mm low-temperature MAS/DNP probe (green and violet circles) and the rate constants at MAS frequencies between 10 to 35 kHz are obtained with a 1.3 mm MAS/DNP probe (green plusses and violet crosses). The dashed lines serve only as a guide to the eyes.

6.2 Matrix-free DNP for the investigation of powder samples

6.2.1 Systematic investigation of the matrix-free DNP approach in model proteins



Appendix Figure A 3: ^1H - ^{13}C CPMAS spectra of dry ubiquitin powder in natural isotope abundance mixed with AMUPol to a molar ratio of either 1:188 (PA:protein) or 1:38 (PA:protein) at 20 kHz MAS frequency and 95 K. The experiments were performed with (μw on, green) or without (μw off, violet) microwave irradiation. The ^1H DNP enhancement factors ε were determined to 24 and 60 by simple microwave on/off comparison for the molar ratios of 1:188 and 1:38 (PA:protein), respectively.



Appendix Figure A 4: ^1H - ^{13}C CPMAS spectra of lysozyme powder in natural isotope abundance mixed with varying amounts of AMUPol and rehydrated with varying amounts of water at 5 kHz MAS frequency and 98 K. The experiments were performed with (μw on, green) or without (μw off, violet) microwave irradiation. ^1H DNP enhancement factors and ^1H DNP build-up time constants were determined for all molar ratios and hydration levels and are summarized in Appendix Table A 1 to Appendix Table A 4. The ^1H DNP enhancement factors were 7, 10, 14, and 20 for 0% water content, 5, 18, 29, and 41 for a hydration level of 11%, and non-determinable, 40, 55, and 36 for 21% water content for the molar ratios of 1:80, 1:16, 1:8, and 1:4 (PA:protein), respectively.

Appendix Table A 1: ^1H DNP enhancement factors ϵ , ^1H DNP build-up time constants T_B and relative sensitivity $\epsilon T_B^{-1/2}$ for three different spectral regions of ^1H - ^{13}C CPMAS spectra of hen egg white lysozyme powder mixed with AMUPol to a molar ratio of 1:80 (PA:protein) at varying hydration levels (w/w) and 98 K. The build-up time constants were determined by fitting the build-up curves (Appendix Figure A 5) to Equation 35. n.d. corresponds to non-determinable due to low signal-to-noise of the spectra.

Hydration level	Functional Group	T_B / s	ϵ	$\epsilon T_B^{-1/2} / \text{s}^{-1/2}$
0%	C _O	2.69 ± 0.08	7	4.27
	C _α	2.73 ± 0.06		4.24
	Sidechain	2.69 ± 0.07		4.27
11%	C _O	4.49 ± 0.20	5	2.36
	C _α	4.45 ± 0.20		2.37
	Sidechain	4.39 ± 0.17		2.38
21%	C _O	n.d.	n.d.	n.d.
	C _α	n.d.		n.d.
	Sidechain	n.d.		n.d.

Appendix Table A 2: ^1H DNP enhancement factors ϵ , ^1H DNP build-up time constants T_B and relative sensitivity $\epsilon T_B^{-1/2}$ for three different spectral regions of ^1H - ^{13}C CPMAS spectra of hen egg white lysozyme powder mixed with AMUPol to a molar ratio of 1:16 (PA:protein) at varying hydration levels (w/w) and 98 K. The build-up time constants were determined by fitting the build-up curves (Appendix Figure A 5) to Equation 35.

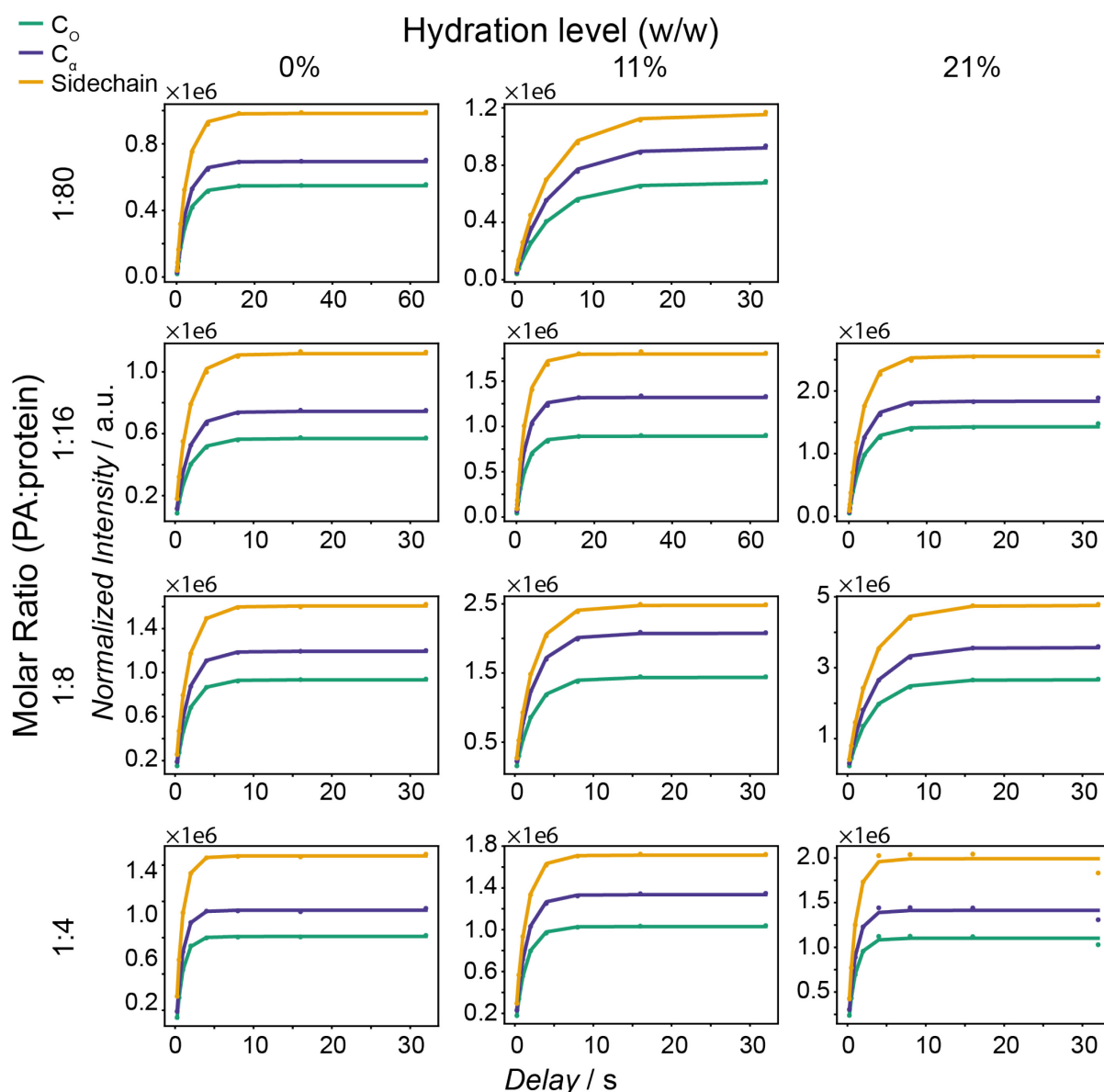
Hydration level	Functional Group	T_B / s	ϵ	$\epsilon T_B^{-1/2} / \text{s}^{-1/2}$
0%	C _O	1.64 ± 0.06	10	7.81
	C _α	1.67 ± 0.08		7.74
	Sidechain	1.67 ± 0.08		7.74
11%	C _O	2.54 ± 0.10	18	11.29
	C _α	2.57 ± 0.10		11.23
	Sidechain	2.55 ± 0.10		11.27
21%	C _O	3.44 ± 0.18	40	21.57
	C _α	3.44 ± 0.15		21.57
	Sidechain	3.41 ± 0.14		21.66

Appendix Table A 3: ^1H DNP enhancement factors ϵ , ^1H DNP build-up time constants T_B and relative sensitivity $\epsilon T_B^{-1/2}$ for three different spectral regions of ^1H - ^{13}C CPMAS spectra of hen egg white lysozyme powder mixed with AMUPol to a molar ratio of 1:8 (PA:protein) at varying hydration levels (w/w) and 98 K. The build-up time constants were determined by fitting the build-up curves (Appendix Figure A 5) to Equation 35.

Hydration level	Functional Group	T_B / s	ϵ	$\epsilon T_B^{-1/2} / \text{s}^{-1/2}$
0%	C _O	1.52 ± 0.03	14	11.36
	C _α	1.51 ± 0.03		11.39
	Sidechain	1.52 ± 0.03		11.36
11%	C _O	2.26 ± 0.07	29	19.29
	C _α	2.28 ± 0.07		19.21
	Sidechain	2.26 ± 0.06		19.29
21%	C _O	2.94 ± 0.08	55	32.08
	C _α	2.95 ± 0.08		32.02
	Sidechain	2.93 ± 0.08		32.13

Appendix Table A 4: ^1H DNP enhancement factors ϵ , ^1H DNP build-up time constants T_B and relative sensitivity $\epsilon T_B^{-1/2}$ for three different spectral regions of ^1H - ^{13}C CPMAS spectra of hen egg white lysozyme powder mixed with AMUPol to a molar ratio of 1:4 (PA:protein) at varying hydration levels (w/w) and 98 K. The build-up time constants were determined by fitting the build-up curves (Appendix Figure A 5) to Equation 35.

Hydration level	Functional Group	T_B / s	ϵ	$\epsilon T_B^{-1/2} / \text{s}^{-1/2}$
0%	C _O	0.84 ± 0.02	20	21.82
	C _α	0.84 ± 0.02		21.82
	Sidechain	0.83 ± 0.01		21.95
11%	C _O	1.34 ± 0.04	41	35.42
	C _α	1.35 ± 0.05		35.29
	Sidechain	1.31 ± 0.04		35.82
21%	C _O	0.97 ± 0.12	36	36.55
	C _α	0.97 ± 0.13		36.55
	Sidechain	0.97 ± 0.14		36.55



Appendix Figure A 5: Build-up curves to obtain the ^1H DNP build-up time constants T_B of lysozyme powder in natural isotope abundance mixed with varying amounts of AMUPol and rehydrated to varying hydration levels at 5 kHz MAS frequency and 98 K. The ^{13}C signal of three distinct spectral regions of the protein was normalized to the number of accumulated transients and integrated for each polarization delay, which were varied between 1 ms and either 32768 ms or 65536 ms. The resulting time-dependent polarization build-up of each sample was fitted to a monoexponential function (Equation 38) and all fits agree well with the fitted data as indicated with the adjusted R^2 parameter being at least 0.9898 for all fits. All determined T_B values are listed in Appendix Table A 1 to Appendix Table A 4.

6.2.2 Characterization of $A\beta_{1-42}$ -adsorbing materials using matrix-free DNP

Appendix Table A 5: ^1H DNP build-up time constants T_B , ^1H DNP enhancement factors ϵ , and relative sensitivities $\epsilon T_B^{-1/2}$ of multi crystalline cellulose in natural isotope abundance with PDA functionalization in natural isotope abundance. The build-up time constants are determined by fitting the normalized integral intensity with a monoexponential function (Equation 38). The enhancement factors are obtained by simple microwave on/off comparison.

Resonance	T_B / s	ϵ	$\epsilon T_B^{-1/2} / \text{s}^{-1/2}$
C ₁	5.6 ± 0.3	33	13.9
C ₄	5.5 ± 0.3		14.1
C ₂ , C ₃ and C ₅	5.7 ± 0.3		13.8
C ₆	5.9 ± 0.3		13.6

Appendix Table A 6: ^1H DNP build-up time constants T_B , ^1H DNP enhancement factors ϵ , and relative sensitivities $\epsilon T_B^{-1/2}$ of multi crystalline cellulose in natural isotope abundance functionalized with PDA in natural isotope abundance and u-[^{13}C , ^{15}N]-lysine. The build-up time constants are determined by fitting the normalized integral intensity with a monoexponential function (Equation 38). The enhancement factors are obtained by simple microwave on/off comparison.

Resonance	T_B / s	ϵ	$\epsilon T_B^{-1/2} / \text{s}^{-1/2}$
C _O	3.6 ± 0.3	45	23.7
C ₁	7.1 ± 0.5		16.9
C ₄	7.3 ± 0.5		16.7
C ₂ , C ₃ , and C ₅	7.0 ± 0.5		17.0
C ₆	7.6 ± 0.5		16.3
C _{α}	6.8 ± 0.5		17.3
Lys-C _{ϵ}	6.2 ± 0.5		18.1
Sidechain	4.5 ± 0.4		21.2

Appendix Table A 7: ^1H DNP build-up time constants T_B , ^1H DNP enhancement factors ϵ , and relative sensitivities $\epsilon T_B^{-1/2}$ of multi crystalline cellulose in natural isotope abundance functionalized with PDA in natural isotope abundance and u- $^{13}\text{C},^{15}\text{N}$]-lysine and adsorbed u- $^{13}\text{C},^{15}\text{N}$]-Arg-u- $^{13}\text{C},^{15}\text{N}$]-Lys-A β_{1-42} . The build-up time constants are determined by fitting the normalized integral intensity with a monoexponential function (Equation 38). The enhancement factors are obtained by simple microwave on/off comparison.

Resonance	T_B / s	ϵ	$\epsilon T_B^{-1/2} / \text{s}^{-1/2}$
C_O	3.9 ± 0.2	45	22.8
C_1	5.1 ± 0.2		19.9
C_4	5.2 ± 0.2		19.7
$C_2, C_3, \text{ and } C_5$	5.0 ± 0.2		20.1
C_6	5.3 ± 0.2		19.5
C_α	4.9 ± 0.2		20.3
Lys- C_ϵ	4.5 ± 0.2		21.2
Sidechain	4.1 ± 0.2		22.2

Appendix Table A 8: ^1H DNP build-up time constants T_B , ^1H DNP enhancement factors ϵ , and relative sensitivities $\epsilon T_B^{-1/2}$ of silica particles in natural isotope abundance functionalized with PDA in natural isotope abundance and u- $^{13}\text{C},^{15}\text{N}$]-lysine. The build-up time constants are determined by fitting the normalized integral intensity with a monoexponential function (Equation 38). The enhancement factors are obtained by simple microwave on/off comparison.

Resonance	T_B / s	ϵ	$\epsilon T_B^{-1/2} / \text{s}^{-1/2}$
C_O	4.0 ± 0.21	5.1	2.6
C_α	4.8 ± 0.1	4.4	2.0
Lys- C_ϵ	4.5 ± 0.2	5.0	2.4
Sidechain	4.1 ± 0.2	4.1	2.0

Appendix Table A 9: ^1H DNP build-up time constants T_B , ^1H DNP enhancement factors ϵ , and relative sensitivities $\epsilon T_B^{-1/2}$ of silica particles in natural isotope abundance functionalized with PDA in natural isotope abundance and u- $^{13}\text{C},^{15}\text{N}$]-lysine and adsorbed u- $^{13}\text{C},^{15}\text{N}$]-Arg-u- $^{13}\text{C},^{15}\text{N}$]-Lys-A β_{1-42} . The build-up time constants are determined by fitting the normalized integral intensity with a monoexponential function (Equation 38). The enhancement factors are obtained by simple microwave on/off comparison.

Resonance	T_B / s	ϵ	$\epsilon T_B^{-1/2} / \text{s}^{-1/2}$
C_O	4.0 ± 0.21	1.8	0.9
C_α	4.8 ± 0.1	2.6	1.2
Lys- C_ϵ	4.5 ± 0.2	2.4	1.1
Sidechain	4.1 ± 0.2	1.8	0.9

Appendix Table A 10: Relative sensitivity gains of DNP-enhanced ^1H - ^{13}C CPMAS experiments at 100 K over solid-state NMR ^1H - ^{13}C CPMAS experiments at 295 K and their corresponding linewidths for multi crystalline cellulose in natural isotope abundance functionalized with PDA in natural isotope abundance. The sample measured at 295 K was dry powder and the sample measured at 100 K was rehydrated to 60% (w/w) with 20 mM AMUPol dissolved in 33:67 $\text{H}_2\text{O}:\text{D}_2\text{O}$. If two values are given, the first value corresponds to the low-field and the second values to the high-field resonance of the annotated carbon.

Resonance	Relative Sensitivity Gain	Linewidth at 295 K	Linewidth at 100 K
C_1	96	2.9	3.5
C_4	120; 104	2.9; 4.9	2.8; 7.0
C_3	104	2.6	2.9
C_2 and C_5	116	2.7	3.1
C_6	116; 104	2.0; 2.7	2.1; 3.8

Appendix Table A 11: Relative sensitivity gains of DNP-enhanced ^1H - ^{13}C CPMAS experiments at 100 K over solid-state NMR ^1H - ^{13}C CPMAS experiments at 295 K and their corresponding linewidths for multi crystalline cellulose in natural isotope abundance. The cellulose samples for both measurements were functionalized with PDA, the sample for measurements at 100 K was further functionalized with u - $[^{13}\text{C}, ^{15}\text{N}]$ -lysine and has adsorbed u - $[^{13}\text{C}, ^{15}\text{N}]$ -Arg- u - $[^{13}\text{C}, ^{15}\text{N}]$ -Lys- $\text{A}\beta_{1-42}$ peptides. The sample measured at 295 K was dry powder and the sample measured at 100 K was rehydrated to 60% (w/w) with 20 mM AMUPol dissolved in 33:67 $\text{H}_2\text{O}:\text{D}_2\text{O}$. If two values are given, the first value corresponds to the low-field and the second values to the high-field resonance of the annotated carbon.

Resonance	Relative Sensitivity Gain	Linewidth at 295 K	Linewidth at 100 K
C_1	128	2.9	3.5
C_4	160; 139	2.9; 4.9	2.8; 6.2
C_3	139	2.6	2.7
C_2 and C_5	160	2.7	3.7
C_6	160; 139	2.0; 2.7	2.1; 3.8

Appendix Table A 12: Signal areas of multiple contact ^1H - ^{13}C CPMAS spectra and therefrom derived masses of lysine and $\text{A}\beta_{1-42}$ peptides in PDA- and u - $[^{13}\text{C}, ^{15}\text{N}]$ -lysine-functionalized micro crystalline cellulose with and without adsorbed $\text{A}\beta_{1-42}$ peptides at 8 kHz MAS frequency and 100 K. The given signal areas are relative to the C_1 signal area (100 ppm) of cellulose which was used as a reference compound with known mass. Due to signal overlap of the $\text{A}\beta_{1-42}$ and lysine resonances, the lysine signal area was determined using the cellulose sample without adsorbed $\text{A}\beta_{1-42}$ peptides. To extract the signal area corresponding to $\text{A}\beta_{1-42}$ peptides, the lysine signal area was subtracted from the corresponding signal area in the cellulose sample with adsorped $\text{A}\beta_{1-42}$. The given masses were calculated with Equation 36, where a total mass of 21.7 mg was used to calculate the mass of lysine and 29.2 mg was used to calculate the mass of $\text{A}\beta_{1-42}$ peptides.

Resonance	Lysine		$\text{A}\beta_{1-42}$ peptides	
	Signal area / a.u.	Mass / μg	Signal area / a.u.	Mass / μg
C_O	0.1177	22.80	0.0542	2.50
Arg- C_ϵ	–	–	0.0138	4.29
C_α	0.1189	23.03	0.0527	3.00
C_β & Lys- C_ϵ	0.1989	19.26	0.0397	2.31
C_α & Sidechain	0.9356	36.24	0.2362	1.12

Appendix Table A 13: Signal areas of multiple contact ^1H - ^{13}C CPMAS spectra and therefrom derived masses of lysine and $\text{A}\beta_{1-42}$ peptides in PDA- and u - $[^{13}\text{C}, ^{15}\text{N}]$ -lysine-functionalized micro crystalline cellulose with and without adsorbed $\text{A}\beta_{1-42}$ peptides at 12.7 kHz MAS frequency and 100 K. The given signal areas are relative to the C_1 signal area (100 ppm) of cellulose which was used as a reference compound with known mass. Due to signal overlap of the $\text{A}\beta_{1-42}$ and lysine resonances, the lysine signal area was determined using the cellulose sample without adsorped $\text{A}\beta_{1-42}$ peptides. To extract the signal area corresponding to $\text{A}\beta_{1-42}$ peptides, the lysine signal area was subtracted from the corresponding signal area in the cellulose sample with adsorped $\text{A}\beta_{1-42}$. The given masses were calculated with Equation 36, where a total mass of 21.7 mg was used to calculate the mass of lysine and 29.2 mg was used to calculate the mass of $\text{A}\beta_{1-42}$ peptides.

Resonance	Lysine		$\text{A}\beta_{1-42}$ peptides	
	Signal area / a.u.	Mass / μg	Signal area / a.u.	Mass / μg
C_O	0.1185	22.80	0.0712	3.29
Arg-C_ϵ	–	–	0.0041	1.26
C_α	0.1361	23.03	0.0539	3.06
C_β & Lys-C_ϵ	0.1770	19.26	0.0336	1.49
C_α & Sidechain	0.8888	36.24	0.2036	0.97

6.2.3 Site-specific investigation of API-carrying polymeric micelles

Appendix Table A 14: Resonance assignment, ^1H DNP build-up time constants T_B , ^1H DNP enhancement factors ϵ , and relative sensitivity $\epsilon T_B^{-1/2}$ of MBM polymer micelles formulations in mixture with either 8 nmol/mg TEKPol or 8 nmol/mg TOTAPOL at 102 K and 8 kHz MAS frequency. The asterisk indicates values with low reliability due to low signal intensity of the corresponding peak in the microwave off spectrum.

	Resonance	^{13}C Chemical shift / ppm	ϵ	T_B / s	$\epsilon T_B^{-1/2}$ / $\text{s}^{-1/2}$
TEKPol	a	24.2	10	1.350 ± 0.005	7.41
	b	174.0		1.355 ± 0.013	7.38
	c	48.1		1.357 ± 0.013	7.37
	d, e, f	34.8 – 30.4		1.36 ± 0.03	7.35
	g	24.2		1.45 ± 0.08	6.90
	h	17.5	14*	1.339 ± 0.016	10.45*
TOTAPOL	a	24.2	5	1.277 ± 0.007	3.92
	b	174.0		1.241 ± 0.018	4.03
	c	48.1		1.272 ± 0.015	3.93
	d, e, f	34.5 – 30.4		1.35 ± 0.04	3.70
	g	24.2		1.27 ± 0.05	3.94
	h	17.3	7*	1.43 ± 0.14	4.90*

Appendix Table A 15: Relative sensitivity gains of DNP-enhanced ^1H - ^{13}C CPMAS experiments of MBM micelles formulated with either 8 nmol/mg TEKPol or 8 nmol/mg TOTAPOL at 102 K and 12 MAS frequency over ^1H - ^{13}C CPMAS experiments of pure MBM micelles at 297 K and 20 kHz MAS frequency.

Resonance		Relative sensitivity gain	
Peak	^{13}C chemical shift / ppm	TEKPol	TOTAPOL
a	24.2	11	4
b	174.0	15	5
c	48.1	22	9
d, e, f	34.8 – 30.4	16	7
g	24.2	11	4
h	17.5	1.9	0.9

Appendix Table A 16: ^{13}C resonance assignment of efavirenz in MBM micelles and as a pure compound. The numbering of the carbons can be found in the structure of efavirenz, which is displayed in Figure 24. The assignment of the pure compound is taken from ref. [120] and the used numbering of the carbons are adopted.

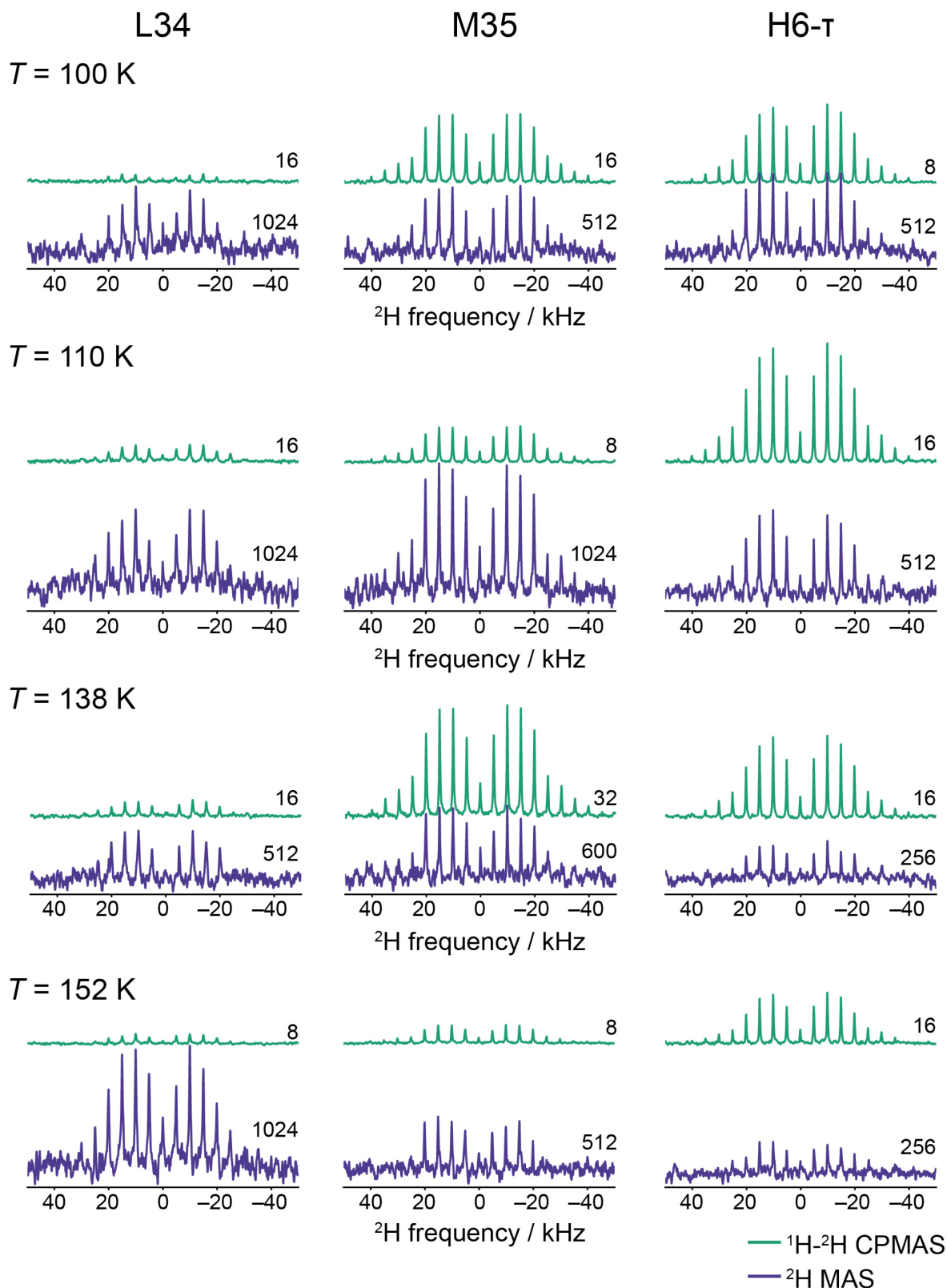
Carbon	^{13}C Chemical shift / ppm	
	MBM micelles	Pure compound
1	147.2	147.5
2	78.0	79.5
3	134.8	134.9; 134.3
4	116.5 ^a	114.4
5	116.5 ^a	119.0
6	131.1	133.4
7	127.3 ^a	128.6
8	127.3 ^a	127.1
9	66.5	68.2; 66.2
10	99.8	97.0; 96.4; 95.8
11	-0.8	-0.7; -1.5
12	9.1	9.1; 8.4; 7.8
13	9.1	9.1; 8.4; 7.8
14	124.2	123.2

6.3 Quantification of Methyl Group Dynamics under DNP conditions

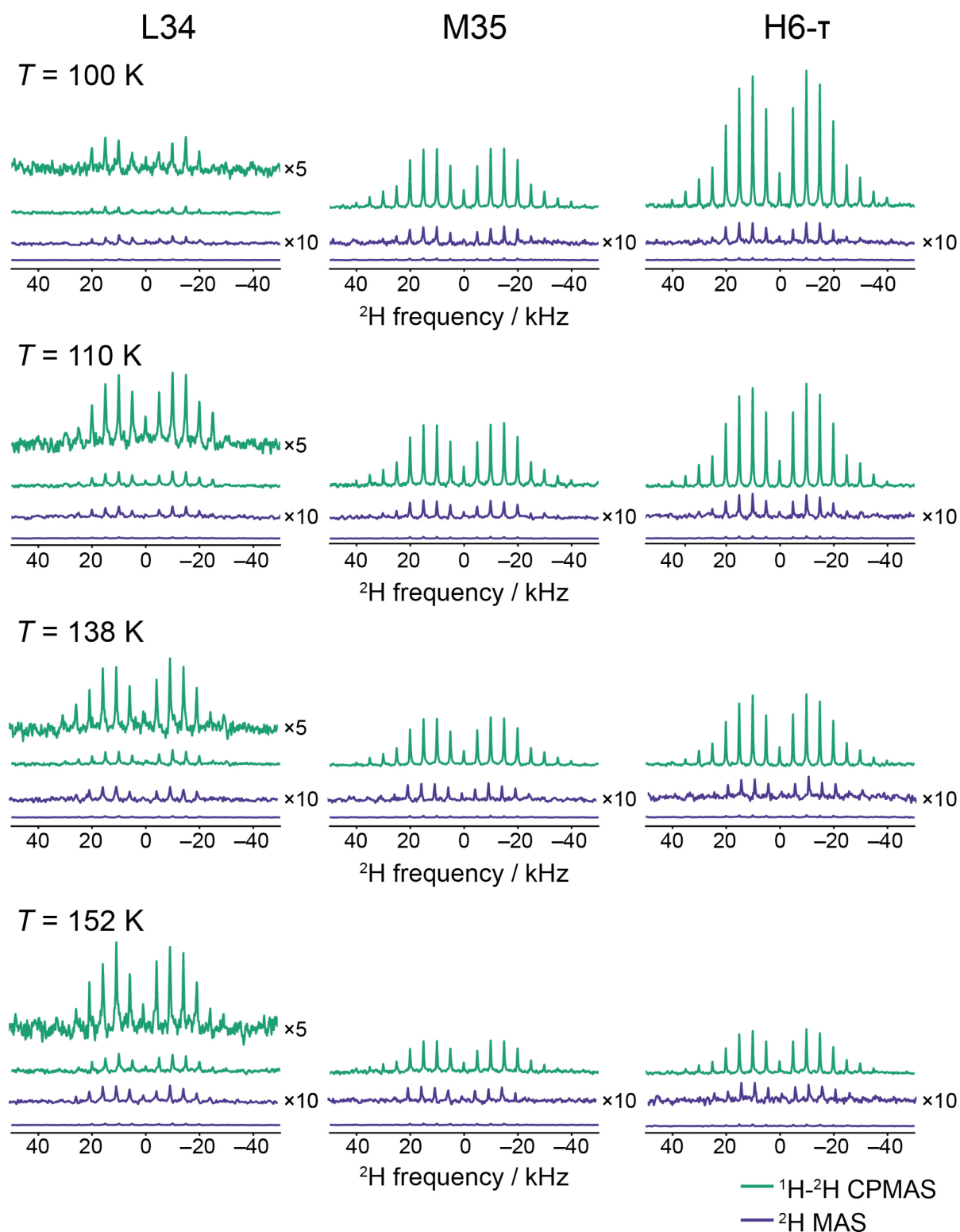
6.3.1 Investigation of Methyl Group Dynamics in A β ₁₋₄₀ fibrils by DNP-enhanced ¹H-²H CPMAS NMR

Appendix Table A 17: ¹H DNP build-up time constants T_B , ¹H DNP enhancement factors ϵ , and relative sensitivities $\epsilon T_B^{-1/2}$ of two A β ₁₋₄₀ fibril samples, each with a selectively deuterated methyl group at the given position for three different spectral regions at 5 kHz MAS frequency and 115 K. Both protein samples have been mixed with AMUPol to a molar ratio of 1:15 (PA:protein) and rehydrated with deuterium-depleted water to a hydration level of 60% (w/w). The build-up curves are obtained by a saturation recovery sequence using a ¹H-¹³C CP step as excitation. The resulting data was fitted to a monoexponential function (Equation 35) to obtain the ¹H DNP build-up time constant. The enhancement factors are determined by a simple microwave on/off comparison.

Label	Spectral region	T_B / s	ϵ	$\epsilon T_B^{-1/2} / s^{-1/2}$
H6- τ	C _O	0.74 ± 0.03	18	20.92
	C _{α}	0.75 ± 0.02		20.78
	Sidechain	0.77 ± 0.02		20.51
M35	C _O	0.93 ± 0.02	15	15.55
	C _{α}	0.93 ± 0.02		15.55
	Sidechain	0.94 ± 0.02		15.47



Appendix Figure A 6: Signal comparison of DNP-enhanced ^1H - ^2H CPMAS experiments (green) and ^2H MAS experiments (violet) of three different selectively deuterated samples of $\text{A}\beta_{1-40}$ fibrils which are each mixed with a molar ratio of 1:16 (PA:protein) with AMUPol at 5 kHz MAS frequency and temperatures between 100 to 152 K. All spectra are scaled to the same intensity scale to visualize differences in the signal and noise amplitudes. No further normalization was performed. The number of accumulated transients for each spectrum is denoted at the right side of each spectrum.



Appendix Figure A 7: Signal comparison of DNP-enhanced ^1H - ^2H CPMAS experiments (green) and ^2H MAS experiments (violet) of three different selectively deuterated samples of $\text{A}\beta_{1-40}$ fibrils which are each mixed with a molar ratio of 1:16 (PA:protein) with AMUPol at 5 kHz MAS frequency and temperatures between 100 to 152 K. The spectra were normalized by the number of accumulated transients and scaled to the same height. The ^2H MAS spectra and the ^1H - ^2H CPMAS spectra of the L34 label are additionally displayed in a scaled version for better visibility. The applied scaling factor is given at the right side of the respective spectrum.

Appendix Table A 18: Overview of number of accumulated transients, obtained signal amplitudes A_{Signal} for either ^2H MAS or DNP-enhanced ^1H - ^2H CPMAS experiments, and the resulting relative sensitivity gains of the ^1H - ^2H CPMAS experiments over the ^2H MAS experiments for A β -L34-d₃ fibrils. The given signal amplitudes were normalized with the given number of accumulated transients before calculation of the relative sensitivity gains. The resulting values were further normalized with the square root of the typical ratio of used repetition delays which was set to 10 (3 s for the CPMAS experiments and 0.3 s for the ^2H MAS experiments).

Temperature / K	Number of accumulated transients		$A_{\text{Signal}} / \text{a.u.}$		Relative sensitivity gain
	^2H MAS	^1H - ^2H CPMAS	^2H MAS	^1H - ^2H CPMAS	
100	1024	16	943	6445	2.2
110	1024	16	1267	17448	4.4
138	512	16	1472	16846	3.6
152	1024	8	1864	17901	3.0

Appendix Table A 19: Overview of number of accumulated transients, obtained signal amplitudes A_{Signal} for either ^2H MAS or DNP-enhanced ^1H - ^2H CPMAS experiments, and the resulting relative sensitivity gains of the ^1H - ^2H CPMAS experiments over the ^2H MAS experiments for A β -M35-d₃ fibrils. The given signal amplitudes were normalized with the given number of accumulated transients before calculation of the relative sensitivity gains. The resulting values were further normalized with the square root of the typical ratio of used repetition delays which was set to 10 (3 s for the CPMAS experiments and 0.3 s for the ^2H MAS experiments).

Temperature / K	Number of accumulated transients		$A_{\text{Signal}} / \text{a.u.}$		Relative sensitivity gain
	^2H MAS	^1H - ^2H CPMAS	^2H MAS	^1H - ^2H CPMAS	
100	512	16	1843	69137	11.9
110	1024	8	2095	71205	10.7
138	600	32	1939	55743	9.1
152	512	8	1389	38046	8.7

Appendix Table A 20: Overview of number of accumulated transients, obtained signal amplitudes A_{Signal} for either ^2H MAS or DNP-enhanced ^1H - ^2H CPMAS experiments, and the resulting relative sensitivity gains of the ^1H - ^2H CPMAS experiments over the ^2H MAS experiments for $\text{A}\beta\text{-H6-}\tau\text{-d}_3$ fibrils. The given signal amplitudes were normalized with the given number of accumulated transients before calculation of the relative sensitivity gains. The resulting values were further normalized with the square root of the typical ratio of used repetition delays which was set to 10 (3 s for the CPMAS experiments and 0.3 s for the ^2H MAS experiments).

Temperature / K	Number of accumulated transients		$A_{\text{Signal}} / \text{a.u.}$		Relative sensitivity gain
	^2H MAS	^1H - ^2H CPMAS	^2H MAS	^1H - ^2H CPMAS	
100	512	8	2493	155988	19.8
110	512	16	2426	118949	15.5
138	256	16	2596	79972	9.7
152	256	16	1908	51790	8.6

Appendix Table A 21: Overview of number of accumulated transients, obtained noise amplitudes A_{Noise} of ^2H MAS experiments and DNP-enhanced ^1H - ^2H CPMAS experiments for $\text{A}\beta\text{-L34-}\text{d}_3$ fibrils. The noise amplitudes were determined as root-mean-square values of a signal-free spectral region and further normalized to the square root of the given number of accumulated transients.

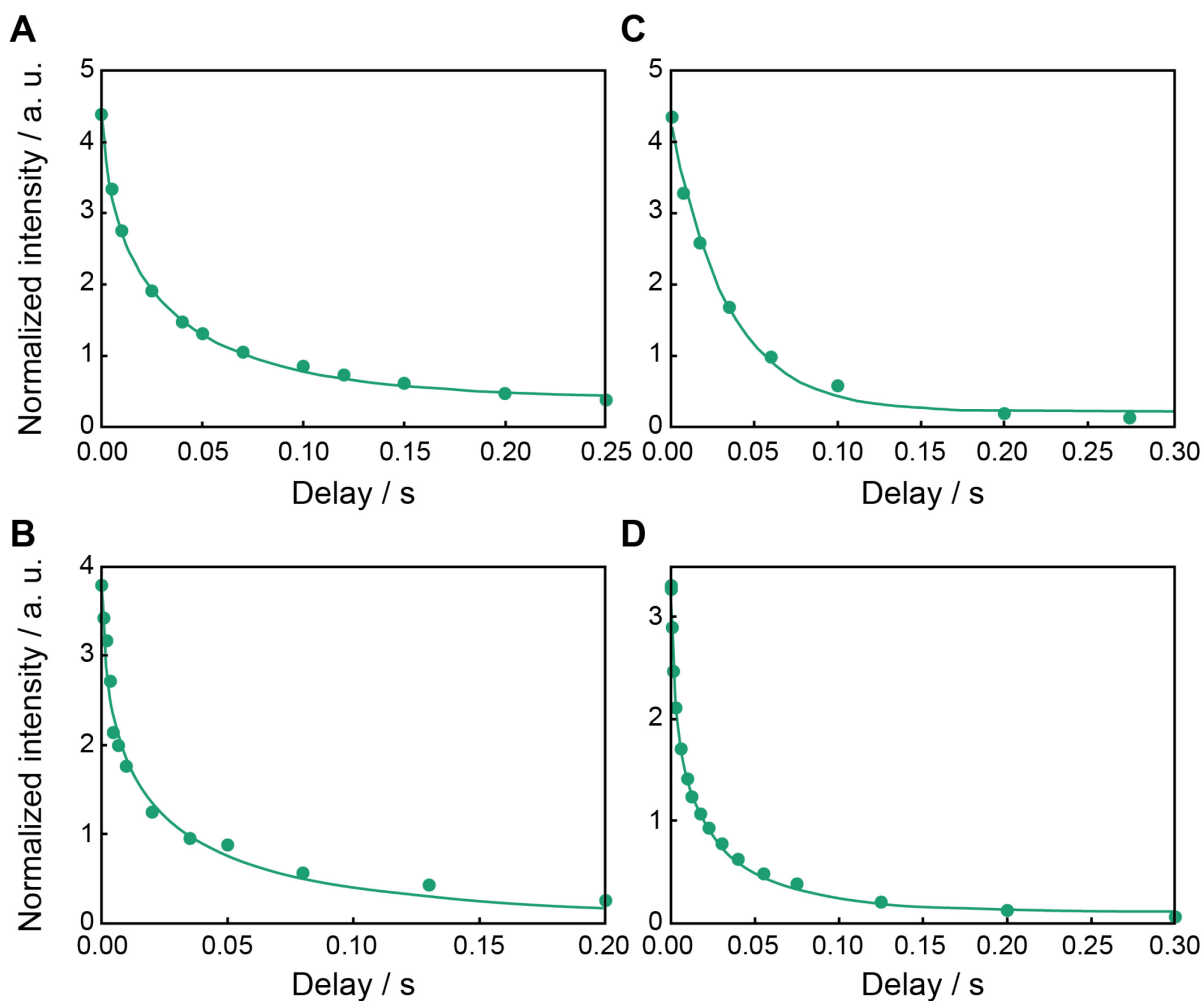
Temperature / K	Number of accumulated transients		$A_{\text{Noise}} / \text{a.u.}$	
	^2H MAS	^1H - ^2H CPMAS	^2H MAS	^1H - ^2H CPMAS
100	512	8	1767	3842
110	512	16	1993	4918
138	256	16	2719	3059
152	256	16	3790	3293

Appendix Table A 22: Overview of number of accumulated transients, obtained noise amplitudes A_{Noise} of ^2H MAS experiments and DNP-enhanced ^1H - ^2H CPMAS experiments for A β -M35-d₃ fibrils. The noise amplitudes were determined as root-mean-square values of a signal-free spectral region and further normalized to the square root of the given number of accumulated transients.

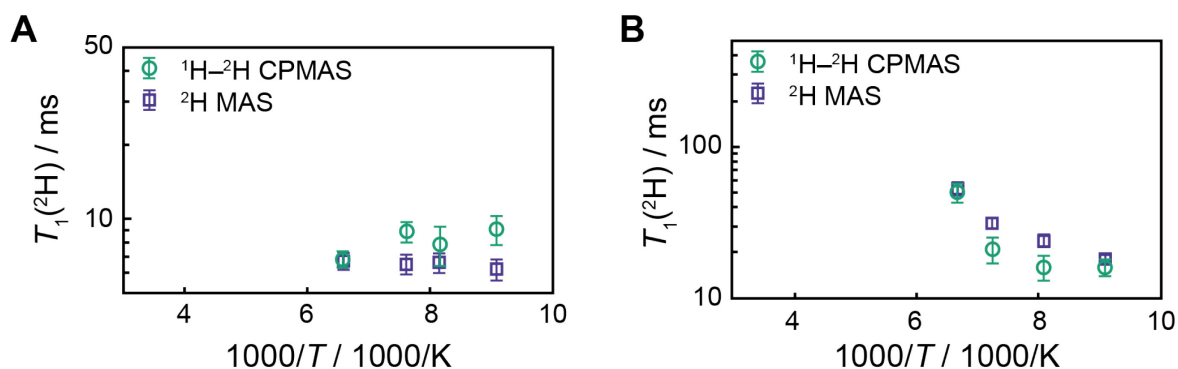
Temperature / K	Number of accumulated transients		$A_{\text{Noise}} / \text{a.u.}$	
	^2H MAS	^1H - ^2H CPMAS	^2H MAS	^1H - ^2H CPMAS
100	512	8	2767	4424
110	512	16	2713	5559
138	256	16	4826	4751
152	256	16	3076	3508

Appendix Table A 23: Overview of number of accumulated transients, obtained noise amplitudes A_{Noise} of ^2H MAS experiments and DNP-enhanced ^1H - ^2H CPMAS experiments for A β -H6- τ -d₃ fibrils. The noise amplitudes were determined as root-mean-square values of a signal-free spectral region and further normalized to the square root of the given number of accumulated transients.

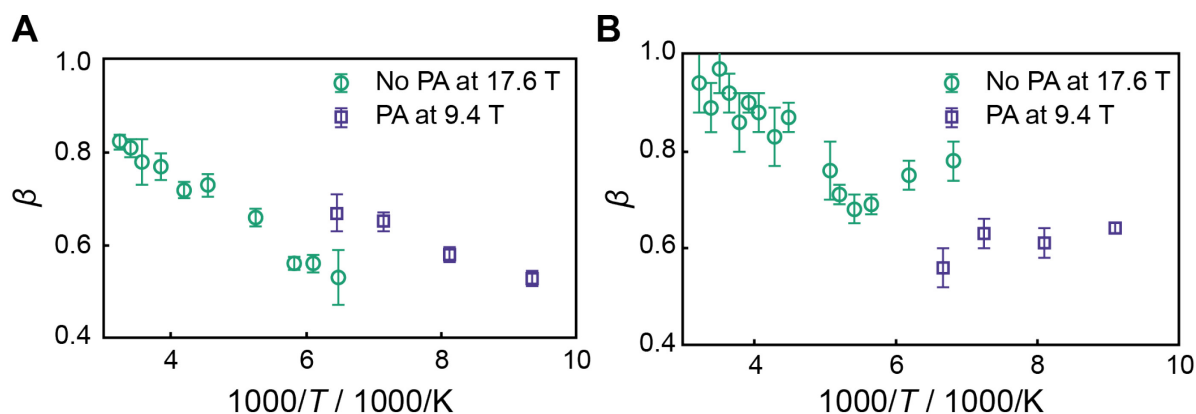
Temperature / K	Number of accumulated transients		$A_{\text{Noise}} / \text{a.u.}$	
	^2H MAS	^1H - ^2H CPMAS	^2H MAS	^1H - ^2H CPMAS
100	512	8	2531	2982
110	512	16	2829	4528
138	256	16	3936	2550
152	256	16	3202	3214



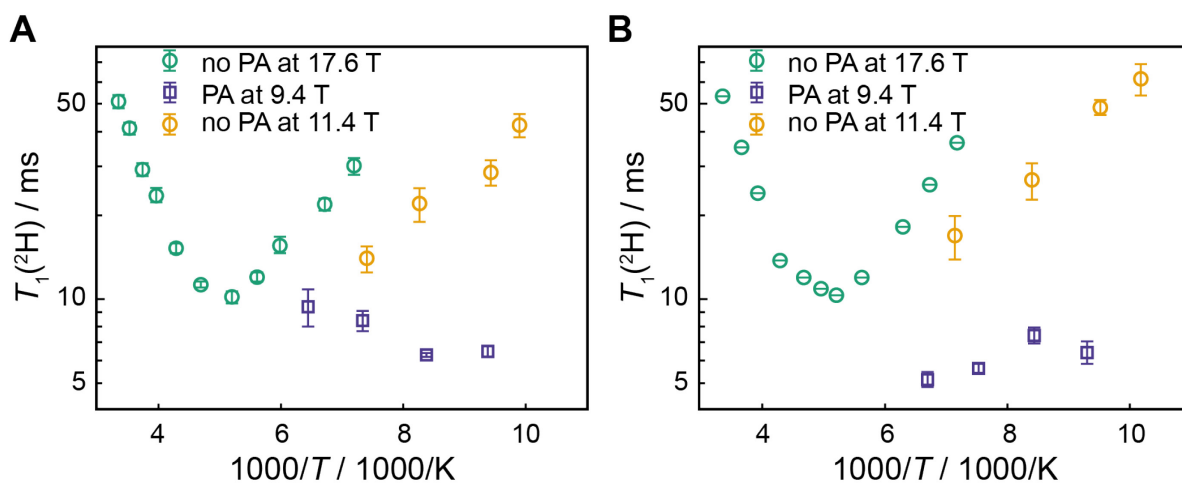
Appendix Figure A 8: Magnetization decay curves to determine ^2H T_1 relaxation time constants of three selectively deuterated methyl groups in different $\text{A}\beta_{1-40}$ fibrils obtained with microwave irradiation and temperatures between 110 to 131 K. (A & B) ^2H T_1 relaxation time constant (A) and ^2H T_{1Q} relaxation time constant (B) determined for the selectively deuterated methyl group of M35 in $\text{A}\beta_{1-40}$ fibrils. The experiments were performed at 5 kHz MAS frequency and 124 K. (C) ^2H T_1 relaxation time constant determined for the selectively deuterated methyl group of L34 in $\text{A}\beta_{1-40}$ fibrils. The experiment was performed at 5 kHz MAS frequency and 131 K. (D) ^2H T_1 relaxation time constant determined for the selectively deuterated methyl group of H6- τ in $\text{A}\beta_{1-40}$ fibrils. The experiment was performed at 5 kHz MAS frequency and 110 K. All samples were mixed with AMUPol to a final molar ratio of 1:16 (PA:protein). The relaxation data (circles) were acquired using DNP-enhanced ^1H - ^2H CPMAS excitation and were fitted (solid green line) either to a stretched exponential function (Equation 39) in the case of the H6- τ and the M35 label or to a monoexponential function (Equation 38) in the case of the L34 label.



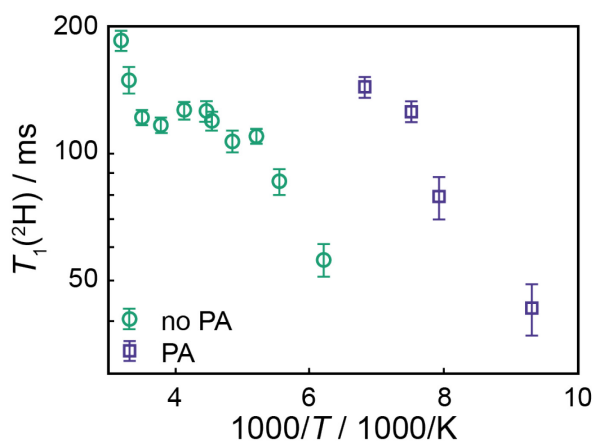
Appendix Figure A 9: Comparison of excitation methods for determining $T_1(^2\text{H})$ relaxation time constants for selectively deuterated methyl groups in two different labeled $\text{A}\beta_{1-40}$ fibrils in the presence of AMUPol and at 5 kHz MAS frequency and 9.4 T. The deuterated methyl group was part of either M35 (A) or L34 (B). The relaxation time constants were measured for the same sample with either with DNP-enhanced ^1H - ^2H CPMAS excitation (green circles) or ^2H MAS excitation without microwave irradiation (violet squares).



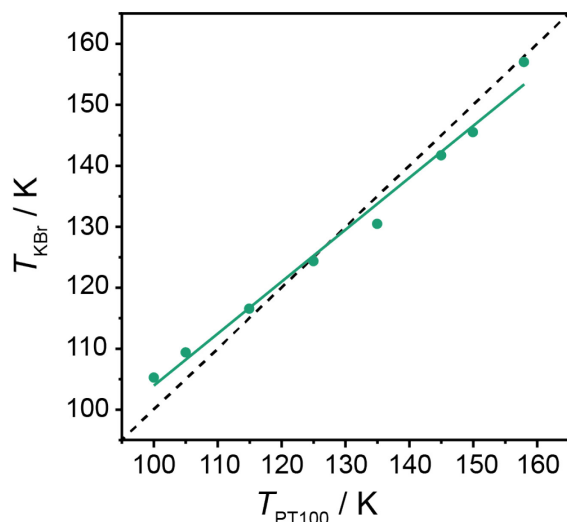
Appendix Figure A 10: Obtained values of the stretching factor β of the $\text{A}\beta_{1-40}\text{-H6-}\tau$ (A) and -M35 (B) samples either in absence of any PA and at 17.6 T (green circles) or in presence of AMUPol as a PA and 9.4 T (violet squares). The $\text{A}\beta$ samples in presence of PA were mixed with AMUPol to a molar ratio of 1:16 (PA:protein). To obtain the β values, relaxation time data were fitted to Equation 39 (*cf.* exemplary curves in Appendix Figure A 8). The data at 17.6 T are taken from the literature.^[89, 128]



Appendix Figure A 11: $T_1(^2\text{H})$ relaxation time constants for the selectively deuterated methyl groups in the two HP36 (globular chicken villin headpiece subdomain protein) constructs (A: surface-exposed L63, B: L69 in the hydrophobic core). The data are measured in the absence of a PA under static conditions at either 17.6 T (green circles) or 11.4 T (yellow circles) and in presence of AMUPol (molar ratio of 1:16 (PA:protein)) and with DNP-enhanced ^1H - ^2H CPMAS experiments (violet squares). The relaxation time data obtained with DNP were fitted with a monoexponential function (Equation 38) and the static measurements at 17.6 T were fitted with a stretched exponential function (Equation 39) and the measurements at 11.4 T were fitted with a monoexponential function (Equation 38). The static measurements are taken from the literature.^[64, 68, 144]



Appendix Figure A 12: $T_1(^2\text{H})$ relaxation time constants for the selectively deuterated methyl group in a short disordered peptide at 9.4 T and varying temperatures. The peptide consists of nine residues of the following sequence: GGKG[M- CD_3]GFGL. The $T_1(^2\text{H})$ relaxation time constants are obtained by either a DNP-enhanced ^1H - ^2H CPMAS experiment at 12 kHz MAS frequency (violet squares) or direct excitation of ^2H under static conditions and in absence of a PA (green circles). All relaxation data were fitted to a monoexponential function (Equation 38). The relaxation data are taken from the literature.^[131]



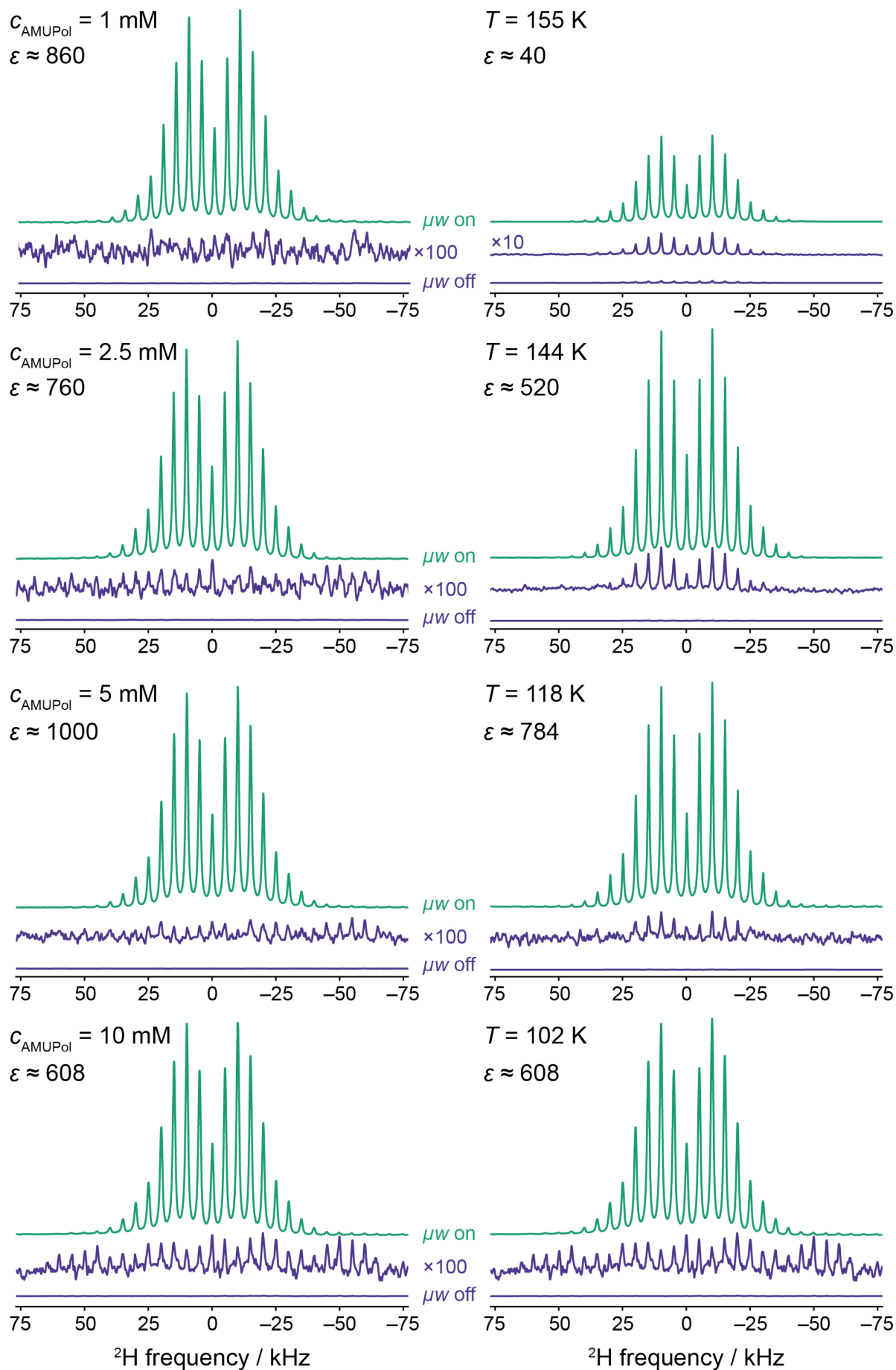
Appendix Figure A 13: Temperature calibration curve to calibrate the probe temperatures measured with the PT100 temperature sensor in the probe to the actual sample temperature T_{KBr} . The calibration is performed by measuring the the $T_1(^{79}\text{Br})$ relaxation time constant at typical DNP temperatures used for this study and under microwave irradiation. The actual sample temperature T_{KBr} is obtained by correlating the $T_1(^{79}\text{Br})$ relaxation time constant to the temperatures (Equation 37) as explained by Thurber and Tycko^[92a] and Miéville *et al.*^[92b] The calibration curve is determined by plotting the actual sample temperature T_{KBr} against the measured temperature of the PT100 sensor T_{PT100} . All temperatures measured for the protein samples are calibrated to this curve.

6.3.1 Systematic investigation of methyl group dynamics under DNP conditions

The build-up curves are obtained by a saturation recovery sequence using a ^1H - ^{13}C CP step as excitation. The resulting data was fitted to a monoexponential function to obtain the ^1H DNP build-up time constant.

Appendix Table A 24: ^1H DNP enhancement factors ϵ , ^1H DNP build-up time constants T_{B} , and relative sensitivities $\epsilon T_{\text{B}}^{-1/2}$ of ethanol- d_3 at 5 kHz MAS frequency, 102 K and varying concentrations of AMUPol. The sample consisted of 30 vol-% ethanol- d_3 , 50 vol-% glycerol, and 20 vol-% deuterium-depleted water, mixed with varying concentrations of AMUPol. The enhancement factors are determined by a simple microwave on/off comparison of ^1H - ^2H CPMAS spectra. The respective spectra are shown in Appendix Figure A 14.

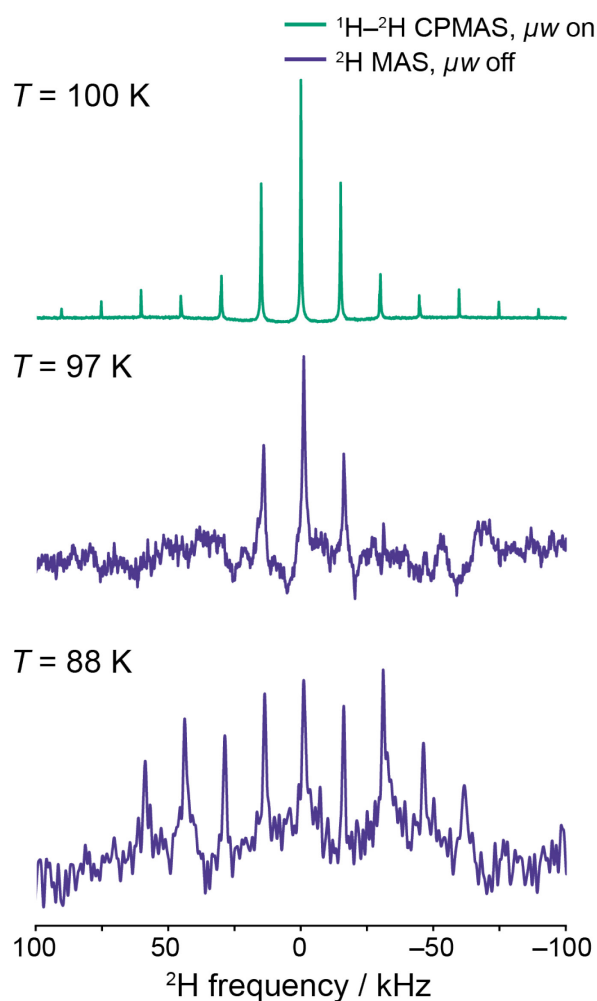
$c_{\text{AMUPol}} / \text{mM}$	ϵ	T_{B} / s	$\epsilon T_{\text{B}}^{-1/2} / \text{s}^{-1/2}$
1	860	7.84 ± 0.09	307
2.5	760	7.51 ± 0.11	277
5	1000	3.63 ± 0.11	525
10	608	2.93 ± 0.11	355



Appendix Figure A 14: ^1H - ^2H CPMAS spectra with (μw on, green) or without (μw off, violet) microwave irradiation of 30 vol-% ethanol- d_3 and mixed with 50 vol-% glycerol, and 20 vol-% deuterium-depleted water at 5 kHz MAS frequency and either varying AMUPol concentrations and 102 K (A) or 19 mM AMUPol and varying temperatures (B). All spectra are normalized to the same signal intensity to visualize differences in signal intensity. The spectra without microwaved irradiation are further scaled by the given factor in the middle for better visibility of the signal in the μw off spectra.

Appendix Table A 25: ^1H DNP enhancement factors ϵ , ^1H DNP build-up time constants T_{B} , and relative sensitivities $\epsilon T_{\text{B}}^{-1/2}$ of ethanol- d_3 at 5 kHz MAS frequency, 10 mM AMUPol, and varying temperatures. The sample consisted of 30 vol-% ethanol- d_3 , 50 vol-% glycerol, and 20 vol-% deuterium-depleted water, mixed with 10 mM AMUPol. The enhancement factors are determined by a simple microwave on/off comparison of ^1H - ^2H CPMAS spectra. The respective spectra are shown in Appendix Figure A 14.

Temperature / K	ϵ	T_{B} / s	$\epsilon T_{\text{B}}^{-1/2} / \text{s}^{-1/2}$
102	608	2.929 ± 0.111	355
118	784	2.904 ± 0.004	460
144	520	2.921 ± 0.004	304
155	40	3.027 ± 0.011	23



Appendix Figure A 15: ${}^1\text{H}$ - ${}^2\text{H}$ CPMAS spectrum (green) and ${}^2\text{H}$ MAS spectra (violet) of 30 vol-% ethanol- d_3 and mixed with 10 mM ASYMPol-POK, 50 vol-% glycerol, and 20 -% deuterium-depleted water at 15 kHz MAS frequency and varying temperatures. The ${}^1\text{H}$ - ${}^2\text{H}$ CPMAS spectrum is recorded with microwave irradiation and the ${}^2\text{H}$ MAS spectra is recorded without microwave irradiation. The ${}^2\text{H}$ MAS spectrum at 88 K was recorded at the lowest temperature possible with the involved setup and the spectra at 97 K was acquired with additional heating.

Appendix Table A 26: Overview of number of accumulated transients $N_{\text{Transients}}$, obtained signal amplitudes A_{Signal} for either ^2H MAS in absence of a PA or DNP-enhanced ^1H - ^2H CPMAS experiments with 5 mM AMUPol, and the resulting relative sensitivity gains of the DNP-enhanced ^1H - ^2H CPMAS experiments over the ^2H MAS experiments for ethanol- d_3 . Both ethanol samples consisted of 30 vol-% ethanol- d_3 , 50 vol-% glycerol, and 20 vol-% deuterium-depleted water. The given signal amplitudes were normalized with the given number of accumulated transients before calculation of the relative sensitivity gains. The resulting values were further normalized with the square root of the typical ratio of used repetition delays which was set to 10 (1 s for the CPMAS experiments and 0.1 s for the ^2H MAS experiments).

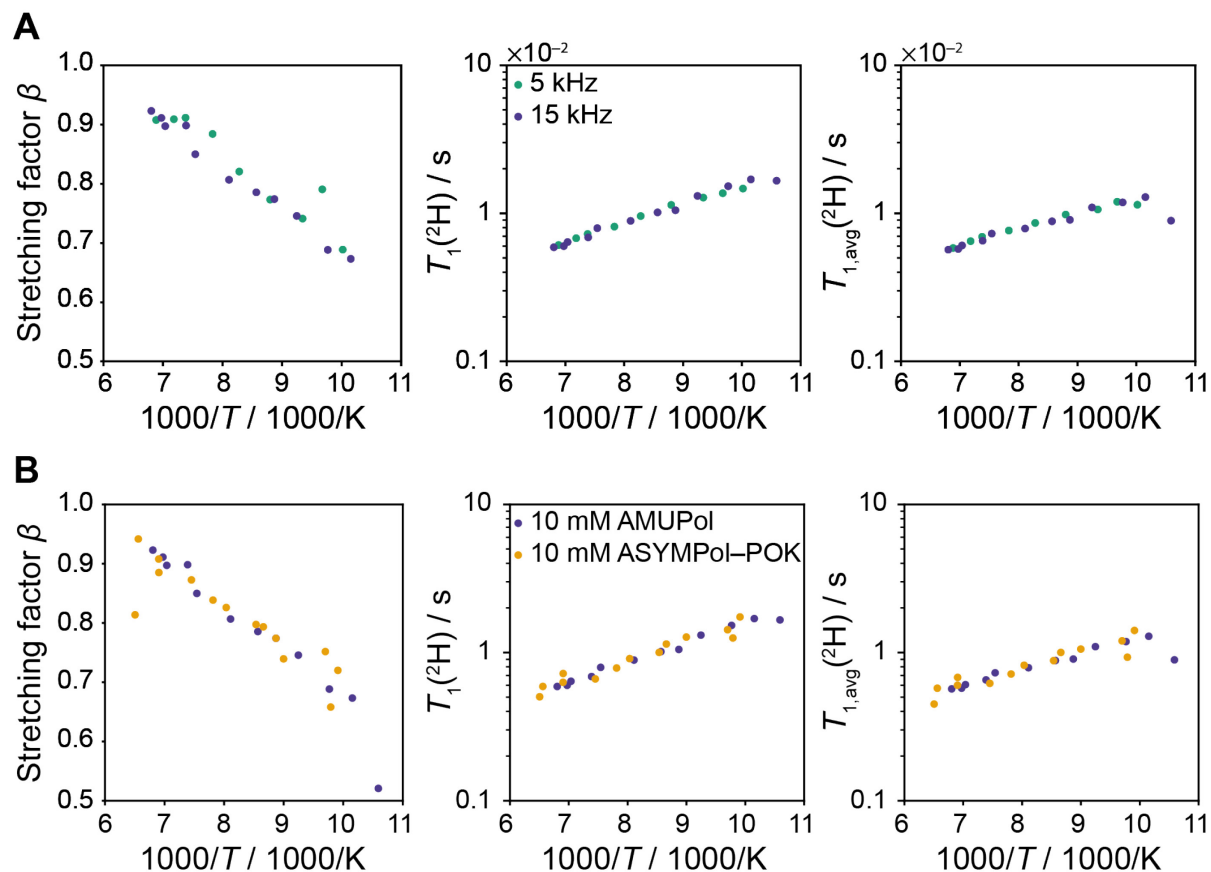
T / K	No PA		ASYMPol-POK		Relative Sensitivity Gain
	$N_{\text{Transients}}$	$A_{\text{Signal}} / \text{arb. u.}$	$N_{\text{Transients}}$	$A_{\text{Signal}} / \text{arb. u.}$	
99	16384	1353	256	48871	21.35
115	8192	10573	256	253533	16.32
142	16384	55139	256	454874	1.46

Appendix Table A 27: Overview of number of accumulated transients $N_{\text{Transients}}$, obtained signal amplitudes A_{Signal} for either ^2H MAS in absence of a PA or DNP-enhanced ^1H - ^2H CPMAS experiments with 5 mM AMUPol, and the resulting relative sensitivity gains of the DNP-enhanced ^1H - ^2H CPMAS experiments over the ^2H MAS experiments for ethanol- d_3 . Both ethanol samples consisted of 30 vol-% ethanol- d_3 , 50 vol-% glycerol, and 20 vol-% deuterium-depleted water. The given signal amplitudes were normalized with the given number of accumulated transients before calculation of the relative sensitivity gains. The resulting values were further normalized with the square root of the typical ratio of used repetition delays which was set to 10 (2 s for the CPMAS experiments and 0.1 s for the ^2H MAS experiments).

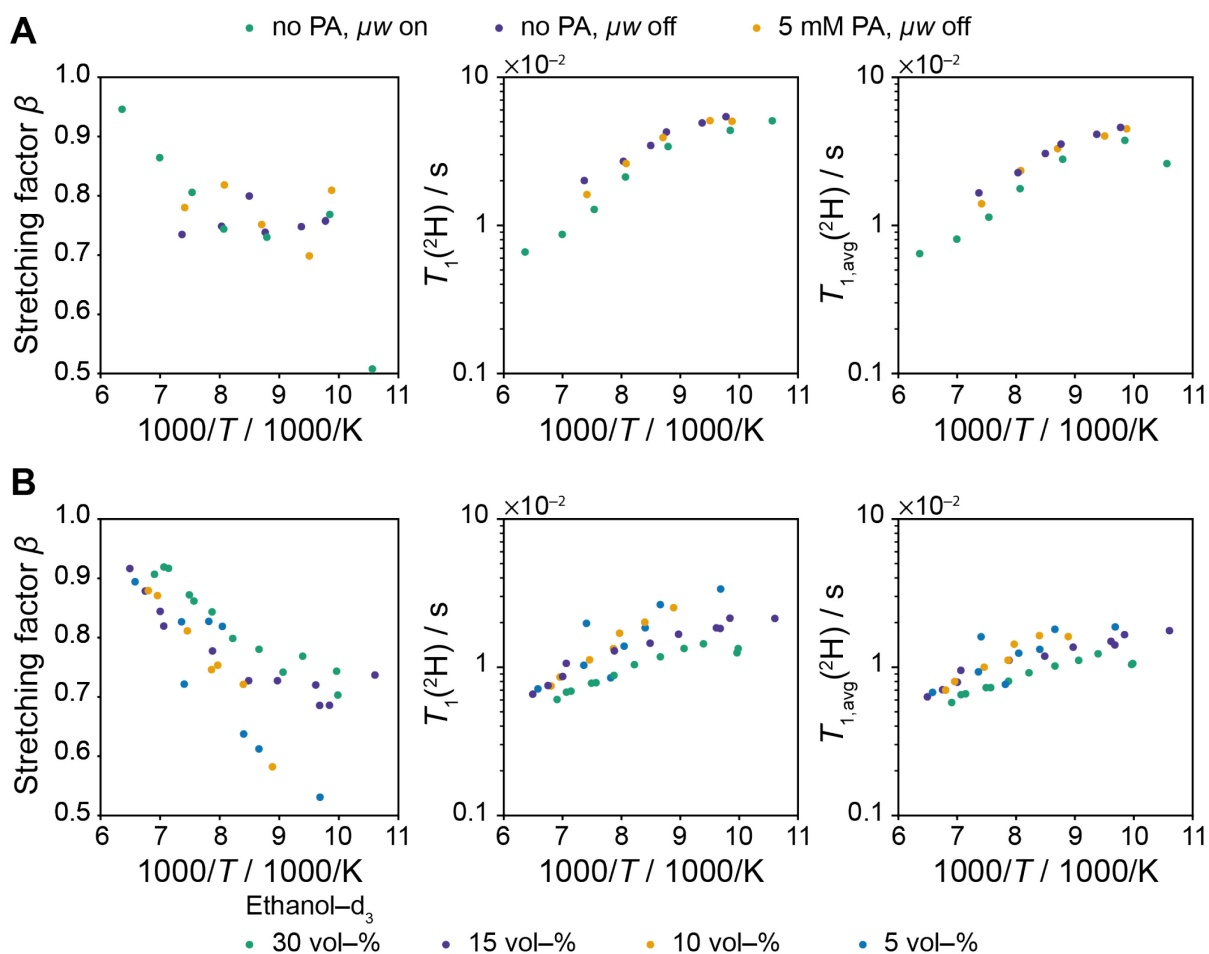
T / K	No PA		AMUPol		Relative Sensitivity Gain
	$N_{\text{Transients}}$	$A_{\text{Signal}} / \text{arb. u.}$	$N_{\text{Transients}}$	$A_{\text{Signal}} / \text{arb. u.}$	
99	16384	1353	256	48871	7.23
115	8192	10573	256	253533	4.80
142	16384	55139	256	454874	1.65

Appendix Table A 28: Overview of number of accumulated transients $N_{\text{Transients}}$, obtained signal amplitudes A_{Noise} for either ^2H MAS in absence of a PA or DNP-enhanced ^1H - ^2H CPMAS experiments with either 5 mM AMUPol or 5 mM ASYMPol-POK. All ethanol samples consisted of 30 vol-% ethanol- d_3 , 50 vol-% glycerol, and 20 vol-% deuterium-depleted water. The noise amplitudes were determined as root-mean-square values of a signal-free spectral region and further normalized to the square root of the given number of accumulated transients.

	Temperature / K	$N_{\text{Transients}}$	$A_{\text{Noise}} / \text{arb. u.}$
ASYMPol -POK	99	128	2685
	115	512	2850
	142	256	4080
AMUPol	99	256	3425
	115	256	5270
	142	256	3634
No PA	99	16384	4960
	115	8192	3250
	142	16384	3674



Appendix Figure A 16: Stretching factor β , ^2H spin-lattice relaxation time constant $T_1(^2\text{H})$, and mean ^2H spin-lattice relaxation time constant $T_{1,\text{avg}}(^2\text{H})$ of 30 vol-% ethanol- d_3 either mixed with 10 mM AMUPol and obtained at varying MAS frequencies (A) or mixed with two different PAs and obtained at 15 kHz MAS frequency (B). Ethanol- d_3 is mixed with 50 vol-% glycerol and 20 vol-% deuterium-depleted water and either 10 mM AMUPol (A&B) or 10 mM ASYMPol-POK (B). All relaxation data were obtained at varying temperatures using ^1H - ^2H CPMAS for all series. The relaxation values are obtained by fitting the relaxation time series to a stretched exponential function (Equation 39).



Appendix Figure A 17: Stretching factor β , ^2H spin-lattice relaxation time constant $T_1(^2\text{H})$, and mean ^2H spin-lattice relaxation time constant $T_{1,\text{avg}}(^2\text{H})$ of either 30 vol-% ethanol- d_3 with (μw on) or without (μw off) microwave irradiation and in absence of a PA or in presence of 5 mM ASYMPol-POK (A) or different volume percentages of ethanol- d_3 mixed with a concentration of 5 mM ASYMPol-POK (B). (A) Ethanol- d_3 is mixed with 50 vol-% glycerol and 20 vol-% deuterium-depleted water and either no PA or 5 mM ASYMPol-POK. The relaxation data were obtained at varying temperatures and 15 kHz MAS frequency using either ^1H - ^2H CPMAS for all series, except the data series without PA or without microwave irradiation (μw off), these relaxation data were obtained with ^2H MAS experiments. (B) The samples consist of varying amounts of ethanol- d_3 in 50 vol-% glycerol, varying amounts of deuterium-depleted water, and 5 mM ASYMPol-POK. The relaxation values are obtained by fitting the relaxation time series to a stretched exponential function (Equation 39).

7. References

- [1] M. D. Berg, C. J. Brandl, *RNA Biol.* **2021**, *18*, 316-339.
- [2] W. H. Bragg, *Philos. Trans. R. Soc. A* **1915**, *215*, 253-274.
- [3] S. Curry, *Interdiscip. Sci. Rev.* **2015**, *40*, 308-328.
- [4] J. D. Watson, F. H. C. Crick, *Nature* **1953**, *171*, 737-738.
- [5] K. Lundstrom, *Cell. Mol. Life Sci.* **2006**, *63*, 2597-2607.
- [6] T. R. Alderson, L. E. Kay, *Cell* **2021**, *184*, 577-595.
- [7] R. Puthenveetil, O. Vinogradova, *J. Biol. Chem.* **2019**, *294*, 15914-15931.
- [8] a) S. Yan, C. L. Suiter, G. Hou, H. Zhang, T. Polenova, *Acc. Chem. Res.* **2013**, *46*, 2047-2058; b) A. Loquet, B. Habenstein, A. Lange, *Acc. Chem. Res.* **2013**, *46*, 2070-2079; c) A. K. Schütz, *Biochem. Soc. Trans.* **2021**, *49*, 131-144.
- [9] a) K. Bertelsen, B. Paaske, L. Thøgersen, E. Tajkhorshid, B. Schiøtt, T. Skrydstrup, N. C. Nielsen, T. Vosegaard, *J. Am. Chem. Soc.* **2009**, *131*, 18335-18342; b) M. Weingarh, A. Prokofyev, E. A. W. van der Crujisen, D. Nand, A. M. J. J. Bonvin, O. Pongs, M. Baldus, *J. Am. Chem. Soc.* **2013**, *135*, 3983-3988; c) V. S. Mandala, J. K. Williams, M. Hong, *Annu. Rev. Biophys.* **2018**, *47*, 201-222; d) M. Doroudgar, J. Morstein, J. Becker-Baldus, D. Trauner, C. Glaubitz, *J. Am. Chem. Soc.* **2021**, *143*, 9515-9528; e) S. Y. P. Novischi, A. Karoly-Lakatos, K. Chok, C. Bonifer, J. Becker-Baldus, C. Glaubitz, *Commun. Biol.* **2024**, *7*, 43.
- [10] a) G. Comellas, C. M. Rienstra, *Annu. Rev. Biophys.* **2013**, *42*, 515-536; b) M. T. Colvin, R. Silvers, B. Frohm, Y. Su, S. Linse, R. G. Griffin, *J. Am. Chem. Soc.* **2015**, *137*, 7509-7518; c) M. A. Walti, F. Ravotti, H. Arai, C. G. Glabe, J. S. Wall, A. Bockmann, P. Guntert, B. H. Meier, R. Riek, *Proc. Natl. Acad. Sci. U. S. A.* **2016**, *113*, E4976-4984; d) M. T. Colvin, R. Silvers, Q. Z. Ni, T. V. Can, I. Sergeev, M. Rosay, K. J. Donovan, B. Michael, J. Wall, S. Linse, R. G. Griffin, *J. Am. Chem. Soc.* **2016**, *138*, 9663-9674; e) L. Vugmeyster, M. A. Clark, I. B. Falconer, D. Ostrovsky, D. Gantz, W. Qiang, G. L. Hoatson, *J. Biol. Chem.* **2016**, *291*, 18484-18495; f) B. Busi, J. R. Yarava, A. Bertarello, F. Freymond, W. Adamski, D. Maurin, M. Hiller, H. Oschkinat, M. Blackledge, L. Emsley, *J. Phys. Chem. B* **2021**, *125*, 2212-2221; g) L. M. Becker, M. Berbon, A. Vallet, A. Grelard, E. Morvan, B. Bardiaux, R. Lichtenecker, M. Ernst, A. Loquet, P. Schanda, *Angew. Chem., Int. Ed.* **2023**, *62*, e202219314.

- [11] I. Kuprov, *Spin: From Basic Symmetries to Quantum Optimal Control*, Springer International Publishing, **2023**.
- [12] D. C. Apperley, R. K. Harris, P. Hodgkinson, *Solid-State NMR: Basic Principles and Practice*, Momentum Press, **2012**.
- [13] A. W. Overhauser, *Phys. Rev.* **1953**, *92*, 411-415.
- [14] T. R. Carver, C. P. Slichter, *Phys. Rev.* **1953**, *92*, 212-213.
- [15] T. Biedenbänder, V. Aladin, S. Saeidpour, B. Corzilius, *Chem. Rev.* **2022**, *122*, 9738-9794.
- [16] L. R. Becerra, G. J. Gerfen, R. J. Temkin, D. J. Singel, R. G. Griffin, *Phys. Rev. Lett.* **1993**, *71*, 3561-3564.
- [17] G. J. Gerfen, L. R. Becerra, D. A. Hall, R. G. Griffin, R. J. Temkin, D. J. Singel, *J. Chem. Phys.* **1995**, *102*, 9494-9497.
- [18] P. Wenk, M. Kaushik, D. Richter, M. Vogel, B. Suess, B. Corzilius, *J. Biomol. NMR* **2015**, *63*, 97-109.
- [19] a) K. R. Thurber, R. Tycko, *Journal of Chemical Physics* **2014**, *140*, 184201; b) F. Mentink-Vigier, S. Paul, D. Lee, A. Feintuch, S. Hediger, S. Vega, G. De Paëpe, *Phys. Chem. Chem. Phys.* **2015**, *17*, 21824-21836.
- [20] S. Hediger, D. Lee, F. Mentink-Vigier, G. De Paëpe, in *Handbook of High Field Dynamic Nuclear Polarization* (Eds.: V. K. Michaelis, R. G. Griffin, B. Corzilius, S. Vega), Wiley, **2020**, p. 87.
- [21] M. H. Levitt, *Spin Dynamics: Basics of Nuclear Magnetic Resonance*, Wiley, **2013**.
- [22] G. De Paëpe, *Annu. Rev. Phys. Chem.* **2012**, *63*, 661-684.
- [23] a) G. R. Khutsishvili, *Sov. Phys. Uspekhi* **1966**, *8*, 743; b) Y. Hovav, A. Feintuch, S. Vega, *Journal of Chemical Physics* **2011**, *134*.
- [24] K. Kundu, F. Mentink-Vigier, A. Feintuch, S. Vega, in *Handbook of High Field Dynamic Nuclear Polarization* (Eds.: V. K. Michaelis, R. G. Griffin, B. Corzilius, S. Vega), Wiley, **2020**, p. 15.
- [25] G. Parigi, C. Luchinat, in *Paramagnetism in Experimental Biomolecular NMR* (Eds.: C. Luchinat, G. Parigi, E. Ravera), The Royal Society of Chemistry, **2018**, p. 1.
- [26] A. S. Lilly Thankamony, J. J. Wittmann, M. Kaushik, B. Corzilius, *Prog. Nucl. Magn. Reson. Spectrosc.* **2017**, *102-103*, 120-195.

- [27] C. Song, K. N. Hu, C. G. Joo, T. M. Swager, R. G. Griffin, *J. Am. Chem. Soc.* **2006**, *128*, 11385-11390.
- [28] C. Sauvee, M. Rosay, G. Casano, F. Aussenac, R. T. Weber, O. Ouari, P. Tordo, *Angew. Chem., Int. Ed.* **2013**, *52*, 10858-10861.
- [29] F. Mentink-Vigier, I. Marín-Montesinos, A. P. Jagtap, T. Halbritter, J. van Tol, S. Hediger, D. Lee, S. T. Sigurdsson, G. De Paëpe, *J. Am. Chem. Soc.* **2018**, *140*, 11013-11019.
- [30] a) J.-L. Muñoz-Gómez, I. Marín-Montesinos, V. Lloveras, M. Pons, J. Vidal-Gancedo, J. Veciana, *Org. Lett.* **2014**, *16*, 5402-5405; b) G. Mathies, M. A. Caporini, V. K. Michaelis, Y. Liu, K.-N. Hu, D. Mance, J. L. Zweier, M. Rosay, M. Baldus, R. G. Griffin, *Angew. Chem., Int. Ed.* **2015**, *54*, 11770-11774; c) F. Mentink-Vigier, G. Mathies, Y. Liu, A.-L. Barra, M. A. Caporini, D. Lee, S. Hediger, R. G. Griffin, G. De Paëpe, *Chem. Sci.* **2017**, *8*, 8150-8163; d) X. Cai, A. Lucini Paioni, A. Adler, R. Yao, W. Zhang, D. Beriashvili, A. Safeer, A. Gurinov, A. Rockenbauer, Y. Song, M. Baldus, Y. Liu, *Chem. Eur. J.* **2021**, *27*, 12758-12762; e) T. Halbritter, R. Harrabi, S. Paul, J. van Tol, D. Lee, S. Hediger, S. T. Sigurdsson, F. Mentink-Vigier, G. De Paëpe, *Chem. Sci.* **2023**, *14*, 3852-3864.
- [31] a) E. L. Dane, T. Maly, G. T. Debelouchina, R. G. Griffin, T. M. Swager, *Org. Lett.* **2009**, *11*, 1871-1874; b) L. F. Pinto, I. Marín-Montesinos, V. Lloveras, J. L. Muñoz-Gómez, M. Pons, J. Veciana, J. Vidal-Gancedo, *Chem. Commun.* **2017**, *53*, 3757-3760.
- [32] M. Rosay, Massachusetts Institute of Technology (Massachusetts Institute of Technology), **2001**.
- [33] J. Bachler, V. Fuentes-Landete, D. A. Jahn, J. Wong, N. Giovambattista, T. Loerting, *Phys. Chem. Chem. Phys.* **2016**, *18*, 11058-11068.
- [34] M. Hirai, S. Ajito, M. Sugiyama, H. Iwase, S.-i. Takata, N. Shimizu, N. Igarashi, A. Martel, L. Porcar, *Biophys. J.* **2018**, *115*, 313-327.
- [35] R. Ghosh, Y. Xiao, J. Kragelj, K. K. Frederick, *J. Am. Chem. Soc.* **2021**, *143*, 18454-18466.
- [36] Y. Xiao, R. Ghosh, K. K. Frederick, *Front. Mol. Biosci.* **2022**, *8*, 789478.
- [37] a) K.-N. Hu, H.-h. Yu, T. M. Swager, R. G. Griffin, *J. Am. Chem. Soc.* **2004**, *126*, 10844-10845; b) Y. Matsuki, T. Maly, O. Ouari, H. Karoui, F. Le Moigne, E. Rizzato, S.

- Lyubenova, J. Herzfeld, T. Prisner, P. Tordo, R. G. Griffin, *Angew. Chem., Int. Ed.* **2009**, *48*, 4996-5000.
- [38] J. Viger-Gravel, P. Berruyer, D. Gajan, J.-M. Basset, A. Lesage, P. Tordo, O. Ouari, L. Emsley, *Angew. Chem., Int. Ed.* **2017**, *56*, 8726-8730.
- [39] I. Gelis, V. Vitzthum, N. Dhimole, M. A. Caporini, A. Schedlbauer, D. Carnevale, S. R. Connell, P. Fucini, G. Bodenhausen, *J. Biomol. NMR* **2013**, *56*, 85-93.
- [40] M. Kaushik, H. Lingua, G. Stevanato, M. Elokova, M. Lelli, A. Lesage, O. Ouari, *Phys. Chem. Chem. Phys.* **2022**, *24*, 12167-12175.
- [41] F. J. Scott, S. Eddy, T. Gullion, F. Mentink-Vigier, *J. Phys. Chem. Lett.* **2024**, *15*, 8743-8751.
- [42] a) S. W. Jacob, R. Herschler, *Cryobiology* **1986**, *23*, 14-27; b) G. M. Fahy, *Cryobiology* **1986**, *23*, 1-13; c) A. Tjernberg, N. Markova, W. J. Griffiths, D. Hallén, *SLAS Discovery* **2006**, *11*, 131-137.
- [43] a) V. Vitzthum, F. Borcard, S. Jannin, M. Morin, P. Miéville, M. A. Caporini, A. Sienkiewicz, S. Gerber-Lemaire, G. Bodenhausen *ChemPhysChem* **2011**, *12*, 2929-2932; b) H. Takahashi, D. Lee, L. Dubois, M. Bardet, S. Hediger, G. De Paëpe, *Angew. Chem., Int. Ed.* **2012**, *51*, 11766-11769; c) H. Takahashi, S. Hediger, G. De Paëpe, *Chem. Commun.* **2013**, *49*, 9479-9481; d) A. J. Rossini, A. Zagdoun, M. Lelli, A. Lesage, C. Copéret, L. Emsley, *Acc. Chem. Res.* **2013**, *46*, 1942-1951; e) A. Lesage, M. Lelli, D. Gajan, M. A. Caporini, V. Vitzthum, P. Miéville, J. Alauzun, A. Roussey, C. Thieuleux, A. Mehdi, G. Bodenhausen, C. Coperet, L. Emsley, *J. Am. Chem. Soc.* **2010**, *132*, 15459-15461; f) T. Biedenbänder, A. Rodgers, M. Schröder, L. Vugmeyster, B. Corzilius, *J. Magn. Reson. Open* **2024**, *21*, 100161.
- [44] a) N. Bloembergen, *Physica* **1949**, *15*, 386-426; b) D. Suter, R. R. Ernst, *Phys. Rev. B* **1985**, *32*, 5608-5627; c) M. Ernst, B. Meier, in *Solid State NMR of Polymers, Vol. 84* (Eds.: T. Asakura, I. Ando), Elsevier Science, **1998**, pp. 83-122.
- [45] R. R. Ernst, G. Bodenhausen, A. Wokaun, *Principles of Nuclear Magnetic Resonance in One and Two Dimensions*, Clarendon Press, **1990**.
- [46] V. Aladin, B. Corzilius, *eMagRes* **2020**, *9*, 239-249.
- [47] A. Pines, M. G. Gibby, J. S. Waugh, *J. Chem. Phys.* **1972**, *56*, 1776-1777.
- [48] E. R. Bensons, Master's thesis, University of Rostock, **2024**.

- [49] F. Bloch, *Phys. Rev.* **1946**, *70*, 460-474.
- [50] A. G. Redfield, in *Adv. Magn. Opt. Reson., Vol. 1* (Ed.: J. S. Waugh), Academic Press, **1965**, pp. 1-32.
- [51] N. Bloembergen, E. M. Purcell, R. V. Pound, *Phys. Rev.* **1948**, *73*, 679-712.
- [52] I. Solomon, *Phys. Rev.* **1955**, *99*, 559-565.
- [53] a) M. G. Gibby, A. Pines, J. S. Waugh, *Chem. Phys. Lett.* **1972**, *16*, 296-299; b) J. L. White, J. F. Haw, *J. Am. Chem. Soc.* **1990**, *112*, 5896-5898; c) J. S. Higgins, A. H. Hodgson, R. V. Law, *J. Mol. Struct.* **2002**, *602-603*, 505-510; d) K. Takegoshi, T. Terao, *Journal of Chemical Physics* **2002**, *117*, 1700-1707.
- [54] a) K. Pervushin, R. Riek, G. Wider, K. Wüthrich, *Proc. Natl. Acad. Sci. U. S. A.* **1997**, *94*, 12366-12371; b) K. Pervushin, R. Riek, G. Wider, K. Wüthrich, *Journal of the American Chemical Society* **1998**, *120*, 6394-6400; c) R. Sprangers, L. E. Kay, *Nature* **2007**, *445*, 618-622; d) S. Schütz, R. Sprangers, *Prog. Nucl. Magn. Reson. Spectrosc.* **2020**, *116*, 56-84.
- [55] a) A. H. Linden, W. T. Franks, U. Akbey, S. Lange, B. J. van Rossum, H. Oschkinat, *J. Biomol. NMR* **2011**, *51*, 283-292; b) Q. Z. Ni, E. Markhasin, T. V. Can, B. Corzilius, K. O. Tan, A. B. Barnes, E. Daviso, Y. Su, J. Herzfeld, R. G. Griffin, *J. Phys. Chem. B* **2017**, *121*, 4997-5006.
- [56] O. B. Peersen, S. O. Smith, *Concepts Magn. Reson.* **1993**, *5*, 303-317.
- [57] R. N. Purusottam, G. Bodenhausen, P. Tekely, *Journal of Biomolecular NMR* **2013**, *57*, 11-19.
- [58] D. Daube, V. Aladin, J. Heiliger, J. J. Wittmann, D. Barthelmes, C. Bengs, H. Schwalbe, B. Corzilius, *J. Am. Chem. Soc.* **2016**, *138*, 16572-16575.
- [59] M. M. Hoffmann, S. Bothe, T. Gutmann, F.-F. Hartmann, M. Reggelin, G. Buntkowsky, *J. Phys. Chem. C* **2017**, *121*, 2418-2427.
- [60] a) J. Mao, V. Aladin, X. Jin, A. J. Leeder, L. J. Brown, R. C. D. Brown, X. He, B. Corzilius, C. Glaubitz, *J. Am. Chem. Soc.* **2019**, *141*, 19888-19901; b) V. Aladin, M. Vogel, R. Binder, I. Burghardt, B. Suess, B. Corzilius, *Angew. Chem., Int. Ed.* **2019**, *58*, 4863-4868; c) V. Aladin, B. Corzilius, *Solid State Nucl. Magn. Reson.* **2019**, *99*, 27-35; d) V. Aladin, P. A. Trenkler, B. Corzilius, *Exp. Results* **2020**, *1*, e10; e) V. Aladin, A. K. Sreemantula, T. Biedenbänder, A. Marchanka, B. Corzilius, *Chem. Eur. J.* **2023**, *29*,

- e202203443; f) T. Biedenbänder, E. R. Bensons, B. Corzilius, *ChemPhysChem* **2023**, *24*, e202300206.
- [61] a) M. M. Hoffmann, S. Bothe, T. Gutmann, G. Buntkowsky, *J. Phys. Chem. C* **2017**, *121*, 22948-22957; b) H. Park, B. Uluca-Yazgi, S. Heumann, R. Schlogl, J. Granwehr, H. Heise, P. P. M. Schleker, *J. Magn. Reson.* **2020**, *312*, 106688.
- [62] a) A. J. Horsewill, *Prog. Nucl. Magn. Reson. Spectrosc.* **1999**, *35*, 359-389; b) G. Usevičius, A. Eggeling, I. Pocius, V. Kalendra, D. Klose, M. Mączka, A. Pöpl, J. Banys, G. Jeschke, M. Šimėnas, in *Molecules*, Vol. 28, **2023**.
- [63] F. A. Perras, Y. Matsuki, S. A. Southern, T. Dubroca, D. F. Flesariu, J. Van Tol, C. P. Constantinides, P. A. Koutentis, *J. Chem. Phys.* **2023**, *158*.
- [64] L. Vugmeyster, D. Ostrovsky, J. J. Ford, A. S. Lipton, *J. Am. Chem. Soc.* **2010**, *132*, 4038-4039.
- [65] N. P. Benetis, I. A. Zelenetckii, Y. A. Dmitriev, *Low Temp. Phys.* **2019**, *45*, 427-440.
- [66] R. R. Vold, R. L. Vold, in *Advances in Magnetic and Optical Resonance*, Vol. 16 (Ed.: W. S. Warren), Academic Press, **1991**, pp. 85-171.
- [67] V. Macho, L. Brombacher, H. W. Spiess, *Appl. Magn. Reson.* **2001**, *20*, 405-432.
- [68] L. Vugmeyster, D. Ostrovsky, K. Penland, G. L. Hoatson, R. L. Vold, *J. Phys. Chem. B* **2013**, *117*, 1051-1061.
- [69] R. Santamaria, *Molecular Dynamics*, Springer Nature Switzerland, **2023**.
- [70] Y. Miao, Z. Yi, D. C. Glass, L. Hong, M. Tyagi, J. Baudry, N. Jain, J. C. Smith, *J Am Chem Soc* **2012**, *134*, 19576-19579.
- [71] H. Saitô, I. Ando, A. Ramamoorthy, *Prog. Nucl. Magn. Reson. Spectrosc.* **2010**, *57*, 181-228.
- [72] V. Ladizhansky, R. S. Palani, M. Mardini, R. G. Griffin, *Chem. Rev.* **2024**.
- [73] S. E. Ashbrook, *Phys. Chem. Chem. Phys.* **2009**, *11*, 6892-6905.
- [74] M. J. Bayro, M. Huber, R. Ramachandran, T. C. Davenport, B. H. Meier, M. Ernst, R. G. Griffin, *J. Chem. Phys.* **2009**, *130*, 114506.
- [75] a) E. R. Andrew, A. Bradbury, R. G. Eades, V. T. Wynn, *Phys. Lett.* **1963**, *4*, 99-100; b) E. R. Andrew, S. Clough, L. F. Farnell, T. D. Gledhill, I. Roberts, *Phys. Lett.* **1966**, *21*, 505-506; c) M. H. Levitt, D. P. Raleigh, F. Creuzet, R. G. Griffin, *J. Chem. Phys.* **1990**, *92*, 6347-6364; d) D. P. Raleigh, A. C. Kolbert, M. H. Levitt, R. G. Griffin, *Isr. J. Chem.*

- 1988**, 28, 263-269; e) D. P. Raleigh, M. H. Levitt, R. G. Griffin, *Chem. Phys. Lett.* **1988**, 146, 71-76; f) M. G. Colombo, B. H. Meier, R. R. Ernst, *Chem. Phys. Lett.* **1988**, 146, 189-196.
- [76] S. A. Southern, F. A. Perras, *J. Magn. Reson.* **2024**, 364, 107710.
- [77] G. Lipari, A. Szabo, *J. Am. Chem. Soc.* **1982**, 104, 4546-4559.
- [78] A. G. Palmer, III, M. Rance, P. E. Wright, *J. Am. Chem. Soc.* **1991**, 113, 4371-4380.
- [79] a) H. W. Spiess, H. Sillescu, *J. Magn. Reson. (1969-1992)* **1981**, 42, 381-389; b) A. S. Ulrich, S. L. Grage, *Stud. Phys. Theor. Chem.* **1998**, 84, 190-211; c) L. Vugmeyster, A. Rodgers, D. Ostrovsky, C. James McKnight, R. Fu, *J. Magn. Reson.* **2023**, 352, 107493.
- [80] G. Parigi, E. Ravera, C. Luchinat, *Prog. Nucl. Magn. Reson. Spectrosc.* **2019**, 114-115, 211-236.
- [81] I. V. Sergeev, C. M. Quinn, J. Struppe, A. M. Gronenborn, T. Polenova, *Magn. Reson.* **2021**, 2, 239-249.
- [82] E. R. Bensons, Bachelor's thesis, University of Rostock, **2022**.
- [83] J. J. Helmus, C. P. Jaroniec, *J. Biomol. NMR* **2013**, 55, 355-367.
- [84] P. Virtanen, R. Gommers, T. E. Oliphant, M. Haberland, T. Reddy, D. Cournapeau, E. Burovski, P. Peterson, W. Weckesser, J. Bright, S. J. van der Walt, M. Brett, J. Wilson, K. J. Millman, N. Mayorov, A. R. J. Nelson, E. Jones, R. Kern, E. Larson, C. J. Carey, Í. Polat, Y. Feng, E. W. Moore, J. VanderPlas, D. Laxalde, J. Perktold, R. Cimrman, I. Henriksen, E. A. Quintero, C. R. Harris, A. M. Archibald, A. H. Ribeiro, F. Pedregosa, P. van Mulbregt, A. Vijaykumar, A. P. Bardelli, A. Rothberg, A. Hilboll, A. Kloeckner, A. Scopatz, A. Lee, A. Rokem, C. N. Woods, C. Fulton, C. Masson, C. Häggström, C. Fitzgerald, D. A. Nicholson, D. R. Hagen, D. V. Pasechnik, E. Olivetti, E. Martin, E. Wieser, F. Silva, F. Lenders, F. Wilhelm, G. Young, G. A. Price, G.-L. Ingold, G. E. Allen, G. R. Lee, H. Audren, I. Probst, J. P. Dietrich, J. Silterra, J. T. Webber, J. Slavič, J. Nothman, J. Buchner, J. Kulick, J. L. Schönberger, J. V. de Miranda Cardoso, J. Reimer, J. Harrington, J. L. C. Rodríguez, J. Nunez-Iglesias, J. Kuczynski, K. Tritz, M. Thoma, M. Newville, M. Kümmerer, M. Bolingbroke, M. Tartre, M. Pak, N. J. Smith, N. Nowaczyk, N. Shebanov, O. Pavlyk, P. A. Brodtkorb, P. Lee, R. T. McGibbon, R. Feldbauer, S. Lewis, S. Tygier, S. Sievert, S. Vigna, S. Peterson, S. More, T. Pudlik, T. Oshima, et al., *Nat. Methods* **2020**, 17, 261-272.
- [85] R. L. Johnson, K. Schmidt-Rohr, *J. Magn. Reson.* **2014**, 239, 44-49.

- [86] C. P. Jaroniec, C. Filip, R. G. Griffin, *J. Am. Chem. Soc.* **2002**, *124*, 10728-10742.
- [87] A. Bertarello, P. Berruyer, U. Skantze, S. Sardana, M. Sardana, C. S. Elmore, M. Schade, E. Chiarparin, S. Schantz, L. Emsley, *J. Magn. Reson.* **2021**, *329*, 107030.
- [88] a) R. Luxenhofer, A. Schulz, C. Roques, S. Li, T. K. Bronich, E. V. Batrakova, R. Jordan, A. V. Kabanov, *Biomaterials* **2010**, *31*, 4972-4979; b) K. Ulrich, Master's thesis, Julius-Maximilians-University Würzburg (Julius-Maximilians-University Würzburg), **2022**.
- [89] D. F. Au, D. Ostrovsky, R. Fu, L. Vugmeyster, *J. Biol. Chem.* **2019**, *294*, 5840-5853.
- [90] J. R. Harris, *Electron microscopy in biology: a practical approach*, Oxford University Press, Oxford, **1991**.
- [91] D. A. Torchia, *J. Magn. Reson. (1969-1992)* **1978**, *30*, 613-616.
- [92] a) K. R. Thurber, R. Tycko, *J. Magn. Reson.* **2009**, *196*, 84-87; b) P. Miéville, V. Vitzthum, M. A. Caporini, S. Jannin, S. Gerber-Lemaire, G. Bodenhausen, *Magn. Reson. Chem.* **2011**, *49*, 689-692.
- [93] P. A. Beckmann, E. Schneider, *J. Chem. Phys.* **2012**, *136*, 054508.
- [94] P. Berruyer, M. Gericke, P. Moutzouri, D. Jakobi, M. Bardet, L. Karlson, S. Schantz, T. Heinze, L. Emsley, *Carbohydr. Polym.* **2021**, *262*, 117944.
- [95] M. Gierth, Master's thesis, RWTH Aachen University, **2023**.
- [96] V. Ladizhansky, *Solid State Nucl. Magn. Reson.* **2009**, *36*, 119-128.
- [97] B. Corzilius, in *Paramagnetism in Experimental Biomolecular NMR* (Eds.: C. Luchinat, G. Parigi, E. Ravera), The Royal Society of Chemistry, **2018**, p. 0.
- [98] M. Brandt, Internship thesis, University of Rostock, **2024**.
- [99] V. Aladin, Dissertation, University of Rostock, **2021**.
- [100] W. A. Decatur, M. J. Fournier, *Trends Biochem. Sci.* **2002**, *27*, 344-351.
- [101] A. Lapinaite, B. Simon, L. Skjaerven, M. Rakwalska-Bange, F. Gabel, T. Carlomagno, *Nature* **2013**, *502*, 519-523.
- [102] J. F. Kuhn, E. J. Tran, E. S. Maxwell, *Nucleic Acids Res.* **2002**, *30*, 931-941.
- [103] a) A. Marchanka, B. Simon, G. Althoff-Ospelt, T. Carlomagno, *Nat. Commun.* **2015**, *6*, 7024; b) M. Ahmed, A. Marchanka, T. Carlomagno, *Angew. Chem., Int. Ed.* **2020**, *59*, 6866-6873.

- [104] N. K. Goto, K. H. Gardner, G. A. Mueller, R. C. Willis, L. E. Kay, *J. Biomol. NMR* **1999**, *13*, 369-374.
- [105] Ü. Akbey, W. T. Franks, A. Linden, S. Lange, R. G. Griffin, B.-J. van Rossum, H. Oschkinat, *Angew. Chem., Int. Ed.* **2010**, *49*, 7803-7806.
- [106] B. Reif, *Chem. Rev.* **2022**, *122*, 10019-10035.
- [107] A. Bertarello, P. Berruyer, M. Artelsmair, C. S. Elmore, S. Heydarkhan-Hagvall, M. Schade, E. Chiarparin, S. Schantz, L. Emsley, *J. Am. Chem. Soc.* **2022**, *144*, 6734-6741.
- [108] A. K. Schütz, T. Vagt, M. Huber, O. Y. Ovchinnikova, R. Cadalbert, J. Wall, P. Güntert, A. Böckmann, R. Glockshuber, B. H. Meier, *Angew. Chem., Int. Ed.* **2015**, *54*, 331-335.
- [109] D. Lee, S. Hediger, G. De Paëpe, *Solid State Nucl. Magn. Reson.* **2015**, *66-67*, 6-20.
- [110] a) J.-X. Lu, W. Qiang, W.-M. Yau, Charles D. Schwieters, Stephen C. Meredith, R. Tycko, *Cell* **2013**, *154*, 1257-1268; b) Nikolaos G. Sgourakis, W.-M. Yau, W. Qiang, *Structure* **2015**, *23*, 216-227.
- [111] F. Malz, H. Jancke, *J. Pharm. Biomed. Anal.* **2005**, *38*, 813-823.
- [112] A. F. Mehlkopf, D. Korbee, T. A. Tiggelman, R. Freeman, *J. Magn. Reson. (1969-1992)* **1984**, *58*, 315-323.
- [113] a) L. Di, H. E. Kerns, T. G. Carter, *Curr. Pharm. Des.* **2009**, *15*, 2184-2194; b) S. Sathigari, G. Chadha, Y. H. P. Lee, N. Wright, D. L. Parsons, V. K. Rangari, O. Fasina, R. J. Babu, *AAPS PharmSciTech* **2009**, *10*, 81-87; c) B. N. V. Hari, N. Narayanan, K. Dhevendaran, D. Ramyadevi, *Mater. Sci. Eng. C* **2016**, *67*, 522-532.
- [114] a) M. Pereira-Silva, I. Jarak, A. C. Santos, F. Veiga, A. Figueiras, *Eur. J. Pharm. Sci.* **2020**, *153*, 105461; b) X. Hou, T. Zaks, R. Langer, Y. Dong, *Nat. Rev. Mater.* **2021**, *6*, 1078-1094.
- [115] a) V. P. Torchilin, *Nat. Rev. Drug Discov.* **2005**, *4*, 145-160; b) E. Blanco, H. Shen, M. Ferrari, *Nat. Biotechnol.* **2015**, *33*, 941-951.
- [116] a) X. Zhang, H. Chibli, R. Mielke, J. Nadeau, *Bioconjugate Chem.* **2011**, *22*, 235-243; b) J. Li, S. Shen, F. Kong, T. Jiang, C. Tang, C. Yin, *RSC Adv.* **2018**, *8*, 24633-24640.
- [117] a) J. Viger-Gravel, A. Schantz, A. C. Pinon, A. J. Rossini, S. Schantz, L. Emsley, *J. Phys. Chem. B* **2018**, *122*, 2073-2081; b) Y. Guo, Y. Hu, X. Zheng, X. Cao, Q. Li, Z. Wei, Z. Zhu, S. Zhang, *Talanta* **2021**, *221*.

- [118] a) R. X. Zhuo, B. Du, Z. R. Lu, *J. Control. Release* **1999**, *57*, 249-257; b) Y. Huang, J. Lu, X. Gao, J. Li, W. Zhao, M. Sun, D. B. Stolz, R. Venkataramanan, L. C. Rohan, S. Li, *Bioconjugate Chem.* **2012**, *23*, 1443-1451; c) M. Dirksen, C. Dargel, L. Meier, T. Brändel, T. Hellweg, *Colloid Polym. Sci.* **2020**, *298*, 505-518.
- [119] a) A. J. Rossini, C. M. Widdifield, A. Zagdoun, M. Lelli, M. Schwarzwälder, C. Copéret, A. Lesage, L. Emsley, *J. Am. Chem. Soc.* **2014**, *136*, 2324-2334; b) A. C. Pinon, J. Schlagnitweit, P. Berruyer, A. J. Rossini, M. Lelli, E. Socie, M. Tang, T. Pham, A. Lesage, S. Schantz, L. Emsley, *J. Phys. Chem. C* **2017**, *121*, 15993-16005.
- [120] E. G. R. d. Sousa, E. M. d. Carvalho, R. A. d. S. San Gil, T. C. d. Santos, L. B. Borré, O. A. Santos-Filho, J. Ellena, *J. Pharm. Sci.* **2016**, *105*, 2656-2664.
- [121] A. G. Palmer, *J. Magn. Reson.* **2016**, *266*, 73-80.
- [122] G. Lipari, A. Szabo, *J. Am. Chem. Soc.* **1982**, *104*, 4559-4570.
- [123] T. Biedenbänder, V. de Jesus, M. Schmidt-Dengler, M. Helm, B. Corzilius, B. Fürtig, *Nucleic Acids Res.* **2022**, *50*, 2334-2349.
- [124] a) G. L. Olsen, D. C. Echodu, Z. Shajani, M. F. Bardaro, G. Varani, G. P. Drobny, *J. Am. Chem. Soc.* **2008**, *130*, 2896-2897; b) G. L. Olsen, M. F. Bardaro, Jr., D. C. Echodu, G. P. Drobny, G. Varani, *J. Am. Chem. Soc.* **2010**, *132*, 303-308; c) L. Vugmeyster, D. Ostrovsky, *J. Chem. Phys.* **2014**, *140*; d) X. Shi, C. M. Rienstra, *J. Am. Chem. Soc.* **2016**, *138*, 4105-4119; e) L. Vugmeyster, *Solid State Nucl. Magn. Reson.* **2021**, *111*, 101710; f) S. C. Döller, M. Brodrecht, N. B. Haro Mares, H. Breitzke, T. Gutmann, M. Hoffmann, G. Buntkowsky, *J. Phys. Chem. C* **2021**, *125*, 25155-25164; g) Ü. Akbey, *J. Magn. Reson.* **2021**, *327*, 106974.
- [125] a) T. Maly, G. T. Debelouchina, V. S. Bajaj, K. N. Hu, C. G. Joo, M. L. Mak-Jurkauskas, J. R. Sirigiri, P. C. van der Wel, J. Herzfeld, R. J. Temkin, R. G. Griffin, *J. Chem. Phys.* **2010**, *128*, 052211; b) A. J. Rossini, J. Schlagnitweit, A. Lesage, L. Emsley, *J. Magn. Reson.* **2015**, *259*, 192-198.
- [126] R. Harrabi, T. Halbritter, F. Aussenac, O. Dakhlaoui, J. van Tol, K. K. Damodaran, D. Lee, S. Paul, S. Hediger, F. Mentink-Vigier, S. T. Sigurdsson, G. De Paëpe, *Angew. Chem., Int. Ed.* **2022**, *61*, e202114103.
- [127] a) K. Takegoshi, M. Ito, T. Terao, *Chem. Phys. Lett.* **1996**, *260*, 159-165; b) D. Marks, N. Zumbulyadis, S. Vega, *J. Magn. Reson., Ser. A* **1996**, *122*, 16-36; c) M. Murakami, T. Shimizu, M. Tansho, K. Takegoshi, *Solid State Nucl. Magn. Reson.* **2009**, *36*, 172-

- 176; d) L. Müller, *Chem. Phys.* **1981**, *61*, 235-248; e) L. Müller, R. Eckman, A. Pine, *Chem. Phys. Lett.* **1980**, *76*, 149-154.
- [128] L. Vugmeyster, D. Ostrovsky, Matthew A. Clark, Isaac B. Falconer, Gina L. Hoatson, W. Qiang, *Biophys. J.* **2016**, *111*, 2135-2148.
- [129] a) A. B. Barnes, B. Corzilius, M. L. Mak-Jurkauskas, L. B. Andreas, V. S. Bajaj, Y. Matsuki, M. L. Belenky, J. Lugtenburg, J. R. Sirigiri, R. J. Temkin, J. Herzfeld, R. G. Griffin, *Phys. Chem. Chem. Phys.* **2010**, *12*, 5861-5867; b) M. J. Bayro, G. T. Debelouchina, M. T. Eddy, N. R. Birkett, C. E. MacPhee, M. Rosay, W. E. Maas, C. M. Dobson, R. G. Griffin, *J. Am. Chem. Soc.* **2011**, *133*, 13967-13974.
- [130] T. K. Chiu, J. Kubelka, R. Herbst-Irmer, W. A. Eaton, J. Hofrichter, D. R. Davies, *Proc. Natl. Acad. Sci. U. S. A.* **2005**, *102*, 7517-7522.
- [131] L. Vugmeyster, D. Ostrovsky, A. Rodgers, K. Gwin, S. L. Smirnov, C. J. McKnight, R. Fu, *Chem. Eur. J.* **2024**, *25*, e202300565.
- [132] a) G. L. Hoatson, *Journal of Magnetic Resonance (1969-1992)* **1991**, *94*, 152-159; b) R. L. Vold, W. H. Dickerson, R. R. Vold, *J. Magn. Reson. (1969-1992)* **1981**, *43*, 213-223.
- [133] a) M. Rosay, L. Tometich, S. Pawsey, R. Bader, R. Schauwecker, M. Blank, P. M. Borchard, S. R. Cauffman, K. L. Felch, R. T. Weber, R. J. Temkin, R. G. Griffin, W. E. Maas, **2010**, *12*, 5850-5860; b) J. Viger-Gravel, C. E. Avalos, D. J. Kubicki, D. Gajan, M. Lelli, O. Ouari, A. Lesage, L. Emsley, *Angew. Chem., Int. Ed.* **2019**, *58*, 7249-7253.
- [134] A. Mishra, M. A. Hope, G. Stevanato, D. J. Kubicki, L. Emsley, *J. Phys. Chem. C* **2023**, *127*, 11094-11102.
- [135] a) B. Reif, Y. Xue, V. Agarwal, M. S. Pavlova, M. Hologne, A. Diehl, Y. E. Ryabov, N. R. Skrynnikov, *J. Am. Chem. Soc.* **2006**, *128*, 12354-12355; b) Ü. Akbey, A. J. Nieuwkoop, S. Wegner, A. Voreck, B. Kunert, P. Bandara, F. Engelke, N. C. Nielsen, H. Oschkinat, *Angew. Chem., Int. Ed.* **2014**, *53*, 2438-2442; c) Ü. Akbey, *J. Biomol. NMR* **2022**, *76*, 23-28.
- [136] S. Chatterjee, A. Venkatesh, S. T. Sigurdsson, F. Mentink-Vigier, *J. Phys. Chem. Lett.* **2024**, *15*, 2160-2168.
- [137] J. Becker-Baldus, A. Yeliseev, T. T. Joseph, S. T. Sigurdsson, L. Zoubak, K. Hines, M. R. Iyer, A. van den Berg, S. Stepnowski, J. Zmuda, K. Gawrisch, C. Glaubitz, *ACS Omega* **2023**, *8*, 32963-32976.

- [138] S. R. Chaudhari, P. Berruyer, D. Gajan, C. Reiter, F. Engelke, D. L. Silverio, C. Copéret, M. Lelli, A. Lesage, L. Emsley, *Phys. Chem. Chem. Phys.* **2016**, *18*, 10616-10622.
- [139] F. A. Perras, S. L. Carnahan, W.-S. Lo, C. J. Ward, J. Yu, W. Huang, A. J. Rossini, *J. Chem. Phys.* **2022**, *156*, 124112.
- [140] a) E. A. Nanni, A. B. Barnes, Y. Matsuki, P. P. Woskov, B. Corzilius, R. G. Griffin, R. J. Temkin, *J. Magn. Reson.* **2011**, *210*, 16-23; b) M. Rosay, M. Blank, F. Engelke, *J. Magn. Reson.* **2016**, *264*, 88-98; c) A. Porea, C. Reiter, A. I. Dimitriadis, E. de Rijk, F. Aussenac, I. Sergeyev, M. Rosay, F. Engelke, *J. Magn. Reson.* **2019**, *302*, 43-49.
- [141] M. Brandt, Master's thesis, University of Rostock, **2024**.
- [142] S. Pothoczki, I. Pethes, L. Pusztai, L. Temleitner, K. Ohara, I. Bakó, *J. Phys. Chem. B* **2021**, *125*, 6272-6279.
- [143] G. M. Bernard, V. K. Michaelis, in *Handbook of High Field Dynamic Nuclear Polarization* (Eds.: V. K. Michaelis, R. G. Griffin, B. Corzilius, S. Vega), Wiley, **2020**.
- [144] L. Vugmeyster, D. Ostrovsky, A. S. Lipton, *J. Phys. Chem. B* **2013**, *117*, 6129-6137.

8. Acknowledgements

Writing a dissertation is a major undertaking that I would never have completed without the support of countless people.

Firstly, I want to thank my supervisor **Björn Corzilius**. Thank you for your unending wisdom and expertise. Thank you for appreciating some late submissions of abstracts, even if the deadline was closing in by the hour. Thank you for showing me a light at the end of the tunnel when everything was going wrong and giving me a lot of opportunities for travelling and presenting my work to an international audience. I will miss discussions starting with “*Ich hab das mal durchgerechnet...*”. And lastly, thank you for bringing some culture to this Ebbelwoi-missing place regional folk call Mecklenburg-Vorpommern.

Thanks to my second expert assessor **Prof. Dr. Thomas Vosegaard** for reading and grading this work.

I would also like to thank the Joachim Herz foundation for the financial and non-material support in form of the Add-on scholarship. Particularly, I want to thank **Dr. Karin Liau** and **Dr. Philipp Giesemann** as you both are tremendously helpful for arranging everything related to the Add-on scholarship and more.

Thanks to all my cooperation partners. Your work was much required for the result of this work. Thank you for the insightful discussions as well as the excellent quality of your provided samples. Thanks to **Dr. Alexander Marchanka** and **Arun Kumar Sreemantula** from University Hannover; **Dr. Jacqueline Heskamp** and **Christoph Kamper** from the University Medicine Rostock and Fraunhofer Institute for Cell Therapy and Immunology IZI; **Kersten Ulrich** and **Prof. Dr. Ann-Christin Pöppler** from the University of Würzburg; and **Prof. Dr. Liliya Vugmeyster** and **Aryana Rodgers** from the University of Colorado Denver; **Marcel Brandt** and **Dietmar Paschek** from the University of Rostock.

I want to thank my interns and students for your work during my PhD: **Eduard Mock** and **Edwards Bensons**. Especially, Eddy, as he was not only a student assistant, a Bachelor student, a scientific assistant, a Master student, and finally a colleague, but also one of my dearest friends in Rostock. Thank you for sharing an office with me and having an open ear for minor design questions. Thank you for always playing Star Wars Memes for procrastination.

You were an absolute necessity for improving the day-to-day work. I would lie if I wouldn't mention you as an integral part of my PhD. Now, you are truly free.

I want to thank my other colleagues as well: **Dr. Victoria Aladin**, which gave me the idea to start my PhD in Rostock. **Dr. Siavash Saeidpour** with whom I shared an office at the start. **Mirjam Schröder**, who joined the working group shortly after and who improved not only the daily work, but also the bouldering and sport climbing sessions. **Florian Taube**, who was an enrichment for work travels (together with Mirjam). I've always wondered why I did stay in time but thank you! And last, but not least, **Dorothea Kreiß**. Du warst und bist wirklich wundervoll. Auch wenn unsere Arbeitszeiten nur wenig überlappt haben, danke das du mich und Eddy währenddessen ausgehalten hast! And the newest member: **Ronja Rößler**. Welcome to the everyday chaos! I also want to thank **Kenneth Millow** and **Lasse Serger**, our newest collection of scientific assistants.

I want to thank the PIMP group: Vica and **Dr. Vanessa de Jesus**. Especially Vanie, who set me on this path. Without your enthusiasm and especially endurance, I may have been some lame biochemist working on membrane proteins. Instead, I ended up with NMR relaxation. I know that this is even worse from your perspective! Simultaneously, I want to thank **Dr. Boris Fürtig**. You and Vanessa were incredible and understanding supervisors and we ended my time in Frankfurt with nice results and a beautiful publication. I hope for future tRNA reunions!

I want to thank the other working groups of the institute (AG Ludwig, AG Wagner, and AG Boldt) for the nice environment, the funny Trotzenburg-Stammtische and other PC-Seminar-Nachbesprechungen. I want to thank **Anika Wilhelms** for the continuous support regarding laboratory stuff. I want to thank **David Kotwica**, **Lennart Kruse**, and Eddy for some afternoon “breaks” which we settled always on good terms.

I want to thank my friends, both from Rostock, Frankfurt, and Darmstadt. Special thanks to the Gulasch-Gruppe (**Oliver Siering**, **Roan Groh**, and **Dr. Jakob Silberberg**). You are and always will be one of the best! Without you, studying biochemistry would have been unexciting. I miss our Auswärtsfahrten and the Gulasch-Essen. At the same time, I want to thank **Julius Tamm** offering me always safe harbor in Darmstadt if I missed home. I am grateful for you for so many reasons. Thanks to the Bouldering crew in Rostock: **Franz**, **Arminius**, and **Simon**! And David, I will soon have time, therefore the question remains: Wann kluften?

In the end I want to thank my family. Meine Geschwister, **Anja, Jan** und **Lisa**. Ihr wart und seid ein riesengroßer Einfluss auf mein Leben. Auch wenn es dank der großen Distanz in den letzten Jahren schwierig war, sich zu treffen, freue ich mich immer auf das alljährliche Treffen an Weihnachten. **Meine Eltern**, ohne euch wäre das alles gar nicht möglich gewesen. Ohne euren Rückhalt und Unterstützung hätte ich nicht studieren können und wäre auch nicht der Mensch, der ich heute bin.

And finally, I want to thank my girlfriend: **Sophie**, danke für deinen unendlichen Support, vor allem in der letzten Zeit! Danke, dass du immer für mich da bist. Und vor allem: Danke, dass es dich in meinem Leben gibt!

9. Publications

1. **Thomas Biedenbänder**, Aryana Rodgers, Mirjam Schröder, Liliya Vugmeyster, Björn Corzilius. Investigation of biomolecular dynamics by sensitivity-enhanced ^1H - ^2H CPMAS NMR using matrix-free dynamic nuclear polarization. *J. Magn. Reson. Open* **2024**, 21, 100161.
2. **Thomas Biedenbänder**, Edvards R. Bensons, Björn Corzilius. Serial Polarization Transfer by Combination of Cross-Relaxation and Rotational Resonance for Sensitivity-Enhanced Solid-State NMR. *ChemPhysChem* **2023**, 24, e202300206.
3. Victoria Aladin, Arun K. Sreemantula, **Thomas Biedenbänder**, Alexander Marchanka, Björn Corzilius. Specific Signal Enhancement on an RNA-Protein Interface by Dynamic Nuclear Polarization. *Chem. Eur. J.* **2023**, 29, e202203443.
4. Vanessa de Jesus, **Thomas Biedenbänder**, Jennifer Vögele, Jens Wöhnert, Boris Fürtig. NMR assignment of non-modified tRNA^{Ile} from *Escherichia coli*. *Biomol. NMR Assign.* **2022**, 16, 165.
5. **Thomas Biedenbänder***, Vanessa de Jesus*, Martina Schmidt-Dengler, Mark Helm, Björn Corzilius, Boris Fürtig. RNA modifications stabilize the tertiary structure of tRNA^{Met} by locally increasing conformational dynamics. *Nucleic Acids Res.* **2022**, 50, 2334.
6. **Thomas Biedenbänder**, Victoria Aladin, Siavash Saeidpour, Björn Corzilius. Dynamic nuclear polarization for sensitivity enhancement in bio molecular solid-state NMR *Chemical Reviews* **2022**, 122, 9738.
7. Oliver Binas*, Vanessa de Jesus*, Tom Landgraf*, Albrecht E. Völklein*, Jason Martins, Daniel Hyman, Hannes Berg, Jasleen Kaur Bains, **Thomas Biedenbänder**, Boris Fürtig,** ^{19}F -NMR-based fragment screening for 14 different biologically active RNAs and 10 DNA and protein counter-screens. *ChemBioChem* **2021**, 22, 423.

* shared first authorship

** shortened list of authors

10. Conference contributions

Thomas Biedenbänder, Vanessa de Jesus, Harald Schwalbe Boris Fürtig. Biophysical Studies of prokaryotic initiator tRNA^{fMet}. **Poster Presentation**, *40th Danish NMR Meeting*, Korsør, Denmark, 2019

Thomas Biedenbänder, Vanessa de Jesus, Harald Schwalbe Boris Fürtig. Biophysical Studies of prokaryotic initiator tRNA^{fMet}. **Poster Presentation**, *15th EUROMAR/ISMAR 2019*, Berlin, Germany, 2019

Thomas Biedenbänder, Victoria Aladin, Björn Corzilius. The Role of Methyl Dynamics in DNP. **Poster Presentation**, *62nd ENC*, online conference, 2021.

Thomas Biedenbänder, Björn Corzilius. Dynamic Nuclear Polarization: NMR on steroids. **Oral Presentation**, *Departments Meeting of the Department Life, Light and Matter*, Rostock, Germany, 2021

Thomas Biedenbänder, Victoria Aladin, Björn Corzilius. The Role of Methyl Dynamics in DNP. **Poster Presentation**, *17th EUROMAR 2021*, online conference, 2021.

Thomas Biedenbänder, Victoria Aladin, Björn Corzilius. The Role of Methyl Dynamics in DNP. **Poster Presentation**, *42nd GDCh FGMR Annual Discussion Meeting*, online conference, 2021.

Thomas Biedenbänder, Victoria Aladin, Björn Corzilius. The Role of Methyl Dynamics in DNP. **Poster Presentation**, *18th EUROMAR 2022*, Utrecht, The Netherlands, 2022.

Thomas Biedenbänder, Victoria Aladin, Björn Corzilius. The Role of Methyl Dynamics in DNP. **Oral Presentation**, *61st Rocky Mountain Conference on Magnetic Resonance*, Copper Mountain, CO, USA, 2022.

Thomas Biedenbänder, Victoria Aladin, Björn Corzilius. The Role of Methyl Dynamics in DNP. **Round Table Discussion**, *2022 Alpine Conference on Magnetic Resonance in Solids*, Chamonix-Mont Blanc, France, 2022.

Thomas Biedenbänder, Victoria Aladin, Björn Corzilius. The Role of Methyl Dynamics in DNP. **Poster Presentation**, *43rd GDCh FGMR Annual Discussion Meeting*, Karlsruhe, Germany, 2022.

Thomas Biedenbänder, Björn Corzilius. Dipolar Recoupling in Solid-State NMR: Techniques and Applications towards SCREAM-DNP. **Oral Presentation**, *Perspectives of Physical and Theoretical Chemistry*, Bad Malente, Germany, 2023.

Thomas Biedenbänder, Victoria Aladin, Liliya Vugmeyster, Björn Corzilius. A ^2H approach towards the Role of Methyl Dynamics under DNP. **Oral Presentation**, *19th EUROMAR 2023*, Glasgow, UK, 2023.

Thomas Biedenbänder, Edvards R. Bensons, Victoria Aladin, Liliya Vugmeyster, Björn Corzilius. Methyl Dynamics and their Potential in low-temperature DNP-enhanced NMR. **Oral Presentation**, *Add-on Meeting of the Joachim Herz Foundation*, Jena, Germany, 2023.

Thomas Biedenbänder, Edvards R. Bensons, Björn Corzilius. Serial Polarization Transfer by Combination of Cross-Relaxation and Rotational Resonance for Sensitivity-Enhanced Solid-State NMR. **Oral Presentation**, *2023 Alpine Conference on Magnetic Resonance in Solids*, Chamonix-Mont Blanc, France, 2023.

Thomas Biedenbänder, Victoria Aladin, Liliya Vugmeyster, Björn Corzilius. A ^2H approach towards the investigation of Methyl Dynamics under DNP. **Oral Presentation**, *HYP23: International Hyperpolarization Conference*, Leipzig, Germany, 2023.

Thomas Biedenbänder, Edvards R. Bensons, Victoria Aladin, Liliya Vugmeyster, Björn Corzilius. Spin Talk: Understanding Dynamics despite of Paramagnetic Relaxation. **Oral Presentation**, *Perspectives of Physical and Theoretical Chemistry*, Bad Malente, Germany, 2024.

Thomas Biedenbänder, Marcel Brandt, Edvards R. Bensons, Aryana Rodgers, Mirjam Schröder, Liliya Vugmeyster, Björn Corzilius. Understanding Biomolecular Dynamics and Relaxation in DNP-enhanced solid-state NMR. **Poster Presentation**, *45th GDCh FGMR Annual Discussion Meeting*, Rostock, Germany, 2024.

